

Development of Approaches to Quantify Superloads and Their Impacts on the Iowa Road Infrastructure System

Final Report
September 2024



IOWA STATE UNIVERSITY
Institute for Transportation

Sponsored by
Iowa Highway Research Board
(IHRB Project TR-781)
Iowa Department of Transportation
(InTrans Project 19-726)

About the Program for Sustainable Pavement Engineering and Research

The overall goal of the Program for Sustainable Pavement Engineering and Research (PROSPER) is to advance research, education, and technology transfer in the area of sustainable highway and airport pavement infrastructure systems.

About the Institute for Transportation

The mission of the Institute for Transportation (InTrans) at Iowa State University is to save lives and improve economic vitality through discovery, research innovation, outreach, and the implementation of bold ideas.

Iowa State University Nondiscrimination Statement

Iowa State University does not discriminate on the basis of race, color, age, ethnicity, religion, national origin, pregnancy, sexual orientation, gender identity, genetic information, sex, marital status, disability, or status as a US veteran. Inquiries regarding nondiscrimination policies may be directed to the Office of Equal Opportunity, 3410 Beardshear Hall, 515 Morrill Road, Ames, Iowa 50011, telephone: 515-294-7612, hotline: 515-294-1222, email: eooffice@iastate.edu.

Disclaimer Notice

The contents of this report reflect the views of the authors, who are responsible for the facts and the accuracy of the information presented herein. The opinions, findings and conclusions expressed in this publication are those of the authors and not necessarily those of the sponsors.

The sponsors assume no liability for the contents or use of the information contained in this document. This report does not constitute a standard, specification, or regulation.

The sponsors do not endorse products or manufacturers. Trademarks or manufacturers' names appear in this report only because they are considered essential to the objective of the document.

Iowa DOT Statements

Federal and state laws prohibit employment and/or public accommodation discrimination on the basis of age, color, creed, disability, gender identity, national origin, pregnancy, race, religion, sex, sexual orientation or veteran's status. If you believe you have been discriminated against, please contact the Iowa Civil Rights Commission at 800-457-4416 or the Iowa Department of Transportation affirmative action officer. If you need accommodations because of a disability to access the Iowa Department of Transportation's services, contact the agency's affirmative action officer at 800-262-0003.

The preparation of this report was financed in part through funds provided by the Iowa Department of Transportation through its "Second Revised Agreement for the Management of Research Conducted by Iowa State University for the Iowa Department of Transportation" and its amendments.

The opinions, findings, and conclusions expressed in this publication are those of the authors and not necessarily those of the Iowa Department of Transportation.

Technical Report Documentation Page

1. Report No. IHRB Project TR-781	2. Government Accession No.	3. Recipient's Catalog No.	
4. Title and Subtitle Development of Approaches to Quantify Superloads and Their Impacts on the Iowa Road Infrastructure System		5. Report Date September 2024	
		6. Performing Organization Code	
7. Author(s) Yongsung Koh (orcid.org/0000-0003-0582-1898), Halil Ceylan (orcid.org/0000-0003-1133-0366), Sunghwan Kim (orcid.org/0000-0002-1239-2350), and In-Ho Cho (orcid.org/0000-0002-2265-9602)		8. Performing Organization Report No. InTrans Project 19-726	
9. Performing Organization Name and Address Program for Sustainable Pavement Engineering and Research Institute for Transportation Iowa State University 2711 South Loop Drive, Suite 4700 Ames, IA 50010-8664		10. Work Unit No. (TRAIS)	
		11. Contract or Grant No.	
12. Sponsoring Organization Name and Address Iowa Highway Research Board Iowa Department of Transportation 800 Lincoln Way Ames, IA 50010		13. Type of Report and Period Covered Final Report	
		14. Sponsoring Agency Code	
15. Supplementary Notes Visit https://intrans.iastate.edu for color pdfs of this and other research reports.			
16. Abstract <p>Superheavy loading vehicles, commonly referred to as superloads, exhibit non-standardized loading configurations along with high gross vehicle weights and axle loadings, all of which may cause unexpected distresses on Iowa road infrastructure systems compared to those caused by conventional vehicle class types categorized by the Federal Highway Administration. Superloads encompass various types of vehicles, including implements of husbandry and superheavy loads, prevalent in the Midwestern region of the United States. The determination of critical load factors affecting road damage due to superloads is intricate due to their non-standardized loading configurations and high loading capacities.</p> <p>This study developed methodologies to quantify superloads and evaluate their impact on Iowa's road infrastructure, encompassing jointed plain concrete pavements, flexible pavements, and granular roads. It employed extensive mechanistic-based numerical analysis, life-cycle cost analysis, artificial intelligence (AI)-based predictive modeling, forensic investigations, field data analysis, and prototype tool development, with the research aimed at comprehensively evaluating superload impacts on various road types and structures.</p> <p>Through extensive numerical analyses, incorporating both mechanistic and empirical methodologies, critical findings regarding the effects of different superload types on pavement and granular road distress, associated treatment cost, and service life reduction emerged. Moreover, the Road Infrastructure-Superload Analysis Tool (RISAT) developed in this study has the potential to provide a user-friendly platform for engineers and planners to evaluate structural damages and associated treatment costs induced by superload traffic. The integration of AI-based predictive models into the RISAT enables users to input pavement and superload properties to obtain highly accurate predictions of pavement damages, treatment costs, and service life reductions. Incorporating field data into the RISAT also enhanced its reliability and applicability to pavement management practices, providing engineers and planners with valuable insights for informed decision-making regarding pavement design, maintenance, and rehabilitation strategies.</p>			
17. Key Words artificial intelligence—implements of husbandry—Iowa road infrastructure—life-cycle cost analysis—RISAT—road damage-associated cost—structural damage analysis—superheavy loads—superloads		18. Distribution Statement No restrictions.	
19. Security Classification (of this report) Unclassified.	20. Security Classification (of this page) Unclassified.	21. No. of Pages 292	22. Price NA

DEVELOPMENT OF APPROACHES TO QUANTIFY SUPERLOADS AND THEIR IMPACTS ON THE IOWA ROAD INFRASTRUCTURE SYSTEM

**Final Report
September 2024**

Principal Investigator

Halil Ceylan, Professor and Director
Program for Sustainable Pavement Engineering and Research (PROSPER)
Institute for Transportation, Iowa State University

Co-Principal Investigators

Sunghwan Kim, Research Scientist
Institute for Transportation, Iowa State University

In-Ho Cho, Associate Professor
Iowa State University

Research Assistant

Yongsung Koh

Authors

Yongsung Koh, Halil Ceylan, Sunghwan Kim, and In-Ho Cho

Sponsored by
Iowa Highway Research Board and
Iowa Department of Transportation
(IHRB Project TR-781)

Preparation of this report was financed in part
through funds provided by the Iowa Department of Transportation
through its Research Management Agreement with the
Institute for Transportation (InTrans Project 19-726)

A report from
Institute for Transportation
Iowa State University
2711 South Loop Drive, Suite 4700
Ames, IA 50010-8664
Phone: 515-294-8103 / Fax: 515-294-0467
<https://intrans.iastate.edu>

TABLE OF CONTENTS

ACKNOWLEDGMENTS	xvii
EXECUTIVE SUMMARY	xix
CHAPTER 1. INTRODUCTION	1
Problem Statement	1
Research Objectives and Scope	1
Report Organization.....	2
CHAPTER 2. LITERATURE REVIEW	5
CHAPTER 3. SELECTION OF SUPERLOAD TYPES.....	11
CHAPTER 4. MECHANISTIC QUANTIFICATION OF SUPERLOAD IMPACTS ON RIGID PAVEMENTS	15
Characterization of Superloads: Critical Loading Location	15
Mechanistic Analysis for Potential Damage Evaluation: FEM-Based Analysis	21
LCCA for Mechanistic-Based Service Life Reduction and Permit Fee Decision	33
Development of AI-Based Prediction Models	48
Summary and Key Findings.....	67
CHAPTER 5. MECHANISTIC QUANTIFICATION OF SUPERLOAD IMPACTS ON FLEXIBLE PAVEMENTS.....	70
Characterization of Superloads: Nucleus Segment.....	70
Mechanistic Analysis for Potential Damage Evaluation: LET-Based Analysis	76
LCCA for Mechanistic-Based RSL and Permit Fee Decision.....	82
Development of AI-Based Prediction Models	88
Summary and Key Findings.....	104
CHAPTER 6. MECHANISTIC QUANTIFICATION OF SUPERLOAD IMPACTS ON GRANULAR ROADS.....	107
Characterization of Superloads: Nucleus Segment.....	107
Mechanistic Analysis for Potential Damage Evaluation: LET-Based Analysis	108
LCCA for Mechanistic-Based RSL and Permit Fee Decision.....	112
Development of AI-Based Prediction Models	116
Summary and Key Findings.....	121
CHAPTER 7. FORENSIC INVESTIGATION OF IOWA COUNTY ROADS AND HIGHWAYS	124
Forensic Investigation for Potential Instrumentation Sites	125
Forensic Investigation of Road Conditions According to Superload Traffic	139
Summary and Key Findings.....	143
CHAPTER 8. FIELD INSTRUMENTATION AND MONITORING	146
Field Instrumentation and Monitoring at JPCP Section	146
Field Instrumentation and Monitoring at Flexible Pavement Section	166
Field Instrumentation and Monitoring at Granular Road Section	184

Summary and Key Findings.....	196
CHAPTER 9. DEVELOPMENT OF USER-FRIENDLY PROTOTYPE TOOL FOR QUANTIFYING SUPERLOAD IMPACTS ON IOWA ROAD INFRASTRUCTURE	200
Integration of Superload and M-E Road Analysis Techniques into RISAT.....	200
Features of RISAT	204
CHAPTER 10. REPAIR, REHABILITATION, AND FUNDING ALTERNATIVES	212
CHAPTER 11. CONCLUSIONS	214
Overall Conclusions.....	214
Conclusions for JPCP Cases	215
Conclusions for Flexible Pavement Cases	217
Conclusions for Granular Road Cases	219
Conclusions for Development of Prototype Tool: RISAT	220
CHAPTER 12. RECOMMENDATIONS FOR IMPLEMENTATION AND FUTURE RESEARCH.....	222
REFERENCES	227
APPENDIX A. FORENSIC INVESTIGATION DATA	233
Forensic Investigation Data from Union County.....	233
Forensic Investigation Data from Keokuk County	238
Forensic Investigation Data from Monona County	240
Forensic Investigation Data from Tama County.....	244
APPENDIX B. INSTALLATION AND UTILIZATION OF P-WIM SYSTEM.....	245
Installation Process	245
Calibration of Piezoelectric Sensors	249
Traffic Data Collection	250
APPENDIX C. USER GUIDE FOR RISAT	253
Illustrative Example Using RISAT: Analysis for Dual-Row Modular SHL Traveling on JPCP	253
Illustrative Example Using RISAT: Analysis for Manure Tanker IoH Traveling on Flexible Pavement.....	264

LIST OF FIGURES

Figure 1. Loading locations across the PCC slab	16
Figure 2. Critical loading locations on the JPCP at the (a) bottom of PCC slab led by Kinze 1305 row crop, (b) bottom of PCC slab led by Goldhofer THP/SL-S, (c) top of PCC slab led by Kinze 1305 row crop, and (d) top of PCC slab led by Goldhofer THP/SL-S	17
Figure 3. Examples of influence-line stress responses for critical tensile stress	20
Figure 4. S-N curve using data from previous experimental tests for PCC slabs.....	23
Figure 5. Damage ratio analysis results: (a) the configuration of box-whisker plot, (b) box-whisker plots comparing damage ratios based on bottom-up transverse cracking of PCC slabs under IoHs, (c) damage ratios based on bottom-up transverse cracking of PCC slabs under SHLs, (d) damage ratios based on the top-down transverse cracking of PCC slabs under IoHs, and (e) damage ratios based on top-down transverse cracking of PCC slabs under SHLs	25
Figure 6. Loading locations across the PCC slab applying shoulder alternatives	30
Figure 7. Critical loading locations generating critical tensile stress: (a) at the bottom of PCC slab and (b) at the top of PCC slab led by Kinze 1305 flotation from category 1	31
Figure 8. Reduction rate of critical tensile stress compared to granular shoulder models at the (a) bottom of PCC slab under IoHs, (b) bottom of PCC slab under SHLs, (c) top of PCC slab under IoHs, and (d) top of PCC slab under SHLs	33
Figure 9. Overall flow chart for LCCA	35
Figure 10. Overall steps of RDAC determination for JPCP section subjected to superload	37
Figure 11. Determination of equivalent number of standard trucks from JPCP performance curve.....	38
Figure 12. Reduction in service life due to a single pass of superload for JPCP PCC layer: (a) with 0°F/in. temperature gradient, (b) with 4°F/in. temperature gradient, and (c) with -4°F/in. temperature gradient.....	40
Figure 13. Reduction in service life due to a single pass of dual-row modular SHL traveling on different JPCP structures with 0°F/in. temperature gradient	41
Figure 14. RDACs due to a single pass of superload types traveling at 25% of terminal service life of JPCP	42
Figure 15. RDACs due to a single pass of the three most damage-causing types of superload traveling at varying times on JPCP.....	43
Figure 16. RDACs due to a single pass of dual-row modular type SHL traveling at 25% of terminal service life of different JPCP structures' PCC layer: (a) with 0°F/in. temperature gradient, (b) with 4°F/in. temperature gradient, and (c) with -4°F/in. temperature gradient.....	45
Figure 17. Determination of critical loading locations of modular type SHL generating critical tensile stress at the bottom of PCC layer of JPCP	46
Figure 18. Increase rate of critical tensile stress at the bottom of the 8 in. thick PCC slab between JPCPs with 15 ft and 20 ft wide transverse joint spacings	47
Figure 19. RDACs of JPCP for different treatment types and discount rates when subjected to a single pass of the three most damage-causing types of superload carrying 50% payload level	48

Figure 20. Overall steps for ANN modeling for JPCPs under different superload types	50
Figure 21. Tenfold cross validation technique for ANN model performance evaluation	51
Figure 22. ANN model performances predicting the critical tensile stress at the bottom of the PCC slab when subjected to IoHs including (a) grain carts, (b) manure tankers, (c) agricultural trailers, and (d) agricultural trucks, and when subjected to SHLs including (e) single-row modular types, (f) dual-row modular types, and (g) drop-deck types.....	55
Figure 23. ANN model performances predicting the critical tensile stress at the top of the PCC slab when subjected to IoHs including (a) grain carts, (b) manure tankers, (c) agricultural trailers, and (d) agricultural trucks, and when subjected to SHLs including (e) single-row modular types, (f) dual-row modular types, and (g) drop-deck types	57
Figure 24. Performance evaluation of ANN models constructed with two hidden layers, seven neurons per each hidden layer, and five backpropagation algorithms when predicting critical tensile stress at the (a) bottom of the PCC slab and (b) top of the PCC slab	58
Figure 25. Architectural optimization of ANN models for the case of a dual-row modular type SHL constructed with the Bayesian Regularization algorithm when predicting critical tensile stress at the (a) bottom of the PCC slab and (b) top of the PCC slab	59
Figure 26. Sensitivity analysis results for the critical tensile stress at the bottom of a PCC slab when varying the JPCP structural variables including (a) PCC slab thickness, (b) composite modulus of subgrade reaction, and (c) temperature gradient, and when varying the loading variables including (d) axle weight and (e) Axle weight per a PCC slabPCC slab weight	63
Figure 27. Sensitivity analysis results for the critical tensile stress at the top of PCC slab when varying the JPCP structural variables including (a) PCC slab thickness, (b) composite modulus of subgrade reaction, and (c) temperature gradient, and when varying the loading variables including (d) axle weight and (e) Axle weight per a PCC slabPCC slab weight	66
Figure 28. Flow chart of the mechanistic-based analysis for flexible pavements under superloads.....	71
Figure 29. Overlapping of pavement responses according to the depth under a number of tire loadings of Goldhofer THP/SL-S	72
Figure 30. Incremental tire loads (a) and corresponding normalized critical vertical strain at the top of the subgrade right below the first tire load (b) of flexible pavement under Goldhofer THP/SL-S dual-row modular.....	73
Figure 31. Conceptual drawing of the superposition method	74
Figure 32. (a) Configuration of box-whisker plot and (b and c) the linear graphs for total rutting ratio of flexible pavements under IoHs and SHLs, respectively	80
Figure 33. Logarithmic graphs for bottom-up fatigue damage ratio of flexible pavements under (a) IoHs and (b) SHLs	80
Figure 34. Detailed steps for LCCA to determine RDACs of flexible pavements under superloads.....	83
Figure 35. RDACs related to the bottom-up fatigue cracking due to a single pass of superload traveling at 50% of terminal service life of flexible pavement	84

Figure 36. RDACs related to bottom-up fatigue cracking due to a single pass of the three most damage-causing types of superload traveling at a varying time on flexible pavement	85
Figure 37. RDACs related to the bottom-up fatigue cracking due to a single pass of single-row modular type SHL traveling at 50% of terminal service life of different flexible pavement structures	86
Figure 38. RDACs related to the bottom-up fatigue cracking due to a single pass of a superload with 50% payload level traveling at 50% of terminal service life of flexible pavements having different AC materials.....	87
Figure 39. RDACs of flexible pavement for different treatment types and payload levels due to a single pass of the three most bottom-up fatigue crack-causing types of superload	88
Figure 40. Overall steps for ANN modeling for flexible pavements under different superload types.....	89
Figure 41. ANN model performances predicting the critical horizontal tensile strain at the bottom of the AC layer when subjected to IoHs including (a) grain carts, (b) manure tankers, (c) agricultural trailers, and (d) agricultural trucks, and when subjected to SHLs including (e) single-row modular, (f) dual-row modular, and (g) drop-deck.....	93
Figure 42. ANN model performances predicting the critical vertical strain at 6 in. below the top of the subgrade when subjected to IoHs including (a) grain carts, (b) manure tankers, (c) agricultural trailers, and (d) agricultural trucks, and when subjected to SHLs including (e) single-row modular, (f) dual-row modular, and (g) drop-deck.....	95
Figure 43. Performance evaluation of ANN models constructed with two hidden layers, seven neurons per each hidden layer, and five backpropagation algorithms when predicting (a) critical tensile strain at the bottom of the AC layer and (b) critical vertical strain at 6 in. below the top of the subgrade	96
Figure 44. Architecture optimization of ANN models for the agricultural trailer case constructed with the Bayesian Regularization algorithm when predicting (a) critical tensile strain at the bottom of the AC layer, critical vertical strain at (b) 6 in. below the top of the subgrade, (c) mid-depth of the subbase layer, (d) mid-depth of the base layer, and (e) mid-depth of the AC layer	98
Figure 45. Sensitivity analysis results for the critical tensile strain at the bottom of AC layer when varying the flexible pavement structural variables including (a) AC layer thickness, (b) base layer, and (c) subbase layer, and when varying the loading variables including (d) axle weight and (e) Nucleus segment loadroad segment weight	101
Figure 46. Sensitivity analysis results for the critical vertical strain at 6 in. below the top of the subgrade when varying the flexible pavement structural variables including (a) AC layer thickness, (b) base layer, and (c) subbase layer, and when varying the loading variables including (d) axle weight and (e) Nucleus segment loadroad segment weight	103
Figure 47. Linear graphs for total rutting ratio of granular roads under (a) IoHs and (b) SHLs.....	111
Figure 48. Detailed steps for LCCA to determine RDAC of granular road under superload.....	112

Figure 49. RDACs related to the total rutting due to a single pass of superload traveling at 50% of terminal service life of granular road	113
Figure 50. RDACs related to the total rutting due to a single pass of the three most damage-causing types of superload traveling at a varying time on granular road.....	114
Figure 51. RDACs related to the total rutting due to a single pass of single-row modular SHL traveling at 50% of terminal service life of road structures with different top granular layer thickness	115
Figure 52. RDACs of granular road for different treatment types and payload levels due to a single pass of the three most total rutting-causing types of superload.....	116
Figure 53. Overall steps for ANN modeling for granular roads under different superloads	117
Figure 54. ANN model performances predicting the critical vertical strain at 150 mm below the top of the subgrade when subjected to IoHs including (a) grain carts, (b) manure tankers, (c) agricultural trailers, and (d) agricultural trucks, and when subjected to SHLs including (e) single-row modular, (f) dual-row modular, and (g) drop-deck types	120
Figure 55. Performance evaluation of ANN models constructed with two hidden layers, six neurons per each hidden layer, and five backpropagation algorithms when predicting critical vertical strain at 6 in. below the top of the subgrade	120
Figure 56. Architecture optimization of ANN models for dual-row modular SHL case constructed with the Bayesian Regularization algorithm when predicting critical vertical strain at (a) 6 in. below the top of the subgrade and (b) mid-depth of the top granular layer	121
Figure 57. High-speed profiler used for IRI measurement	125
Figure 58. Locations of forensic investigation sites in Union County: (a) Osage and North Osage streets and (b) Rea Road and Cherry Street	126
Figure 59. Summary of the forensic investigation results conducted in Union County at (a) Osage Street, (b) North Osage Street, (c) Cherry Street, and (d) Rea Road	127
Figure 60. Locations of forensic investigation sites in Keokuk County: 170th Street and 120th Avenue	129
Figure 61. Summary of the forensic investigation results conducted in Keokuk County at (a) 170th Street and (b) 120th Avenue.....	130
Figure 62. Locations of forensic investigation sites in Monona County: (a) Filbert Avenue, 295th Street, E60, and Linden Avenue and (b) K45 and 133rd Street.....	132
Figure 63. Summary of the forensic investigation results conducted in Monona County at (a) Filbert Avenue, (b) 295th Street, (c) E60 (JPCP), (d) E60 (composite pavement), (e) K45, and (f) 133rd Street	133
Figure 64. Locations of forensic investigation sites in Tama County: V18 and 190th, 200th, 220th, and 240th streets.....	137
Figure 65. Summary of the forensic investigation results conducted in Tama County at (a) V18 and (b) 190th, (c) 200th, (d) 220th, and (e) 240th streets	138
Figure 66. Travel route in Union County taken by a modular SHL during three consecutive days	140
Figure 67. Body configuration of modular SHL with dollies that traveled road sections in Union County	141

Figure 68. Distress severity survey at (a) Cherry Street - high severity section, (b) Cherry Street - low severity section, and (c) Rea Road before the first passage of SHL and after the third passage of SHL	143
Figure 69. Site information for K45	147
Figure 70. Major components of the data acquisition system: (a) strain gauge based on (b) Wheatstone bridge circuit, (c) thermistor, (d) STS4-16-TE4 (right) and ZL6 (left), and the (e) overall configuration of the remote data acquisition system operating in conjunction with the (f) P-WIM system	151
Figure 71. Pre-testing of the data acquisition system in the (a) laboratory, focusing particularly on the sensors: (b) strain gauges, (c) thermistor, and (d) moisture sensors	152
Figure 72. Sensor installation plan for JPCP section: (a) plane view and (b) cross-sectional view	153
Figure 73. JPCP reconstruction process: (a) excavation of existing composite pavement, (b) removal and (c) gradation, to (d) expose the subgrade soil.....	154
Figure 74. Pre-testing of each soil layer: (a) LWD test, (b) DCP test, and (c) sand cone test, and their (d) testing spots	155
Figure 75. Activities prior to PCC paving: (a) coring holes using a coring probe truck (b) down to the subgrade surface, (c) installing wooden structure and enclosure at the earth shoulder, and (d) building sensor trees.....	156
Figure 76. Overall steps of the data acquisition system installation: (a) installing moisture sensors and (b) sensor trees, (c) protecting sensor cables through flexible PVC pipe, (d) pre-placing concrete over sensor trees, (e) PCC paving, (f) connecting the external power supply, (g) installing P-WIM system, and (h) collecting the field data.....	158
Figure 77. In situ JPCP data collected on December 19, 2021 including (a) strain and (b) temperature in the PCC slab, and on June 19, 2022 including (c) strain and (d) temperature in the PCC slab.....	160
Figure 78. In situ JPCP data collected on December 19, 2021 including (a) water content and (b) temperature in soil layers, and on June 19, 2022 including (c) water content and (d) temperature in soil layers	161
Figure 79. Sets of figures of transportation vehicles (top-left), FEMs (top-right), in situ JPCP strain data (bottom-left), and FEM-based analysis results (bottom-right) for (a) class 9 truck, (b) overweight class 9 truck, (c) drop-deck SHL, and (d) agricultural truck	163
Figure 80. (a) MIRA ultrasonic tomograph and images of sensor trees embedded at (b) Center_Edge and (c) Center_Mid	165
Figure 81. (a) Schematic drawing of field data scaling and the (b) verification of field data using FEM-based analysis results	166
Figure 82. Site information for V18	167
Figure 83. Major components of the data acquisition system: (a) strain gauge, (b) soil compression sensor, (c) earth pressure cell, (d) STS4-16-TE4 (right) and ZL6 (left), and the (e) overall configuration of the remote data acquisition system	172
Figure 84. Sensor installation plan for full-depth flexible pavement section: (a) plane view and (b) cross-sectional view	173

Figure 85. Activities prior to data acquisition system installation: (a) installing a wooden structure, (b) investigating underground facilities via Iowa One Call, (c) preparing sensor trees, and (d) arranging an excavator.....	174
Figure 86. Steps of the data acquisition system installation: (a) pre-cutting a portion of the road, (b) trench cutting for the PVC pipe route, (c) excavating the designated portion of the road, (d) installing the sensors, (e) protecting sensor cables through flexible PVC pipe, (f) repairing the damaged road, (g) connecting the external power supply, and (h) installing P-WIM system.....	176
Figure 87. In situ full-depth flexible pavement data collected on June 2, 2023 including (a) strain and (b) temperature in the AC layer, and on November 2, 2023 including (c) strain and (d) temperature in the AC layer	178
Figure 88. In situ vertical displacement data measured at 6 in. below the top of the subgrade collected on (a) June 2, 2023, and (b) on November 2, 2023	179
Figure 89. In situ full-depth flexible pavement data collected on June 2, 2023 including (a) water content and (b) temperature in soil layers, and on November 2, 2023 including (c) water content and (d) temperature in soil layers.....	180
Figure 90. Pavement response of the sensor installation section to the (a) passage of a class 9 truck, exhibiting the resulting horizontal strain at the bottom of the AC layer through (b) LET-based analysis and (c) in situ AC layer strain data, and the resulting vertical strain at 6 in. below the top of the subgrade via (d) LET-based analysis and (e) in situ subgrade strain data.....	181
Figure 91. Pavement response of the sensor installation section to the (a) passage of an agricultural truck, exhibiting the resulting horizontal strain at the bottom of the AC layer through (b) LET-based analysis and (c) in situ AC layer strain data, and the resulting vertical strain at 6 in. below the top of the subgrade via (d) LET-based analysis and (e) in situ subgrade strain data	182
Figure 92. Site information for 190th Street.....	185
Figure 93. (a) Sensors of the data acquisition system including (b) soil compression sensors, (c) thermistors, (d) earth pressure cell, and the (e) overall configuration of the remote data acquisition system	188
Figure 94. Sensor installation plan for granular road section: (a) plane view and (b) cross-sectional view	189
Figure 95. Steps of the sensor installation: (a) trench cutting for the PVC pipe route, (b) excavating the designated area of the road, (c) installing the sensors, (d) protecting sensor cables through flexible PVC pipe, (e) backfilling and compacting the damaged road, and (f) activating the external power supply.....	191
Figure 96. In situ granular road data including (a) vertical displacement and (b) temperature collected on June 4, 2023, and (c) vertical displacement and (d) temperature collected on November 4, 2023	192
Figure 97. In situ granular road data collected on June 4, 2023 including (a) water content and (b) temperature in each layer, and on November 4, 2023 including (c) water content and (d) temperature in each layer	193

Figure 98. Granular road response of the sensor installation section to the (a) passage of a class 9 truck, exhibiting the resulting vertical strain at the mid-depth of the top granular layer through (b) LET-based analysis and (c) in situ strain data, and the resulting vertical strain at 6 in. below the top of the subgrade via (d) LET-based analysis and (e) in situ strain data	194
Figure 99. Granular road response of the sensor installation section to the (a) passage of an agricultural truck, exhibiting the resulting vertical strain at the mid-depth of the top granular layer through (b) LET-based analysis and (c) in situ strain data, and the resulting vertical strain at 6 in. below the top of the subgrade via (d) LET-based analysis and (e) in situ strain data	195
Figure 100. Flowchart of RISAT employing ANN-based prediction models for JPCP analysis under various superload types	201
Figure 101. Flowchart of RISAT employing ANN-based prediction models for flexible pavement analysis under various superload types	201
Figure 102. Interface of the navigation panels of RISAT: (a) predictive model selection, (b) road type selection, (c) superload type selection, (d) question, and (e) basic information input.....	205
Figure 103. A sub-tool of the RISAT designed for JPCP analysis under the grain cart category	206
Figure 104. Details of sub-tool components of RISAT: (a) basic project and road information, (b) pavement structural properties, (c) recommended input range and value, (d) schematic drawing depicting pavement structure, (e) loading properties of the superload, (f) additional information for M-E analysis, and (g) analysis results	209
Figure 105. Additional functions of sub-tool: (a) buttons for accessing developer details, research documentation, and analysis and design specifications and criteria and (b) buttons for exporting results, cleaning cells, and going back to the navigation panel	210
Figure 106. A sub-tool of the RISAT designed for flexible pavement analysis under the single-row modular SHL category	211
Figure 107. Contents of the output Excel file providing a table summarizing the outputs	211
Figure 108. Integration of RISAT into pavement asset management protocols	222
Figure 109. Representative distresses and features of each road section: (a) Osage Street, (b) North Osage Street, (c) Rea Road, and (d) Cherry Street	234
Figure 110. Cross-sectional structural information for (a) Cherry Street and (b) Rea Road.....	236
Figure 111. Comparison of distress severities before and after the third passage of the modular SHL over (a) Cherry Street and (b) Rea Road.....	238
Figure 112. Representative distresses of each road section: (a) 170th Street and (b) 120th Avenue	239
Figure 113. Proposed cross-sectional structural information of unbound PCC overlay project for 170th Street, scheduled for June 2021.....	240
Figure 114. Representative distresses of each road section: (a) K45, (b) E60 (AC-surfaced pavement section), (c) E60 (PCC-surfaced pavement section), (d) Filbert Avenue, and (e) 295th Street.....	243

Figure 115. Proposed cross-sectional structural information of reconstruction projects on (a) E60 and 295th Street and (b) K45 scheduled for October 2021 and July 2021, respectively	243
Figure 116. Representative distresses and features of V18	244
Figure 117. Main components of a P-WIM system: (a) TRS unit, (b) piezoelectric sensors, (c) piezo channel box, (d) mastic tapes, and (e) metal plates	246
Figure 118. Installation procedures of a P-WIM system	248
Figure 119. Class 6 trucks provided by Monona County engineer (top) and Tama County engineer (bottom)	249
Figure 120. An example of measurement data collected from Monona County	251
Figure 121. An example of measurement data collected from Tama County	251
Figure 122. Initiate Microsoft Excel-based file named RISAT.xlsm	254
Figure 123. RISAT navigation panel asking users to choose predictive model type	254
Figure 124. RISAT navigation panel asking users to choose pavement system	255
Figure 125. RISAT navigation panel asking users to choose superload type.....	256
Figure 126. RISAT navigation panel asking users to answer basic inquiries regarding the availability of property information related to the chosen pavement system (top) and superload (bottom)	258
Figure 127. RISAT navigation panel asking users to input basic project information.....	259
Figure 128. Details of RISAT sub-tool components for JPCP analysis: (a) basic project information, (b) JPCP structural properties, (c) recommended input range and value, and (d) schematic drawing depicting JPCP pavement structure	260
Figure 129. Details of RISAT sub-tool components for JPCP analysis including superload properties (top) and schematic drawing depicting loading configuration of superload (bottom)	262
Figure 130. Details of RISAT sub-tool components for JPCP analysis, requesting additional information for M-E analysis and providing options for data scaling	263
Figure 131. RISAT outputs related to JPCP under dual-row modular SHL.....	263
Figure 132. Excel-based output file generation from RISAT regarding JPCP analysis under dual-row modular SHL	264
Figure 133. Details of RISAT sub-tool components for flexible pavement analysis: (a) basic project information, (b) flexible pavement structural properties, (c) recommended input range and value, and (d) schematic drawing depicting flexible pavement structure	267
Figure 134. Details of RISAT sub-tool components for flexible pavement analysis including superload properties (top) and schematic drawing depicting loading configuration of superload (bottom)	268
Figure 135. Details of RISAT sub-tool components for flexible pavement analysis, requesting additional information for M-E analysis and providing options for data scaling.....	269
Figure 136. RISAT outputs related to flexible pavement under manure tanker IoH.....	269
Figure 137. Excel-based output file generation from RISAT regarding the flexible pavement analysis under manure tanker IoH	270

LIST OF TABLES

Table 1. A summary of definitions of superload in different states.....	5
Table 2. An overview of general and OS/OW traffic permits in the state of Iowa	8
Table 3. Previous studies on the impacts of superloads on pavement systems	10
Table 4. Visual descriptions and details of IoHs carrying 100% payload level	11
Table 5. Visual descriptions and details of SHLs carrying 100% payload level.....	13
Table 6. Categorization of critical loading locations of IoHs	18
Table 7. Categorization of critical loading locations of SHLs.....	19
Table 8. Comprehensive experimental matrices for JPCP FEA	22
Table 9. Averaged damage ratios of JPCPs under IoHs using different transfer functions.....	27
Table 10. Averaged damage ratios of JPCPs under SHLs using different transfer functions	28
Table 11. Comprehensive analysis matrices for FEA and LCCA	34
Table 12. Comprehensive analysis matrix for JPCP FEA	51
Table 13. Details of multilayer ANN modeling for JPCPs under superloads	52
Table 14. Explanatory variable ranges for sensitivity analysis of JPCPs under superloads.....	60
Table 15. Summary of sensitivity analysis results for JPCPs under superloads.....	67
Table 16. Linear calculation of critical pavement responses by superposition method	75
Table 17. Number of tire loads in a nucleus segment of different superload types.....	76
Table 18. Comprehensive analysis matrix for LET-based flexible pavement analysis	77
Table 19. Averaged damage ratios of flexible pavements under superloads.....	81
Table 20. Details of multilayer ANN modeling for flexible pavements under superloads	91
Table 21. Explanatory variable ranges for sensitivity analysis of flexible pavements under superloads.....	99
Table 22. Summary of sensitivity analysis results for flexible pavements under superloads.....	104
Table 23. Number of tire loads in a nucleus segment of different superload types.....	108
Table 24. Comprehensive analysis matrix for LET-based granular road analysis	109
Table 25. Averaged damage ratios of granular roads under superloads	111
Table 26. Details of multilayer ANN modeling for granular roads under superloads.....	118
Table 27. Items and locations for forensic investigations.....	124
Table 28. Traffic type and volume for a specific hour surveyed on May 7, 2020.....	128
Table 29. Traffic type and volume for a specific hour surveyed on April 1, 2021.....	130
Table 30. Traffic type and volume for a specific hour surveyed on April 29, 2021.....	135
Table 31. Traffic type and volume for a specific hour surveyed on July 7, 2022	139
Table 32. Loading information of modular SHL with and without an engine block.....	141
Table 33. Summary of road section information under JPCP reconstruction.....	148
Table 34. Brief specifications of data acquisition system components for JPCP	149
Table 35. Summary of pre-testing results for each soil layer in two potential field instrumentation sections.....	155
Table 36. Summary of FEM information implementing K45 and traffic loads	164
Table 37. Summary of V18 information.....	168
Table 38. Brief specifications of data acquisition system components for flexible pavement....	170
Table 39. Summary of LET-based model information implementing V18 and traffic loads.....	183
Table 40. Summary of 190th Street information	185
Table 41. Brief specifications of data acquisition system components for granular road	187
Table 42. LET-based model information implementing 190th Street and traffic loads	196

Table 43. Input and output variables in RISAT when analyzing JPCPs	202
Table 44. Input and output variables in RISAT when analyzing flexible pavements	203
Table 45. Calibration of the P-WIM systems installed at K45 and V18	250
Table 46. Input variables applied to RISAT for analysis of JPCP under dual-row modular SHL	253
Table 47. Input variables applied to RISAT for analysis of flexible pavement under manure tanker IoH.....	265

ACKNOWLEDGMENTS

The authors gratefully acknowledge sponsorship for this project from the Iowa Department of Transportation (DOT) and the Iowa Highway Research Board (IHRB).

The authors gratefully acknowledge the project technical advisory committee (TAC) members, including Karen Albert (Montgomery County), Lee Bjerke (Iowa County Engineers Association Service Bureau [ICEASB]), Zach Gunsolley (Iowa DOT), Todd Kinney (Clinton County), Brian Moore (ICEASB), Mark Nahra (Woodbury County), John Riherd (Butler County), Brad Skinner (Appanoose County), Jacob Thorius (Washington County), and Danny Waid (formerly ICEASB), for their guidance, support, and direction throughout the research.

Special thanks are also extended to Ben Daleske (Tama County), Lyle Brehm (formerly Tama County, now Poweshiek County), and Dustin Wallis (formerly Monona County) for their generous assistance and significant contributions in sharing information and experiences related to field instrumentation. The authors express sincere gratitude to Brian Keierleber (Buchanan County) and Andrew McGuire (Keokuk County) for their assistance in forensic investigations. Furthermore, the authors extend their heartfelt appreciation to the research team members from the Institute for Transportation's Program for Sustainable Pavement Engineering and Research (PROSPER) at Iowa State University for their timely assistance during the course of this project.

EXECUTIVE SUMMARY

In contrast to conventional vehicle classifications outlined by the Federal Highway Administration (FHWA), transportation vehicles for superheavy payloads, termed superloads in this study, have presented a considerable risk to the sustainability of road infrastructure. Such superloads, which carry a diverse range of heavy cargo such as agricultural and livestock products, excavators, and wind towers, pose a significant threat to the resilience of road systems due to their substantial weight and unconventional loading configurations. The determination of critical load factors impacting road damage resulting from superloads is complex and is influenced not only by the numbers of tires and axles but also by variables that include tire pressure and tire types. The configurations of tires and axles, along with their respective load distributions, have emerged as pivotal considerations in predicting pavement or granular road damages caused by the operation of heavy transportation vehicles. These concerns are further exacerbated by the general industry trend favoring high-capacity and efficiency-oriented transportation vehicles for transporting significantly heavy and bulky agricultural commodities or industrial products. Superloads are discernible from conventional vehicles not only by their high gross vehicle weights (GVWs) and axle loads, often exceeding state permit limits, but also by their non-standardized tire and axle arrangements characterized by a wide spectrum of dimensions encompassing number, spacing, and loading. Such non-standardized loading configurations constitute a primary factor contributing to unexpected road damages particularly evident in the Midwestern region of the United States.

Two prominent categories of superloads include implements of husbandry (IoHs) and superheavy loads (SHLs). An IoH typically consists of a tractor-trailer combination or solely a tractor, with the primary weight distribution predominantly concentrated on the rear axle group due to cargo placement. In contrast, SHLs are characterized by non-generic body configurations equipped with numerous tires and axles to transport exceptionally heavy cargo such as large engine blocks or wind turbines. Standardizing SHLs within FHWA classifications presents a formidable challenge in that the permit criteria for SHLs in the United States vary from state to state, with some states granting permits by GVW, axle weight, and tire weight, while other states grant their permits by performing a mechanistic road analysis that reflects actual road conditions. Both IoHs and SHLs typically exhibit characteristics such as high GVW or single-axle weight, often surpassing 96 kips or 24 kips, respectively, particularly grain carts and tank wagons operating on highways. Moreover, their total vehicle width may exceed lane widths due to wide transverse tire spacing or a large number of tires per axle. Their slow-moving nature can also potentially lead to increased damage on pavement and granular road systems.

Establishment of permits based on GVW or axle weight, rooted in the evaluation of potential structural damage induced by overweight traffic, has significantly influenced road design and service-life determination practices. A widely utilized method for evaluating structural damage, the generalized fourth-power law derived from the American Association of State Highway Officials (AASHTO) Road Test, offers a simplified means of estimating pavement damage in relation to traffic load, emphasizing a power-of-four relationship. However, this approach has a definite limitation in that it can only calculate lumped pavement damage for sufficiently thick pavement and specific loads rather than separately calculating different types of structural damage. In line with the transition toward mechanistic-empirical (M-E) analysis and design

paradigms, contemporary pavement analysis and design tools, such as the AASHTOWare Pavement ME Design software, include integrated advanced methodologies. AASHTOWare Pavement ME Design software employs JULEA, a layered elastic theory (LET)-based pavement analysis program, in its framework for estimating flexible pavement responses and uses artificial neural network (ANN) models as surrogate models for finite element models (FEM) in estimating rigid-pavement responses. Despite the capabilities of the AASHTOWare Pavement ME Design software in supporting comprehensive pavement design under various traffic loadings, challenges persist in predicting extrapolated mechanistic pavement responses, particularly for non-standardized loading configurations encountered in superloads like IoHs and SHLs. These challenges are compounded by their elevated GVWs or axle weights, rendering the mechanistic basis for predicting pavement and granular road distresses notably intricate.

The primary objective of this study was to develop approaches to quantifying these kinds of superloads and their impact on the Iowa road infrastructure system. This study specifically addressed significant research needs including (1) development of methods and tools that the Iowa Department of Transportation (DOT) and county engineers can use to evaluate superloads to determine their impact on the life of pavement structures and granular roads and their service lives, (2) identification of methods for repairing and rehabilitating existing Iowa road structures, and (3) suggestions for possible funding options for offsetting the resulting damages induced by superload traffic.

The culmination of this research effort yielded comprehensive insights into the impacts of superloads on various road systems, including jointed plain concrete pavements (JPCPs), flexible pavements, and granular roads. Through extensive numerical analyses, incorporating both mechanistic and empirical methodologies, critical findings emerged regarding the effects of different superload types on pavement and granular road distresses, associated treatment costs, and service life reductions. Moreover, the development of the Road Infrastructure-Superload Analysis Tool (RISAT) provides a user-friendly platform for engineers and planners to evaluate the structural damages and associated treatment costs induced by superload traffic, enabling informed decision-making and efficient management of road infrastructure. This study not only advances understanding of the challenges posed by superloads on road infrastructure but also provides practical tools and methodologies for mitigating their detrimental effects. By addressing the complex interplay between superload characteristics and road responses, this research contributes to the development of sustainable strategies for preserving and maintaining Iowa's road network amidst the evolving demands of heavy transportation vehicles.

The key findings from this study and recommendations for implementation are outlined as follows:

- The study employed a multifaceted approach involving numerical analysis, life-cycle cost analysis (LCCA), artificial intelligence (AI)-based predictive modeling, forensic investigations, field data analysis, and prototype-tool development.
- More than 33,000 cases of JPCPs, 25,000 cases of flexible pavements, and 3,300 cases of granular roads were mechanistically analyzed while considering 34 types of superloads and

their payload levels. Grain carts and modular SHLs emerged as primary contributors to structural damage to all three road types.

- An LCCA was conducted using a database derived from numerical analysis. This facilitated the evaluation of road damage-associated costs (RDACs) and reduction in service life across all three road categories under diverse superload scenarios, emphasizing that grain carts and modular SHLs also exhibited significant impacts on treatment cost and service life reduction for all three road types.
- This study developed ANN-based prediction models tailored to predicting critical pavement and granular road responses under various superload conditions for JPCPs, flexible pavements, and granular roads. These models exhibited high accuracy in predicting critical pavement and granular road responses for evaluating fatigue-related damage in JPCPs, rutting and fatigue-related damages in flexible pavements, and rutting damage in granular roads.
- The research team conducted field instrumentation and monitoring on selected road sections to collect empirical data on pavement and granular road responses under superload traffic. Remote data acquisition systems comprised of various sensors and components were successfully installed on the selected road sections, supporting real-time monitoring of pavement and granular road responses under environmental conditions and traffic loads, especially for superload traffic. The field data collected were used to validate the mechanistic-based analysis models developed for JPCPs, flexible pavements, and granular roads.
- The RISAT was developed to offer a user-friendly interface for analyzing potential pavement damages and treatment costs under various superload scenarios. The ANN-based models were integrated into the RISAT, allowing users to input pavement and superload properties to obtain highly accurate predictions of pavement damages, treatment costs, and service life reductions. Incorporating field data into the RISAT enhanced its reliability and applicability in pavement management practices, providing engineers and planners with valuable insights for informed decision-making regarding pavement design, maintenance, and rehabilitation strategies.

CHAPTER 1. INTRODUCTION

Problem Statement

Iowa state law limits the weight of vehicles by axle and gross vehicle weight (GVW). While such laws standardize traditional vehicles by size and weight, the agricultural implement industry is a vehicle sector that has changed substantially in recent years, most notably in terms of manufacturing larger vehicles. This has resulted in heavier farm implements that, if filled to full capacity, can be substantially overweight in terms of current law. Similarly, there are other superloads and heavy traffic generators (e.g., non-divisible vehicles, trucks carrying wind turbines or engine blocks) that can potentially be overweight on Iowa's road infrastructure systems. Recently, with the enactment of Iowa Senate File 2376 in January 2023, there has been an allowance for permitted vehicles to exceed the gross weights specified in Iowa Code section 321.463 by up to 12%. This development has added complexity to the design of road infrastructure systems due to the increased challenges posed by overweight traffic. Local law enforcement typically does not have the equipment necessary to measure weights of overweight vehicles, so most counties report overloaded vehicles to the Iowa Department of Transportation (DOT) Motor Vehicle Division. However, response from the Iowa DOT's vehicle enforcement agency is not always timely, and many such reports receive no response at all. Given this legal and enforcement environment, when designing and constructing county roads, counties must adapt by accounting for the percentage of overweight vehicle traffic traveling on the county road system. Currently, since this percentage (i.e., percent superloads) is more or less subjective based on guesswork, there is a need for a better way of determining more accurate traffic types and counts that take into account the presence of superloads.

Research Objectives and Scope

The primary objective of this study was to develop approaches to quantifying superloads and their impact on the Iowa road infrastructure system by (1) developing methods and tools that the Iowa DOT and county engineers can use to evaluate the impacts of superloads on the life of pavement structures, (2) identifying methods for repairing and rehabilitating existing Iowa pavement structures and granular roads subjected to superloads, and (3) deriving possible funding options for offsetting pavement and granular road damages resulting from superload traffic. Specific objectives established to achieve these primary objectives include the following:

- Synthesize the impacts of superloads, including implements of husbandry (IoHs) and superheavy loads (SHLs), on pavement and granular road performance, and identify and evaluate other states' practices in this regard.
- Evaluate structural design features, bearing capacities, and field performance of Iowa highways and county roads heavily traveled by superloads.
- Quantify the impacts of superloads on both pavements and granular roads, evaluating structural damages and superload permit options.

- Perform life-cycle cost analysis (LCCA) to support road design and rehabilitation strategies for superloads and document the impacts of superloads through economic analysis.
- Develop a tool capable of offering a comprehensive evaluation of structural damages and their associated costs for pavements in the face of diverse superload scenarios.
- Provide funding alternatives to offset the damage done to granular and paved roads, including, but not limited to, options for legislative action, surcharges, impact fees, development fees, or licensing fees for superloads.
- Identify repair and rehabilitation alternatives to extend the service life of Iowa highways and county roads heavily traveled by superloads.

Report Organization

This report consists of 12 chapters and 3 appendices as follows:

- Chapter 1 presents an introductory section encompassing the problem statement, research objectives, and scope of the study.
- Chapter 2 provides a comprehensive literature review of previous studies related to IoHs' and SHLs' impacts on pavement and granular road systems, including damage evaluation, LCCA, data-driven modeling, and a discussion of the current status of legislative actions or permit fee decisions related to superload traffic with non-standardized/non-divisible loading configurations.
- Chapter 3 furnishes detailed specifications of representative superloads selected for this study, covering a diverse range of types commonly encountered on Iowa highways and county roads.
- Chapter 4 presents a mechanistic-based analysis procedure and corresponding results for rigid pavements, specifically focusing on jointed plain concrete pavements (JPCPs), under superload traffic. To conduct the JPCP analysis under superloads, a meticulously detailed methodology is discussed, outlining step-by-step procedures for determining mechanistic-based loading inputs of various superload types. This facilitated the implementation of finite element model (FEM)-based JPCP analysis, utilizing experimental matrices composed of Iowa JPCP structures and superloads. A mechanistic basis for permit fee decisions is suggested through performing LCCA, using finite element analysis (FEA) results as a foundational database. Surrogate data-driven models were then constructed based on the FEA results, ensuring high accuracy in predicting critical pavement responses related to representative structural damages of JPCPs when subjected to a single pass of various superload types, thereby extensively broadening the scope of constrained mappings in terms of loading variables.

- Chapter 5 presents a mechanistic-based analysis procedure and corresponding results for full-depth flexible pavements under superload traffic. To conduct the flexible pavement analysis under superloads, a detailed methodology (i.e., nucleus segment approach) to determine mechanistic-based loading inputs of various superload types was adopted. This facilitated the implementation of layered elastic theory (LET)-based flexible pavement analysis, utilizing experimental matrices composed of Iowa flexible pavement structures and superloads. A mechanistic basis for permit fee decisions is suggested again for flexible pavement systems through performing LCCA, using LET-based analysis results as a foundational database. Surrogate data-driven models were constructed based on the LET-based analysis results, ensuring high accuracy in predicting critical pavement responses related to representative structural damages of flexible pavements when subjected to a single pass of various superload types.
- Chapter 6 presents a mechanistic-based analysis procedure and corresponding results for granular roads under superload traffic. To conduct the granular road analysis under superloads, nucleus segments, mechanistic-based loading inputs, of various superload types were determined and described. LET-based granular road analysis results are presented, utilizing experimental matrices composed of Iowa granular road structures and superloads. A mechanistic basis for permit fee decisions is again suggested for granular road systems through performing LCCA, using LET-based analysis results as a foundational database. Surrogate data-driven models were constructed based on the LET-based granular road analysis results, ensuring high accuracy in predicting critical road responses related to rutting damage of granular roads when subjected to a single pass of various superload types.
- Chapter 7 describes forensic investigations conducted at potential field instrumentation sites, including rigid pavement, flexible pavement, and granular road sections heavily traveled by superloads. The chapter presents on-site investigations of road sections subjected to heavily-loaded SHLs, providing an empirical evaluation of the impacts of superload traffic on the respective road systems.
- Chapter 8 provides the overall detailed field instrumentation procedures covering every aspect ranging from sensor preparation to installation. The chapter details the installation of remote data acquisition systems and a portable weigh-in-motion (P-WIM) system used on three different road systems to measure JPCP, full-depth flexible pavement, and granular road sections. In situ monitoring data collected from the data acquisition systems underwent meticulous evaluation and verification through mechanistic-based computational analysis results.
- Chapter 9 introduces a user-friendly prototype analysis tool, the Road Infrastructure-Superload Analysis Tool (RISAT), developed for the Iowa DOT and city and county engineers for efficiently quantifying superload impacts on Iowa road infrastructure.
- Chapter 10 suggests practical options in terms of repair and rehabilitation alternatives to extend the service life of Iowa highways and county roads heavily traveled by superloads, and funding alternatives intended to offset damage to Iowa pavements and granular roads.

- Chapter 11 provides comprehensive research conclusions derived from the entire study, presenting detailed mechanistic and empirical findings and recommendations for each road system subjected to superload traffic.
- Chapter 12 summarizes recommendations for implementation and presents an outline of future research directions suggested by the findings of this study.
- Appendix A presents the detailed results of the forensic investigations conducted in Union, Keokuk, Monona, and Tama Counties.
- Appendix B outlines the detailed methodologies for the installation, calibration, and data collection processes of the P-WIM system.
- Appendix C provides a comprehensive RISAT user guide, presenting illustrative examples to facilitate its practical usage.

CHAPTER 2. LITERATURE REVIEW

The term superload has emerged to describe non-standardized/non-divisible vehicles that significantly deviate from the traditional vehicle classes defined by the Federal Highway Administration (FHWA) (FHWA 2014). Such superloads, including IoHs carrying manure or agricultural products and SHLs carrying wind turbines or huge engine blocks, exceed the dimensions stipulated by state permit limits, posing challenges for both local roads and highways. In other words, IoHs and SHLs designed for transporting heavy cargo have unique loading configurations with varying tire sizes and arrangements, making it challenging to predict pavement or granular road damages using traditional analysis approaches.

State regulations for superload permits vary, with some states considering factors such as GVW, axle weight, or tire weight, while others perform mechanistic pavement analysis to establish permit limits and fees. The Texas Department of Motor Vehicles, for example, sets criteria based on GVW and maximum permissible axle weight or axle group weight, defining an SHL as a vehicle that exceeds 254,300 lb GVW or maximum permissible axle weight or axle group weight, or exceeds 200,000 lb for axle spacing less than 95 ft (TxDMV 2024). Iowa's permitting laws, specifically Iowa Code 321.463 defines the standard permit limits for IoHs, specifying that single-axle weights or GVWs should not exceed 24 kips or 96 kips, respectively, while SHLs with a combination of axles are subjected to gross weight permits on particular groups of axles categorized by primary or non-primary road system. Recent amendments to Iowa legislation revised existing Iowa Code 321.463, resulting in a 12% increase in the maximum legal weight based on the number of axles and distance. This adjustment allows unlimited trips on all state roads and designated routes of the interstate system and certain city/county roads, reflecting the recent trend of pursuing high transportation efficiency. Previous National Cooperative Highway Research Program (NCHRP) research based on a literature review and a web-based survey also explored regulatory practices of permitting superheavy commercial vehicles operating in the United States, with findings revealing considerable variation in permits issued for superheavy commercial vehicles across different states (Papagiannakis 2015). As found in previous studies, the absence of standardized regulations at both federal and state levels, coupled with a lack of detailed guidelines, poses challenges in accurately predicting potential pavement and granular road damage resulting from superloads. Furthermore, conventional analysis methods employed to assess pavement or granular road service lives under typical traffic conditions, such as the equivalent single axle load (ESAL) concept, are readily applicable to FHWA-classified vehicles but encounter limitations when applied to superloads due to their non-generic loading configurations. Table 1 summarizes the definitions of a superload in terms of weight as defined in different states (Papagiannakis 2015).

Table 1. A summary of definitions of superload in different states

State	Superload GVW (kips)	Tire weight limit (lb/in.)	Permit axle load limit (kips) for single, tandem, tridem, and quad axles	Comments
Alabama	>150	700	22, 44, 66, 88	
Alaska	>150	700	30, 56, 70, 80	
Arizona	>250	-	-	

State	Superload GVW (kips)	Tire weight limit (lb/in.)	Permit axle load limit (kips) for single, tandem, tridem, and quad axles	Comments
Arkansas	-	-	20, 40, 60, 68	
California	-	620	Depends on axle spacing and route type	
Colorado	>200	-	27, 50, 65, 72	
Connecticut	>140	600	22.4, 40, 60, 80	
Delaware	>120	-	20, 40, 60, 80	
D.C.	>248	-	31, 62, 93, 124*	*actual weight depends on spacing/tire pressure
Florida	>199	550	-	
Georgia	>150	-	23, -, 60, 92	
Hawaii	-	-	-	Over legal weights require bridge analysis
Idaho	>200	600	Depends on route type	
Illinois	>187	-	29, 54, 75, 100	
Indiana	>120	800	28, 48, 60, 80	
Iowa	>156	-	20, 40, 60, 80	
Kansas	>150	-	24, 49, 60, 65	
Kentucky	>200	700	20, 48, 60, 80	
Louisiana	>254	700	24, 45, 60, 80	Analysis performed off highway system only
Maine	>150	600	*, 39.1, 62.1, 110	*Single axle weight limited by tire width
Maryland	>150	-	27, 52, 63, -	
Massachusetts	130 permit max	800	Depends on axle spacing	
Michigan	>164	700	Depends on route, vehicle width, and tire size	Unit tire pressures 525/450 for rig/flex under restrictions
Minnesota	>144	600	20, 40*, 60, 72	*46 with bridge check
Mississippi	>190	550	12, 48, 57/*63, 64/*72	*Axle weights on interstate/off interstate. SASHTO agreement for GVW <120 kips
Missouri	>160	-	20, 46, 60, 72	SASHTO agreement for GVW <120 kips
Montana	126 permit max	500	22, 48, 51.75, 55.4	
Nebraska	>160	-	20, 34, 60	
Nevada	106 permit max	-	Depends on axle spacing and route	

State	Superload GVW (kips)	Tire weight limit (lb/in.)	Permit axle load limit (kips) for single, tandem, tridem, and quad axles	Comments
New Hampshire	-	-	27.5, 50, 67.5, 80	
New Jersey	-	800	Based on tire unit weight	
New Mexico	-	-	Depends on route	
New York	>199.9	-	Depends on route, axle spacing, and vehicle configuration	Engineering review for GVW >140 kips
North Carolina	>132	-	25, 50, 60, 68	
North Dakota	>150	-	12*, 45, 60, 68	*steer axle
Ohio	>120	-	29, 36/*50, 47/*60, 60/*80	*spacing 4 ft/4 ft, 1 in.
Oklahoma	>150	-	-, 40, 60, 65	
Oregon	>200	600	21.5/43/depends on spacing	
Pennsylvania	>201	800	27, 52, 63, 72	
Rhode Island	120 permit limit	-	Depends on route and vehicle configuration	
South Carolina	>130	-	20, 40, 60, 80	
South Dakota	>200	600	53.3% higher than bridge formula weight limits	
Tennessee	160 permit limit	-	20, 40, 60, 80	SASHTO agreement for GVW <120 kips
Texas	>254.3	-	25, 46, 60, 70	Pavement analysis when GVW >500 or tire weight >6 kips
Utah	>125	600	29.5, 50, 61.75	
Vermont	>150	600	Depends on tire size	
Virginia	>150	-	24, 44, 75/*54.5, 100/*64.5	*Interstate/other
Washington	>200	500/600	22, 43, 65, 70	
West Virginia	120 permit limit	-	28, 45, 50, 55	
Wisconsin	191 permit limit	-	20, 60, 81, 90	
Wyoming	>150	-	25, 55, 65, 74	

Source: Papagiannakis 2015

The main feature of an IoH is that it consists of a tractor and trailer or just a tractor by itself in which the highest loading portion tends to be allocated mostly at the rear axle group due to the placement of the cargo load. An SHL, on the other hand, will have a number of tires and axles in a non-divisible and non-generic body configuration to transport a superheavy cargo. Both IoHs and SHLs tend to have (1) high GVW or single-axle weights exceeding 96 kips or 24 kips, respectively, in the cases of grain carts or tank wagons operated on highways, (2) total vehicle

widths likely to exceed lane width due to a body configuration with wide transverse tire spacing or a large number of tires per axle, and (3) slow-moving behavior that might tend to cause relatively high damage to pavement systems. An overview of general traffic and oversize/overweight (OS/OW) permits in the state of Iowa, including superload traffic, can be found in Table 2 (Iowa DOT 2023a).

Table 2. An overview of general and OS/OW traffic permits in the state of Iowa

Permit type	Single trip	Annual		Annual OS/OW	Multitrip
Cost	\$35	\$50		\$400	\$200
Axle weight	20,000 lb per axle*	20,000 lb per axle		20,000 lb per axle	20,000 lb per axle
Gross weight	No limit	80,000 lb		156,000 lb	156,000 lb
Height	No limit	13 ft 10 in.	15 ft 5 in.	15 ft 5 in.	15 ft 5 in.
Length	No limit	120 ft	120 ft	120 ft	120 ft
Width	No limit	12 ft 15 in.	16 ft	13 ft 5 in.	16 ft
Interstate travel	Allowed	Allowed	Allowed	No interstate highway travel more than 80,000 lb	Allowed
Special mobile equipment except cranes	Allowed up to 36,000 lb single axle; 126,000 lb gross weight with qualifying tires**	Allowed up to 36,000 lb single axle; 80,000 lb gross weight with qualifying tires**		Allowed up to 36,000 lb single axle; 126,000 lb gross weight with qualifying tires**	

Source: Iowa DOT 2023a

*Cranes with pneumatic tires meeting the definition of an indivisible vehicle may have a maximum of 24,000 lb per axle; single-trip permit and round-trip permits only; with travel allowed on the interstate system.

**Formula for construction equipment with flotation pneumatic tires: Axle weight = 20,000 lb + (tire width – 18) × 1,882 lb.

Following the trend of moving from past empirical design to mechanistic-empirical (M-E) analysis and design, the American Association of State Highway and Transportation Officials (AASHTO) AASHTOWare Pavement ME Design software (AASHTO 2022) employed JULEA (Uzan 2001), an LET-based pavement analysis program, in its framework for estimating flexible pavement responses, and artificial neural network (ANN) models as surrogate models for FEMs in estimating rigid-pavement responses. However, the application of M-E pavement analysis and design to superload traffic is particularly challenging due to non-standardized loading configurations and higher GVW or axle weights, requiring analysis and design approaches different from those of pavement systems under general traffic. A previous FHWA project (Nimeri et al. 2018) attempted to determine the essential properties of SHLs, leading to the development of an innovative flexible pavement analysis methodology that focuses on identifying the nucleus segment, or the most influencing tire segment among all the tires of an SHL, resulting in more accurate and less time-consuming prediction of flexible pavement damages. However, the application of this methodology has been limited to a few analysis cases,

emphasizing the need for further research to expand its effectiveness across various superload types and pavement structures. Khazanovich (2022) recently quantified structural damages of flexible and rigid pavements caused by IoHs and developed rudimentary software tools for predicting flexible pavement damages using PittLAYER-VE, a layered viscoelastic-analysis program, and neural network models for predicting rigid pavement damage when experiencing IoH loadings. Vandenbossche et al. (2021) also quantified potential flexible and rigid pavement damages caused by five superload vehicle profiles provided by the Pennsylvania DOT (PennDOT) and developed neural network models for predicting pavement damages under single or tandem axles with axle weights exceeding permit limits. Although previous studies have suggested M-E damage-prediction models of pavements under superloads, few single analysis and ANN models for IoHs or SHLs developed in previous research can deal with the wide dimensional variation of loading configurations of recently released commercial superloads defined as IoHs in many categories such as grain carts, manure tankers, agricultural trailers, or agricultural trucks, and SHLs such as the single-row modular, dual-row modular, or drop-deck types.

Table 3 lists the scope and contribution of previous studies to the understanding of the impacts of superloads on pavement systems.

Table 3. Previous studies on the impacts of superloads on pavement systems

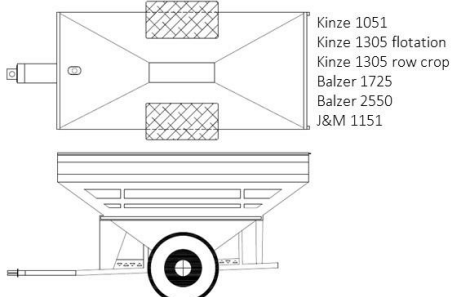
Authors	Superload type	Pavement/ bridge	Tasks
Fanous et al. (2000)	IoH	Flexible and rigid pavement	<ul style="list-style-type: none"> • Determination of relative damaging power
Lim et al. (2012)	IoH	Flexible and rigid pavement	<ul style="list-style-type: none"> • Determination of pavement responses under selected IoHs • Recommendation of policies for state DOT regulations
Wang et al. (2012)	IoH	Rigid pavement	<ul style="list-style-type: none"> • Damage evaluation of IoHs using FEA
Stone et al. (2012)	SHL	Flexible pavement and bridge	<ul style="list-style-type: none"> • Characterization of SHLs • Bridge and flexible pavement damage evaluation under selected SHLs
Papagiannakis (2015)	SHL	Flexible and rigid pavement	<ul style="list-style-type: none"> • Documentation of the practices states follow in issuing permits for SHLs
Phares et al. (2017)	IoH	Bridge	<ul style="list-style-type: none"> • Characterization of IoHs • Damage evaluation of bridges subjected to selected IoHs
Hajj et al. (2018)	SHL	Flexible pavement	<ul style="list-style-type: none"> • Characterization of SHLs • M-E damage evaluation of flexible pavements subjected to SHLs • LCCA of flexible pavements under SHLs • Development of analysis software package
Vandenbossche et al. (2021)	SHL	Flexible and rigid pavement	<ul style="list-style-type: none"> • M-E structural pavement damage determination under selected SHL loading configurations • Development of predictive tool
Khazanovich (2022)	IoH	Flexible and rigid pavement	<ul style="list-style-type: none"> • M-E damage evaluation of pavements subjected to IoHs • Development of rudimentary software tools

CHAPTER 3. SELECTION OF SUPERLOAD TYPES

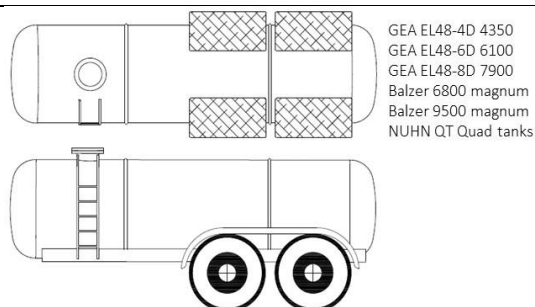
This study aimed to investigate superloads, encompassing 18 types of IoHs and 16 types of SHLs commonly used in the Midwestern region of the United States, as loading inputs. That is, a total of 34 types of superload vehicles and an FHWA class 9 truck (reference vehicle) were included in this study for quantifying their impact on pavement and granular road systems. Payload levels of 100%, 75%, 50%, and 0% that each of the 34 superloads can carry were considered as part of the study.

Table 4 and Table 5 provide visual descriptions and the specified loading conditions for each IoH and SHL type carrying a 100% payload level. The weight of each payload was determined based on the specific capability of handling payloads associated with each commercially released superload. Despite falling into the single category of superload, both IoHs and SHLs exhibit distinct loading configurations and applications, leading to their further categorization into several different classes. For example, Table 4 and Table 5 reveal that IoHs can be categorized into grain carts, manure tankers, agricultural trailers, and agricultural trucks, depending on their intended use, while in contrast SHLs can be classified as modular or drop-deck types based on their loading configurations. Note that in Table 5, among all SHL axle possibilities, the heaviest axle group has been chosen to represent axle and tire weights. The loading inputs of all these superload types, including four payload levels, were equally applied to paved and unpaved road systems for the purpose of conducting mechanistic-based analysis and ANN-based surrogate modeling.

Table 4. Visual descriptions and details of IoHs carrying 100% payload level

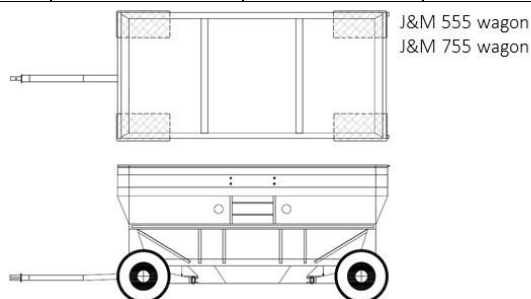
Grain cart (6 types)						
	Name of trailer	No. of axles	No. of tires in an axle	Axle weight (lb)	Tire loading (lb)	Axle spacing (in.)
Kinze 1051	1	2 (single tire)	78,100	39,050	-	96
Kinze 1305 flotation	1	2 (single tire)	112,400	56,200	-	100
Kinze 1305 row crop	1	4 (single tire)	115,470	28,868	-	30, 90, 30
Balzer 1725	2	2 (single tire)	65,500	32,750	78	126
Balzer 2550	3	2 (single tire)	62,500	31,250	78	126
J&M 1151	1	2 (single tire)	82,500	41,250	-	120

**Manure tanker
(6 types)**



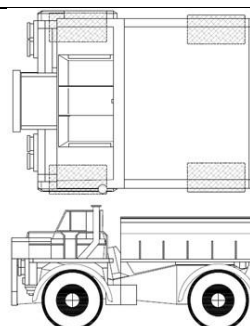
Name of trailer	No. of axles	No. of tires in an axle	Axle weight (lb)	Tire loading (lb)	Axle spacing (in.)	Tire spacing (in.)
GEA EL48-4D 4350	2	2 (single tire)	46,843	23,422	72	95
GEA EL48-6D 6100	3	2 (single tire)	43,152	21,576	72	95
GEA EL48-8D 7900	4	2 (single tire)	42,095	21,047	72	95
Balzer 6800 magnum	2	2 (single tire)	60,700	30,350	86	122
Balzer 9500 magnum	3	2 (single tire)	55,667	27,833	86	122
NUHN QT Quad Tanks	4	2 (single tire)	65,400	32,700	76	114

**Agricultural trailer
(2 types)**



Name of trailer	No. of axles	No. of tires in an axle	Axle weight (lb)	Tire loading (lb)	Axle spacing (in.)	Tire spacing (in.)
J&M 555 wagon	2	2 (single tire)	22,615	11,308	132	88
J&M 755 wagon	2	2 (single tire)	30,125	15,063	137	92

**Agricultural truck
(4 types)**



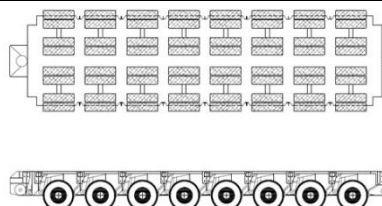
Terragator 2505
Terragator TG7300C
Terragator TG8400C
Case 340B

Name of trailer	No. of axles	No. of tires in an axle	Axle weight (lb)	Tire loading (lb)	Axle spacing (in.)	Tire spacing (in.)
Terragator 2505	3	1, 2, 2 (single tire)	25,620	12,810	77, 230	96
Terragator TG7300C	2	1, 2 (single tire)	28,000	14,000	202	90
Terragator TG8400C	2	2 (single tire)	27,048	13,524	202	90
Case 340B	3	2 (single tire)	32,550	16,275	82, 164	102

Sources: Koh et al. 2022a, Koh et al. 2024

Table 5. Visual descriptions and details of SHLs carrying 100% payload level

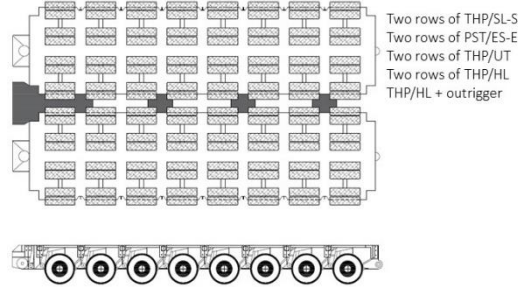
**Single-row modular
(8 types)**



Goldhofer THP/SL-S
Goldhofer THP/ET
Goldhofer PST/ES-E
Goldhofer THP/UT
Goldhofer THP/SL-L
Goldhofer THP/HL-L
Goldhofer THP/SL
Goldhofer THP/HL

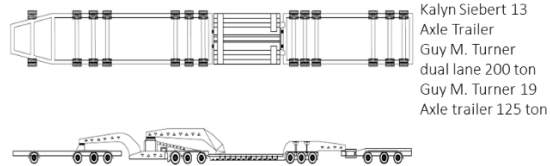
Name of trailer	No. of axles	No. of tires in an axle	Axle weight (lb)	Tire loading (lb)	Axle spacing (in.)	Tire spacing (in.)
Goldhofer THP/SL-S	8+	4 (single tire)	34,400	8,600	59	32, 44, 32
Goldhofer THP/ET	8+	4 (single tire)	50,706	12,676	55	38, 22, 38
Goldhofer PST/ES-E	8+	4 (single tire)	132,000	33,000	63	23, 34, 23
Goldhofer THP/UT	8+	4 (dual tire)	55,116	6,890	59	41, 30 41
Goldhofer THP/SL-L	8+	4 (dual tire)	57,500	7,188	59	33, 38, 33
Goldhofer THP/HL-L	8+	4 (dual tire)	57,500	7,188	59	37, 37, 37
Goldhofer THP/SL	8+	4 (dual tire)	99,000	12,375	59	33, 38, 33
Goldhofer THP/HL	8+	4 (dual tire)	99,200	12,400	59	37, 37, 37

**Dual-row modular
(5 types)**



Name of trailer	No. of axles	No. of tires in an axle	Axle weight (lb)	Tire loading (lb)	Axle spacing (in.)	Tire spacing (in.)
Two rows of Goldhofer THP/SL-S	8+	8 (single tire)	68,800	8,600	59	32, 44, 32, 48, 32, 34, 32
Two rows of Goldhofer PST/ES-E	8+	8 (single tire)	264,000	33,000	63	23, 34, 23, 54, 23, 34, 23
Two rows of Goldhofer THP/UT	8+	8 (dual tire)	110,232	6,890	59	41, 30, 41, 54, 41, 30, 41
Two rows of Goldhofer THP/HL	8+	8 (dual tire)	198,400	12,400	59	37, 37, 37, 54, 37, 37, 37
Goldhofer THP/HL + outrigger	8+	8 (dual tire)	99,200	6,200	59	12, 42, 37, 37, 37, 42, 12

**Drop-deck type
(3 types)**



Name of trailer	No. of axles	No. of tires in an axle	Axle weight (lb)	Tire loading (lb)	Axle spacing (in.)	Tire spacing (in.)
Kalyn Siebert 13 Axle Trailer	13 (tridem axle groups)	2 (dual tire)	22,078	5,520	60	105
Guy M. Turner dual lane 200 ton	19 (tandem axle groups)	4 (dual tire)	40,000	5,000	69	55, 91, 55
Guy M. Turner 19 Axle trailer 125 ton	19 (tridem axle groups)	4 (dual tire)	22,400	2,800	61	55, 91, 55

Sources: Koh et al. 2022a, Koh et al. 2024

CHAPTER 4. MECHANISTIC QUANTIFICATION OF SUPERLOAD IMPACTS ON RIGID PAVEMENTS

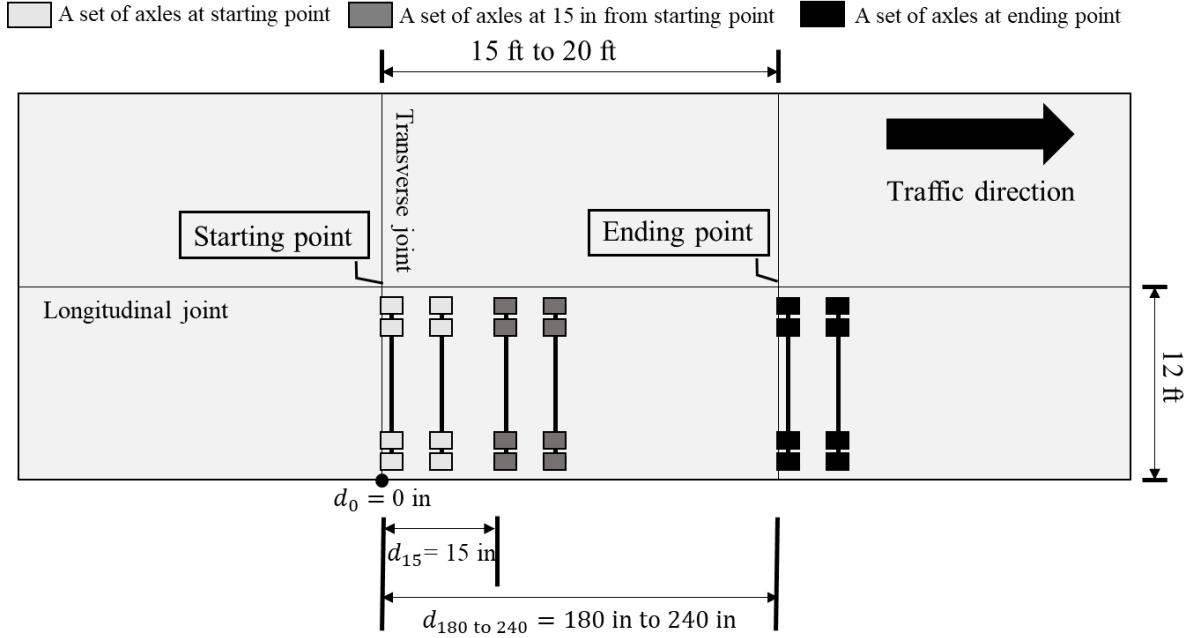
The scope of this chapter is to (1) characterize the superloads traveling on JPCP systems, (2) conduct mechanistic-based JPCP damage calculation and evaluation, especially for bottom-up and top-down fatigue damages resulting from characterized superload loading inputs, using an FEM-based analysis approach, (3) perform LCCA for determining JPCP service life reduction and road damage-associated cost (RDAC) that depend on different superload types and JPCP structures, and (4) develop and optimize artificial intelligence (AI)-based surrogate models for each superload category to accurately predict critical pavement responses related to fatigue damages of JPCPs.

Characterization of Superloads: Critical Loading Location

Methodology

To characterize the loading inputs of superloads with non-standardized loading configurations, mechanistic analysis was conducted using an FEA program, ISLAB2005 (ERES Consultants 1999). This analysis aimed to identify critical pavement responses under different superloads applied to various JPCP structures. The main FEA challenge was how to apply well-defined loading inputs for each superload to determine critical pavement responses across Iowa JPCP structures, which varied in pavement properties such as thickness of the portland cement concrete (PCC) layer, transverse joint spacing, load transfer efficiency (LTE), coefficient of thermal expansion (CTE), composite modulus of subgrade reaction, and temperature gradients of a PCC slab. The influence line-analysis approach, as suggested by Byrum and Hansen (1994), was employed to determine the exact loading location where critical pavement responses occur for each superload, called the critical loading location and represented as a distance from a transverse joint. Each such critical loading location can be categorized in terms of superload type and loading configuration for each vehicle, leading to a better understanding of the relationship between the loading locations and corresponding pavement responses.

To determine critical loading locations for all superload types on JPCP, multiple FEAs were performed by stepping a set of axles across the PCC slab from one transverse joint to the next transverse joint. Figure 1 illustrates the application of a set of axles for each superload at 15 in. intervals to identify the exact critical loading location inducing two types of critical pavement responses: the critical tensile stress at the bottom of the PCC layer and the critical tensile stress at the top of the PCC layer. To obtain critical loading locations of various JPCP structures under different superload types, rigid pavement models representing different transverse joint lengths (15 ft, 17 ft, and 20 ft), transverse joint LTE (50% LTE representing transverse joint without dowel bars and 90% LTE representing transverse joint with dowel bars), and PCC slab temperature gradients (-4°F/in. , -2°F/in. , 0°F/in. , $+2^{\circ}\text{F/in.}$, and $+4^{\circ}\text{F/in.}$), all of which can significantly influence critical loading locations, were used. Note that the LTEs of both 50% and 90% were applied only to the JPCP model with 15 ft of transverse joint, while other models with 17 ft or 20 ft of transverse joint had only an LTE of 90% applied, reflecting realistic JPCP design practices in Iowa.



Koh et al. 2022a, Reprinted with permission from Sage Publications, Inc., © 2022

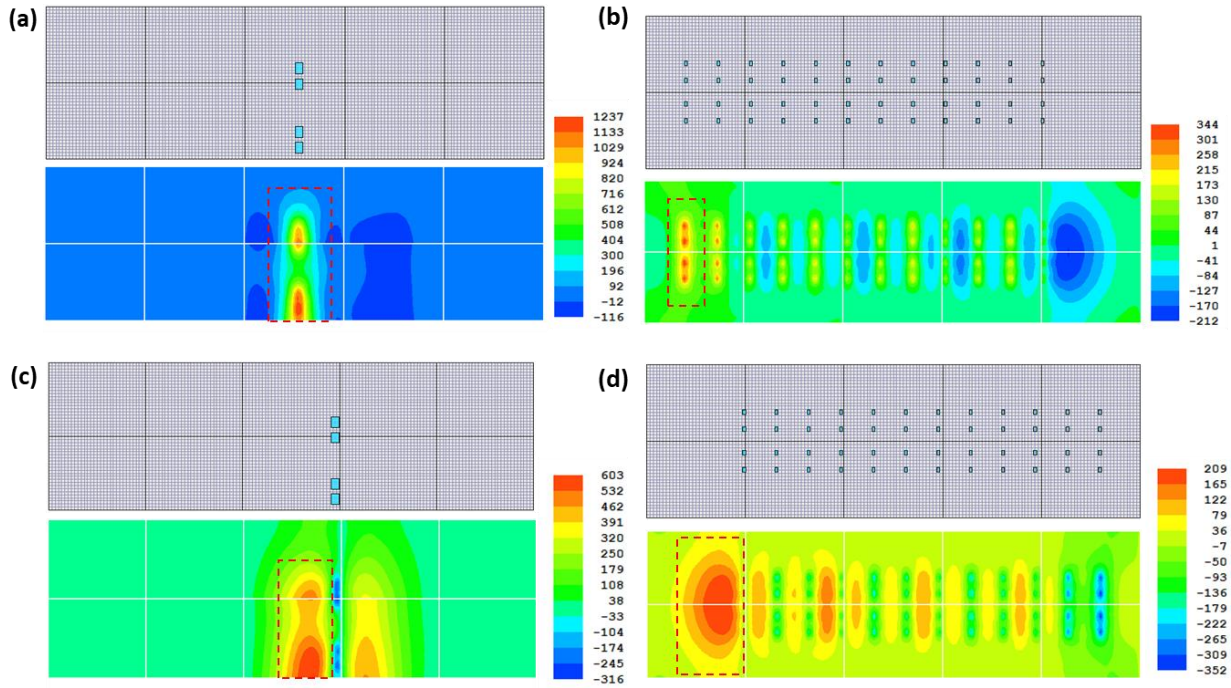
Figure 1. Loading locations across the PCC slab

Note that in the above figure, d_{180} and d_{240} indicate a set of axles at ending points in slabs with 15 ft of transverse joint and 20 ft of transverse joint, respectively.

While previous studies have explored the impact of loading locations on pavement responses using the influence-line approach (Hiller and Roesler 2005), limited investigations have focused on a few vehicles (e.g., FHWA classification vehicles or specific IoH types) using influence-line analysis. Specifically, derivation of critical loading locations and classifications for various superload loading conditions have not been studied. In this study, by obtaining critical loading locations for superloads for as many as possible of the loading configurations used in recently released commercial superloads, they can be classified into several categories so that the critical loading locations of the vehicles included in each category could then be easily derived.

Critical Loading Locations of Superloads

Figure 2 shows examples of critical loading locations for IoHs and SHLs on the JPCP with 15 ft spacing for the transverse joints, 7 in. for the PCC layer thickness, 50% for the LTE, and 0°F/in. for the temperature gradient. Because of the wide vehicle width in the case of IoHs, the tire-loading area often crosses a traffic lane, and due to their large vehicle size SHLs, also usually operate on both traffic lanes, as can be seen in Figure 2.



Koh et al. 2022a, Reprinted with permission from Sage Publications, Inc., © 2022

Figure 2. Critical loading locations on the JPCP at the (a) bottom of PCC slab led by Kinze 1305 row crop, (b) bottom of PCC slab led by Goldhofer THP/SL-S, (c) top of PCC slab led by Kinze 1305 row crop, and (d) top of PCC slab led by Goldhofer THP/SL-S

The critical loading locations of IoHs and SHLs, corresponding to various pavement properties, are categorized in Table 4 and Table 5, respectively. Utilizing these categories associated with critical loading locations simplifies the inference of the critical loading location when a specific loading configuration of a superload is applied to a JPCP structure. The FEA results presented in this chapter reveal that temperature gradients do not affect the superload critical loading locations much differently than the individual loading level, so the effects of temperature gradients are not reflected in Table 6 and Table 7.

Table 6. Categorization of critical loading locations of IoHs

Case	Category	Type	Critical loading location	Relevant IoHs
Critical tensile stresses at the bottom of PCC slab	1	IoH with single-axle	Single-axle located near the mid-slab	Kinze 1305 flotation, Kinze 1305 row crop, Kinze 1051, J&M 1151
	2	IoH with tandem-axle	(2-1) For small axle spacing (<86 in.): tandem-axle located symmetrically within a PCC slab; (2-2) For high axle spacing (>130 in.): one of all axles locates near the mid-slab	(2-1) Balzer 1725, Balzer 6800 magnum, GEA EL48-4D (2-2) J&M 555 wagon, J&M 755 wagon
	3	IoH with tridem-axle	[In case of JPCP with transverse joint: 15 ft, LTE: 50%] (3-1) For small axle spacing (<75 in.): two of all axles located symmetrically within a PCC slab; (3-2) For high axle spacing (>78 in.): one outer axle located on another slab away from the joint [In case of JPCP with transverse joint: 15 ft and 17 ft, LTE: 90%] (3-3) Two of all axles located symmetrically within a PCC slab [In case of JPCP with transverse joint: 20 ft, LTE: 90%] (3-4) All three axles are located symmetrically within a PCC slab	(3-1) GEA EL48-6D (3-2) Balzer 2550, Balzer 9500 magnum (3-3) and (3-4) GEA EL48-6D, Balzer 2550, Balzer 9500 magnum
	4	IoH with quad-axle	[In case of JPCP with transverse joint: 15 ft and 17 ft, LTE: 50% and 90%] (4-1) Two of all axles located symmetrically within a PCC slab [In case of JPCP with transverse joint: 20 ft, LTE: 90%] (4-2) Three of all axles located symmetrically within a PCC slab	(4-1) and (4-2) GEA EL48-8D, NUHN QT Quad
	5	IoH with a special type of axle configuration	Front axle located near the mid-slab	Terragator 2550, Terragator TG7300C, Terragator TG8400C, Case 340B
Critical tensile stresses at the top of PCC slab	1	IoH with single, tandem, tridem, or quad-axle	One outer axle located upon or near the transverse joint	Kinze 1305 flotation, Kinze 1305 row crop, Kinze 1051, J&M 1151, Balzer 1725, Balzer 6800 magnum, GEA EL48-4D, J&M 555 wagon, J&M 755 wagon, GEA EL48-6D, Balzer 2550, Balzer 9500 magnum, GEA EL48-8D, NUHN QT Quad
	2	IoH with a special type of axle configuration	One axle with the highest axle weight located upon or near the transverse joint	Terragator 2550, TerragatorTG 7300, Terragator TG8400C, Case 340B

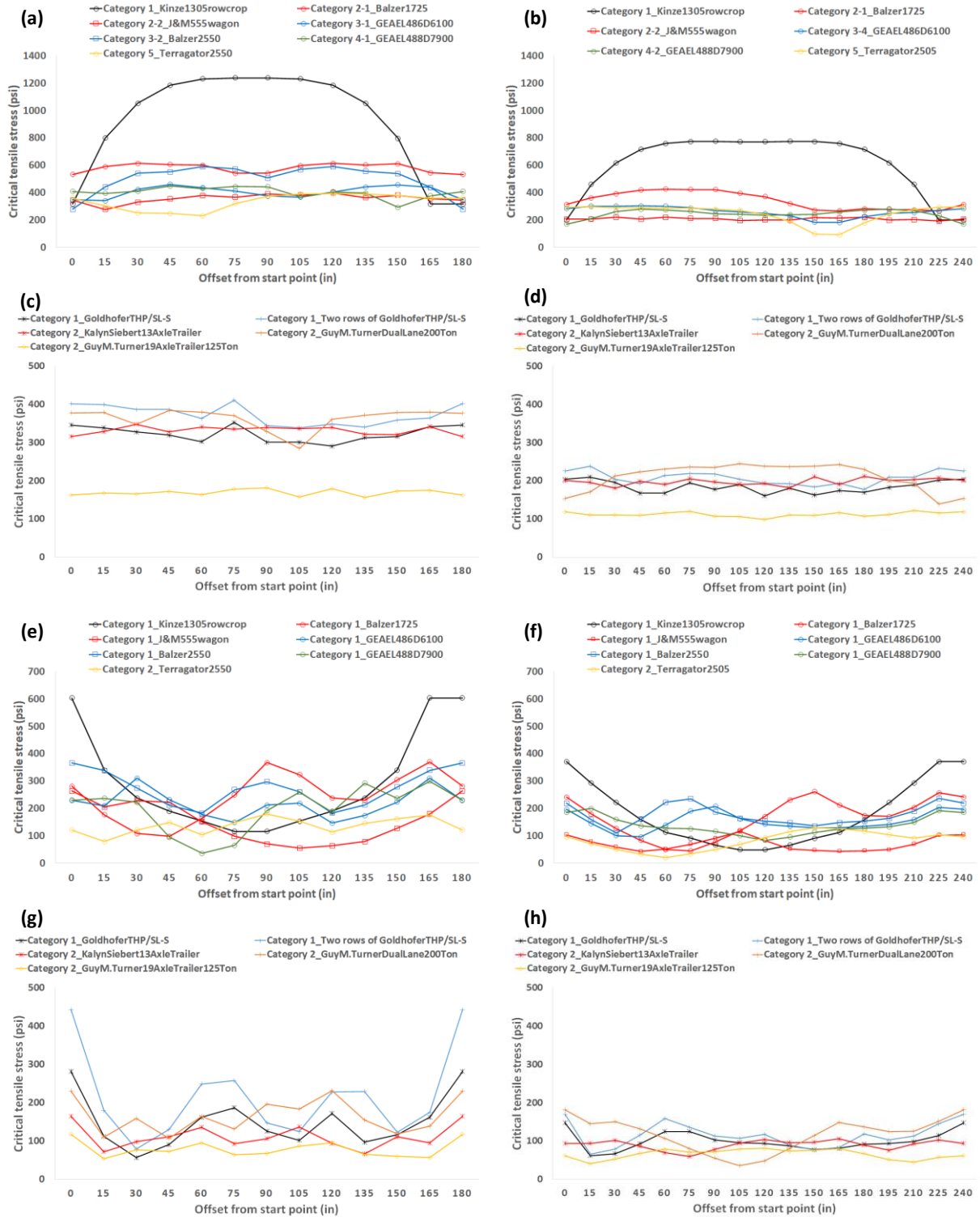
Source: Koh et al. 2022a

Table 7. Categorization of critical loading locations of SHLs

Case	Category	Type	Critical loading location	Relevant SHLs
Critical tensile stresses at the bottom of PCC slab	1	SHL with modular trailers	<p>[In case of JPCP with transverse joint: 15 ft, LTE: 50% and 90%] (1-1) The front or rear axle is located near the mid-slab, and only two axles, including the front or rear axle with the next axle, exist in a slab</p> <p>[In case of JPCP with transverse joint: 17 ft, LTE: 90%] (1-2) The first or last three axles are symmetrically located within a slab</p> <p>[In case of JPCP with transverse joint: 20 ft, LTE: 90%] (1-3) The first or last four axles are symmetrically located within a slab</p>	(1-1), (1-2), and (1-3) All the modular SHLs
	2	SHL with drop-deck trailers	Drop-deck type trailer with tandem-axle groups or tridem-axle groups located with the highest axle weight group in the same way as IoHs with a tandem-axle (2-1) or a tridem-axle (3-1) having small axle spacing from Table 6	All the drop-deck SHLs
Critical tensile stresses at the top of PCC slab	1	SHL with modular trailers	One outer axle located upon or near the transverse joint	All the modular SHLs
	2	SHL with drop-deck trailers	Drop-deck type trailer with tandem and tridem-axle groups located as two separate axle groups near transverse joints having one non-loaded PCC slab between them	All the drop-deck SHLs

Source: Koh et al. 2022a

Figure 3 presents examples of influence-line stress responses corresponding to distances of a set of axles from the starting point. It should be noted that, for clarity, Figure 3 exclusively features representative superloads from each category; the other superloads belonging to each category have critical loading locations similar to those of the representative superloads.



Koh et al. 2022a, Reprinted with permission from Sage Publications, Inc., © 2022

Figure 3. Examples of influence-line stress responses for critical tensile stress

Note that in the above figure, the corresponding details of the stress responses are given as follows: (a) at the bottom of the PCC slab with 15 ft for transverse joint, 7 in. for thickness of

PCC layer, and 50% for transverse joint LTE under IoHs; (b) at the bottom of the PCC slab with 20 ft for transverse joint, 7 in. for thickness of PCC layer, and 90% for transverse joint LTE under IoHs; (c) at the bottom of the PCC slab with 15 ft for transverse joint, 7 in. for thickness of PCC layer, and 50% for transverse joint LTE under SHLs; (d) at the bottom of the PCC slab with 20 ft for transverse joint, 7 in. for thickness of PCC layer, and 90% for transverse joint LTE under SHLs; (e) at the top of the PCC slab with 15 ft for transverse joint, 7 in. for thickness of PCC layer, and 50% for transverse joint LTE under IoHs; (f) at the top of the PCC slab with 20 ft for transverse joint, 7 in. for thickness of PCC layer, and 90% for transverse joint LTE under IoHs; (g) at the top of the PCC slab with 15 ft for transverse joint, 7 in. for thickness of PCC layer, and 50% for transverse joint LTE under SHLs; and (h) at the top of the PCC slab with 20 ft for transverse joint, 7 in. for thickness of PCC layer, and 90% for transverse joint LTE under SHLs.

The graphs in Figure 3 along with Table 6 show that the critical loading locations of IoHs can be differentiated according to their numbers of axles and axle spacings. On the other hand, the modular SHLs with relatively small and consistent axle spacings in Figure 3 and Table 7 generate critical tensile stresses primarily through front or rear axle loading, meaning that the front or rear axle location would be the most critical factor in determining critical loading location. Unlike the modular types, the drop-deck SHLs have relatively wide spacing between each group of axles, so that the drop-deck SHLs with tandem-axle groups (or tridem-axle groups) are subjected to the critical tensile stress at the bottom of the PCC slab when the highest loaded axle group is located similarly to the tandem axle (or tridem axle) IoHs. In the same vein, the drop-deck SHLs generate critical tensile stress at the top of the PCC slab between the two highest loaded axle groups. As outlined in this chapter, superloads, characterized by non-standardized loading configurations, can be systematically categorized based on their critical loading locations, which exhibit a significant correlation with the type and spacing of their axles.

Mechanistic Analysis for Potential Damage Evaluation: FEM-Based Analysis

Methodology

Applying critical loading locations associated with each superload categorized in Table 6 and Table 7, the critical tensile stress at the bottom and top of the PCC slab and corresponding number of load repetitions to failure N_f can be obtained through comprehensive analysis matrices that vary based on the properties of JPCP. In more detail, the set of experimental matrices for FEA shown in Table 8 can be established, with base inputs that include types of roads (i.e., local road and highway) and seasons (i.e., spring, summer, fall, and winter) directly related to the thickness of the PCC layer and the composite modulus of subgrade reaction, respectively. The other subordinate inputs are the joint spacing, LTE, CTE, and temperature gradients of a PCC slab determined to correspond to a reasonable range of values representative of JPCP structures in Iowa. A total of 35 types of traffic loading, comprising 18 IoH types, 16 SHL types, and an FHWA class 9 truck (reference vehicle), were considered as loading inputs for the FEA models. Considering payload levels of 100%, 75%, 50%, and 0% for each of the 34 superloads, excluding the reference vehicle, a total of $34 \times 4 + 1 = 137$ traffic loadings were mechanistically applied to each analysis model.

Table 8. Comprehensive experimental matrices for JPCP FEA

Local road				Highway			
Thickness of PCC layer (in.)				Thickness of PCC layer (in.)			
7, 9				10, 13			
Seasonal composite modulus of subgrade reaction (psi/in.)				Seasonal composite modulus of subgrade reaction (psi/in.)			
Spring	Summer	Fall	Winter	Spring	Summer	Fall	Winter
50	120	120	250	50	120	120	250
Transverse joint spacing (ft): 15				Transverse joint spacing (ft): 17, 20			
CTE ($10^{-6}/^{\circ}\text{F}$): 4.3, 5.2				CTE ($10^{-6}/^{\circ}\text{F}$): 4.3, 5.2			
Temperature gradients ($^{\circ}\text{F/in.}$): -4, -2, 0, 2, 4				Temperature gradients ($^{\circ}\text{F/in.}$): -4, -2, 0, 2, 4			
Elastic modulus of PCC layer (psi): 4×10^6				Elastic modulus of PCC layer (psi): 4×10^6			
Traffic loadings				Traffic loadings			
IoH: 18 types \times 4 payload levels = 72 types				IoH: 18 types \times 4 payload levels = 72 types			
SHL: 16 types \times 4 payload levels = 64 types				SHL: 16 types \times 4 payload levels = 64 types			
FHWA class 9 truck (reference): 1 type				FHWA class 9 truck (reference): 1 type			
Total analysis cases: 10,960 cases				Total analysis cases: 21,920 cases			

Sources: Koh et al. 2022a, Koh et al. 2024

To quantify the potential fatigue damages of JPCP structures under various superloads, the damage ratio (D_r) concept, defined as the ratio of damage caused by the superload loading to damage caused by the FHWA class 9 truck loading, was adopted. Specifically, this study dealt with the damage ratios for two types of fatigue-related transverse cracking in the PCC slab: bottom-up transverse cracking and top-down transverse cracking. The calculations of those two types of damage ratio were conducted using equation 1 and equation 2.

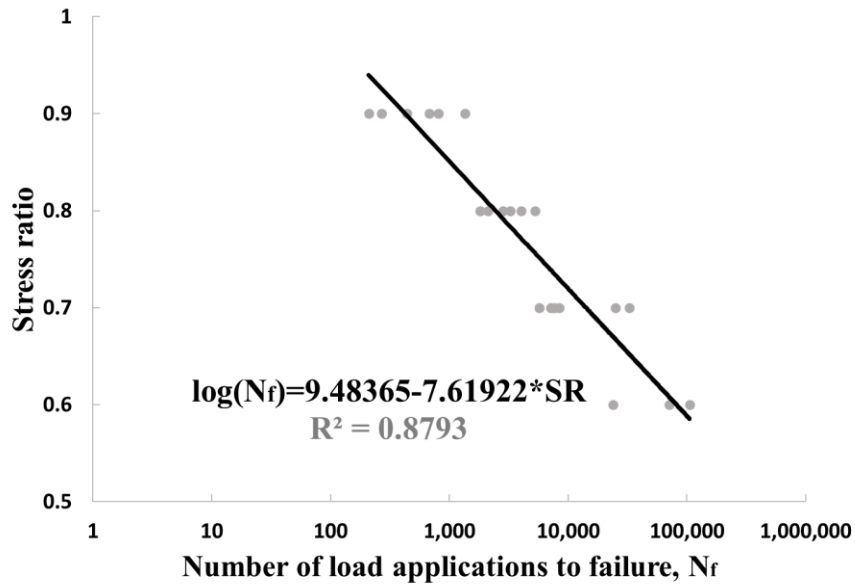
$$\text{Damage ratio for bottom-up transverse cracking } (D_b) = \frac{\frac{1}{N_{b,superload}}}{\frac{1}{N_{b,class\ 9}}} = \frac{N_{b,class\ 9}}{N_{b,superload}} \quad (1)$$

$$\text{Damage ratio for top-down transverse cracking } (D_t) = \frac{\frac{1}{N_{t,superload}}}{\frac{1}{N_{t,class\ 9}}} = \frac{N_{t,class\ 9}}{N_{t,superload}} \quad (2)$$

where $N_{b,superload}$ is the number of load repetitions to failure due to tensile stress at the bottom of the PCC layer under superload, $N_{b,class\ 9}$ is the number of load repetitions to failure due to tensile stress at the bottom of the PCC layer under FHWA class 9 truck, $N_{t,superload}$ is the number of load repetitions to failure due to tensile stress at the top of the PCC layer under superload, and $N_{t,class\ 9}$ is the number of load repetitions to failure due to tensile stress at the top of the PCC layer under FHWA class 9 truck.

To determine the number of load repetitions leading to failure for both bottom-up transverse cracking and top-down transverse cracking, a transfer function reflecting the properties of the Iowa PCC slab was essential. Therefore, an S-N curve was drawn using Iowa State University

(ISU) experimental results based on fatigue tests for air-entrained concrete (Klaiber et al. 1979, Lee et al. 1978). The material properties of the concrete beam used in these fatigue tests align with those currently employed in the construction of Iowa PCC slabs. For instance, the fatigue test employed an Iowa DOT C-3 mix, representing a standard paving mix used in primary paving. This mix includes Type 1 portland cement with a water-cement ratio of 0.43. The coarse aggregate consisted of crushed limestone (specific gravity: 2.53, water absorption: 2.54%) from the Alden Quarry near Alden, Iowa, while Hallett sand (specific gravity: 2.64, water absorption: 1.50%) served as the fine aggregate. Although ISU researchers explored the impact of air content over various ranges on concrete fatigue strength, this study specifically utilized data from the 6.7% case to draw the S-N curve as shown in Figure 4. This case was chosen as it closely aligns with the most common air content employed in Iowa PCC slabs. Note that the stress ratio (SR) in this context refers to the ratio of flexural stress to the modulus of rupture.



Koh et al. 2022a, Reprinted with permission from Sage Publications, Inc., © 2022

Figure 4. S-N curve using data from previous experimental tests for PCC slabs

This study also calculated damage ratios using other transfer functions adopted from the *Guide for Mechanistic-Empirical Design* (ARA, Inc. 2004a) and Portland Cement Association (PCA) (Packard and Tayabji 1985) in addition to those using transfer functions from previous ISU fatigue tests for comparison purposes. Equation 3 and equation 4 show the transfer functions employed for calculating the number of load repetitions to failure based on the *Guide for Mechanistic-Empirical Design* (ARA, Inc. 2004a) and the PCA (Packard and Tayabji 1985), respectively. It is noteworthy that the modulus of rupture for the PCC slab was calculated to be 662.5 psi, a value close to the average modulus of rupture of 667.2 psi calculated from six Iowa sections using long-term pavement performance (LTPP) data.

$$\log(N_{i,j,k,l,m,n}) = C_1 \cdot \left(\frac{MR_i}{\sigma_{i,j,k,l,m,n}} \right)^{C_2} + 0.4371 \quad (3)$$

$$\log N_f = 11.737 - 12.077\left(\frac{\sigma}{MR}\right) \quad \text{for } \frac{\sigma}{MR} \geq 0.55 \quad (4-1)$$

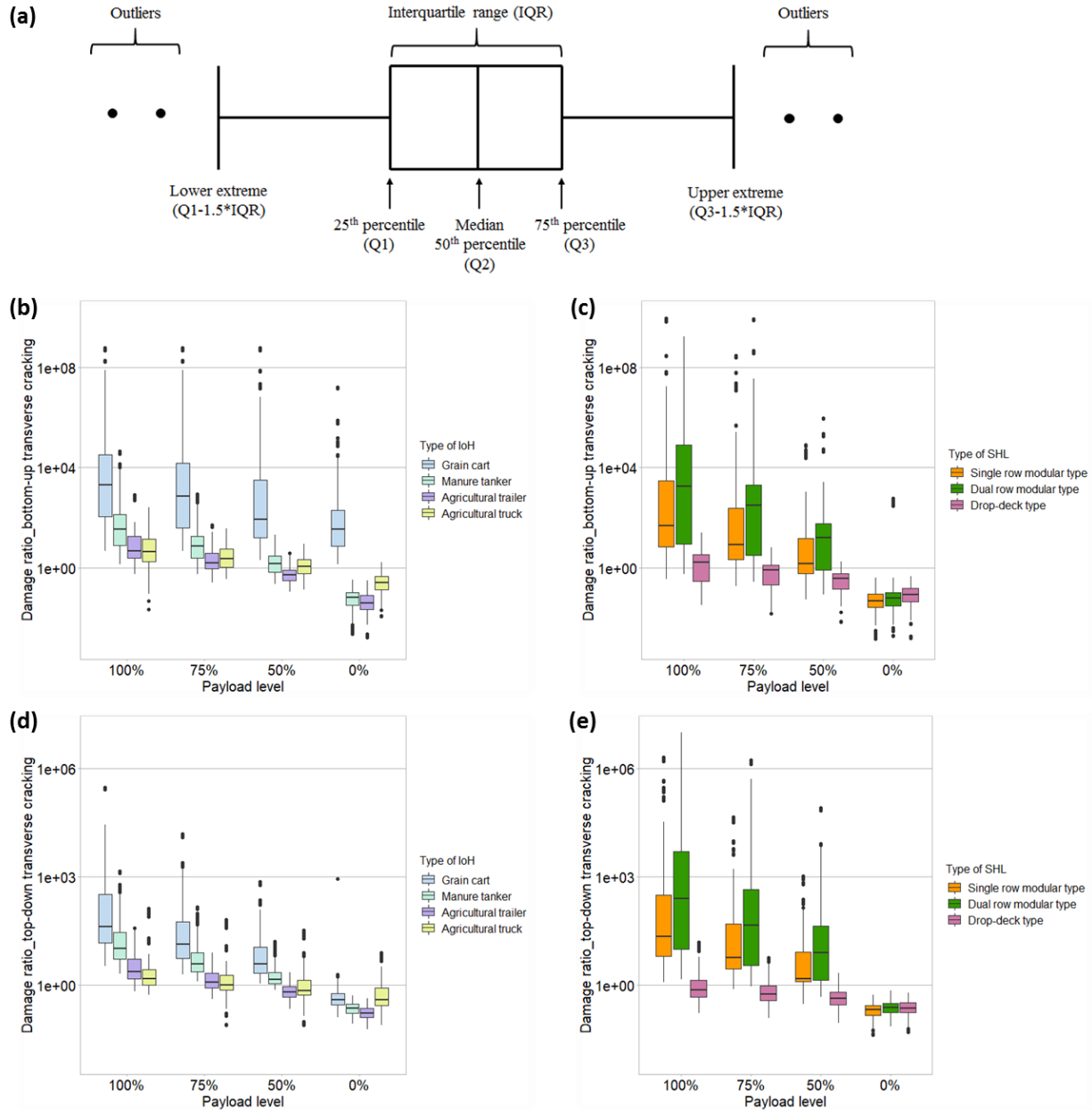
$$\log N_f = \left(\frac{4.2577}{\frac{\sigma}{MR} - 0.4325}\right)^{3.268} \quad \text{for } 0.45 \leq \frac{\sigma}{MR} \leq 0.55 \quad (4-2)$$

$$\log N_f = \text{unlimited} \quad \text{for } \frac{\sigma}{MR} \leq 0.45 \quad (4-3)$$

where $N_{i,j,k,l,m,n}$ is the allowable number of load applications at condition i, j, k, l, m , and n ; MR_i is the PCC modulus of rupture at age i , psi; $MR = \frac{43.5E_c}{10^6} + 488.5$; $\sigma_{i,j,k,l,m,n}$ is the applied stress at condition i, j, k, l, m , and n ; C_1, C_2 is the calibration constant ($C_1 = 2.0, C_2 = 1.22$); and E_c is the modulus of elasticity of the PCC slab.

Damage Ratio Analysis

A comprehensive set of 32,880 FEA results related to bottom-up transverse cracking and top-down transverse cracking were obtained using the experimental matrices shown in Table 8. The degree of JPCP fatigue damage resulting from exposure to superload traffic can be quantified in terms of the number of load repetitions to failure through comparison with an FHWA class 9 truck (i.e., reference vehicle). Given that the experimental matrices for FEA presented in Table 8 encompass the entire spectrum of Iowa JPCP properties, the study enables an evaluation of fatigue-related transverse cracking according to each type of IoH and SHL traveling on JPCP models, as depicted in Figure 5. Moreover, considering the diverse types and capacities of payloads carried by each superload, it is imperative to conduct analyses across various payload levels, ranging from 100% payload level (i.e., full loads) to 0% payload level (i.e., empty loads). This approach allows for the examination of relative fatigue damage in relation to the variation in payload level.



Koh et al. 2022a, Reprinted with permission from Sage Publications, Inc., © 2022

Figure 5. Damage ratio analysis results: (a) the configuration of box-whisker plot, (b) box-whisker plots comparing damage ratios based on bottom-up transverse cracking of PCC slabs under IoHs, (c) damage ratios based on bottom-up transverse cracking of PCC slabs under SHLs, (d) damage ratios based on the top-down transverse cracking of PCC slabs under IoHs, and (e) damage ratios based on top-down transverse cracking of PCC slabs under SHLs

The box-whisker plots above depict that, among IoHs, grain carts tend to induce more significant fatigue-related transverse cracking compared to other IoHs. Grain carts and manure tankers at all payload levels except for the 0% payload also exhibit damage ratios greater than one for both bottom-up transverse cracking and top-down transverse cracking, while agricultural trailers and

agricultural trucks show relatively lower damage ratios, with some JPCP models even showing damage ratios less than one when carrying a 50% payload or lower. Overall, the majority of IoHs, excluding grain carts, result in fatigue damage levels similar to the FHWA class 9 truck when carrying a 50% payload. In the case of SHLs, most FEA results, except for the empty-load case, indicate that the modular SHLs cause significantly greater fatigue-related transverse cracking than the drop-deck SHLs. These results clearly show that, despite the drop-deck SHLs being heavier than the modular SHLs, the modular types with much higher load capacity cause severe fatigue-related transverse cracking at payload levels equal to or greater than 50%. Consequently, drop-deck SHLs cause comparable or even lesser fatigue damage than the FHWA class 9 truck across all payload levels, while the modular SHLs are likely to cause significant fatigue damages at payload levels of 50% or more.

To compare damage ratios produced by the transfer function calculation from previous ISU fatigue tests, other transfer functions adopted from the *Guide for Mechanistic-Empirical Design* (ARA, Inc. 2004a) and the PCA (Packard and Tayabji 1985) were used to calculate damage ratios under the same analysis conditions. Table 9 and Table 10 show that damage ratios calculated from the other two transfer functions exhibit an exaggeratedly wider range than damage ratios calculated using the transfer function derived from the ISU fatigue tests. However, the trends in damage ratios from superloads for both bottom-up and top-down transverse cracking remain similar across all three transfer functions. Note that the damage ratios presented in Table 9 and Table 10 are the overall damage ratios for all IoH or SHL types, while Figure 5 shows the damage ratios for each type of IoH or SHL.

Table 9. Averaged damage ratios of JPCPs under IoHs using different transfer functions

Transfer function		100% payload	75% payload	50% payload	0% payload
		Damage ratio of IoH (bottom-up transverse cracking)			
<i>Guide for Mechanistic-Empirical Design</i> (ARA, Inc. 2004a)	Max.	1.24E+37 (Grain cart)	3.29E+35 (Grain cart)	4.24E+32 (Grain cart)	2.86E+6 (Grain cart)
	Median	7.69E+5	5.41E+10	1.71E+4	3.26E-24
	Min.	9.85E+9 (Agricultural truck)	1.17E-21 (Agricultural truck)	7.79E-47 (Agricultural truck)	<1.00E-100 (Agricultural trailer)
ISU fatigue tests (Klaiber et al. 1979, Lee et al. 1978)	Max.	7.38E+10 (Grain cart)	1.53E+8 (Grain cart)	3.17E+5 (Grain cart)	2.12E+0 (Grain cart)
	Median	3.28E+1	1.42E+1	1.86E+0	1.14E-1
	Min.	2.57E-1 (Agricultural truck)	1.08E-1 (Agricultural truck)	2.16E-2 (Agricultural trailer)	1.57E-3 (Agricultural trailer)
PCA (Packard and Tayabji 1985)	Max.	2.33E+17 (Grain cart)	1.20E+13 (Grain cart)	6.16E+8 (Grain cart)	3.32E+0 (Grain cart)
	Median	2.64E+2	2.51E+1	2.70E+0	3.12E-2
	Min.	1.14E-1 (Agricultural truck)	2.86E-2 (Agricultural trailer)	2.18E-3 (Agricultural trailer)	3.29E-5 (Agricultural trailer)
Transfer function		Damage ratio of IoH (top-down transverse cracking)			
<i>Guide for Mechanistic-Empirical Design</i> (ARA, Inc. 2004a)	Max.	1.04E+48 (Grain cart)	5.95E+44 (Grain cart)	1.03E+39 (Grain cart)	7.25E+13 (Agricultural truck)
	Median	6.64E+12	1.15E+10	1.57E+5	1.75E-42
	Min.	5.92E-22 (Agricultural truck)	<1.00E-100 (Agricultural truck)	<1.00E-100 (Agricultural truck)	<1.00E-100 (Agricultural trailer)
ISU fatigue tests (Klaiber et al. 1979, Lee et al. 1978)	Max.	3.00E+5 (Grain cart)	1.51E+4 (Grain cart)	7.44E+2 (Grain cart)	8.10E+0 (Agricultural truck)
	Median	8.95E+0	5.21E+0	1.62E+0	2.97E-1
	Min.	5.43E-1 (Agricultural truck)	4.20E-1 (Agricultural truck)	8.11E-2 (Agricultural trailer)	6.04E-2 (Agricultural trailer)
PCA (Packard and Tayabji 1985)	Max.	5.66E+8 (Grain cart)	4.77E+6 (Grain cart)	3.88E+4 (Grain cart)	2.83E+1 (Agricultural truck)
	Median	8.48E+1	3.32E+1	2.15E+1	1.44E-1
	Min.	3.76E-1 (Agricultural truck)	1.81E-2 (Agricultural truck)	1.69E-2 (Agricultural truck)	1.13E-2 (Agricultural trailer)

Source: Koh et al. 2022a

Table 10. Averaged damage ratios of JPCPs under SHLs using different transfer functions

Transfer function		100% payload	75% payload	50% payload	0% payload
		Damage ratio of SHL (bottom-up transverse cracking)			
<i>Guide for Mechanistic-Empirical Design</i> (ARA, Inc. 2004a)	Max.	6.34E+37 (Dual-row modular type)	1.25E+36 (Dual-row modular type)	2.51E+32 (Dual-row modular type)	2.56E-5 (Dual-row modular type)
	Median	6.94E+5	1.14E+4	1.86E+1	8.10E-48
	Min.	3.56E-56 (Drop-deck type)	2.62E-81 (Drop-deck type)	<1.00E-100 (Drop-deck type)	<1.00E-100 (Single-row modular type)
ISU fatigue tests (Klaiber et al. 1979, Lee et al. 1978)	Max.	7.16E+13 (Dual-row modular type)	8.15E+9 (Dual-row modular type)	9.30E+5 (Dual-row modular type)	5.79E+2 (Dual-row modular type)
	Median	2.48E+1	1.11E+1	5.41E+0	5.79E-2
	Min.	3.09E-2 (Drop-deck type)	1.46E-2 (Drop-deck type)	6.86E-3 (Drop-deck type)	1.43E-3 (Single-row modular type)
PCA (Packard and Tayabji 1985)	Max.	1.38E+22 (Dual-row modular type)	6.89E+15 (Dual-row modular type)	3.45E+9 (Dual-row modular type)	2.60E+4 (Dual-row modular type)
	Median	1.69E+2	1.49E+1	1.18E+0	1.05E-2
	Min.	3.87E-3 (Drop-deck type)	1.16E-3 (Drop-deck type)	3.49E-4 (Drop-deck type)	2.86E-5 (Single-row modular type)
Transfer function		Damage ratio of SHL (top-down transverse cracking)			
<i>Guide for Mechanistic-Empirical Design</i> (ARA, Inc. 2004a)	Max.	5.19E+52 (Dual-row modular type)	3.30E+50 (Dual-row modular type)	9.58E+45 (Dual-row modular type)	1.96E-4 (Dual-row modular type)
	Median	1.45E+14	3.97E+11	6.96E+4	1.53E-75
	Min.	<1.00E-100 (Drop-deck type)	<1.00E-100 (Drop-deck type)	<1.00E-100 (Drop-deck type)	<1.00E-100 (Single-row modular type)
ISU fatigue tests (Klaiber et al. 1979, Lee et al. 1978)	Max.	1.51E+7 (Dual-row modular type)	9.76E+6 (Dual-row modular type)	8.00E+4 (Dual-row modular type)	7.28E-1 (Dual-row modular type)
	Median	1.37E+1	4.48E+0	1.47E+0	2.27E-1
	Min.	1.68E-1 (Drop-deck type)	1.25E-1 (Drop-deck type)	9.28E-2 (Drop-deck type)	4.30E-2 (Single-row modular type)
PCA (Packard and Tayabji 1985)	Max.	2.98E+11 (Dual-row modular type)	1.47E+11 (Dual-row modular type)	6.85E+7 (Dual-row modular type)	6.03E-1 (Dual-row modular type)
	Median	6.55E+1	1.10E+1	1.85E+0	9.35E-2
	Min.	5.77E-2 (Drop-deck type)	3.59E-2 (Drop-deck type)	2.24E-2 (Drop-deck type)	6.56E-3 (Single-row modular type)

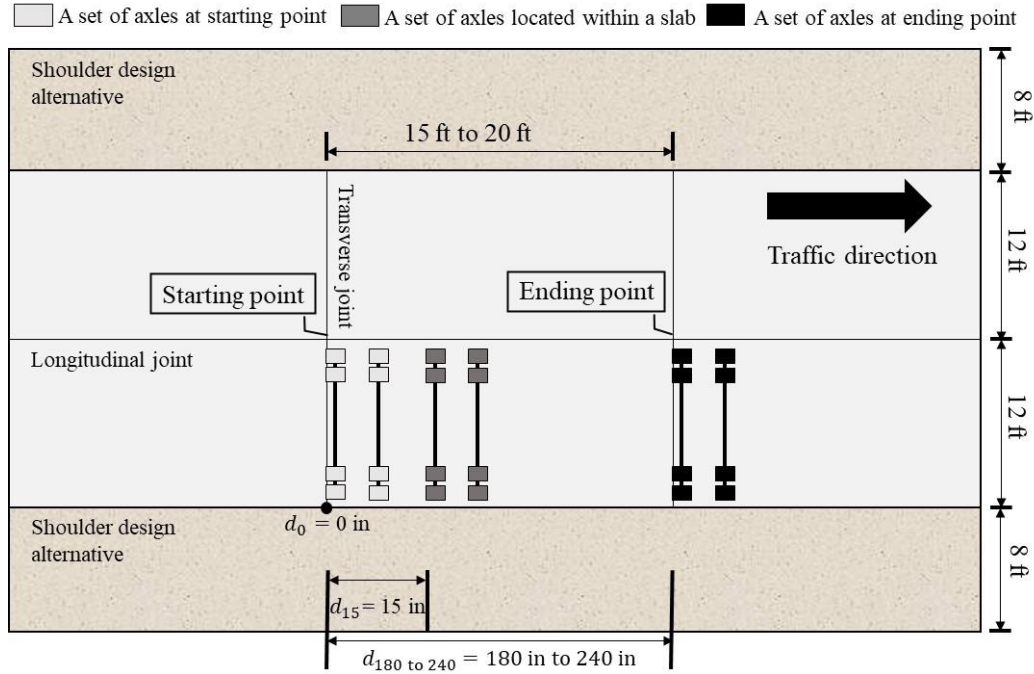
Source: Koh et al. 2022a

Structural Benefits of Shoulder Types on JPCP under Superloads

The FEA performed in the previous section used models without considering any shoulders, assumed to be granular. The rationale behind the granular shoulder application in the FEA models was grounded in the predominant use of granular shoulders rather than paved shoulders on county roads in Iowa (Souleyrette et al. 2001), which are the target state of this study. However, it was still necessary to evaluate the performance of JPCPs according to different shoulder alternatives, including tied PCC or hot-mix asphalt (HMA) shoulders. Therefore, the critical loading location of each superload from FEA matrices that simulated different shoulder alternatives was re-determined and the critical pavement responses to those applying the newly determined critical loading location as a loading condition were re-calculated. To this end, the following shoulder alternatives were added and applied to the existing FEA models outlined in Table 8. Note that the PCC layer thickness and transverse joint spacing were kept constant at 10 in. and 20 ft, respectively, as per the experimental matrices in Table 8. This was done to manage the considerable increase in analysis cases resulting from the inclusion of three distinct shoulder types in determining critical pavement responses described as follows:

- Granular shoulder: No shoulder applied
- Full-depth tied PCC shoulder: The shoulder thickness is the same as the PCC slab (10 in.); the shoulder width is 8 ft for both lanes; the LTE between the PCC slab and the shoulder is applied at 50% and 70%, referring to the *Guide for Mechanistic-Empirical Design* (ARA, Inc. 2004a)
- Partial-depth HMA shoulder: The shoulder thickness is less than that of the PCC slab (8 in.); the shoulder width is 8 ft for both lanes; the LTE between the PCC slab and the shoulder is applied at 10%, referring to the *Guide for Mechanistic-Empirical Design* (ARA, Inc. 2004a)

Before undertaking a comparative analysis of the critical pavement responses of JPCPs according to each shoulder alternative application, the critical loading location for each superload in the JPCP structure, considering different types of shoulder, was again determined. This was accomplished through a repetition of the influence line-analysis approach (Hiller and Roesler 2005), illustrated in Figure 6. The critical loading locations were re-determined by applying the various pavement properties (i.e., transverse joints [15 ft, 17 ft, and 20 ft], transverse joint LTE [50% and 90%], and temperature gradients of a PCC slab [-4°F/in., -2°F/in., 0°F/in., +2°F/in., and +4°F/in.]) to check whether the categorization of critical loading locations following the loading configurations of IoHs and SHLs shown in Table 6 and Table 7 is still valid for the different shoulder alternatives. Subsequently, a randomly selected superload from each category underwent a thorough analysis to identify critical loading locations and the corresponding critical pavement responses related to both bottom-up transverse cracking and top-down transverse cracking, providing a deep understanding of the JPCP performance under diverse superload loading and shoulder conditions.

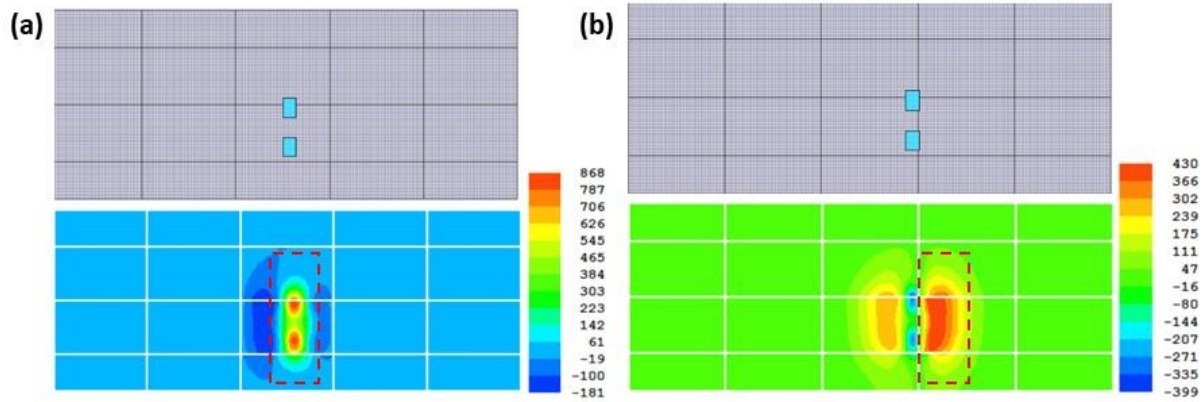


Koh et al. 2022a, Reprinted with permission from Sage Publications, Inc., © 2022

Figure 6. Loading locations across the PCC slab applying shoulder alternatives

Note that in the above figure, d_{180} and d_{240} indicate a set of axles at ending points in slabs with 15 ft of transverse joint and 20 ft of transverse joint, respectively.

The FEA results for JPCPs under various shoulder alternatives validate that the critical loading locations for representative types of superloads can be categorized in the same way as the granular shoulder for other shoulder alternatives, including full-depth PCC and partial-depth HMA shoulders. This means that a randomly selected superload per category traveling on JPCPs with a full-depth tied PCC shoulder or a partial-depth HMA shoulder encounters critical loading locations similar to JPCPs with granular shoulders for both critical tensile stresses at the bottom of the PCC slab and the top of the PCC slab. To illustrate, Figure 7 depicts the critical loading locations of an example IoH from category 1, emphasizing the uniformity in categorization across different shoulder alternatives.

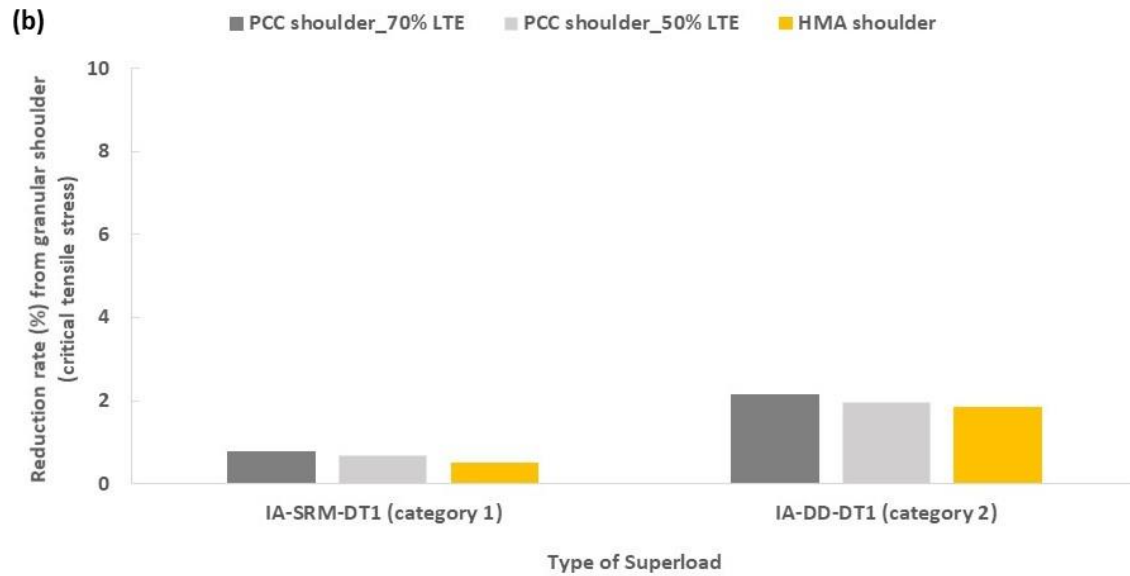
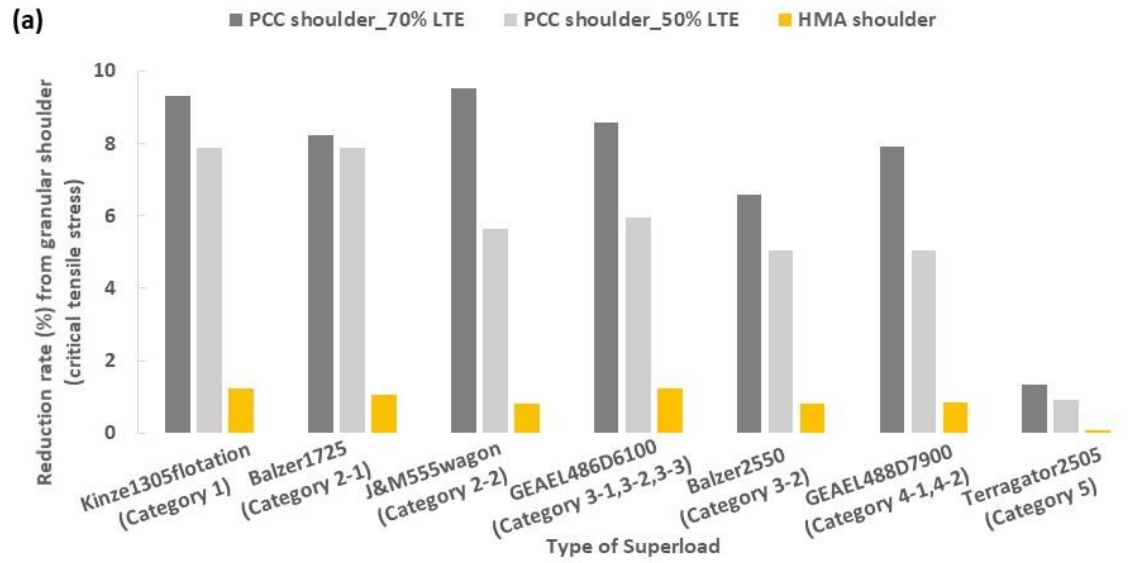


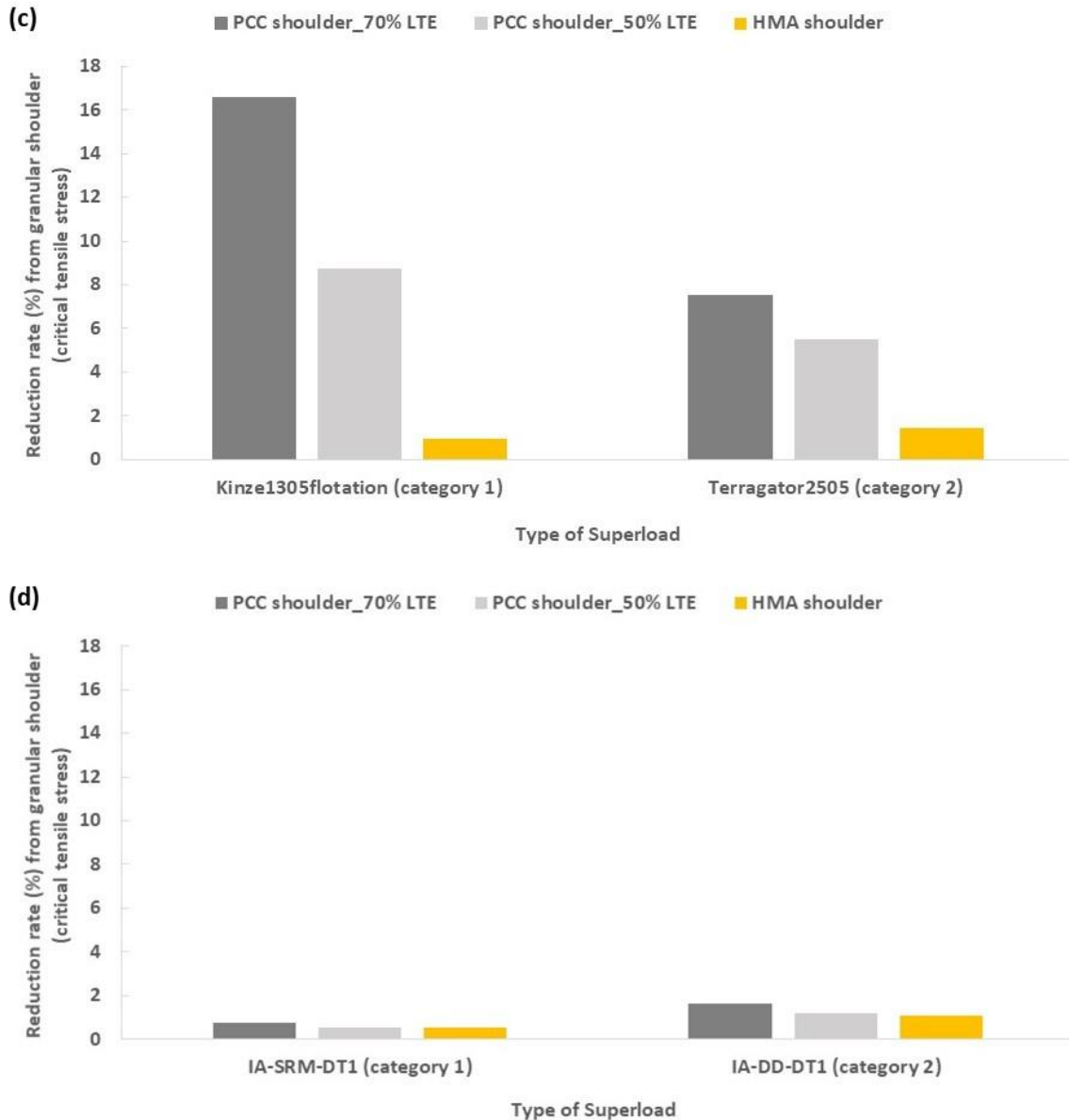
Koh et al. 2022a, Reprinted with permission from Sage Publications, Inc., © 2022

Figure 7. Critical loading locations generating critical tensile stress: (a) at the bottom of PCC slab and (b) at the top of PCC slab led by Kinze 1305 flotation from category 1

Note that in the above figure, the JPCPs have 20 ft of transverse joint spacing, 10 in. of PCC thickness, -2°F/in. of temperature gradient, and the full-depth tied PCC shoulder with 70% LTE between PCC slab and shoulder.

As a final step, the critical pavement responses at the bottom and top of the PCC slab were determined from FEA models representing different types of the shoulder by applying critical loading conditions of representative superloads of each category carrying 100% payload levels. Figure 8 shows the comparative analysis results of the critical pavement responses, on average, generated by the representative superload of each category on different paved shoulder models, as opposed to those produced by granular shoulder models. The results reveal notable reductions in the critical tensile stresses of the PCC slab subjected to IoHs when full-depth PCC shoulders were applied. For instance, in scenarios where the FEA models featured 70% LTE between the PCC slab and PCC shoulder, the critical tensile stresses at the bottom of the PCC slab exhibited an average reduction of approximately 9.3%, while the critical tensile stresses at the top of the PCC slab experienced an average reduction of about 16.6% compared to those generated in JPCPs with a granular shoulder, when subjected to the Kinze 1305 flotation. On the other hand, SHLs exhibited a relatively small reduction in critical tensile stresses when paved shoulders were applied because SHLs operate on both lanes due to their large vehicle size. So, while the results were less affected by the additional paved shoulder application in this analysis, the use of paved shoulders can provide an additional option of operating SHLs in one lane when that lane is wide enough to carry large-sized vehicles.





Koh et al. 2022a, Reprinted with permission from Sage Publications, Inc., © 2022

Figure 8. Reduction rate of critical tensile stress compared to granular shoulder models at the (a) bottom of PCC slab under IoHs, (b) bottom of PCC slab under SHLs, (c) top of PCC slab under IoHs, and (d) top of PCC slab under SHLs

LCCA for Mechanistic-Based Service Life Reduction and Permit Fee Decision

Methodology

This section is dedicated to assessing pavement performance in relation to total fatigue cracking, incorporating both bottom-up fatigue cracking and top-down fatigue cracking on JPCP. The objective is to conduct LCCA to determine (1) the reduction in JPCP service life and (2) the

RDAC influenced by different superload types. To derive these two main LCCA outcomes, additional comprehensive FEA was undertaken, involving analysis matrices shown in Table 11 listing traffic loadings and JPCP structures.

Table 11. Comprehensive analysis matrices for FEA and LCCA

Input parameters	Value				Unit
Thickness of PCC layer	8, 9, 10				in.
Transverse joint spacing	15 for 8 in. and 9 in. of PCC layer thickness 17 for 10 in. of PCC layer thickness 20 for 8 in., 9 in., and 10 in. of PCC layer thickness				ft
Composite modulus of subgrade reaction	Spring	Summer	Fall	Winter	psi/in.
	50	120	120	250	
CTE	4.3				10^{-6} in./in./°F
Temperature gradients	4, 0, -4				°F/in.
Elastic modulus of PCC layer	4,000,000				psi
Traffic loadings	IoH: 18 types × 3 payload levels (100%, 75%, 50%) = 54 types SHL: 16 types × 3 payload levels (100%, 75%, 50%) = 48 types FHWA class 9 truck (reference vehicle): 1 type				-
Total	7,416 analysis cases				

Traffic loading details for all types of superloads are available in Table 6 and Table 7, consistent with the loading inputs used for quantifying JPCP damage. The LCCA was conducted using FEA results derived from more than 7,400 analysis cases, evaluating outcomes across various JPCP and traffic conditions. It is important to note that the JPCP structural properties for the LCCA in this chapter were selected based on data from the Iowa DOT's Pavement Management Information System (PMIS), updated in 2021 (Iowa DOT 2023b). The overall flow chart describing the procedure of the LCCA is illustrated in Figure 9.

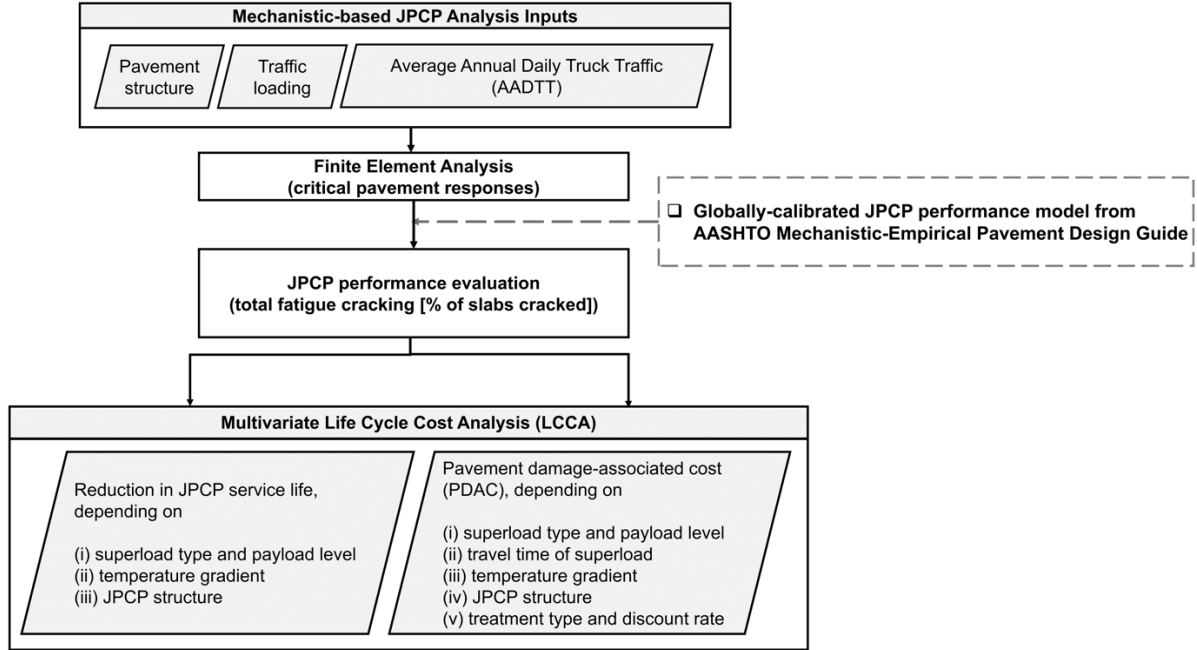


Figure 9. Overall flow chart for LCCA

To evaluate the performance of JPCP under superloads, critical pavement responses obtained from a comprehensive FEA were utilized to develop JPCP fatigue damage-associated performance curves through the application of transfer functions. The critical loading locations categorized for different superload types were also applied to the FEMs as loading inputs, using the FEA software ISLAB2005 to calculate critical tensile stresses at the top and bottom of the PCC slab. Subsequently, the critical pavement responses of the PCC layer were converted to fatigue cracking using a globally calibrated performance model and corresponding calibration constants obtained from the *Guide for Mechanistic-Empirical Design* (ARA, Inc. 2004a) and the latest AASHTOWare Pavement ME Design software (i.e., version 2.6.0) (AASHTO 2022). Equation 5 through equation 7 outline the equations and calibration constants used in the JPCP performance model for calculating total fatigue cracking, integrating both bottom-up fatigue cracking and top-down fatigue cracking of a PCC slab. It is noteworthy that a modulus of rupture value of 662.5 psi was determined and applied to the JPCP performance model. This value aligns with the average modulus of rupture value of 667.2 psi, calculated from the six Iowa sections using LTPP data.

$$TCRACK [\%] = (CRK_{Bottom-up} + CRK_{Top-down} - CRK_{Bottom-up} \cdot CRK_{Top-down}) \cdot 100 \quad (5)$$

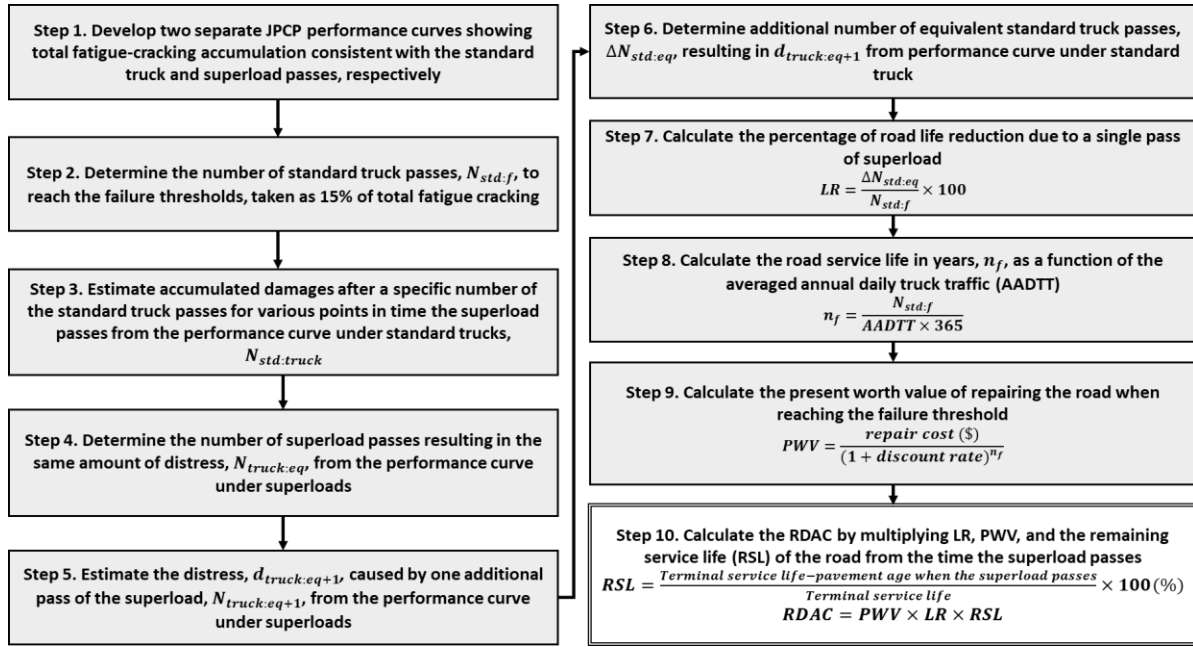
$$CRK = \frac{1}{1 + C_4 F D^{C_5}}; FD = \sum \frac{n_{i,j,k,l,m,n}}{N_{i,j,k,l,m,n}} \quad (6)$$

$$\log(N_{i,j,k,l,m,n}) = C_1 \cdot \left(\frac{MR_i}{\sigma_{i,j,k,l,m,n}} \right)^{C_2} + 0.4371 \quad (7)$$

where $TCRACK$ is the total cracking, %; $CRK_{Bottom-up}$ is the predicted amount of bottom-up cracking; $CRK_{Top-down}$ is the predicted amount of top-down cracking; FD is the accumulated fatigue damage over the design period for current crack spacing occurring at the critical fatigue location in the slab using Miner's rule; C_4 and C_5 are the calibration constants ($C_4 = 0.52$, $C_5 = -2.17$ for global calibration); $n_{i,j,k,l,m,n}$ is the applied number of load applications at condition i, j, k, l, m , and n ; $N_{i,j,k,l,m,n}$ is the allowable number of load applications at condition i, j, k, l, m , and n ; $\sigma_{i,j,k,l,m,n}$ is the applied stress at condition i, j, k, l, m , and n , psi; i is the age; j is the month; k is the axle type; l is the load level; m is the temperature difference; n is the traffic path; MR_i is the PCC modulus of rupture at age i , psi; and C_1 and C_2 is the calibration constants ($C_1 = 2.0$, $C_2 = 1.22$ for global calibration).

The estimation of JPCP service life reduction involves identifying an equivalent number of reference vehicles that would cause a comparable level of total fatigue cracking as a single pass of a superload from the JPCP performance curves drawn for a class 9 truck and superload traffic, respectively. For instance, if the equivalent number of class 9 trucks (referred to as the reference vehicle) requires 80 passes to generate the same distress observed during a single pass of a specific superload at a JPCP service life of 5 years, the JPCP service life reduction for 80 passes of a class 9 truck can be equated to the service life reduction resulting from a single superload pass. Note that the JPCP performance models were developed using total fatigue cracking as a trigger for treatment in calculating JPCP service life reduction. Once the JPCP performance models for each type of superload and class 9 truck were developed, the reduction in service life for various pavement structures and traffic types could be derived using the threshold limit of total fatigue cracking, specifically 15% of slabs cracked, recommended by the FHWA (Visintine et al. 2018) and the latest AASHTOWare Pavement ME Design software (i.e., version 2.6.0) as a pavement performance indicator. The final determination of service life reductions for JPCPs subjected to superloads is derived by averaging the service life reduction results obtained from four distinct JPCP performance models, each applying different composite moduli of subgrade reaction to represent the four seasons. It should be emphasized that a calculated terminal service life of JPCPs falling below 40 years is considered as the JPCP's service lifetime for its subsequent treatment. Conversely, for JPCPs with terminal service lives exceeding 40 years, the reduction in service life calculation is based on a 40-year design life.

The RDAC, initially proposed by Tirado et al. (2010) as a methodology for estimating permit fees for heavy trucks, has been utilized in subsequent studies (Dong et al. 2014, Batioja-Alvarez et al. 2018) for cost-allocation analysis of asphalt pavements exposed to SHL traffic. The RDAC was proposed to be computed by multiplying (1) the percentage of road life reduction (LR) caused by a single pass of a superload, (2) the present-worth value (PWV) of repairing the roads, and (3) the remaining service life (RSL) of the roads at the time the superload passes. In this section, the RDAC concept was adopted to evaluate the economic impact of superloads on JPCPs. Figure 10 outlines the overall steps and provides detailed explanations on determining the RDAC of JPCP when subjected to a single pass of a superload.



Koh et al. 2023a, Reprinted with permission from Sage Publications, Inc., © 2023

Figure 10. Overall steps of RDAC determination for JPCP section subjected to superload

Multivariate RDACs, which vary based on JPCP structure, environmental condition, traffic load, and treatment type, were calculated and compared. This analysis aimed to establish a mechanistic basis for decision-making regarding permit fees for each type of superload. Consistent with the approach used for determining JPCP service life reduction, the RDACs derived from four distinct composite moduli of subgrade reaction, each representing one of the four seasons, were averaged to calculate annual RDAC values. Also, for JPCP structures with terminal service lives exceeding 40 years, a 40-year design life was considered. Figure 11 illustrates an example of determining the additional equivalent number of standard trucks $\Delta N_{std:eq}$ resulting in the same distress as a single additional superload pass.

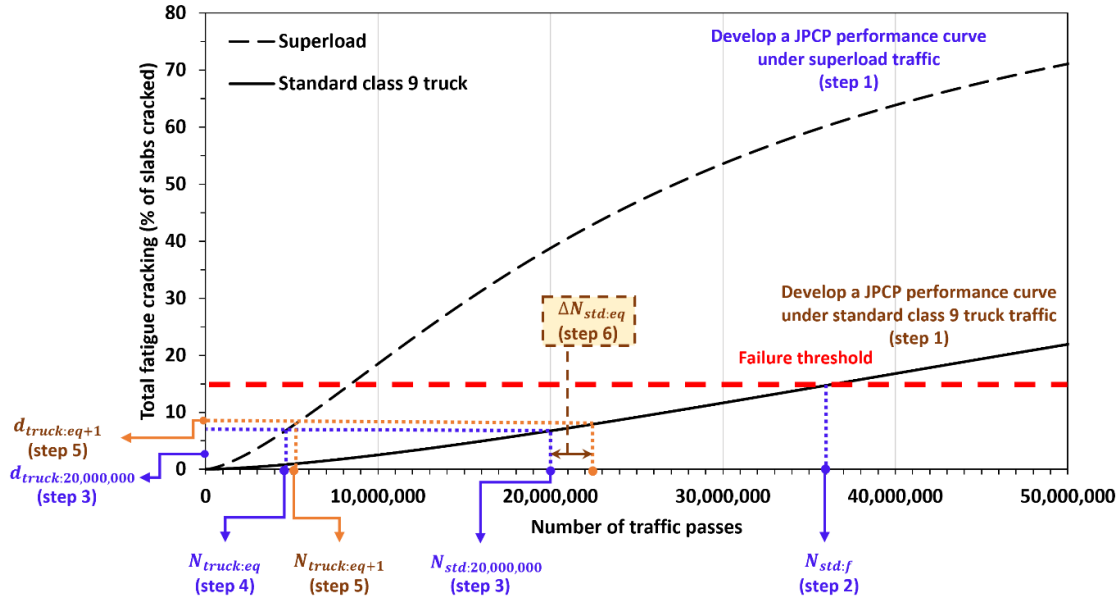
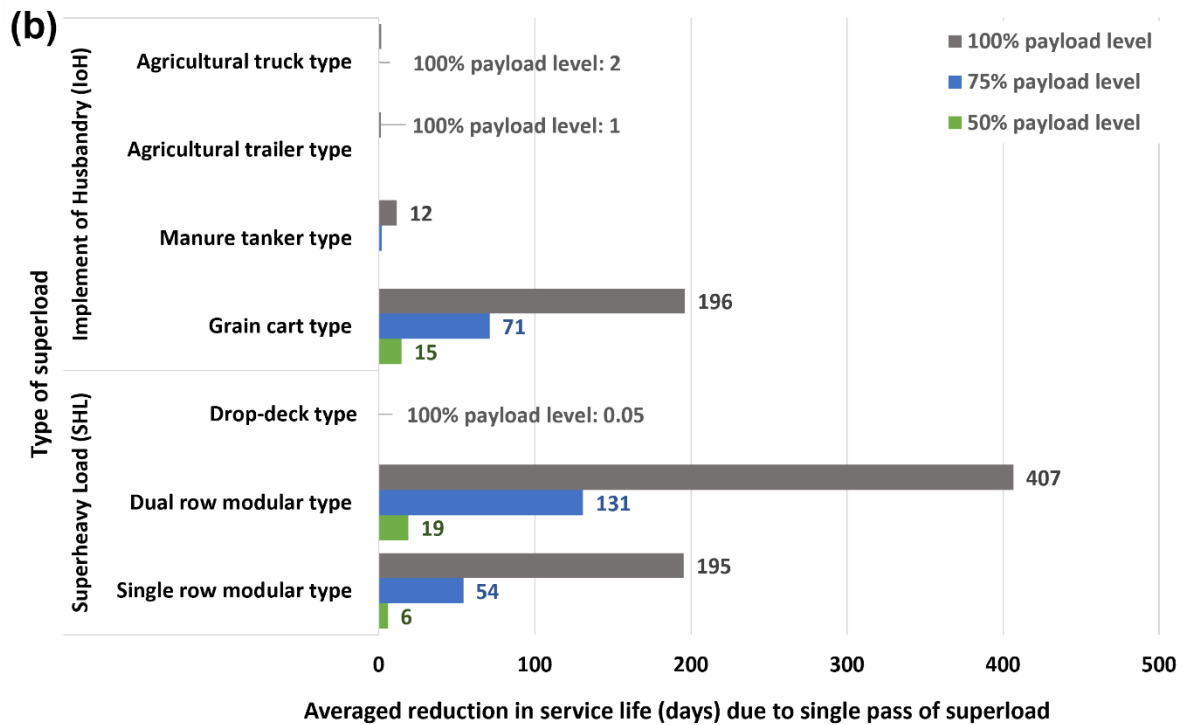
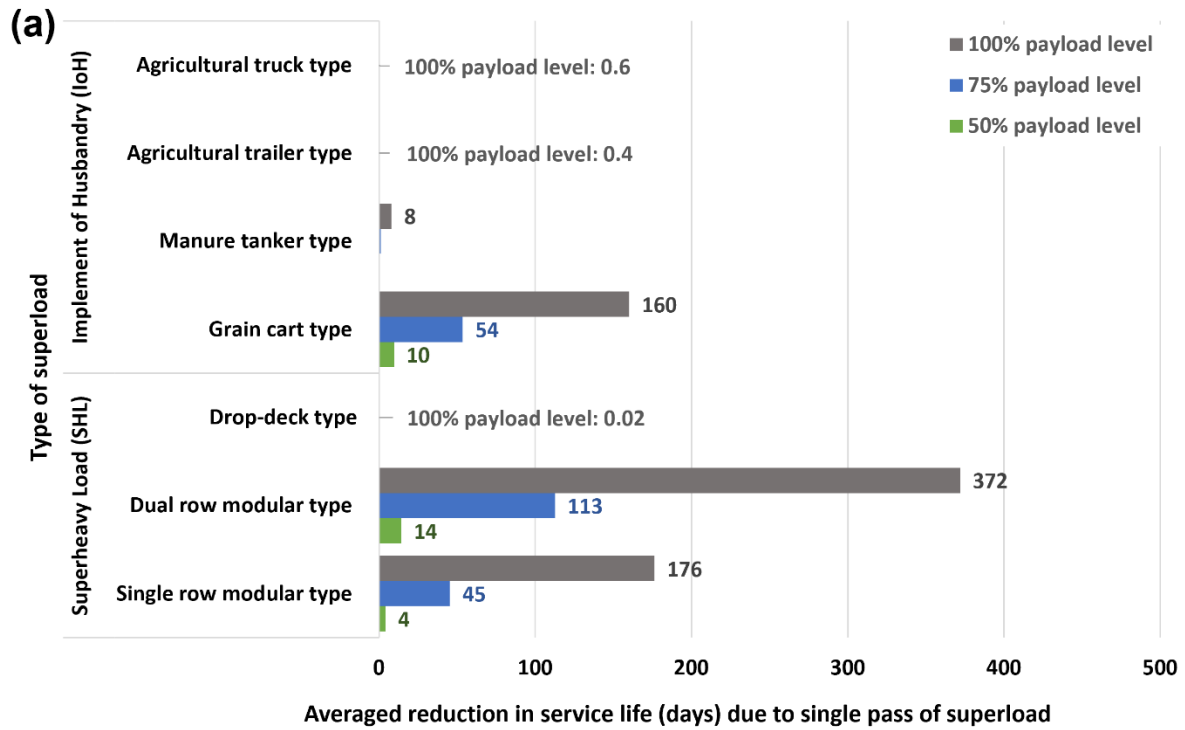


Figure 11. Determination of equivalent number of standard trucks from JPCP performance curve

Multivariate LCCA Results: JPCP Service Life Reduction under Superloads

The JPCP service life reduction was initially expected to exhibit significant variability based on the type of superload and payload levels due to their non-standardized loading configurations. In this section, the reduction in JPCP service life is quantified as the number of days by which the terminal service life is reduced when a single pass of a superload is made at a specific time during the terminal service life. Figure 12 presents graphs illustrating the averaged service life reduction of JPCP resulting from a single pass of a superload, considering an 8 in. thick PCC layer, 20 ft wide transverse joint spacing, and varying temperature gradients.



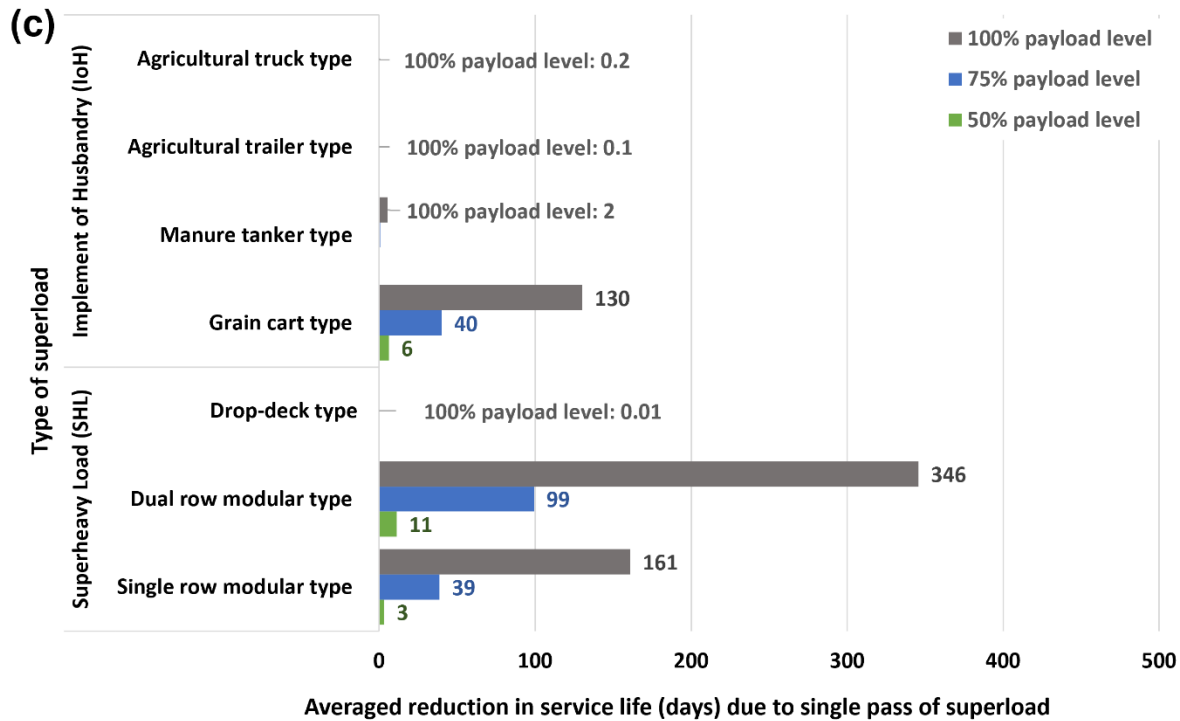


Figure 12. Reduction in service life due to a single pass of superload for JPCP PCC layer: (a) with 0°F/in. temperature gradient, (b) with 4°F/in. temperature gradient, and (c) with -4°F/in. temperature gradient

The analyses confirmed that the three most significant contributors to fatigue damage were the grain cart IoH, a dual-row modular SHL, and a single-row modular SHL. When the payload level is reduced from 100% to 75%, or from 100% to 50%, the average reduction in service life under various superload types decreases by approximately 73% and 97%, respectively. The reduction in service life was also calculated to be greater under downward curling conditions when the temperature gradient is positive compared to the 0°F/in. temperature gradient conditions, meaning that the PCC layer generates more bottom-up fatigue cracking, governing the total fatigue cracking when combined with traffic loads. On the other hand, top-down fatigue cracking caused by curl-up can be intensified and bottom-up fatigue cracking can be alleviated when a PCC layer has a negative temperature gradient. However, top-down fatigue cracking is a smaller proportion of the total fatigue cracking than bottom-up fatigue cracking, so the reduction in service life from negative temperature gradient conditions was calculated to be less than that from 0°F/in. temperature gradient conditions. Note that the graphs in Figure 12 depict only the service life reduction when a single pass of a superload was made at 50% of terminal service life, as the specific timing of the superload pass was found to have a negligible impact on the amount of service life reduction.

To confirm the dependence of service life reduction on the pavement structure, the service life reductions for various JPCP structures subjected to a single pass of a dual-row modular SHL, identified as the superload type causing the most significant reduction in JPCP service life as determined from Figure 12, was derived, as shown in Figure 13.

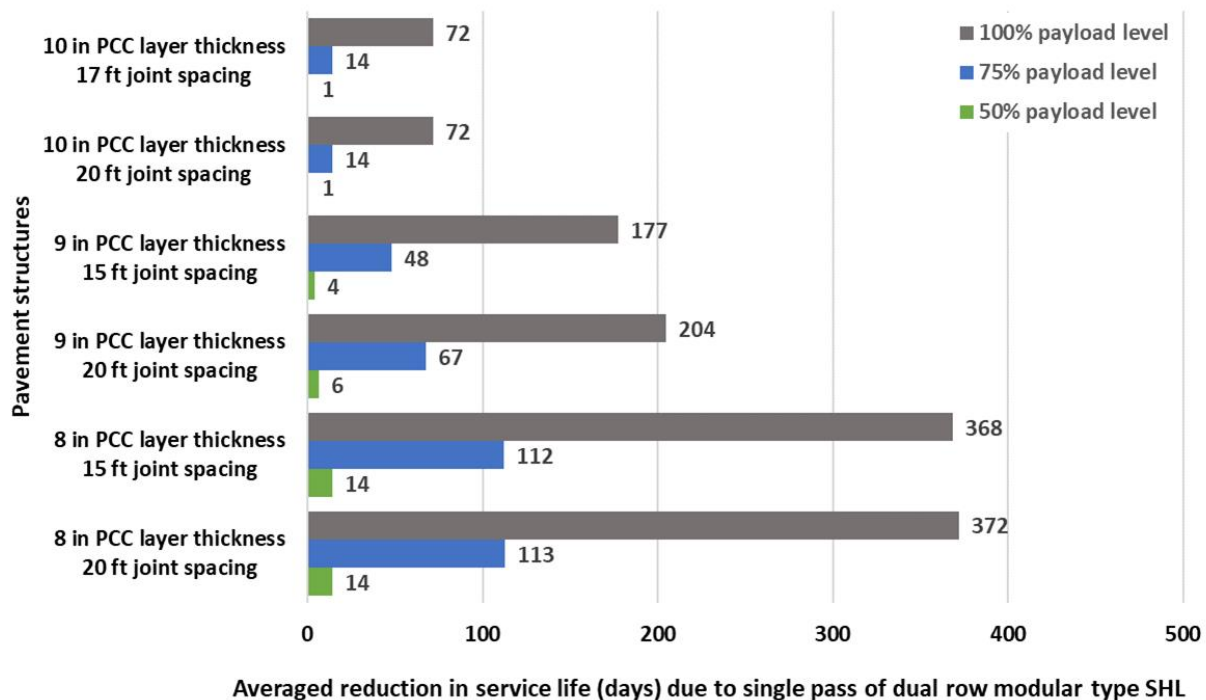


Figure 13. Reduction in service life due to a single pass of dual-row modular SHL traveling on different JPCP structures with 0°F/in. temperature gradient

The resulting service life reduction increased significantly as the PCC layer thickness decreased, and the service life reduction tended to increase slightly as the transverse joint spacing increased in the case of JPCPs with a 0°F/in. temperature gradient. This observation aligns with the anticipated relationship between the JPCP structure and the total fatigue damage. A more in-depth interpretation of this trend is provided in the subsequent RDAC assessment section.

Multivariate LCCA Results: RDAC Assessment

Multivariate RDAC Assessment Case I. RDAC According to Traffic Loading

In this section, RDACs were calculated based on the total fatigue cracking of JPCPs for different superload types. The RDACs corresponding to different superload types and payload levels traveling at 25% of terminal service life of a JPCP with an 8 in. thick PCC layer, 20 ft wide transverse joint spacing, and 0°F/in. temperature gradient were calculated, with the results shown in Figure 14.

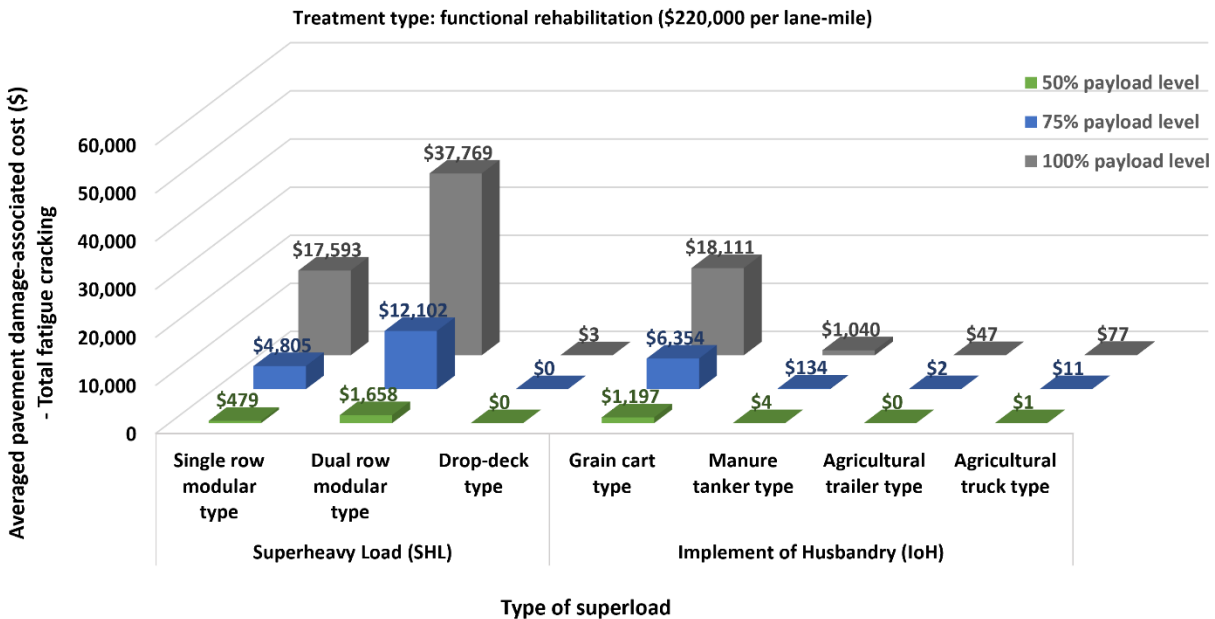


Figure 14. RDACs due to a single pass of superload types traveling at 25% of terminal service life of JPCP

Functional rehabilitation, one of the treatment options, and the corresponding treatment cost per lane-mile (i.e., \$220,000 for non-interstate roadways) when reaching 15% of slabs cracked, the failure threshold, were chosen for the RDAC calculations based on the 2019–2028 Iowa Transportation Asset Management Plan (TAMP) (Iowa DOT 2019). The RDAC results indicate that the dual-row modular SHLs with relatively high axle weights exhibited the highest RDACs, followed by grain cart IoHs and single-row modular SHLs. Conversely, additional averaged RDAC values close to \$0 were obtained for the drop-deck SHLs that have axle weights not much different from the axle weight of a class 9 truck (i.e., 17 kips). Since a 100% payload level of a superload refers to the maximum payload capacity of each commercial superload, most of their axle weights tend to exceed the state’s permit limit. Accordingly, the RDACs under superloads loaded at a 100% payload level may appear more excessive than expected, but when the payload level was reduced from 100% to 75%, or from 100% to 50%, the analyses demonstrated substantial reduction in damage-associated costs, with RDAC reduction rates averaging 81% and 98%, respectively. Furthermore, an intensive analysis of the three superload types causing the most fatigue damage from Figure 14, including single-row modular SHLs, dual-row modular SHLs, and grain cart IoHs, was conducted to evaluate their RDAC dependence on varying travel times on the same JPCP structure. Figure 15 shows that RDACs decreased as the superload traveled at a later time relative to the terminal service life of the JPCP. This trend is mainly attributed to factors such as the discount rate, JPCP service life, n_f , and RSL, all calculated based on travel time.

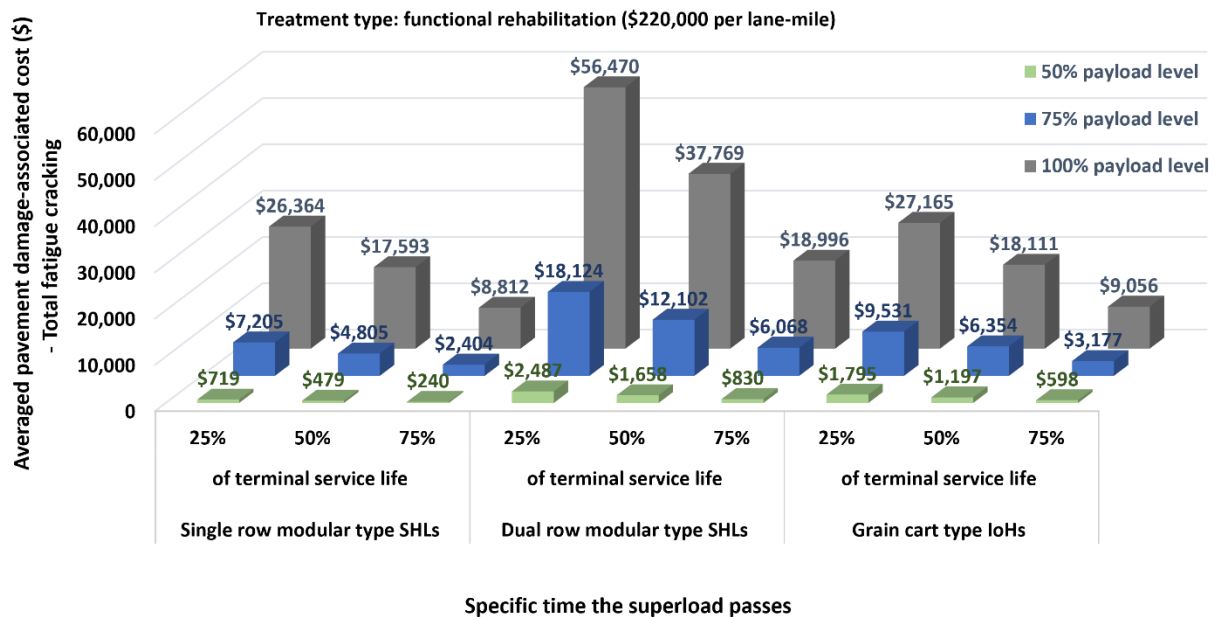
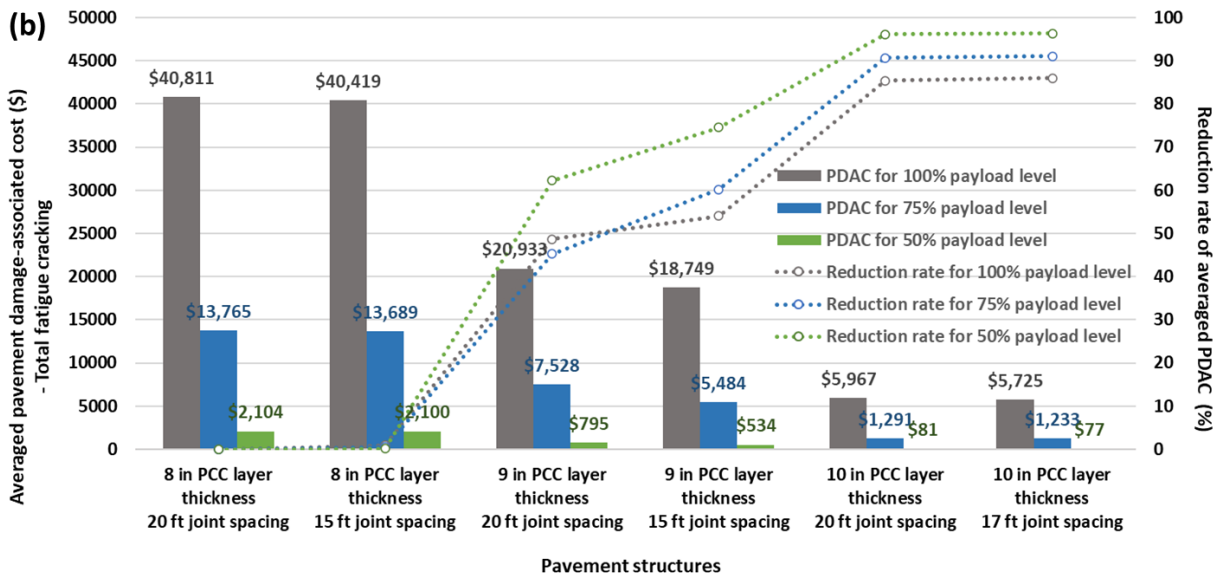
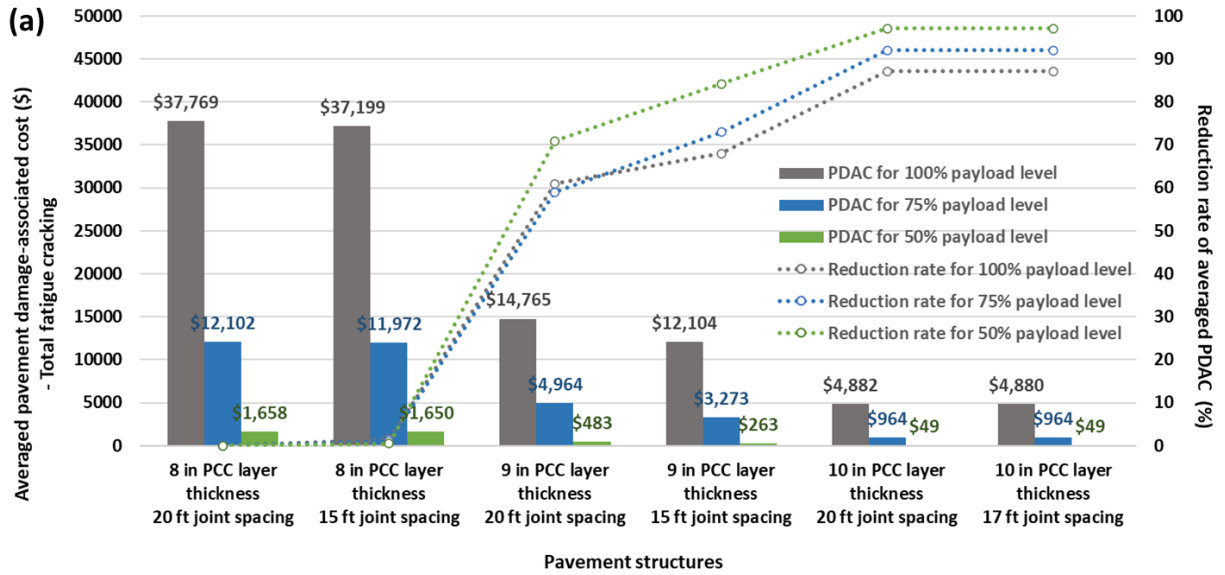


Figure 15. RDACs due to a single pass of the three most damage-causing types of superload traveling at varying times on JPCP

Note that in the above figure, the JPCP had an 8 in. thick PCC layer, 20 ft wide transverse joint spacing, and 0°F/in. temperature gradient.

Multivariate RDAC Assessment Case II. RDAC According to JPCP Structures with Different Temperature Gradients of PCC Layer

The RDACs for different JPCP structures under dual-row modular SHLs, identified as the most significant contributor to fatigue damage, exhibited varying results based on structural variables, including transverse joint spacing and temperature differences following different PCC layer thicknesses, as illustrated in the graphs of Figure 16.



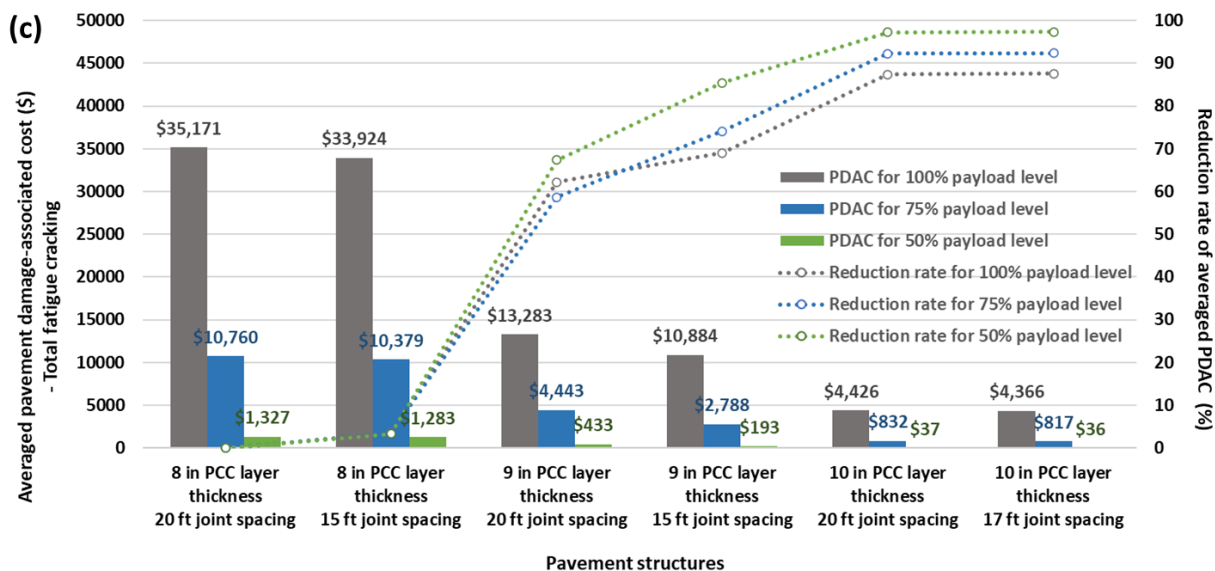


Figure 16. RDACs due to a single pass of dual-row modular type SHL traveling at 25% of terminal service life of different JPCP structures' PCC layer: (a) with 0°F/in. temperature gradient, (b) with 4°F/in. temperature gradient, and (c) with -4°F/in. temperature gradient

Note that the averaged RDAC reduction rate for each pavement structure was calculated based on a JPCP with an 8 in. thick PCC layer and a 15 ft wide transverse joint as a reference pavement structure.

Overall, the averaged RDACs exhibited a tendency to decrease with increasing PCC layer thickness and decreasing transverse joint spacing, regardless of the temperature gradient of the PCC layer (ranging from -4°F/in. to 4°F/in.). This trend aligns with the RDACs associated with a general class 9 truck loading. In other words, general class 9 truck traffic on a JPCP having a positive temperature gradient results in greater bottom-up fatigue cracking, in turn governing total fatigue cracking, due to the downward curling effect when combined with class 9 truck loads in the case of larger transverse joint spacing (Ceylan 2014). JPCPs with higher transverse joint spacing subjected to general class 9 truck loads therefore cause higher RDACs when the PCC layer has a positive temperature gradient. Even if the PCC layer of JPCP has a negative temperature gradient that would intensify the top-down fatigue cracking caused by the curl-up effect, JPCP structures with larger transverse joint spacing still tend to exhibit higher total fatigue cracking and corresponding RDAC due to their structural weakness that is vulnerable to mid-panel transverse cracking. In practice, most JPCPs on-site exhibited negative temperature gradients due to built-in curling resulting from daytime construction (Hansen and Wei 2008).

The graphs in Figure 16 show that the RDACs resulting from a single pass of dual-row modular SHLs on JPCPs with 20 ft transverse joint spacing were slightly higher than those with shorter transverse joint spacing structures, even when applying a temperature gradient varying from -4°F/in. to 4°F/in. to the PCC layer. However, the influence of transverse joint spacing on the RDACs of JPCPs under a single pass of dual-row modular SHLs was found to be less significant than that observed for a general class 9 truck load. The relatively insignificant relationship

between RDACs and transverse joint spacing under a single pass of SHLs is mainly attributed to the non-standardized loading configurations of SHLs with respect to vehicle load distribution and critical loading location. Most modular SHLs feature a single integrated axle group comprised of multiple successive axles with relatively short axle spacing, as depicted in Figure 17, providing a uniform loading distribution over the area of the PCC slabs.

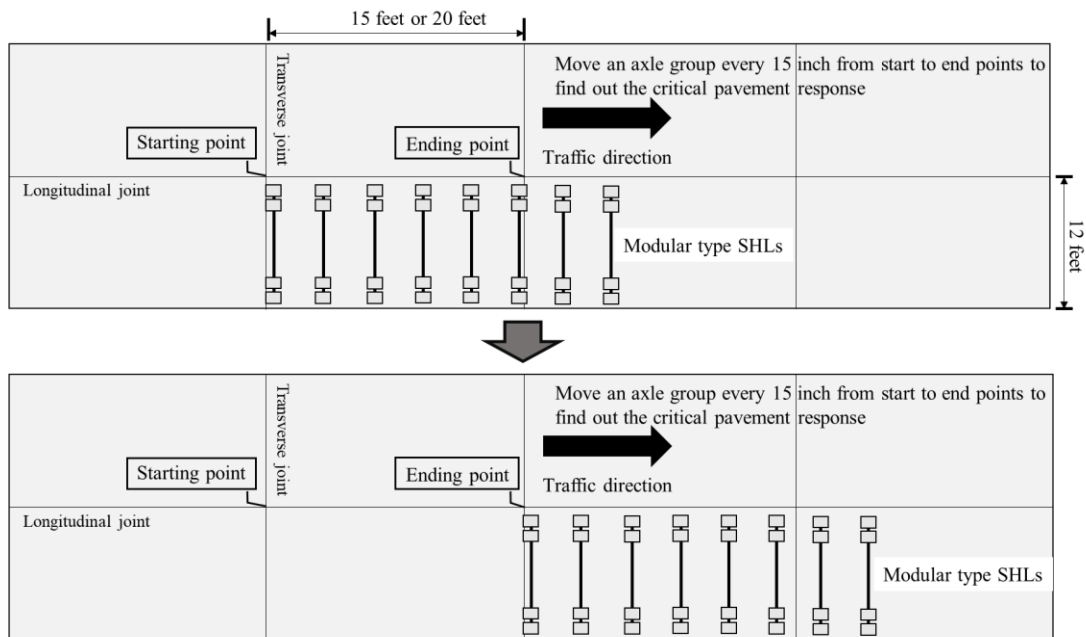


Figure 17. Determination of critical loading locations of modular type SHL generating critical tensile stress at the bottom of PCC layer of JPCP

Note that in the figure above the JPCP had an 8 in. thick PCC layer and 15 ft or 20 ft wide transverse joint spacings.

Consequently, the loading properties of modular SHLs have a greater effect on total fatigue cracking and the corresponding RDACs than the transverse joint spacing effect. As a result, RDAC differences between 12 ft transverse joint JPCP and shorter transverse joint JPCP under modular SHL traffic are calculated to be less than for the general class 9 truck load case. This interpretation becomes clearer when examining critical pavement responses resulting from various axle loadings of SHLs and the tandem axle loading of a general class 9 truck. Figure 18 shows the rate increase in critical tensile stress at the bottom of the PCC slab, the critical pavement response type for bottom-up fatigue cracking, between JPCPs with 15 ft and 20 ft transverse joint spacing, when subjected to one to eight axles of dual-row modular SHLs and the tandem axles of a class 9 truck.

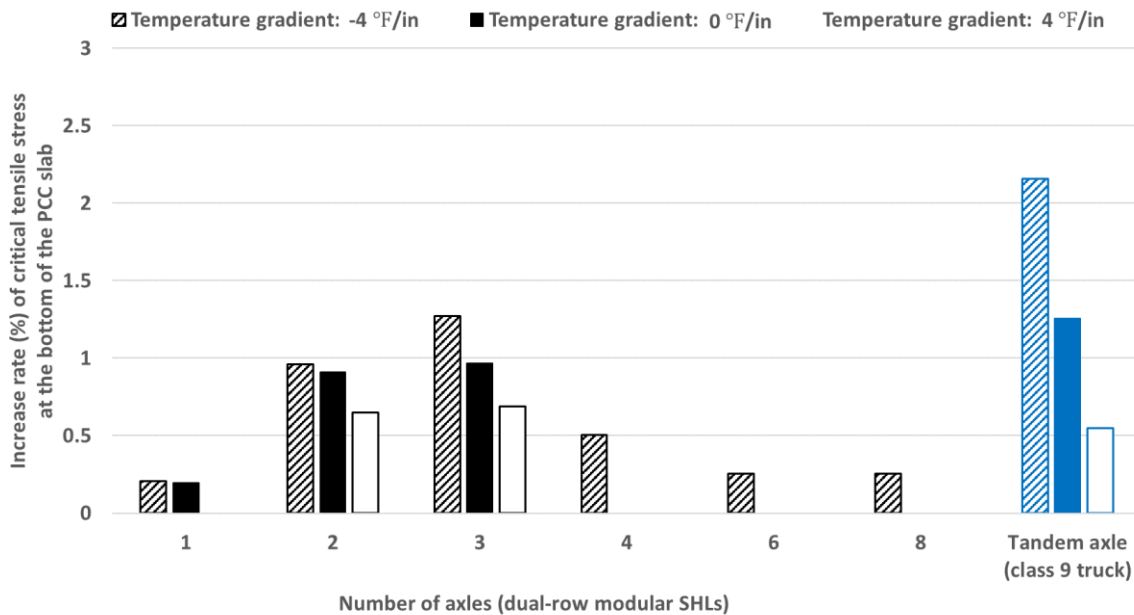


Figure 18. Increase rate of critical tensile stress at the bottom of the 8 in. thick PCC slab between JPCPs with 15 ft and 20 ft wide transverse joint spacings

The critical loading locations of a class 9 truck and a dual-row modular SHL can be determined by moving each axle group every 15 in. from start to endpoints, as shown in Figure 17. The critical tensile stress at the bottom of a PCC slab according to the critical loading location of each axle loading group exhibits the highest difference between JPCPs with 15 ft and 20 ft transverse joint spacing when subjected to two or three axle loadings of dual-row modular SHLs. It was also observed that the difference in critical tensile stress at the bottom of the PCC slab decreased as the number of axles of the dual-row modular SHLs increased by more than three, due to the effect of uniform loading distribution over the area of the PCC slabs. In contrast, a general class 9 truck with tandem axles produced a greater difference in critical tensile stress between two JPCP structures with different transverse joints than the modular SHLs, which generally have more than eight axles. This trend confirms that when dealing with general transportation vehicle types, including class 9 trucks, a JPCP transverse joint has a significant impact on total fatigue damage, while the effect of the transverse joint is relatively smaller in the case of SHL traffic.

Multivariate RDAC Assessment Case III. RDAC According to Management Factors

Various management factors related to agency and user costs throughout the JPCP life cycle can be considered for economic evaluation of maintenance, rehabilitation, and reconstruction activities. In this section, two agency cost factors, treatment type and discount rate, directly affecting RDAC calculation were selected as multivariate management factors. Four levels of treatment types, namely functional rehabilitation, minor structural rehabilitation, major structural rehabilitation, and reconstruction, along with their corresponding treatment costs per lane-mile (\$220,000, \$280,000, \$425,000, and \$700,000, respectively), were taken from the 2019–2028

Iowa TAMP (Iowa DOT 2019) and utilized in the multivariate RDAC analysis. The discount rate, representing the rate of return used for investors to discount future cash flows back to their present values, was considered in the range of 1% to 4% to account for variations in the US discount rate observed between 2017 and 2022. Figure 19 presents RDACs according to treatment type and discount rate of JPCP for an 8 in. thick PCC layer and 20 ft wide transverse joint spacing, considering three representative types of superloads carrying 50% payload levels. The results demonstrate that treatment cost and discount rate directly impact the PWV calculation, influencing the RDAC values. For instance, at a US discount rate of 1% as of June 15, 2022, the present values of RDACs were calculated as \$1,719, \$1,044, \$688, and \$540 for a single pass of a single-row modular SHL, corresponding to future reconstruction, major structural rehabilitation, minor structural rehabilitation, and functional rehabilitation, respectively.

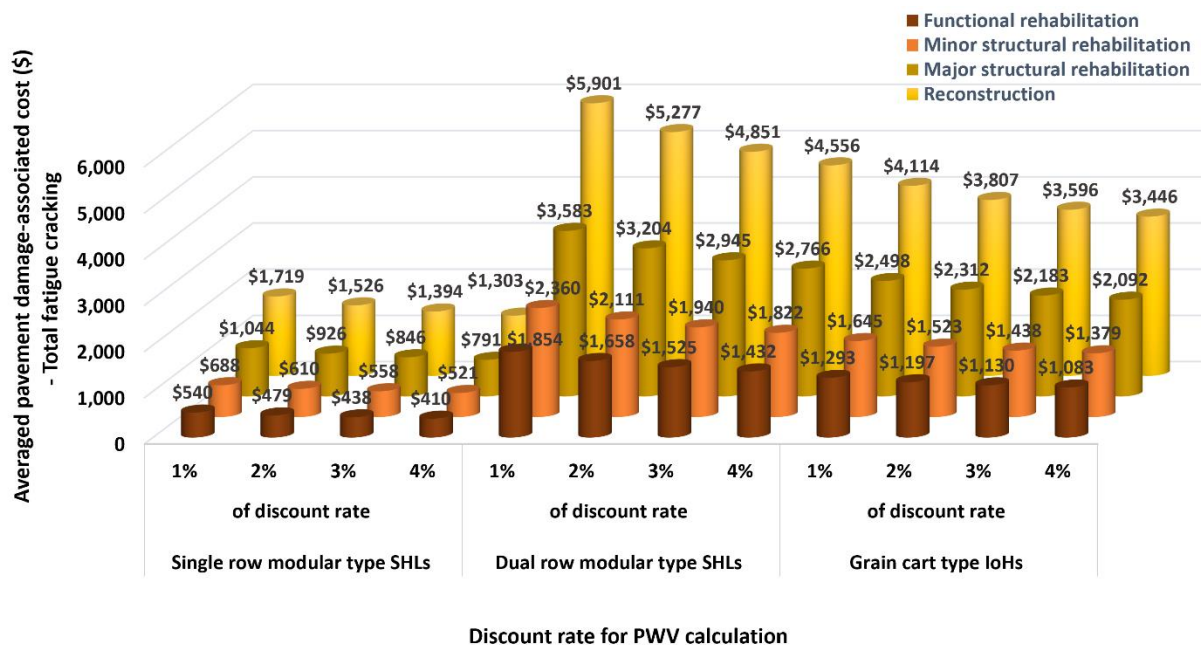


Figure 19. RDACs of JPCP for different treatment types and discount rates when subjected to a single pass of the three most damage-causing types of superload carrying 50% payload level

Note that in the above figure, the JPCP has an 8 in. thick PCC layer, 20 ft wide transverse joint spacing, and 0°F/in. temperature gradient.

Development of AI-Based Prediction Models

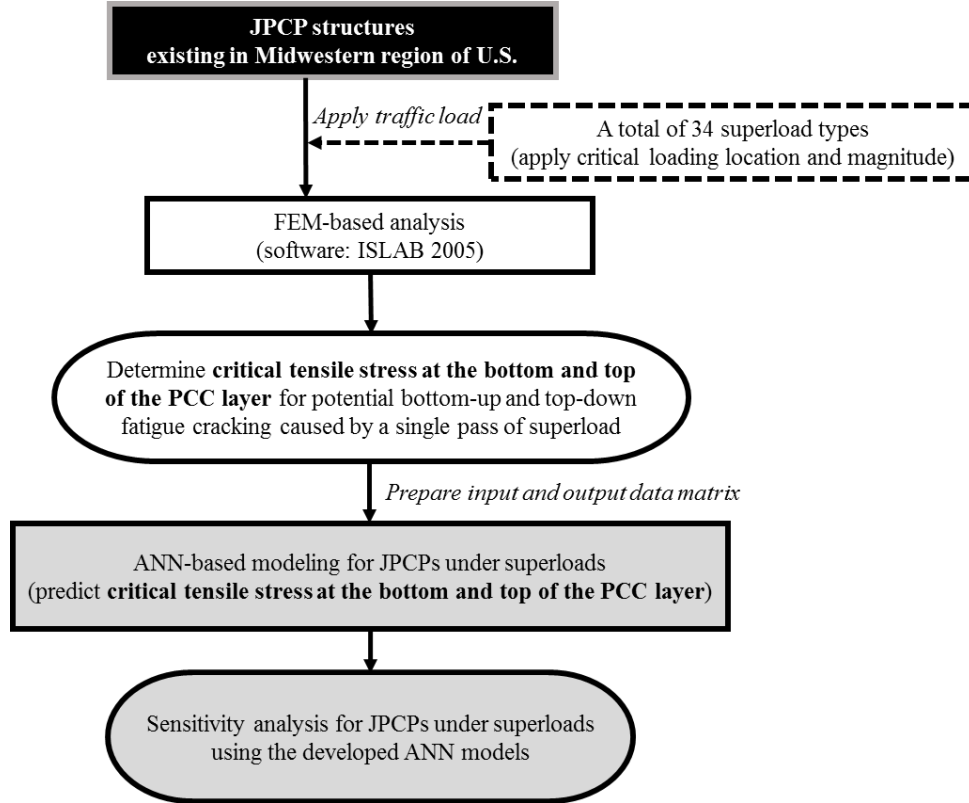
Methodology

The recent advancements in pavement design software, such as AASHTOWare Pavement ME Design, offer robust support for M-E pavement analysis and design, dealing with comprehensive

pavement structures and traffic loadings. However, a notable limitation persists in these tools to comprehend the extensive dimensional variation inherent in loading configurations of recently released commercial superloads that can be defined in many categories, such as IoHs including grain carts, manure tankers, agricultural trailers, or agricultural trucks, and such as SHLs including single-row modular, dual-row modular, or drop-deck types. Considering this limitation, this section suggests a pragmatic solution: the development of separate ANN models for each of the superload categories. This approach allows users to select a specific superload category of interest and utilize the corresponding ANN model within user-friendly pavement design software, such as AASHTOWare Pavement ME Design, to predict critical pavement responses under a single pass of a superload with high prediction accuracy.

The ANN models presented herein are meticulously developed and optimized per each superload category for highly accurate predictions of critical pavement responses, specifically related to bottom-up and top-down fatigue cracking in JPCPs. The development process leverages an FEM-based JPCP analysis database assembled from the prior sections of this chapter, encompassing various critical loading locations and payload levels associated with various superload types. In other words, the ANN-based models suggested in this section not only have implications of being developed based on a database comprised of a wider loading configuration scope of superloads but the database itself also implies mechanistic loading input determination methodologies for JPCP, such as critical loading location determination according to different JPCP structures and superload types.

Note that the optimized ANN models for different superload types were integrated into a prototype tool developed in this study, enabling the quantification of superload impacts on Iowa road infrastructure systems, as detailed in subsequent chapters. Furthermore, a sensitivity analysis was performed on pavement structure and loading parameters using the developed ANN models to identify the significance level of each explanatory variable in generating the target responses. Figure 20 schematically shows the main steps in ANN modeling for JPCPs under superloads.



Koh et al. 2024, Reprinted with permission from Elsevier, © 2024

Figure 20. Overall steps for ANN modeling for JPCPs under different superload types

Note that in the above figure, the gray-colored boxes indicate the main steps of this section.

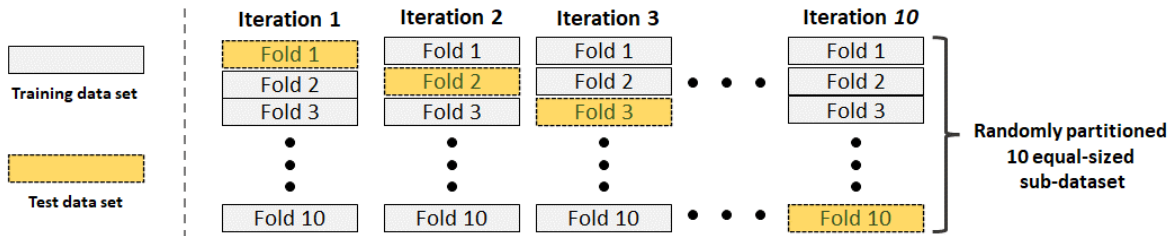
A comprehensive matrix for FEA using ISLAB2005 is outlined in Table 12 for determining critical tensile stress at the top and bottom of the PCC slab of JPCPs (Koh et al. 2024). The FEA was conducted across a spectrum of 34 different superload types, considering four different payload levels. The matrix encompasses all requisite inputs and outputs derived from the ISLAB2005 software, meticulously organized into a structured data matrix. This organized data matrix was subsequently utilized as the foundation for the development and optimization of ANN models. The inclusion of various superload types and payload levels ensures a comprehensive evaluation of fatigue-related damage scenarios within JPCPs, enhancing the robustness and applicability of the resulting ANN models.

Table 12. Comprehensive analysis matrix for JPCP FEA

Local road				Highway			
Thickness of PCC layer (in.)				Thickness of PCC layer (in.)			
7, 8, 9				10, 13			
Seasonal composite modulus of subgrade reaction (psi/in.)				Seasonal composite modulus of subgrade reaction (psi/in.)			
Spring	Summer	Fall	Winter	Spring	Summer	Fall	Winter
50	120	120	250	50	120	120	250
Transverse joint spacing (ft): 15, 20				Transverse joint spacing (ft): 17, 20			
CTE ($10^{-6}/^{\circ}\text{F}$): 4.3, 5.2				CTE ($10^{-6}/^{\circ}\text{F}$): 4.3, 5.2			
Temperature gradients ($^{\circ}\text{F/in.}$): -4, -2, 0, 2, 4				Temperature gradients ($^{\circ}\text{F/in.}$): -4, -2, 0, 2, 4			
Elastic modulus of PCC layer (psi): 4×10^6				Elastic modulus of PCC layer (psi): 4×10^6			
Traffic loadings				Traffic loadings			
IoH: 18 types \times 4 payload levels = 72 types				IoH: 18 types \times 4 payload levels = 72 types			
SHL: 16 types \times 4 payload levels = 64 types				SHL: 16 types \times 4 payload levels = 64 types			
Total analysis cases: 32,640 cases				Total analysis cases: 21,760 cases			

Source: Koh et al. 2024

To construct the ANN-based surrogate model with the highest prediction accuracy, a total of five backpropagation algorithms, including (1) Levenberg-Marquardt (Levenberg 1944, Marquardt 1963), (2) Bayesian Regularization (MacKay 1992), (3) Broyden-Fletcher-Goldfarb-Shanno (BFGS) Quasi-Newton (Broyden 1970a, Broyden 1970b, Fletcher 1970, Goldfarb 1970, Shanno 1970), (4) Resilient Backpropagation (Riedmiller and Braun 1993), and (5) Scaled Conjugate Gradient (Johansson et al. 1991), were employed for comparative assessment. The ANN architectures also underwent optimization by varying the number of hidden layers and neurons per hidden layer, containing randomly initialized weight for each node connection. Separate ANN models were developed and optimized according to different critical pavement response and superload types, i.e., the seven parent class types shown in Table 4 and Table 5. To assess the performance of each ANN model, a robust evaluation using the 10-fold cross-validation technique, as illustrated in Figure 21, was conducted.



Koh et al. 2024, Reprinted with permission from Elsevier, © 2024

Figure 21. Tenfold cross validation technique for ANN model performance evaluation

The evaluation metrics employed included the coefficient of determination, R^2 , average absolute error (AAE), and root mean square error (RMSE). The respective equations defining these three measures, as shown in equations 8 through 10, were applied to quantify the prediction accuracy

of the ANN models developed for the distinct critical pavement responses and superload types under consideration.

$$R^2 = 1 - \frac{\sum_{j=1}^n (y_j^{\text{measured}} - y_j^{\text{predicted}})^2}{\sum_{j=1}^n (y_j^{\text{measured}} - y_{\text{mean}}^{\text{measured}})^2} \quad (8)$$

$$AAE = \frac{\sum_{j=1}^n |y_j^{\text{measured}} - y_j^{\text{predicted}}|}{n} \quad (9)$$

$$RMSE = \sqrt{\frac{\sum_{j=1}^n (y_j^{\text{measured}} - y_j^{\text{predicted}})^2}{n}} \quad (10)$$

where R^2 is the coefficient of determination, AAE is the average absolute error, $RMSE$ is the root mean square error, n is the size of observations, y_j^{measured} is the measured value of j th data node, and $y_j^{\text{predicted}}$ is the predicted value of j th data node.

Development of ANN-Based Surrogate Models

Table 13 provides a summary of essential details pertaining to the multilayer ANN modeling, including information on explanatory variables and target responses of JPCPs under superloads as well as ANN architectures, applying the five different backpropagation algorithms.

Table 13. Details of multilayer ANN modeling for JPCPs under superloads

Multilayer ANN models for JPCPs under superloads			
Explanatory variables	(1) Independent variables: Thickness of PCC layer, joint spacing, temperature gradient, composite modulus of subgrade reaction, axle weight, tire pressure (2) Nondimensional variables: Axle weights per a PCC slab/PCC slab weight, joint spacing/radius of relative stiffness, Korenev's nondimensional temperature gradient (Korenev and Chernigovskaya 1962)		
Target variables	(1) Critical tensile stress at the top of the PCC slab (2) Critical tensile stress at the bottom of the PCC slab		
ANN algorithms	(1) Levenberg-Marquardt, (2) Bayesian Regularization, (3) BFGS Quasi-Newton, (4) Resilient Backpropagation, and (5) Scaled Conjugate Gradient		
Learning rate	0.005		
Distribution function	Gaussian distribution	Distribution function	Hyperbolic tangent
No. of hidden layers	1 to 3	No. of hidden layers	3 to 9

Source: Koh et al. 2024

The three types of nondimensional variables presented in Table 13 combine various structural and loading parameters into an easily scalable single parameter defined by equations 11 through 13. Note that equation 13 provides a key nondimensional parameter for this study by incorporating various superload loading parameters associated with axle weights acting on the PCC slab.

$$\frac{\text{Axle weights per a PCC slab}}{\text{PCC slab weight}} = \frac{\sum \text{Axle weights subjecting to a PCC slab}}{a \times h \times \gamma} \quad (11)$$

$$\frac{L}{l} = \frac{\text{Transverse joint spacing}}{\text{Radius of relative stiffness}} \quad (12-1)$$

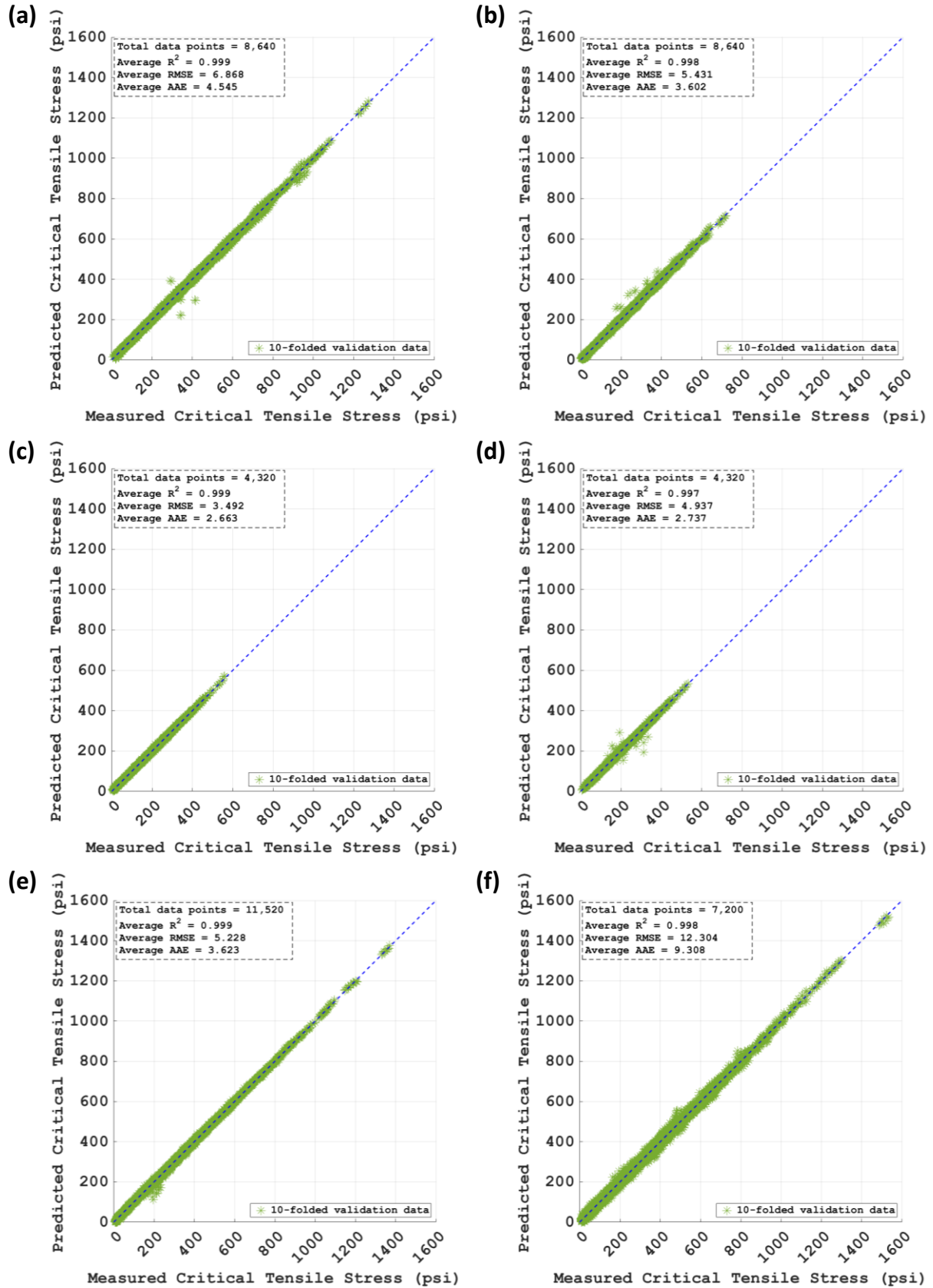
$$l = \sqrt[4]{\frac{Eh^3}{12(1-\mu^2)k}} \quad (12-2)$$

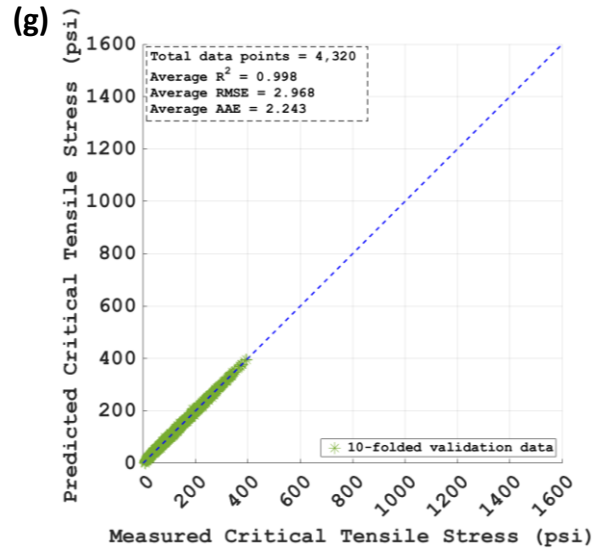
$$\text{Korenev's nondimensional temperature gradient} = \frac{2\alpha(1+\mu)l^2}{h^2} \frac{k}{\gamma} \Delta T \quad (13)$$

where a is the section area of a PCC slab, ft^2 ; h is the thickness of a PCC slab, ft ; γ is the unit weight of a PCC slab, pcf ; E is the modulus of elasticity of a PCC slab, psi ; μ is the Poisson's ratio for a PCC slab; k is the composite modulus of subgrade reaction, psi/in. ; α is the CTE of a PCC slab, $10^{-6}/^\circ\text{F}$; and ΔT is the temperature difference between the top and bottom of a PCC slab, $^\circ\text{F}$.

Performance Evaluation and Architecture Optimization of ANN-Based Surrogate Models

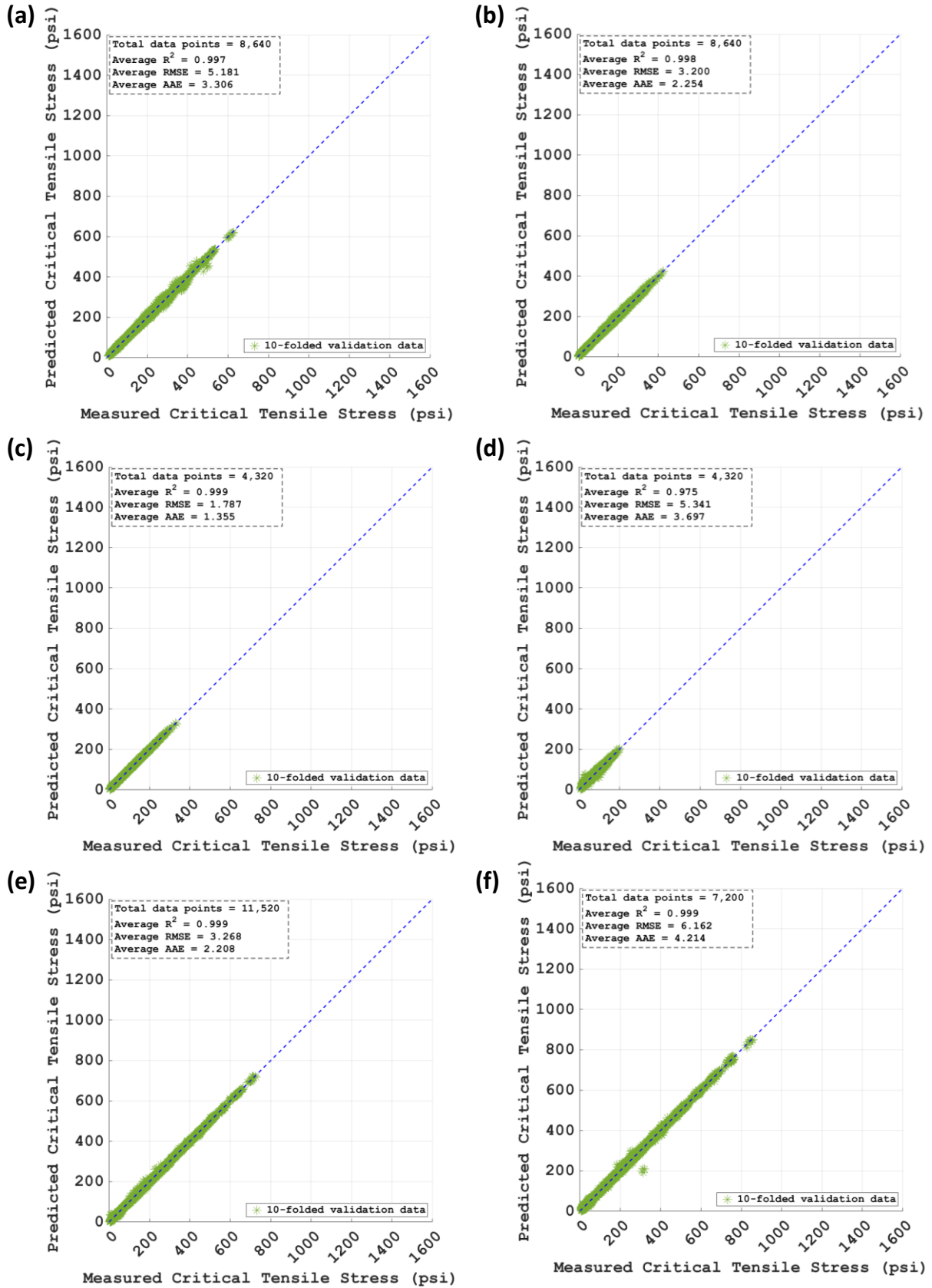
Leveraging the information listed in Table 12 and Table 13, a total of 14 ANN models dependent on 7 different parent superload types, outlined in Table 4 and Table 5, and 2 critical pavement response types were developed. Figure 22 and Figure 23 show the prediction accuracies of the ANN models pertaining to each parent type of superload when predicting the critical tensile stress at the bottom and top of the PCC slab, respectively.

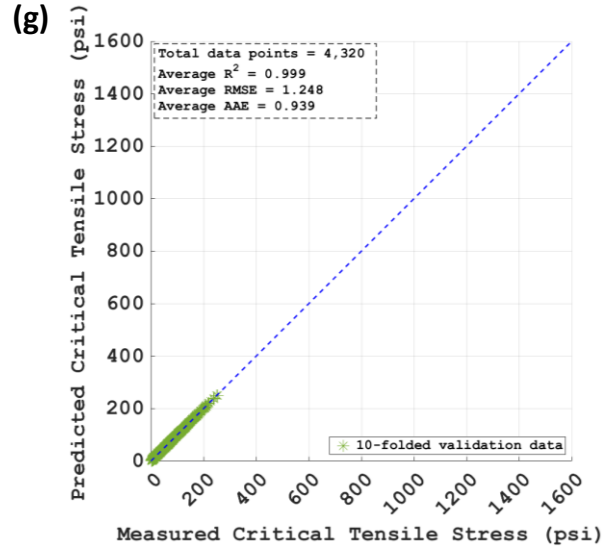




Koh et al. 2024, Reprinted with permission from Elsevier, © 2024

Figure 22. ANN model performances predicting the critical tensile stress at the bottom of the PCC slab when subjected to IoHs including (a) grain carts, (b) manure tankers, (c) agricultural trailers, and (d) agricultural trucks, and when subjected to SHLs including (e) single-row modular types, (f) dual-row modular types, and (g) drop-deck types



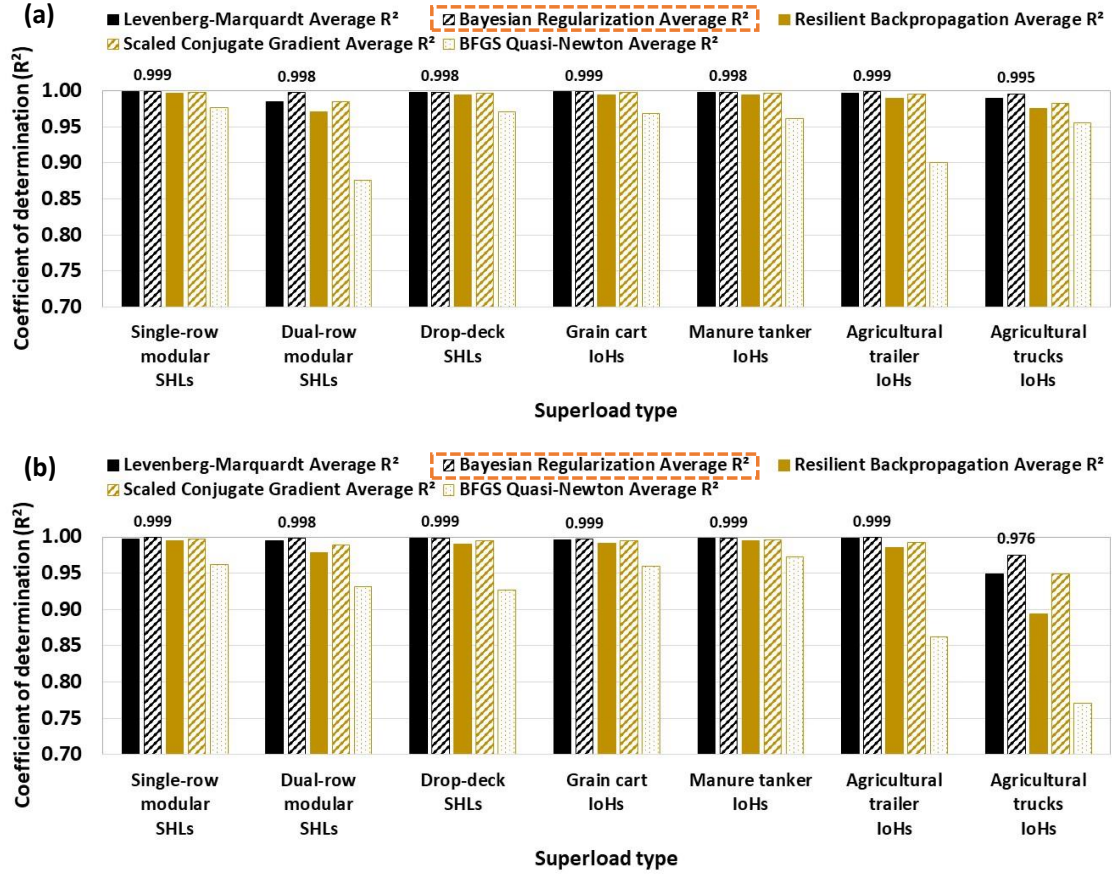


Koh et al. 2024, Reprinted with permission from Elsevier, © 2024

Figure 23. ANN model performances predicting the critical tensile stress at the top of the PCC slab when subjected to IoHs including (a) grain carts, (b) manure tankers, (c) agricultural trailers, and (d) agricultural trucks, and when subjected to SHLs including (e) single-row modular types, (f) dual-row modular types, and (g) drop-deck types

The ANN models shown in Figure 22 and Figure 23 are partial examples among the entire set of ANN modeling matrices used in which the Bayesian Regularization algorithm was applied with two hidden layers and seven neurons per hidden layer. It was confirmed that all the ANN models developed for each superload type exhibit reasonably (1) high R^2 values, equal to or greater than 0.975, (2) low AAE values, equal to or less than 9.308, and (3) low RMSE values, equal to or less than 12.304, when predicting critical tensile stresses at both the bottom and the top of the PCC slab. This underscores the reliability of the developed ANN models in accurately forecasting critical pavement responses under varying superload conditions.

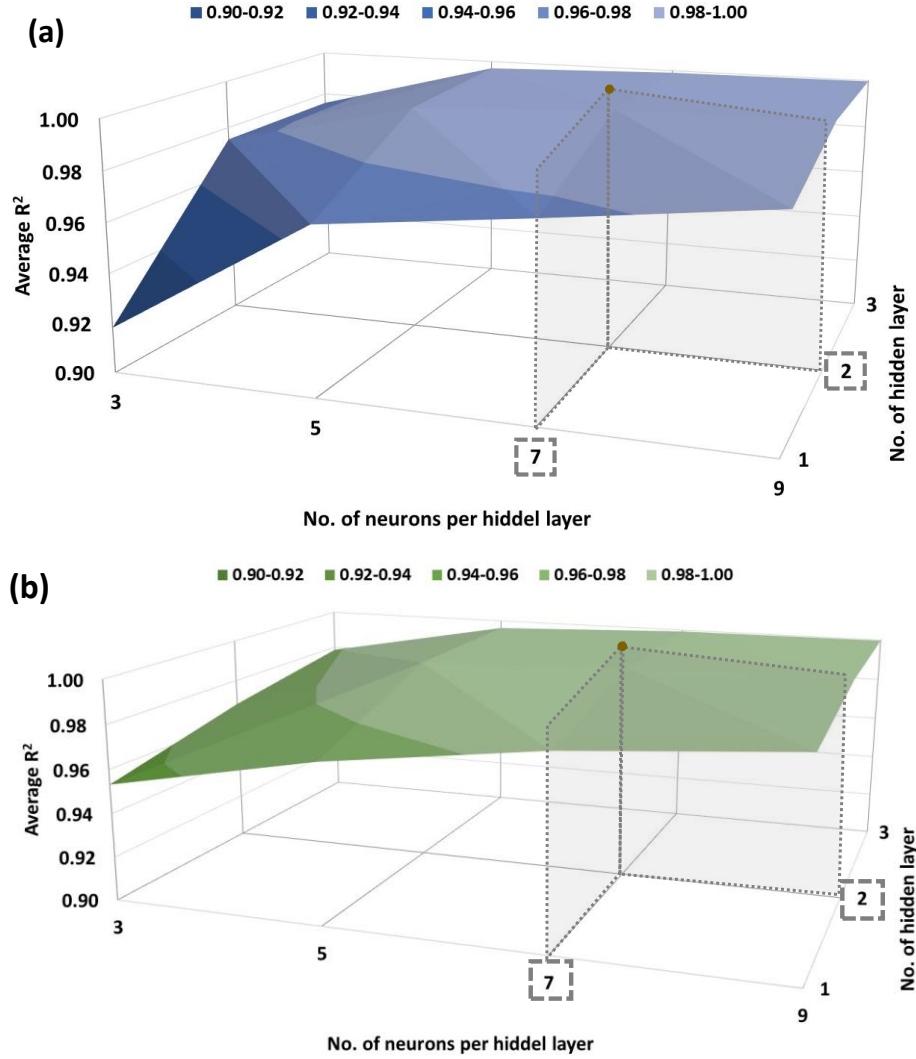
Prediction accuracies of various ANN models, each developed by two hidden layers and seven neurons per hidden layer, employing five different backpropagation algorithms, are presented in Figure 24.



Koh et al. 2024, Reprinted with permission from Elsevier, © 2024

Figure 24. Performance evaluation of ANN models constructed with two hidden layers, seven neurons per each hidden layer, and five backpropagation algorithms when predicting critical tensile stress at the (a) bottom of the PCC slab and (b) top of the PCC slab

It was confirmed that the Bayesian Regularization algorithm, followed by the Levenberg-Marquardt algorithm, exhibited the highest level of accuracy in predicting the critical tensile stress at both the bottom and top of the PCC slab of JPCPs under a single pass of various superload vehicle types. Furthermore, to identify highly efficient and accurate prediction models, the ANN architectures developed using the Bayesian Regularization algorithm underwent optimization procedures, wherein the convergence of R^2 values was assessed in relation to the number of hidden layers and neurons per hidden layer. The selection of the range of the number of hidden layers and neurons for architecture optimization was grounded in considerations of the input and output layers. Consequently, it was observed that ANN model architectures featuring two hidden layers and seven neurons per hidden layer were shown to provide satisfactorily high accuracy in predicting the critical tensile stress at both the bottom and top of the PCC slab. Figure 25 shows the R^2 values of different ANN models, varying with respect to the architectural parameters in the case of dual-row modular SHLs.



Koh et al. 2024, Reprinted with permission from Elsevier, © 2024

Figure 25. Architectural optimization of ANN models for the case of a dual-row modular type SHL constructed with the Bayesian Regularization algorithm when predicting critical tensile stress at the (a) bottom of the PCC slab and (b) top of the PCC slab

Sensitivity Evaluation of ANN-Based Surrogate Models

Given that the optimized ANN-based prediction models offer highly accurate predictions of critical JPCP responses based on the complex interrelationships among various JPCP structural and loading variables, it is critical to perform sensitivity analysis of each explanatory variable for identifying the significance of each explanatory variable in influencing critical pavement responses. To achieve this, one-at-a-time (OAT) local sensitivity analysis (LSA), a widely acknowledged sensitivity analysis methodology recognized for its cost-effectiveness in identifying the impact of input subsets on outputs, was conducted to investigate the sensitivity of input variables of JPCPs subjected to superload traffic. The outcomes of the OAT LSA served two key purposes: (1) validation of the ANN-based models and (2) identification of the

sensitivity of target responses to individual explanatory variables. A normalized sensitivity index (NSI) concept was adopted as a quantitative indicator of the sensitivity level, as shown in equation 14. The sensitivity levels were categorized into three classes: low sensitive ($\text{abs(NSI)} < 0.1$), sensitive ($0.1 \leq \text{abs(NSI)} < 0.5$), and very sensitive ($0.5 \leq \text{abs(NSI)} < 3$), ratings that have been established in previous studies (Rezaei-Tarahomi et al. 2019, Ceylan et al. 2014).

$$\text{NSI} = \frac{\Delta Y_j X_k}{\Delta X_k Y_k} \quad (14)$$

where X_k is the baseline value of input k , ΔX_k is the variation in input k about the baseline, Y_k is the baseline value of output j , and ΔY_j is the variation in output j corresponding to ΔX_k .

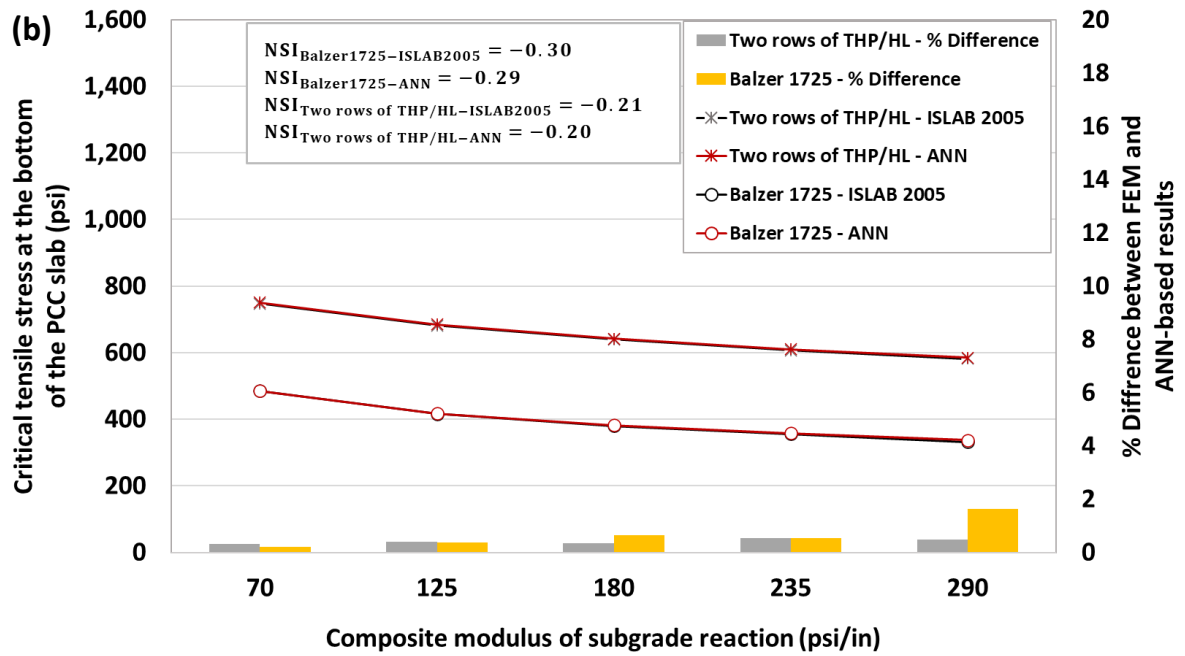
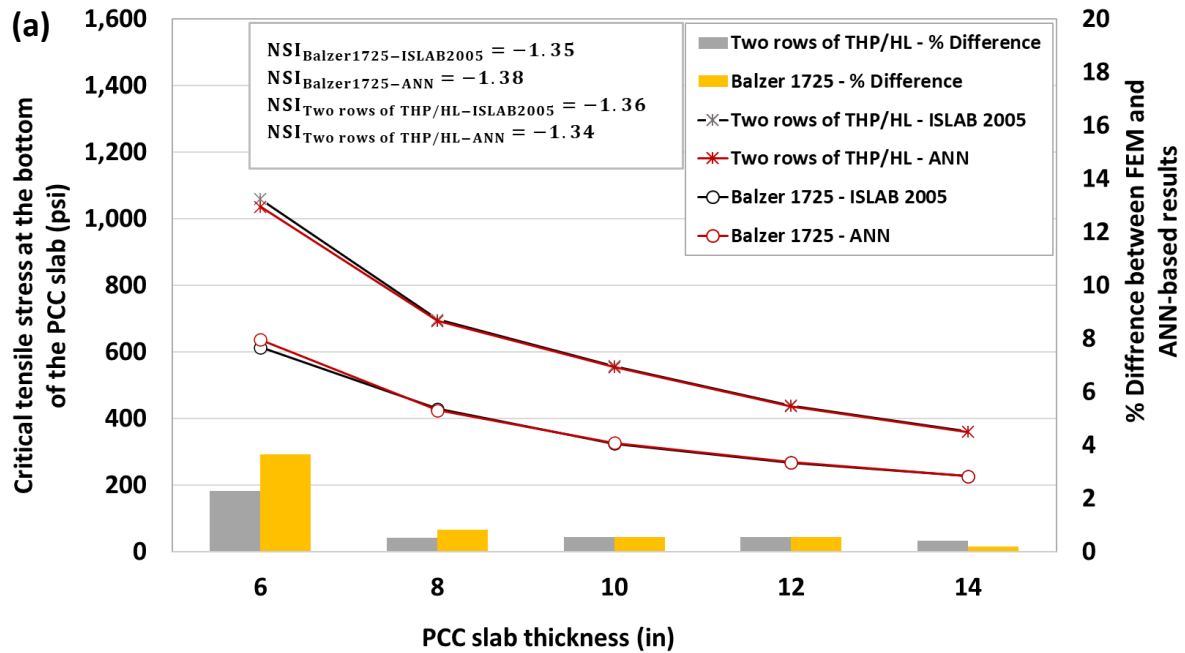
Table 14 summarizes the range of each structural and loading variable considered in the OAT LSA. It is noteworthy that this analysis incorporates the two most critical superload types affecting fatigue cracking: one from among the IoHs and the other from among the SHLs. The sensitivity analysis was conducted by establishing base cases at default settings and varying each explanatory variable between its minimum and maximum magnitudes. Subsequently, the corresponding sensitivities were determined, contributing to a comprehensive understanding of the influence of these variables on critical pavement responses.

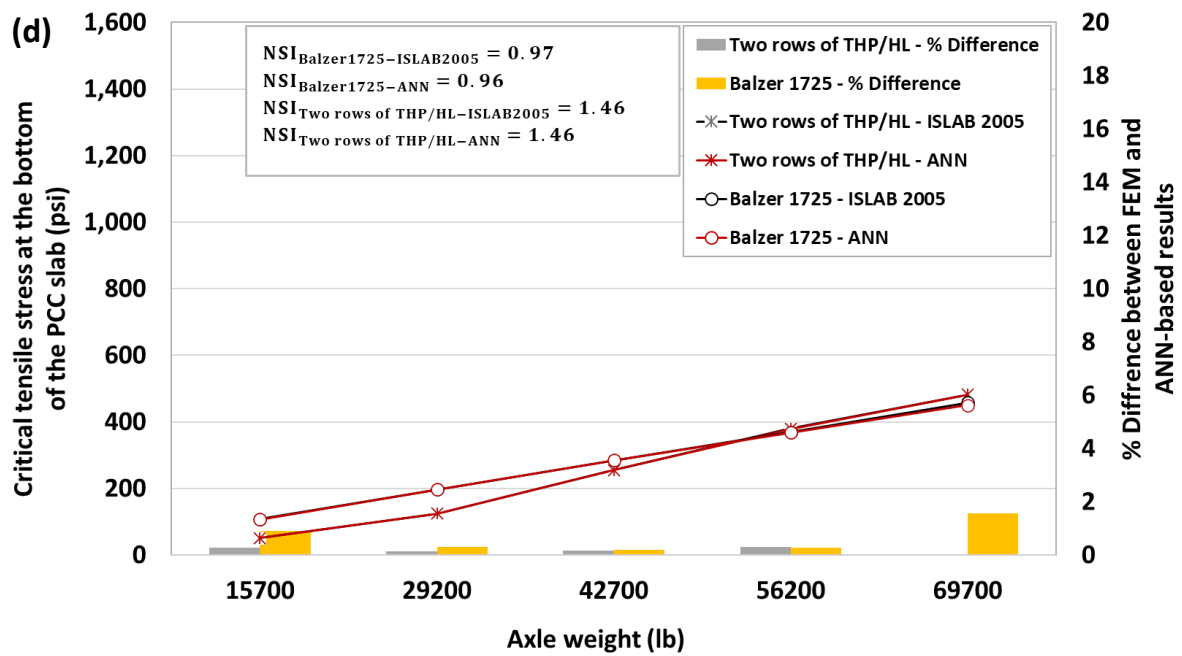
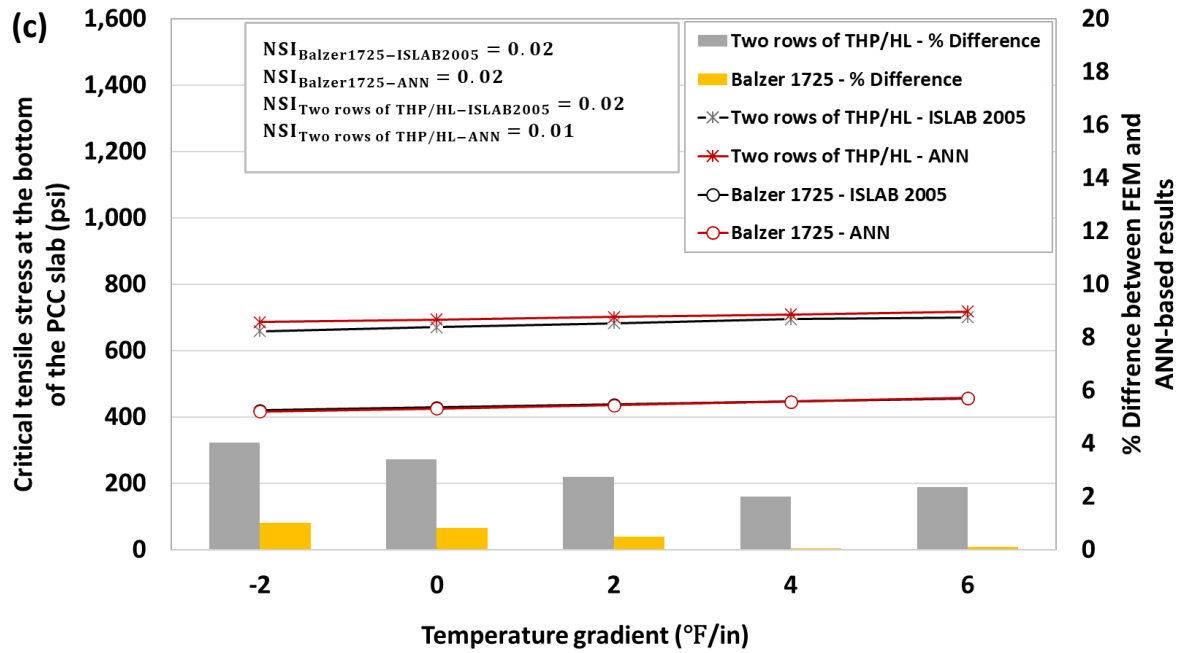
Table 14. Explanatory variable ranges for sensitivity analysis of JPCPs under superloads

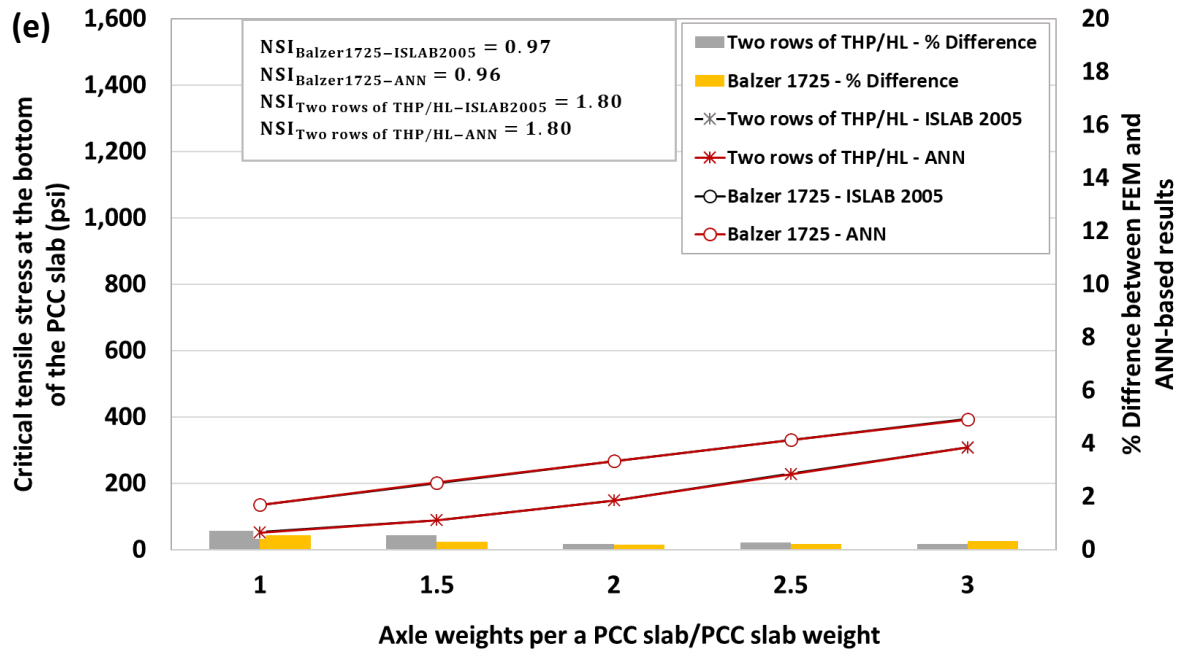
Category	Explanatory variables		Min.	Base line	Max.	Base case
JPCP structural variables	Thickness of PCC slab	in.	6	10	14	8
	Composite modulus of subgrade reaction	psi/in.	70	180	290	120
	Temperature gradient	°F/in.	-6	0	6	0
	Transverse joint spacing	ft	20			
	CTE	$10^{-6}/^{\circ}\text{F}$	4.3			
Loading variables	Superload type (parent type)		Balzer1725 (grain cart – IoH)		Two rows of THP/HL (dual-row modular – SHL)	
	Axle weight	lb	15,700	42,700	69,700	65,200: Balzer1725 98,900: two rows of THP/HL
	Axle weight per a PCC slab PCC slab weight	-	1	2	3	3: Balzer1725 12: two rows of THP/HL

Source: Koh et al. 2024

Based on the evaluation matrices, the critical pavement responses deriving from ANN models and ISLAB2005 were compared for model validation, and their NSIs were calculated for each explanatory variable. Figure 26 and Figure 27 depict the sensitivity analysis results for critical tensile stress at the bottom and top of the PCC slab, respectively.

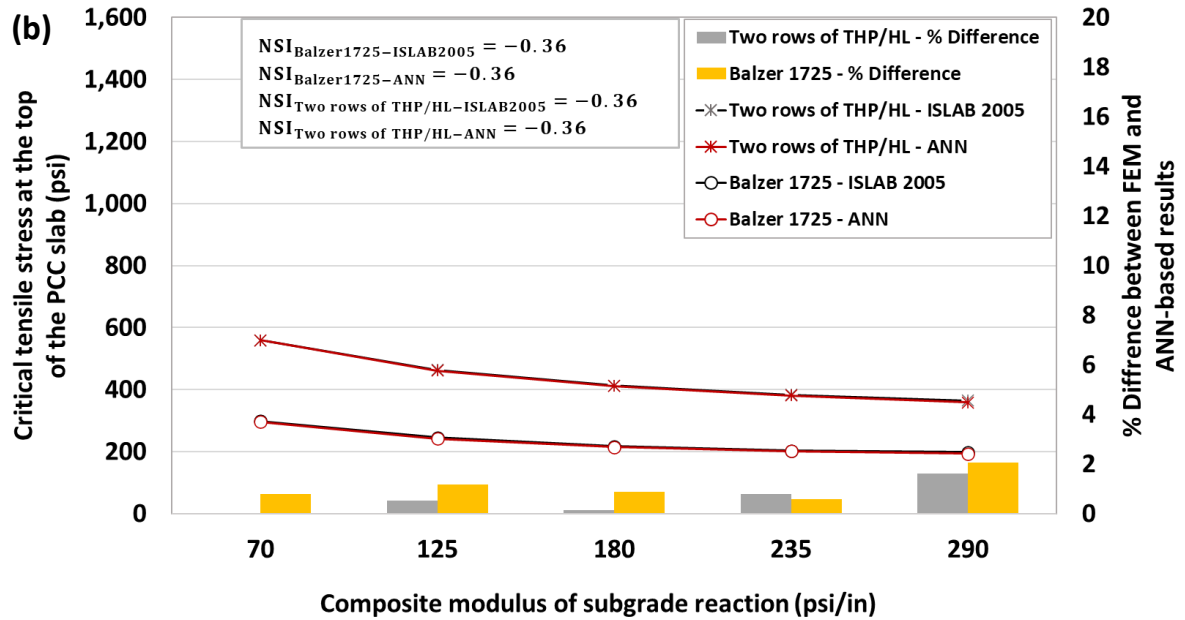
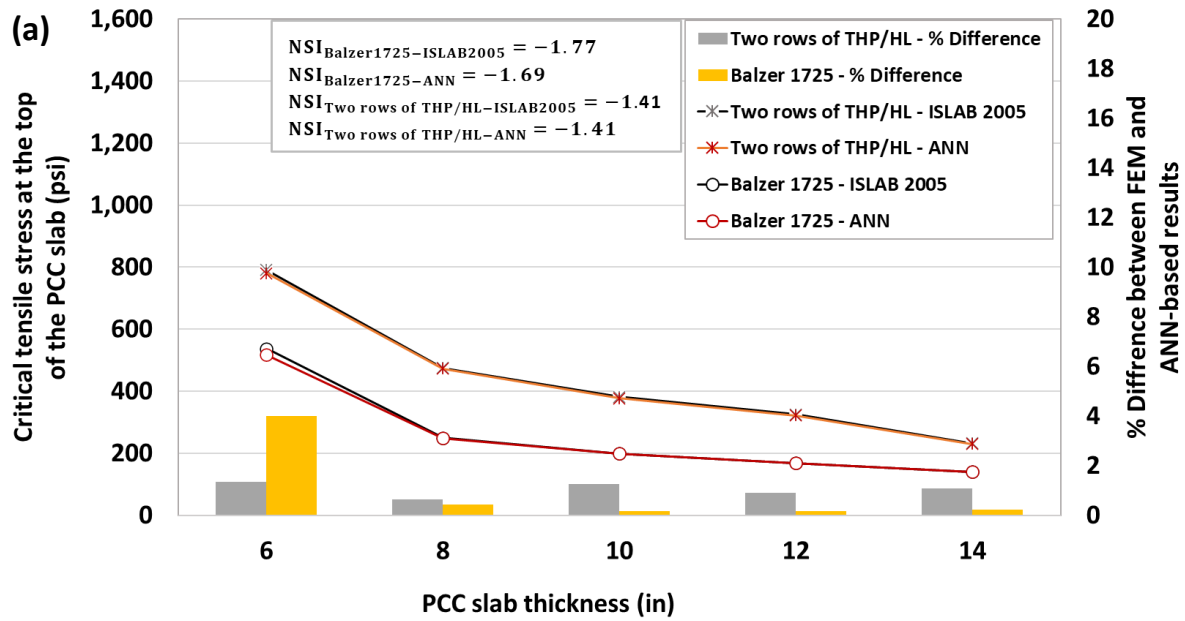


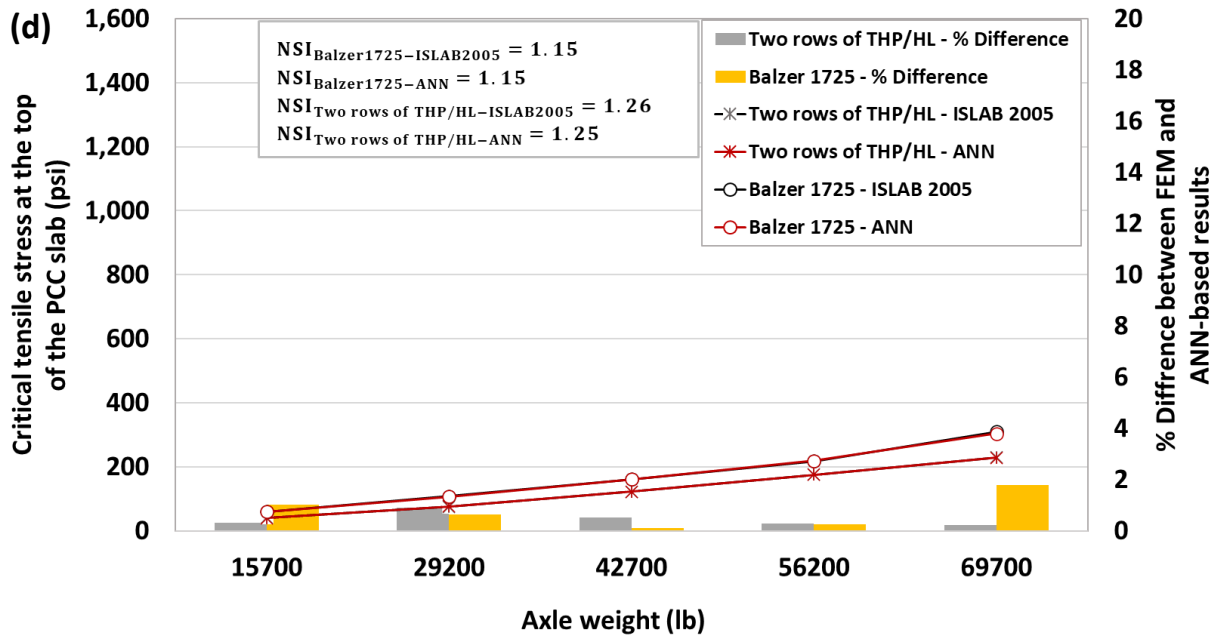
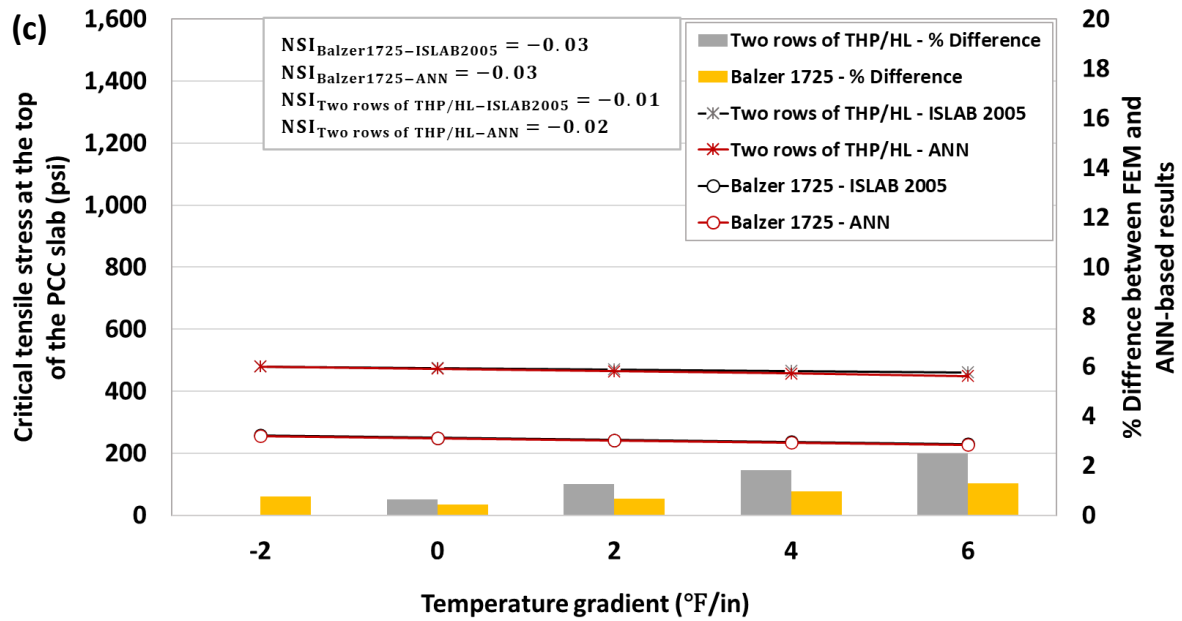


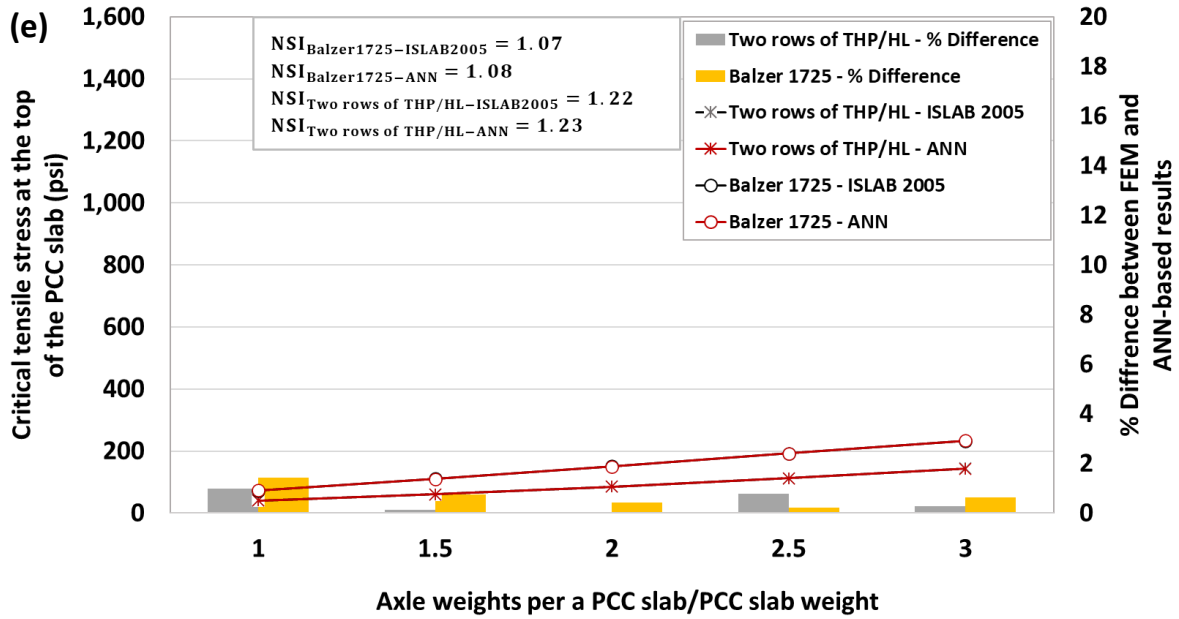


Koh et al. 2024, Reprinted with permission from Elsevier, © 2024

Figure 26. Sensitivity analysis results for the critical tensile stress at the bottom of a PCC slab when varying the JPCP structural variables including (a) PCC slab thickness, (b) composite modulus of subgrade reaction, and (c) temperature gradient, and when varying the loading variables including (d) axle weight and (e) $\frac{\text{Axle weight per a PCC slab}}{\text{PCC slab weight}}$







Koh et al. 2024, Reprinted with permission from Elsevier, © 2024

Figure 27. Sensitivity analysis results for the critical tensile stress at the top of PCC slab when varying the JPCP structural variables including (a) PCC slab thickness, (b) composite modulus of subgrade reaction, and (c) temperature gradient, and when varying the loading variables including (d) axle weight and (e) $\frac{\text{Axle weight per a PCC slab}}{\text{PCC slab weight}}$

All the ANN models were found to predict magnitudes of critical pavement responses similar to those obtained from ISLAB2005, with differences of less than 5% between FEM- and ANN-based results, even though some of the explanatory variables used for the sensitivity analysis were outside the ranges specified in Table 12. The NSIs calculated from those data also indicate that both critical pavement responses were very sensitive to the PCC slab thickness and two loading variables, sensitive to the composite modulus of subgrade reaction, and less sensitive to the temperature gradient. The sensitivity analysis results are summarized in Table 15. Sensitivity levels were determined according to the absolute NSI values, and the NSI plus and minus signs for each indicate an increase (+) or decrease (-) of each distress when the value of each explanatory variable was increased.

Table 15. Summary of sensitivity analysis results for JPCPs under superloads

Category	Explanatory variables	Critical pavement response type	Balzer1725 (grain cart)		Two rows of THP/HL (dual-row modular)	
			NSI	SL	NSI	SL
JPCP structural variables	Thickness of PCC slab	Tensile stress at bottom of PCC slab	-1.38	VS	-1.34	VS
		Tensile stress at top of PCC slab	-1.69	VS	-1.41	VS
	Composite modulus of subgrade reaction	Tensile stress at bottom of PCC slab	-0.29	S	-0.20	S
		Tensile stress at top of PCC slab	-0.36	S	-0.36	S
	Temperature gradient	Tensile stress at bottom of PCC slab	+0.02	LS	+0.01	LS
		Tensile stress at top of PCC slab	-0.03	LS	-0.02	LS
Loading variables	Axle weight	Tensile stress at bottom of PCC slab	+0.96	VS	+1.46	VS
		Tensile stress at top of PCC slab	+1.15	VS	+1.25	VS
	Axle weight per a PCC slab	Tensile stress at bottom of PCC slab	+0.96	VS	+1.80	VS
	PCC slab weight	Tensile stress at top of PCC slab	+1.08	VS	+1.23	VS

Source: Koh et al. 2024

* SL = Sensitivity Level; VS = Very Sensitive; S = Sensitive; LS = Low Sensitive

Summary and Key Findings

This chapter provided mechanistic-based JPCP analysis results using FEA and corresponding JPCP damage and LCCA evaluations. The main objectives of this chapter were to (1) characterize the superloads traveling JPCP systems, (2) conduct mechanistic-based evaluations of JPCP damage, (3) perform LCCA to determine the reduction in JPCP service life and the associated RDAC, and (4) develop AI-based surrogate models tailored to each superload category. Further discussion on each objective is given in the subsequent lists.

- **Characterization of superloads for JPCP systems**
 - FEA was conducted to determine the critical loading location of each superload related to bottom-up and top-down fatigue cracking as a mechanistic-based loading input by adopting the influence-line analysis approach.

- Critical loading locations of IoHs with respect to the critical tensile stress at the bottom and top of PCC slabs were determined based on the axle configuration and transverse joint LTE.
- Critical loading locations of SHLs with respect to the critical tensile stress at the bottom and top of PCC slabs were determined based on the trailer type and transverse joint of the PCC slab.
- **Evaluation of potential JPCP damages subjected to superloads**
 - In the case of IoHs, most types of grain carts generate more significant bottom-up transverse cracking and top-down transverse cracking of the PCC slab than other types of IoHs. Moreover, grain carts and manure tankers at all payload levels except 0% exhibit fatigue damage ratios greater than one. At the same time, agricultural trailers and agricultural trucks exhibit relatively lower damage ratios, even lower than one for some JPCP models when carrying a 50% payload or lower. Overall, most IoHs except for grain carts cause fatigue damage similar to that of FHWA class 9 trucks when carrying a 50% payload level.
 - In the case of SHLs, most FEA results except for the 0% payload case show that modular SHLs cause significantly greater fatigue-related transverse cracking than drop-deck SHLs. Drop-deck SHLs cause similar or even lesser fatigue damages than FHWA class 9 trucks at all payload levels, while modular SHLs are likely to cause significant fatigue damages more than those for FHWA class 9 trucks for payload levels of 50% or more.
 - JPCP structures with different shoulder alternatives such as granular, full-depth PCC, and partial-depth HMA have similar critical loading locations for representative types of superloads to those categories derived in the previous sections. This means that a randomly selected superload per each vehicle category traveling over JPCPs with a full-depth tied PCC shoulder and partial-depth HMA shoulder exhibits similar critical loading locations to those for JPCPs with a granular shoulder with respect to both critical tensile stresses at the bottom of the PCC slab and the top of the PCC slab.
 - Critical tensile stresses of JPCPs carrying IoHs are significantly reduced when full-depth PCC shoulders are used, while SHLs exhibit only a relatively small reduction of critical tensile stresses when paved shoulders are used. This is mainly related to the position of the axle loadings (i.e., offset from the edge of PCC slab or wandering of axle loadings).
- **LCCA for JPCPs under superloads**
 - JPCP performance in terms of accumulated total fatigue cracking caused by the number of superload and class 9 truck passes during the JPCP life cycle were determined based on the comprehensive FEA results, and the amount of service life reduction and multivariate RDACs due to a single superload pass were accordingly obtained.
 - Reduction in JPCP service life was calculated for all superload vehicle types, and dual-row modular SHLs having relatively high axle weights were shown to reduce the JPCP service life the most, followed by the grain cart IoH and single-row modular SHL. Reducing the payload level of all types of superloads from 100% to 75% or from 100% to 50% significantly reduced the service life reduction on average by approximately 70% and 96%, respectively, for a JPCP with an 8 in. thick PCC layer and a 20 ft wide transverse joint spacing. In the case of JPCPs with varying temperature gradients, the service life reduction increased significantly as the PCC layer thickness decreased, and

the service life reduction decreased slightly as the transverse joint spacing decreased due to the non-standardized loading configurations of superloads.

- Trends in RDAC results for JPCPs subjected to superloads were similar to those for service life reduction. Two types of SHL, a dual-row modular and a single-row modular, and a grain cart IoH, exhibited the highest RDACs in terms of total fatigue cracking. When the payload level was reduced from 100% to 75% or from 100% to 50%, the RDACs were significantly reduced by approximately 81% and 98% on average, respectively, for a JPCP with an 8 in. thick PCC layer and 20 ft wide transverse joint spacing. RDACs also depend highly on the travel time of the superloads made on the JPCP section, due to the discount rate, JPCP terminal service life, and RSL of the pavement from the time the superload passes.
 - Results from RDAC analysis of different JPCP structures subjected to superloads show that the averaged RDACs tended to decrease significantly as PCC layer thickness increased, while the averaged RDACs decreased slightly as the transverse joint spacing decreased, even when varying temperature gradients were applied to the PCC slab. A relatively insignificant effect of the transverse joint on RDAC when subjected to superloads is mainly caused by the difference in their loading configurations from those of a general class 9 truck.
 - Management factors, including treatment type and discount rate, also affect the RDACs by directly applying them to PWV calculations.
 - Since a 100% payload level of superload in this study refers to the maximum payload capacity of each commercial superload vehicle, most of their GVWs or axle weights tended to significantly exceed the state's permit limit, so it is recommended to refer to the RDAC results from superloads having 75%, 50%, or lower payload levels by using engineering judgment in cases where the superload as a target in practice has relatively low GVW or axle weight.
 - It is necessary to classify superloads into grain carts, manure tankers, agricultural trailers, and agricultural trucks for IoHs, and into single-row modular, dual-row modular, and drop-deck types for SHLs when establishing mechanistic-based permit fees. This chapter recommends levying a single-trip permit fee based on the superload's axle weight and the superload travel time during the life cycle of the JPCPs. Also, PCC slab thickness and temperature gradient are recommended as determining factors for single-trip superload permit fees.
- **AI-based prediction model development for JPCPs under superloads**
 - A total of 14 ANN models dependent on 7 different parent types of superloads and 2 critical pavement response types were developed based on a data matrix consisting of inputs and outputs from ISLAB2005, a FEM-based rigid pavement analysis program.
 - ANN-based prediction models based on the Bayesian Regularization algorithm, with architectures optimized with two hidden layers and seven neurons per hidden layer, were shown to yield sufficient accuracy in predicting critical tensile stress both at the bottom and the top of the PCC slab.
 - OAT LSA results, identified in terms of NSI, indicate that both critical pavement responses were very sensitive to PCC slab thickness and two loading variables, sensitive to the composite modulus of subgrade reaction, and low sensitive with respect to the temperature gradient.

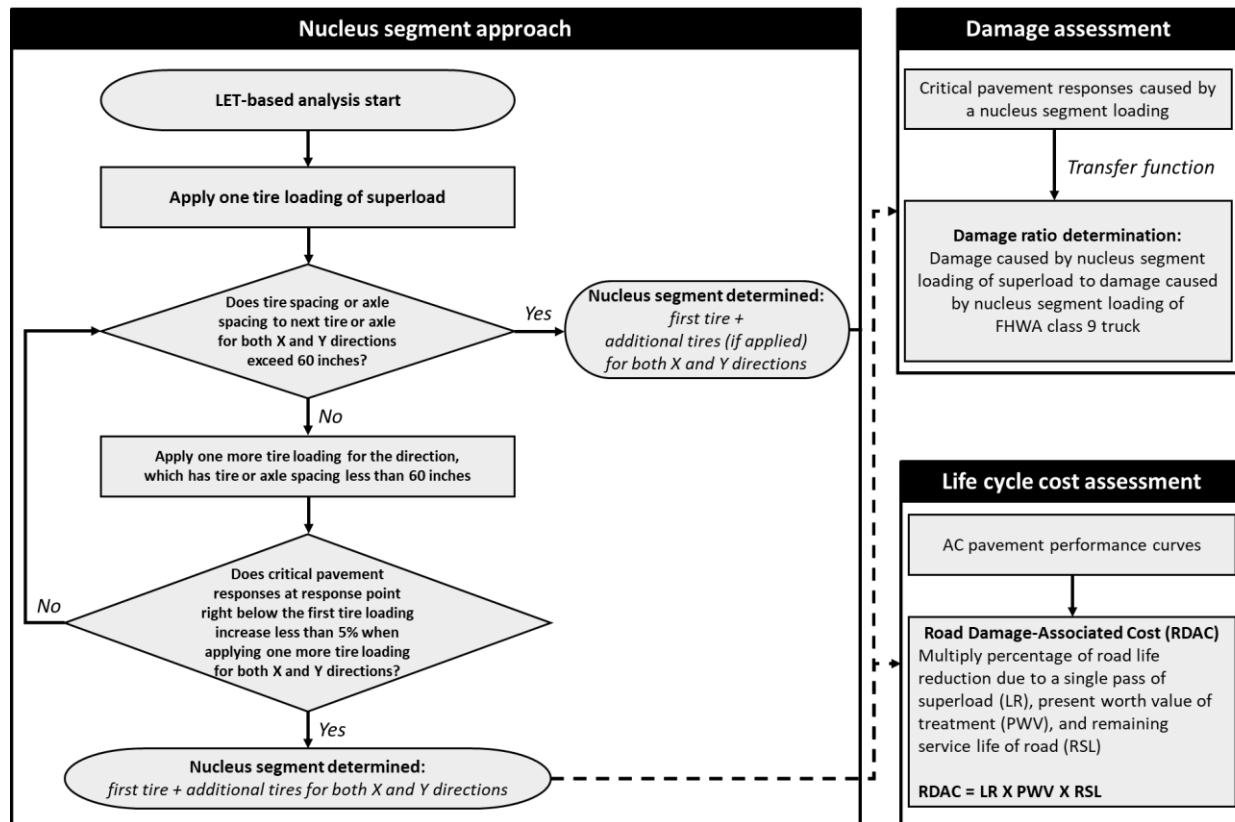
CHAPTER 5. MECHANISTIC QUANTIFICATION OF SUPERLOAD IMPACTS ON FLEXIBLE PAVEMENTS

The scope of this chapter is to (1) characterize the superloads traveling on flexible pavement systems, (2) conduct mechanistic-based flexible pavement damage calculation and evaluation, especially for rutting damage and bottom-up fatigue damage resulting from characterized superload loading inputs, using an LET-based analysis approach, (3) perform LCCA for determining flexible pavement service life reduction and RDAC analysis that depends on different pavement structures, materials, environmental conditions, and superload types, and (4) develop and optimize AI-based surrogate models for each superload category to accurately predict critical pavement responses related to rutting and bottom-up fatigue cracking of flexible pavements when subjected to various types of superloads.

Characterization of Superloads: Nucleus Segment

Methodology

To determine the structural damages and associated treatment costs of asphalt concrete (AC) pavements under various types of IoHs and SHLs, mechanistic-based traffic loading inputs for each superload type should first be determined to obtain accurate critical flexible pavement responses. To identify the mechanistic loading inputs for superloads with non-standardized and diverse loading configurations, the nucleus segment approach proposed by Nimeri et al. (2018) and extensively used by Koh et al. (2022b) was adopted for the LET-based pavement analysis. The nucleus segment approach, also known as the influencing-tire-segment approach, stands out as an innovative loading input identification method for determining the minimum loading group for each type of superload that could produce the maximum critical pavement responses similar to those that occur when the pavement is subjected to the whole loading configuration. Critical pavement responses can be obtained by applying the nucleus segment determined for each superload type as a loading input to the LET-based flexible pavement models, after which potential damages and RDACs could be derived by comparing those distresses with those imposed by an FHWA class 9 truck. MnLayer (Khazanovich and Wang 2007), a multilayer pavement analysis software based on LET, was used in this study to identify the nuclear segment for each superload type and to obtain critical pavement responses associated with each type of structural damage, including critical vertical strains of each layer causing total rutting and critical horizontal tensile strain at the bottom of the AC layer causing bottom-up fatigue cracking in flexible pavements. The comprehensive flow chart in Figure 28 outlines the sequential steps utilized to identify nucleus segments, evaluate flexible pavement damages, and assess RDACs.



Koh et al. 2023a, Reprinted with permission from Sage Publications, Inc., © 2023

Figure 28. Flow chart of the mechanistic-based analysis for flexible pavements under superloads

To obtain the nucleus segment of each superload type, the increase rates of vertical strain at the top of the subgrade directly beneath the initial tire loading point were derived. This specific critical pavement response type was selected for determining the nucleus segment by applying incremental tire loading. In the nucleus segment determination process, it was anticipated that there would be an overlap of vertical strain due to multiple tire loads at a certain depth point. To address this, flexible pavements with the thickest layers above the subgrade (15 in. of AC layer, 12 in. of base layer, and 9 in. of subbase layer) were chosen. This flexible pavement structure was deemed representative of sufficiently overlapped vertical strain at the top of the subgrade. In other words, because the nucleus segment determination is not about deriving the absolute magnitude of the pavement response with respect to the tire load but rather checking the change rate of the pavement response according to incremental tire loading, the pavement structure cases having the thickest layers were selected for nucleus segment determination since an additional tire loading is more influential in the pavement response derived from the first tire loading point as the measurement depth gets deeper and sufficiently overlaps the additional tire-loading effects, as depicted in Figure 29.

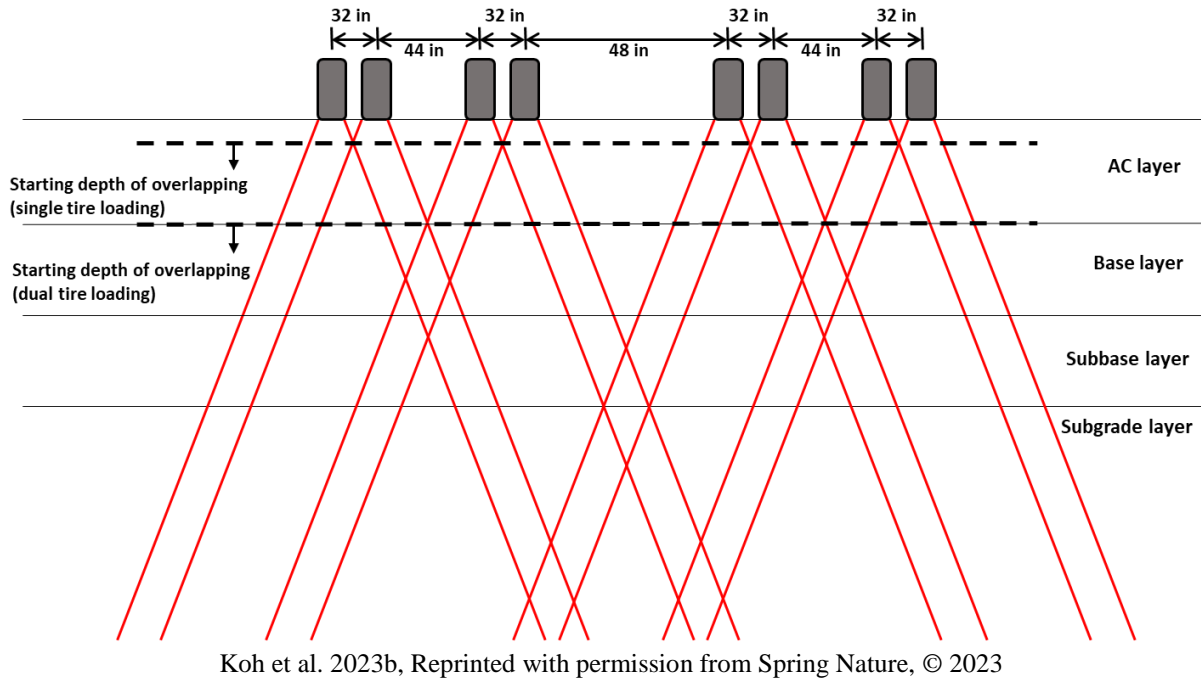
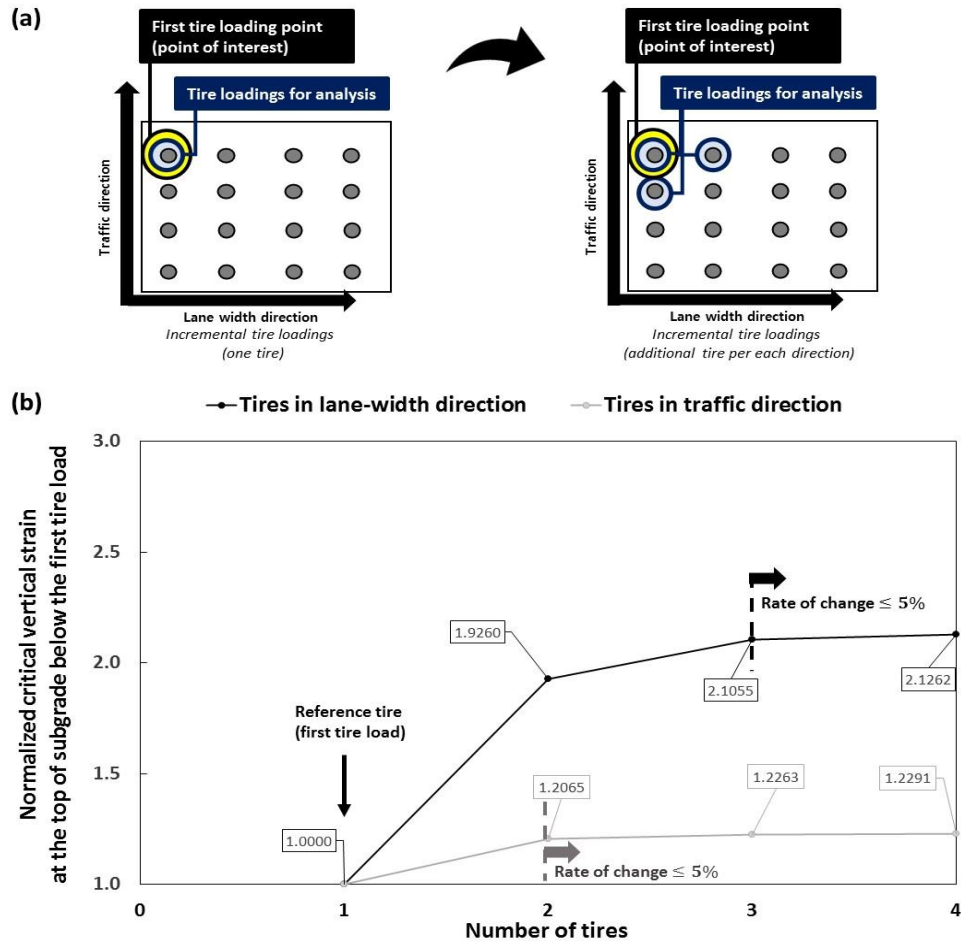


Figure 29. Overlapping of pavement responses according to the depth under a number of tire loadings of Goldhofer THP/SL-S

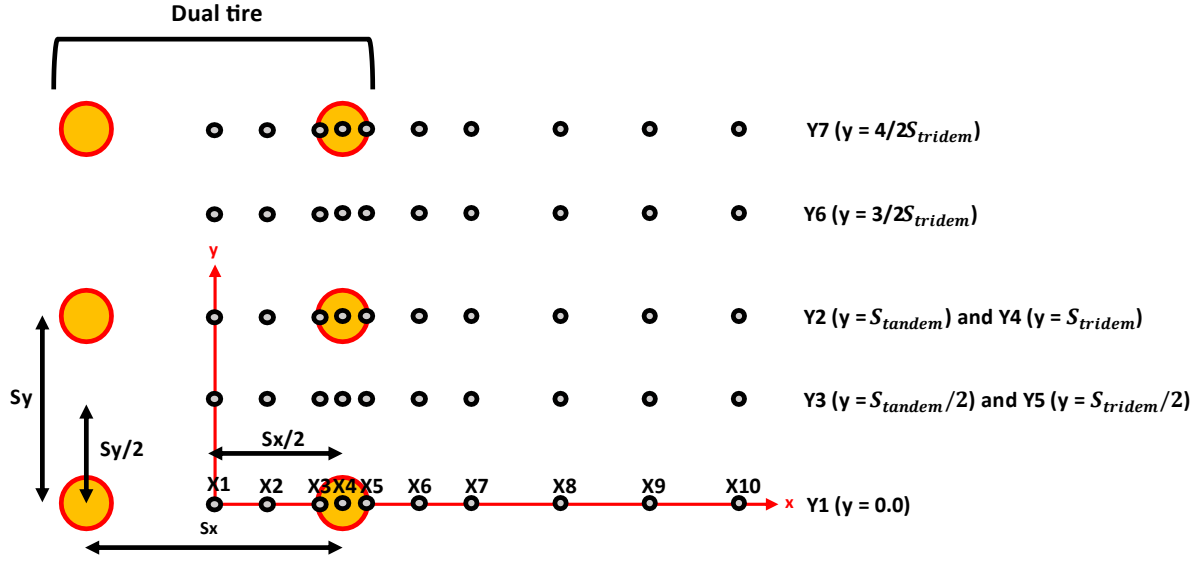
The number of tire loads in a nucleus segment along both traffic and lane-width directions can be derived by determining the number of necessary incremental tire loads that result in a rate of change of less than 5% for vertical strains at the top of the subgrade, right below the first loading point for both directions. The 5% rate of change was set based on the statistical hypothesis-testing theory, following the null hypothesis stating that there is no relationship between two variables being rejected if the observed p -value is less than the pre-specified significance level α . Since there is no specific standard for the minimum rate of change, the authors set the α value to be 5% by engineering decision to satisfy statistical significance requirements. Figure 30 shows an example of nucleus segment determination for a flexible pavement under the Goldhofer THP/SL-S dual-row modular. The number of tire loads in a nucleus segment of a Goldhofer THP/SL-S dual-row modular traveling on flexible pavement can be estimated as: 1 (additional tire) + 1 (first tire load) + 1 (additional tire on another side) = 3 and 2 (additional tires) + 1 (first tire load) + 2 (additional tires on another side) = 5, respectively, for both traffic direction and lane-width direction.



Koh et al. 2023a, Reprinted with permission from Sage Publications, Inc., © 2023

Figure 30. Incremental tire loads (a) and corresponding normalized critical vertical strain at the top of the subgrade right below the first tire load (b) of flexible pavement under Goldhofer THP/SL-S dual-row modular

In addition to the nucleus segment approach, a superposition method was also adopted to further reduce the computational effort when applying traffic loads. The superposition method is a well-known methodology through which critical pavement responses to tandem, tridem, or quad-axle loadings can be calculated by simply combining pavement responses of specific locations obtained from single-axle loading as in linear equations. The *Guide for Mechanistic-Empirical Design* (Witczak and El-Basyouny 2004) introduced a superposition method for layered elastic analysis by applying a set of dual wheels and 70 analysis points (10 points for X-direction and 7 points for Y-direction) shown in Figure 31.



Locations in X-direction

- X1 = 0.0
- X2 = $((T_{spacing}/2) - T_{radius})/2$
- X3 = $(T_{spacing}/2) - T_{radius}$
- X4 = $T_{spacing}/2$
- X5 = $(T_{spacing}/2) + T_{radius}$
- X6 = $(T_{spacing}/2) + T_{radius} + 0.10 \text{ m}$
- X7 = $(T_{spacing}/2) + T_{radius} + 0.20 \text{ m}$
- X8 = $(T_{spacing}/2) + T_{radius} + 0.41 \text{ m}$
- X9 = $(T_{spacing}/2) + T_{radius} + 0.61 \text{ m}$
- X10 = $(T_{spacing}/2) + T_{radius} + 1.22 \text{ m}$

Locations in Y-direction

- Y1: $y = 0.0$
- Y2: $y = S_{tandem}$
- Y3: $y = S_{tandem}/2$
- Y4: $y = S_{tridem}$
- Y5: $y = S_{tridem}/2$
- Y6: $y = S_{tridem}^{3/2}$
- Y7: $y = S_{tridem}^{4/2}$

Koh et al. 2023b, Reprinted with permission from Spring Nature, © 2023

Figure 31. Conceptual drawing of the superposition method

Note that in the above figure, the X-direction is the lane-width direction, and the Y-direction is the traffic direction.

The main assumption of the superposition method, due to the nature of the linearly elastic analysis, is that critical pavement responses with respect to the Y-axis occur either only at a location directly below the axle line (response #1) or the exact mid-line between two axle lines (response #2). Accordingly, the equations of the superposition method shown in Table 16 are suggested for obtaining critical responses under single, tandem, tridem, and quad axles simply by obtaining pavement responses from 70 analysis points under single-axle loading. Note that the applicability of the superposition method to flexible pavements under superloads underwent verification in a previous study conducted by the same authors (Koh et al. 2022b). This verification substantiates the superposition method's reliability and applicability to the flexible pavement systems subjected to superloads.

Table 16. Linear calculation of critical pavement responses by superposition method

Critical responses	Single axle	Tandem axle	Tridem axle	Quad axle
Response #1	$Y1$	$Y1 + Y2$	$Y1 + 2 \times Y4$	$Y1 + 2 \times Y4 + Y7$
Response #2	-	$2 \times Y3$	$2 \times Y5 + Y6$	$2 \times Y5 + 2 \times Y6$

Source: Koh et al. 2023b

Nucleus Segments of Superloads

Utilizing the nucleus segment methodology, the number of tires in the nucleus segments for every type of superload as traffic-loading inputs for flexible pavement systems were derived and summarized in Table 17. Note that superloads carrying a 100% payload level were utilized to determine the nucleus segments, and the nucleus segment with the largest number of tire loads between the nucleus segments derived over four seasons was conservatively chosen as the final nucleus segment of each superload.

Table 17. Number of tire loads in a nucleus segment of different superload types

Name of IoH	No. of tires in nucleus segment (lane-width, traffic)	Name of SHL	No. of tires in nucleus segment (lane-width, traffic)
Kinze 1051	(1, 1)	Goldhofer THP/SL-S	(4, 3)
Kinze 1305 flotation	(1, 1)	Goldhofer THP/ET	(4, 3)
Kinze 1305 row crop	(4, 1)	Goldhofer PST/ES-E	(4, 3)
Balzer 1725	(1, 1)	Goldhofer THP/UT	(8, 3)
Balzer 2550	(1, 1)	Goldhofer THP/SL-L	(8, 3)
J&M 1151	(1, 1)	Goldhofer THP/HL-L	(8, 3)
GEA EL48-4D 4350	(1, 2)	Goldhofer THP/SL	(8, 3)
GEA EL48-6D 6100	(1, 3)	Goldhofer THP/HL	(8, 3)
GEA EL48-8D 7900	(1, 4)	Two rows of Goldhofer THP/SL-S	(5, 3)
Balzer 6800 magnum	(1, 1)	Two rows of Goldhofer PST/ES-E	(5, 3)
Balzer 9500 magnum	(1, 1)	Two rows of Goldhofer THP/UT	(8, 3)
NUHN QT Quad Tanks	(1, 2)	Two rows of Goldhofer THP/HL	(8, 3)
J&M 555 wagon	(1, 1)	Goldhofer THP/HL + outrigger	(8, 3)
J&M 755 wagon	(1, 1)	Kalyn Siebert 13 Axle Trailer	(2, 3)
Terragator 2505	(1, 1) from front axle	Guy M. Turner dual lane 200 ton	(4, 2)
Terragator TG7300C	(1, 1) from front axle	Guy M. Turner 19 Axle trailer 125 ton	(4, 3)
Terragator TG8400C	(1, 1)		
Case 340B	(1, 1)		

Source: Koh et al. 2023a

Mechanistic Analysis for Potential Damage Evaluation: LET-Based Analysis

Methodology

A comprehensive investigation into LET-based flexible pavement analysis was undertaken to evaluate potential structural damage under diverse superload scenarios. MnLayer was again used to obtain critical pavement responses associated with each type of distress, including critical vertical strains of each layer causing total rutting and critical horizontal tensile strain at the bottom of the AC layer causing bottom-up fatigue cracking. Mechanistic loading inputs, designated as nucleus segments and detailed in Table 17, were systematically applied to the LET-based analysis models developed based on the numerical investigation matrix outlined in Table 18.

Table 18. Comprehensive analysis matrix for LET-based flexible pavement analysis

Number of layers (type of layer)				
4 (AC layer, base layer, subbase layer, subgrade)				
Thickness (in.)				
AC layer		Base layer		Subbase layer
6, 8, 10, 12, 15		3, 8, 12		4, 6, 9
Modulus of elasticity (psi)				
Season	AC layer	Base layer	Subbase layer	Subgrade
Spring	500,000	25,000	20,000	5,000
Fall	500,000	35,000	30,000	10,000
Summer	100,000	35,000	30,000	10,000
Winter	2,000,000	50,000	40,000	17,000
Poisson's ratio: 0.35				
Traffic loadings				
IoH: 18 types × 4 payload levels = 72 types				
SHL: 16 types × 4 payload levels = 64 types				
FHWA class 9 truck (reference): 1 type				
Total analysis cases: 24,660 cases				

Source: Koh et al. 2023a

The damage ratio concept that compares the damage caused by a superload with the damage caused by an FHWA class 9 truck, a reference vehicle, was adopted in this chapter again to calculate and evaluate potential comparative damages according to each superload type. Transfer functions from the *Mechanistic-Empirical Pavement Design Guide: A Manual of Practice* (MEPDG) (AASHTO 2015) and the latest AASHTOWare Pavement ME Design software (i.e., version 2.6.2) (AASHTO 2022) were applied during post-processing to convert critical pavement responses into corresponding damages following LET-based analysis. Rutting, one of the main distress types caused by permanent vertical deformation of each layer, can be determined by identifying critical vertical strains at the mid-depth of each layer and 6 in. below the top of the subgrade. Equation 15 through 17 present the calculation of permanent deformation for each layer and the derivation of rutting damage ratio. The total permanent vertical deformation caused by a superload pass was computed by combining all plastic deformations from each layer and comparing this total deformation with that from a class 9 truck to determine the damage ratio. It is noteworthy that water content values of 10% and 15.7% were selected for granular material and fine-grained material, respectively, based on Iowa local data (Cetin et al. 2019, Ceylan et al. 2009). The dynamic modulus of 13,000 psi for performance grade (PG) 58-28, a commonly used asphalt binder in the Midwestern United States, was derived from the Witczak 2000 model of Mn/ROAD tests (Clyne et al. 2003), assuming design traffic under 1 million ESALs and greater than 45 mph design speed to select a proper dynamic modulus from the Witczak 2000 model.

$$\Delta_{p(soil)} = \beta_{s1} k_{s1} \varepsilon_v h_{soil} \left(\frac{\varepsilon_0}{\varepsilon_r} \right) e^{-\left(\frac{\rho}{n} \right)^\beta} \quad (15-1)$$

$$\log \beta = -0.61119 - 0.017638 W_c \quad (15-2)$$

$$\rho = 10^9 \left(\frac{C_0}{(1 - (10^9)^\beta)} \right)^{\frac{1}{\beta}} \quad (15-3)$$

$$C_0 = \ln \left(\frac{a_1 M_r^{b_1}}{a_9 M_r^{b_9}} \right) \quad (15-4)$$

$$\frac{\varepsilon_0}{\varepsilon_r} = \frac{\left(e^{(\rho)^\beta} \times a_1 E_r^{b_1} \right) + \left(e^{\left(\frac{\rho}{10^9} \right)^\beta} \times a_9 E_r^{b_9} \right)}{2} \quad (15-5)$$

$$\Delta_{p(HMA)} = \varepsilon_{p(HMA)} h_{HMA} = \beta_{1r} k_z \varepsilon_{r(HMA)} 10^{k_{1r} n} k_{2r} \beta_{2r} T^{k_{3r} \beta_{3r}} \quad (16-1)$$

$$\varepsilon_{r(HMA)} = \frac{1}{|E^*|} (\sigma_z - \mu \sigma_x - \mu \sigma_y) \quad (16-2)$$

$$\text{Damage ratio for rutting} = \frac{\Delta_{p(total),superload}}{\Delta_{p(total),class 9}} \quad (17)$$

where $\Delta_{p(soil)}$ is the permanent or plastic deformation for the layer/sublayer, in.; n is the number of axle-load repetitions; ε_0 is the intercept determined from laboratory repeated load permanent deformation tests, in./in.; ε_r is the resilient strain imposed in laboratory tests to obtain material properties ε_0 , β , and ρ , in./in.; ε_v is the average vertical resilient or the elastic strain in the layer/sublayer and calculated by the structural response model, in./in.; h_{soil} is the thickness of the unbound layer/sublayer, in.; k_{s1} is the global calibration coefficient ($k_{s1} = 1.673$ for granular materials and 1.35 for fine-grained materials from the MEPDG; $k_{s1} = 0.965$ for granular materials and 0.675 for fine-grained materials from AASHTOWare Pavement ME Design software); β_{s1} is the local calibration constant for the rutting in the unbound layers (1.0 for the global calibration); W_c is the water content, %; M_r is the resilient modulus of the unbound layer or sublayer, psi; a_1 and a_9 are the regression constants ($a_1 = 0.15$, $a_9 = 20.0$); b_1 and b_9 are the regression constants ($b_1 = 0.0$, $b_9 = 0.0$); $\Delta_{p(HMA)}$ is the accumulated permanent vertical deformation in the HMA layer/sublayer, in.; $\varepsilon_{p(HMA)}$ is the accumulated permanent axial strain in the HMA layer/sublayer, in./in.; $\varepsilon_{r(HMA)}$ is the resilient or elastic strain calculated by the structural response model at the mid-depth of each HMA sublayer, in./in.; h_{HMA} is the thickness of the HMA layer/sublayer, in.; T is the mix or pavement temperature, °F; k_z is the depth confinement factor; k_{1r} , k_{2r} , and k_{3r} are the global field calibration parameters ($k_{1r} = -3.35412$, $k_{2r} = 0.4791$, $k_{3r} = 1.5606$ from the MEPDG; $k_{1r} = -2.45$, $k_{2r} = 0.22$, $k_{3r} = 3.01$ from AASHTOWare Pavement ME Design software); β_{1r} , β_{2r} , and β_{3r} are the local or mixture field calibration constants (all set to 1.0 for the global calibration from the MEPDG; $\beta_{1r} = 0.4$, $\beta_{2r} = 1.36$, $\beta_{3r} = 0.52$ from AASHTOWare Pavement ME Design software); E^* is the dynamic modulus of asphalt mixtures, psi; σ_x , σ_y , and σ_z is three-dimensional stress components at response point of HMA layer, psi; μ is the Poisson's ratio of HMA layer; $\Delta_{p(total),superload}$ is the total permanent vertical deformation combining all the plastic deformations from each layer caused by a superload pass; and $\Delta_{p(total),class 9}$ is the total permanent vertical deformation combining all the plastic deformations from each layer caused by an FHWA class 9 truck pass.

Another main distress type of flexible pavements, traffic load-related bottom-up fatigue cracking, that mostly governs initiation of load-related cracking over the top-down fatigue cracking when subjected to superloads, can be calculated by converting the tensile strain at the bottom of the AC layer to the number of repetitions to failure using a transfer function for bottom-up or alligator cracking (AASHTO 2022, 2015). Equations 18 and 19 provide a framework for calculating the number of repetitions to failure and the damage ratio associated with bottom-up fatigue cracking. Note that the percentage air voids in the HMA mixture, denoted as V_a , and the effective asphalt content by volume, denoted as V_b , were selected to vary within the ranges of 4% to 10% and 8% to 15%, respectively. These variations were based on the climatic conditions from climatic stations in three suggested regions, namely Minnesota, Oklahoma, and Phoenix, as outlined in the *Guide for Mechanistic-Empirical Design* (ARA, Inc. 2004b).

$$N_f = 0.00432 \times C \times \beta_{f1} k_1 (\varepsilon_t)^{-k_2 \beta_{f2}} (E)^{-k_3 \beta_{f3}} \quad (18-1)$$

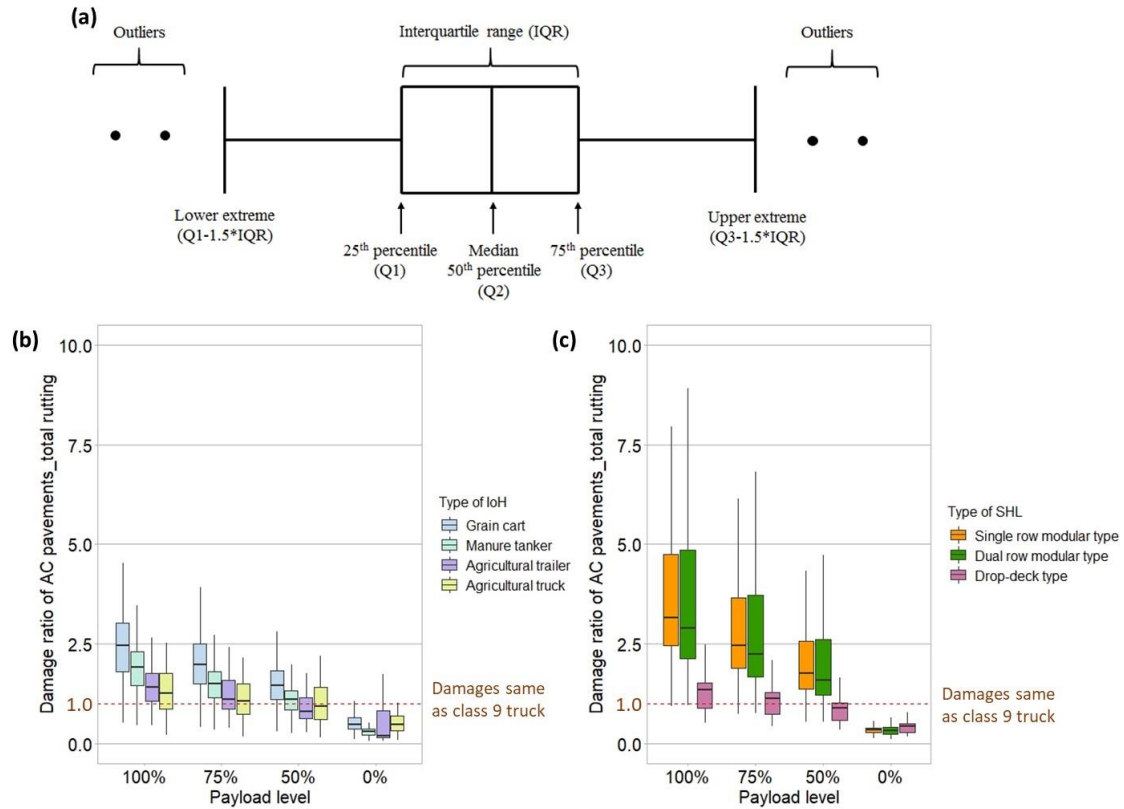
$$C = 10^M; M = 4.84 \left(\frac{V_b}{V_v + V_b} - 0.69 \right) \quad (18-2)$$

$$\text{Damage ratio for bottom - up fatigue cracking} = \frac{\frac{1}{N_{superload}}}{\frac{1}{N_{class 9}}} = \frac{N_{class 9}}{N_{superload}} \quad (19)$$

where N_f is the allowable number of axle-load applications for a flexible pavement and HMA overlays; ε_t is the tensile strain at critical locations and calculated by the structural response model, in./in.; E is the dynamic modulus of the HMA measured in compression, psi; k_1, k_2 , and k_3 are the global field calibration coefficients ($k_1 = 0.007566$, $k_2 = 3.9492$, $k_3 = 1.281$ from the MEPDG; $k_1 = 3.75$, $k_2 = 2.87$, and $k_3 = 1.46$ from AASHTOWare Pavement ME Design software); β_{f1}, β_{f2} , and β_{f3} are the local or the mixture specific field calibration constants (all set to 1.0 for global calibration from the MEPDG; $\beta_{f1} = (5.104 \times h_{HMA}^{-3.416}) \times 1 + 0$, $\beta_{f2} = 1.38$, $\beta_{f3} = 0.88$ from AASHTOWare Pavement ME Design software); V_a is the percent air voids in the HMA mixture; V_b is the effective asphalt content by volume %; $N_{superload}$ is the allowable number of axle-load applications of superload; and $N_{class 9}$ is the allowable number of axle-load applications of an FHWA class 9 truck.

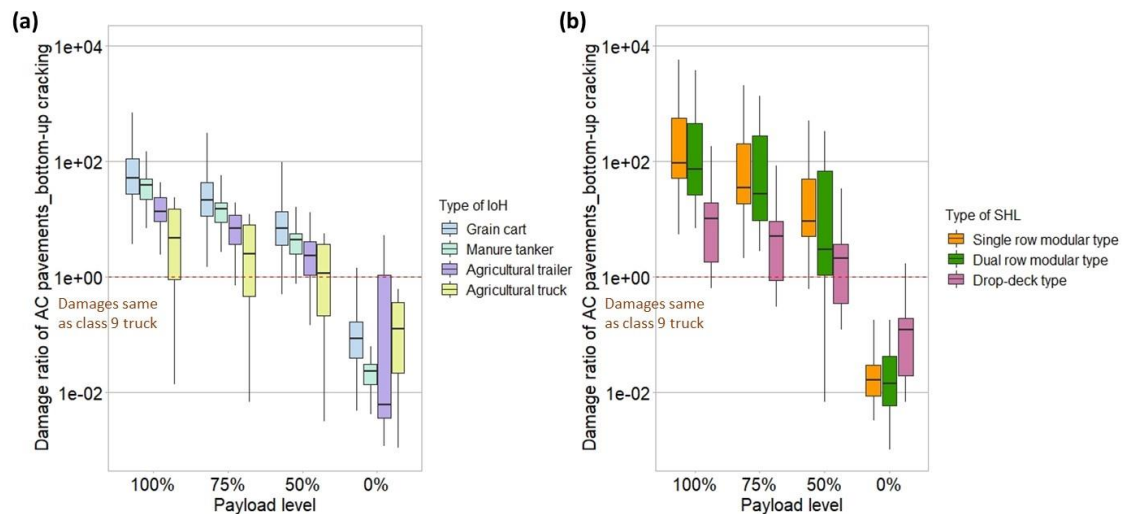
Damage Ratio Analysis

Damage ratios associated with total rutting and bottom-up fatigue cracking of flexible pavements under various superload scenarios calculated from a total of 24,660 LET-based analysis results are presented in Figure 32 and Figure 33.



Koh et al. 2023a, Reprinted with permission from Sage Publications, Inc., © 2023

Figure 32. (a) Configuration of box-whisker plot and (b and c) the linear graphs for total rutting ratio of flexible pavements under IoHs and SHLs, respectively



Koh et al. 2023a, Reprinted with permission from Sage Publications, Inc., © 2023

Figure 33. Logarithmic graphs for bottom-up fatigue damage ratio of flexible pavements under (a) IoHs and (b) SHLs

The payload level of each superload varied from 0% to 100%, allowing an examination of the influence of payload levels on potential damage to the flexible pavement. Upon scrutiny of the box-whisker plots in Figure 32 and Figure 33, along with the summarized findings in Table 19, it becomes evident that, among IoHs, grain carts, and among SHLs, single-row modular and dual-row modular types exhibit a propensity to induce higher total rutting and bottom-up fatigue cracking in flexible pavements when compared to FHWA class 9 trucks, particularly at a payload level of 50% or higher. This observation holds true even when employing different calibration constants from both transfer functions (AASHTO 2022, 2015).

Table 19. Averaged damage ratios of flexible pavements under superloads

Reference	Payload level		100% payload	75% payload	50% payload	0% payload
Transfer functions from MEPDG	Total rutting ratio	IoH – 18 types (critical type)	1.9 (Grain cart: 2.5)	1.6 (Grain cart: 2.0)	1.2 (Grain cart: 1.5)	0.4 (Agricultural trailer: 0.5)
		SHL – 16 types (critical type)	3.2 (Single-row modular: 3.6)	2.5 (Single-row modular: 2.8)	1.8 (Single-row modular: 2.0)	0.4 (Drop-deck: 0.5)
	Bottom-up fatigue damage ratio	IoH – 18 types (critical type)	57.4 (Grain cart: 117.5)	24.3 (Grain cart: 50.3)	8.2 (Grain cart: 17.1)	0.3 (Agricultural trailer: 0.9)
		IoH – 18 types (critical type)	327.6 (Single-row modular: 447.6)	137.7 (Dual-row modular: 179.2)	34.0 (Dual-row modular: 42.9)	0.1 (Drop-deck: 0.2)
Transfer functions from AASHTO Ware Pavement ME software, ver. 2.6.2	Total rutting ratio	IoH – 18 types (critical type)	1.3 (Grain cart: 1.6)	1.0 (Grain cart: 1.3)	0.8 (Grain cart: 1.0)	0.3 (Agricultural trailer: 0.3)
		SHL – 16 types (critical type)	3.0 (Single-row modular: 3.4)	2.4 (Single-row modular: 2.7)	1.7 (Single-row modular: 1.9)	0.4 (Drop-deck: 0.5)
	Bottom-up fatigue damage ratio	IoH – 18 types (critical type)	58.2 (Grain cart: 119.3)	24.5 (Grain cart: 51.0)	8.2 (Grain cart: 17.3)	0.3 (Agricultural trailer: 0.9)
		SHL – 16 types (critical type)	334.1 (Single-row modular: 456.6)	140.0 (Dual-row modular: 182.3)	34.4 (Dual-row modular: 43.4)	0.1 (Drop-deck: 0.2)

Source: Koh et al. 2023a

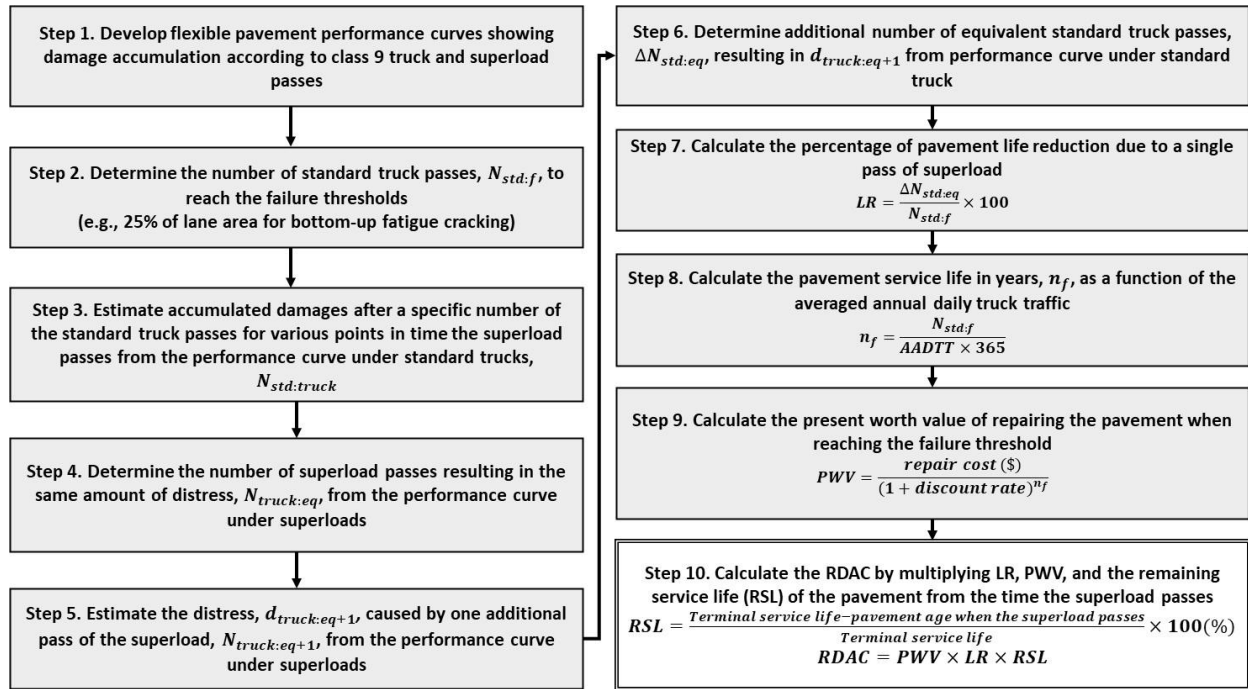
In terms of the total rutting ratio response to an IoH pass, the 50th percentile of damage ratio results generated by manure tankers, agricultural trailers, and agricultural trucks carrying 50% payload levels reached approximately one or less, while the damage ratio results from grain carts

carrying 50% payload levels still exceeded one, meaning that grain carts carrying only 50% of their transporting capacity were still likely to generate greater total rutting than an FHWA class 9 truck. On the other hand, both single-row and dual-row modular SHLs produced total rutting ratios higher than those from the IoHs, both exceeding one when carrying 50% payload levels or greater. Bottom-up fatigue damage ratios of flexible pavements when subjected to IoHs and SHLs carrying 50% payload level or more were likely to significantly exceed one, even higher than the average damage ratios of 400 and 100 in the case of single-row modular SHLs and grain carts, respectively, when carrying 100% payload levels. The graphical representations in Figure 32 (linear graphs) and Figure 33 (logarithmic graphs) underscore that superloads impact bottom-up fatigue cracking to a larger extent than total rutting.

LCCA for Mechanistic-Based RSL and Permit Fee Decision

Methodology

The determination of the PWV associated with the treatment cost for structural distresses in flexible pavements resulting from a single pass of a superload is crucial for evaluating the economic impact of superloads on flexible pavement systems. The RDAC concept (Tirado et al. 2010) was again employed to perform LCCA as done in the JPCP analysis. As outlined in the preceding chapter, RDACs are calculated by multiplying the percentage reduction in pavement life due to a single pass of a superload (LR), the PWV of pavement repairs, and the RSL of the pavement at the time the superload travels over the pavement section. A detailed explanation of the steps involved in determining the RDACs for flexible pavements subjected to a single pass of a superload is provided in Figure 34.



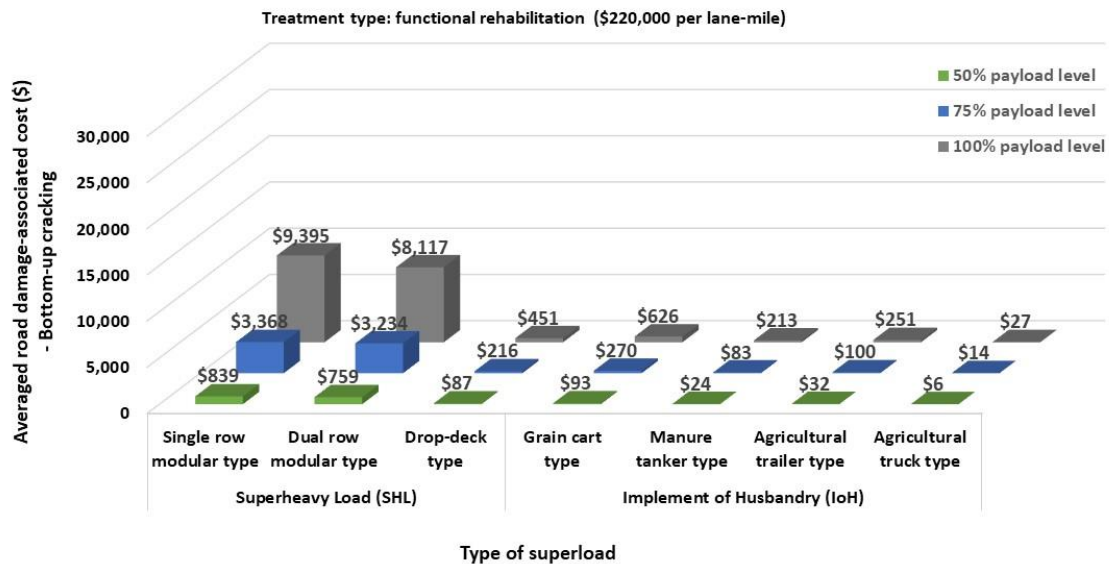
Koh et al. 2023a, Reprinted with permission from Sage Publications, Inc., © 2023

Figure 34. Detailed steps for LCCA to determine RDACs of flexible pavements under superloads

To establish a comprehensive understanding, multivariate RDACs were computed, taking into account variations in pavement structure, material, traffic load, and treatment type. These calculated RDACs were subsequently compared to provide a mechanistic basis for permit fee decision-making for each type of superload. Note that a multivariate LCCA of flexible pavements under superloads was conducted to calculate RDACs for bottom-up fatigue cracking, a type of distress that governs flexible pavement performance and life cycle more than total rutting damage in all superload cases. A calculated terminal service life of flexible pavements of less than 20 years was considered the service lifetime of the pavement before the next treatment. For flexible pavements having terminal service lives over 20 years, the RDACs were calculated based on a 20-year design life. The RDACs for flexible pavements were derived by averaging the LCCA results obtained from four distinct LCCA models, each with four different moduli of elasticity of each layer used to represent the four seasons. To develop flexible pavement performance curves for determining pavement service life, n_f , an annual average daily truck traffic (AADTT) of 1,000 vehicles was applied. In the calculation of the PWV, a discount rate of 2% was selected, which aligns with the US discount rate as of August 2022. This discount rate reflects the rate of return used by investors to discount future cash flows back to their present value. Also, two lanes and 10 mi of flexible pavement sections were used in determination of the final RDACs.

Multivariate RDAC Assessment Case I. RDAC According to Traffic Loading

To assess the influence of traffic loading on the RDAC based on bottom-up fatigue cracking of flexible pavements, various superloads with different payload levels traveling at 50% of the terminal service life of the flexible pavement section, which consisted of an 8 in. AC layer, an 8 in. base layer, a 6 in. subbase layer, 7% of air voids in the HMA mixture, V_a , and 11% of effective asphalt content, V_b , were applied to the LCCA model, as depicted in Figure 35.



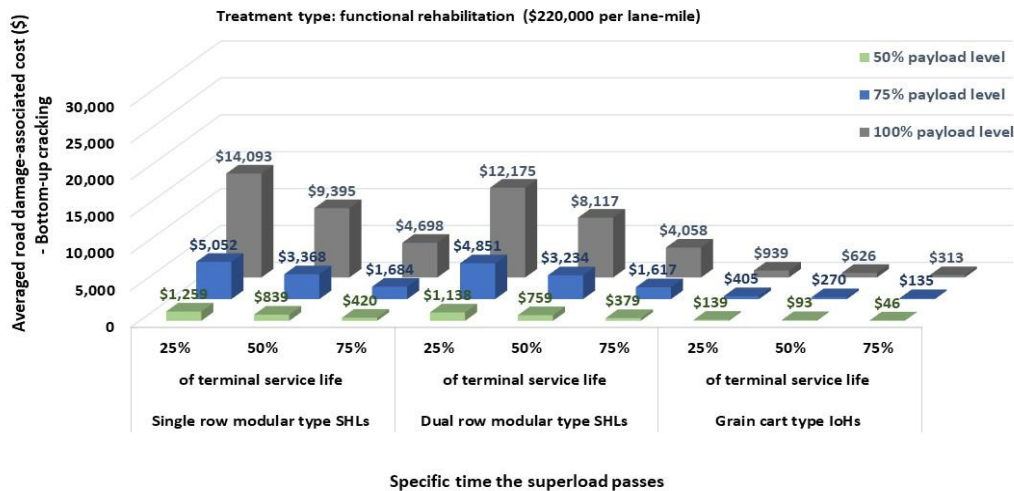
Koh et al. 2023a, Reprinted with permission from Sage Publications, Inc., © 2023

Figure 35. RDACs related to the bottom-up fatigue cracking due to a single pass of superload traveling at 50% of terminal service life of flexible pavement

For the calculation of realistic RDAC values, functional rehabilitation as a treatment type and the corresponding treatment cost per lane-mile (i.e., \$220,000 for non-interstate roadways), when the failure threshold of 25% of bottom-up fatigue cracking is reached, were also chosen from the 2019–2028 Iowa TAMP (Iowa DOT 2019). The results presented in Figure 35 reveal that grain cart IoHs and single-row modular and dual-row modular SHLs, both featuring relatively high tire weights, resulted in the highest RDACs. This observation suggests that RDACs are notably influenced by the tire weight associated with each type of superload, emphasizing the significance of considering this factor in assessing the economic impact of superloads on flexible pavements. While the RDACs generally exhibit an increasing trend with increasing axle weight, it is notable that since this study adopts the nucleus segment approach to find the number of influencing tires, the relationship between RDAC and axle weight is not as proportional as the relationship between the RDAC and tire weight. For instance, a dual-row modular SHLs with more tires on a single axle may possess a higher axle weight, but the weight of its nucleus segment, as considered in this study, might be comparable to that of a single-row modular SHL.

This results in similar RDACs despite the difference in axle weight. The nucleus segment approach, therefore, provides a nuanced understanding of the relationship between RDAC and axle weight, offering insights that extend beyond a straightforward proportional relationship and highlighting the significance of tire weight in determining RDAC outcomes. The payload levels of superloads, initially estimated based on their transportation capacity, also significantly influence RDACs. When the payload levels of superloads were decreased from 100% to 75%, a majority of RDACs exhibited a reduction of more than 50%. Notably, the highest potential RDACs, associated with single-row modular SHLs, witnessed reductions of 64% and 91%, respectively, when the payload levels were decreased from 100% to 75% and from 100% to 50%. It is crucial to acknowledge that the 100% payload level of each superload in this study determined as the transportation capacity of each commercial superload was taken from their commercial manuals or specifications, so their tire and axle weights tend to far exceed a state's overweight permit limit. While the RDACs of superloads carrying 100% payload level may appear substantial, it remains pertinent to evaluate the magnitude of reduction in damage-associated costs when the payload level is scaled down from 100% to 75% or from 100% to 50%.

RDACs for the same flexible pavement structures subjected to a single pass of the three most damage-causing types of superload traveling at varying times were also intensively analyzed and compared, as shown in Figure 36. It is evident from the findings that both the travel time and payload level significantly influence RDAC values, mainly due to the RSL, discount rate, and pavement service life. The observed differences in RDAC values underscore the importance of considering not only the payload level but also the timing of superload travel in evaluating the economic impact on flexible pavement systems.



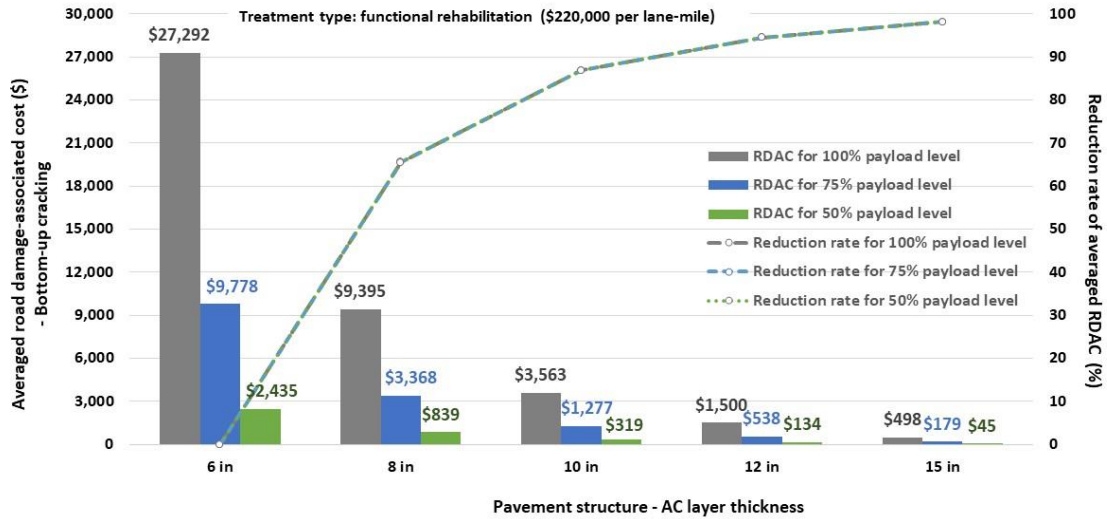
Koh et al. 2023a, Reprinted with permission from Sage Publications, Inc., © 2023

Figure 36. RDACs related to bottom-up fatigue cracking due to a single pass of the three most damage-causing types of superload traveling at a varying time on flexible pavement

Note that in the above figure, the flexible pavement has an 8 in. thick AC layer, 8 in. thick base layer, 6 in. thick subbase layer, 7% of V_a , and 11% of V_b .

Multivariate RDAC Assessment Case II. RDAC According to Flexible Pavement Structures and Materials

RDACs arising from various flexible pavement structures subjected to single-row modular SHLs, the predominant cause of bottom-up fatigue cracking, demonstrated a consistent decrease with increasing AC layer thickness, as illustrated in Figure 37.



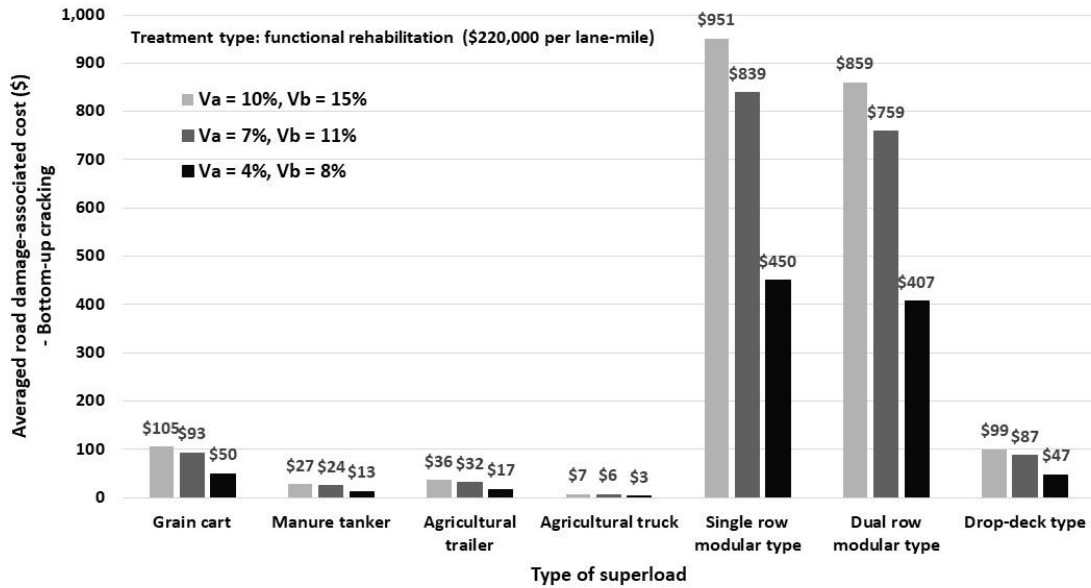
Koh et al. 2023a, Reprinted with permission from Sage Publications, Inc., © 2023

Figure 37. RDACs related to the bottom-up fatigue cracking due to a single pass of single-row modular type SHL traveling at 50% of terminal service life of different flexible pavement structures

Note that in the above figure, the flexible pavement structures have an 8 in. thick base layer, 6 in. thick subbase layer, 7% of V_a , 11% of V_b , and varying AC layer thickness.

The reduction rates of averaged RDACs displayed a uniform pattern with increasing AC layer thickness, exhibiting substantial reductions of 66%, 87%, 94%, and 98%, respectively, as the AC layer thickness was increased from 6 in. to 8 in., 10 in., 12 in., and 15 in. Note that the reduction rate of averaged RDAC for each pavement structure was calculated based on the reference flexible pavement structure, which featured a 6 in. thick AC layer.

In addition to AC layer thickness, material properties of AC, specifically air voids in the HMA mixture, V_a , and effective asphalt content, V_b , were considered as multivariate factors in the LCCA. These properties were varied from 4% to 10% for V_a and 8% to 15% for V_b , as recommended by the *Guide for Mechanistic-Empirical Design* (ARA, Inc. 2004b). Figure 38 illustrates that as both V_a and V_b decrease, average RDACs tend to decrease as well. Notably, significant RDAC reductions were observed in flexible pavement under AC material conditions featuring 4% V_a and 8% V_b . These results emphasize the sensitivity of RDACs to variations in the material properties of the AC layer and provides valuable considerations for optimizing pavement design when experiencing superload traffic.



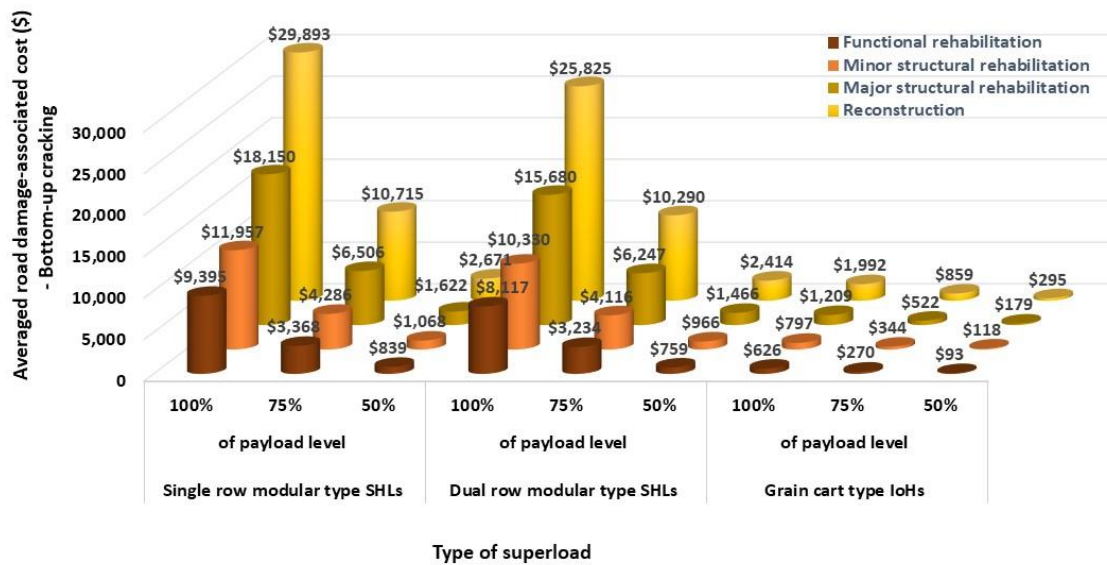
Koh et al. 2023a, Reprinted with permission from Sage Publications, Inc., © 2023

Figure 38. RDACs related to the bottom-up fatigue cracking due to a single pass of a superload with 50% payload level traveling at 50% of terminal service life of flexible pavements having different AC materials

Note that in the above figure, the flexible pavements have 8 in. thick AC layer, 8 in. thick base layer, 6 in. thick subbase layer, and varying V_a and V_b .

Multivariate RDAC Assessment Case III. RDAC According to Management Factors

To help determine the potential permit fee associated with superloads, contingent on the pavement treatment type, an economic evaluation was conducted on flexible pavements subjected to superloads, varying treatment types and corresponding costs. A total of four treatment types for agency cost determination, including functional rehabilitation, minor structural rehabilitation, major structural rehabilitation, reconstruction, and the corresponding treatment costs per lane-mile (\$220,000, \$280,000, \$425,000, and \$700,000, respectively), were adopted from the 2019–2028 Iowa TAMP (Iowa DOT 2019). Figure 39 presents the RDAC results for flexible pavements with an 8 in. thick AC layer, an 8 in. thick base layer, and a 6 in. thick subbase layer for the three most bottom-up fatigue crack-causing types and varying superload payload levels.



Koh et al. 2023a, Reprinted with permission from Sage Publications, Inc., © 2023

Figure 39. RDACs of flexible pavement for different treatment types and payload levels due to a single pass of the three most bottom-up fatigue crack-causing types of superload

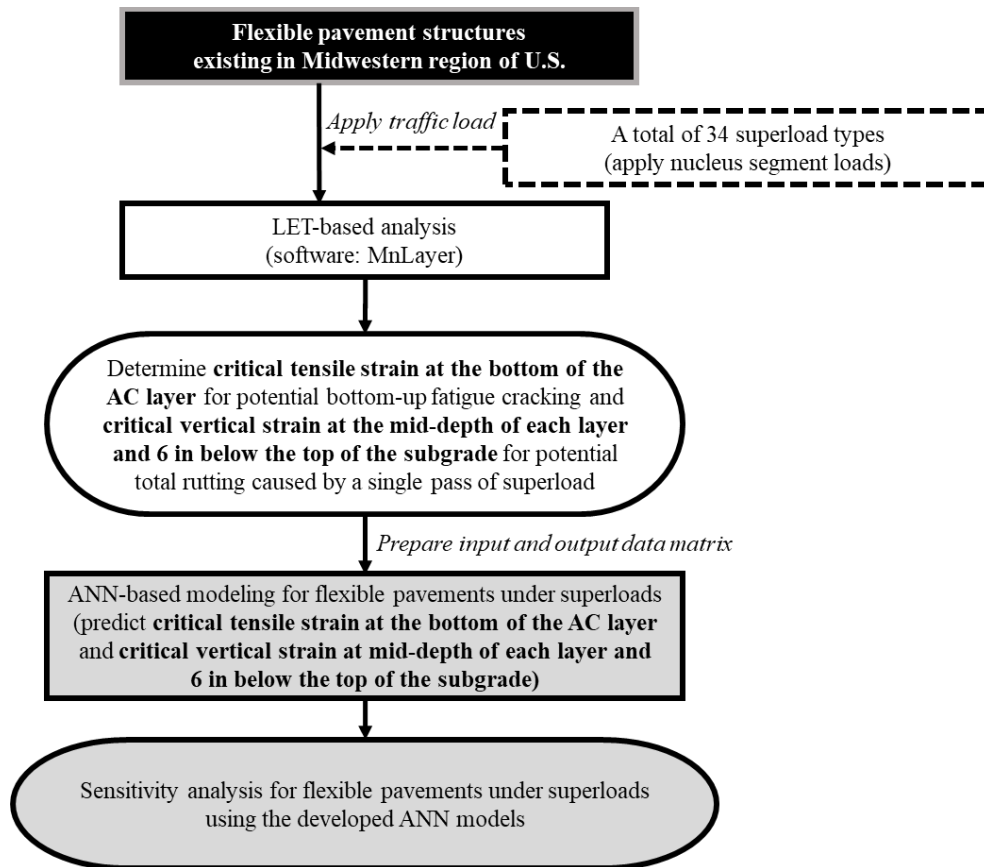
The cost per lane-mile with respect to treatment type was utilized in PWV calculations, incorporating a discount rate of 2% for RDAC calculation. As an example, for a single pass of single-row modular SHLs transporting a 50% payload level, the PWVs of RDACs were determined for future reconstruction, major structural rehabilitation, minor structural rehabilitation, and functional rehabilitation to be \$2,671, \$1,622, \$1,068, and \$839, respectively. These results provide insights into the economic considerations associated with different treatment types for flexible pavements subjected to superloads, aiding in the determination of potential permit fees.

Development of AI-Based Prediction Models

Methodology

This section introduces the development and optimization of ANN-based models designed to predict critical pavement responses associated with representative structural distresses of flexible pavements, including total rutting and bottom-up fatigue cracking, when subjected to a single pass of various superloads. Following a similar approach as detailed in the JPCP chapter, the development of ANN models based on distinct superload types provides users with the flexibility to choose a specific superload category of interest and utilize the corresponding ANN model within user-friendly pavement design software to predict critical pavement responses with high prediction accuracy. The development process leveraged an LET-based flexible pavement analysis database compiled from previous sections in this chapter, covering various nucleus segments and payload levels associated with different superload types. This means that the developed ANN-based models not only derive from a database comprised of a wider loading

configuration scope of superloads but also imply mechanistic methodologies for determining loading inputs for flexible pavements, such as nucleus segment determination according to different superload types. Note that the optimized ANN models for different superload types were integrated into a prototype tool developed in this study. This tool facilitates the quantification of superload impacts on Iowa's road infrastructure systems, a topic explored in subsequent chapters. Additionally, a sensitivity analysis was conducted on pavement structure and loading parameters utilizing the developed ANN models to ascertain the significance level of each explanatory variable in generating the target responses. Figure 40 provides a schematic representation of the primary steps involved in ANN modeling for flexible pavements under superloads.



Koh et al. 2024, Reprinted with permission from Elsevier, © 2024

Figure 40. Overall steps for ANN modeling for flexible pavements under different superload types

Note that in the above figure, the gray-colored boxes indicate the main steps of this section.

To facilitate the development of ANN-based models, a database was prepared using the inputs and outputs of LET-based flexible pavement analysis. This database adheres to the structured matrix outlined in Table 18, containing all necessary inputs and outputs extracted from the MnLayer software. This organized data matrix was subsequently utilized as the foundation for the development and optimization of ANN models. The inclusion of various superload types and

payload levels ensures a comprehensive evaluation of total rutting and bottom-up fatigue-related damage scenarios within flexible pavements, enhancing the robustness and applicability of the resulting ANN models.

A total of five backpropagation algorithms, including (1) Levenberg-Marquardt (Levenberg 1944, Marquardt 1963), (2) Bayesian Regularization (MacKay 1992), (3) BFGS Quasi-Newton (Broyden 1970a, Broyden 1970b, Fletcher 1970, Goldfarb 1970, Shanno 1970), (4) Resilient Backpropagation (Riedmiller and Braun 1993), and (5) Scaled Conjugate Gradient (Johansson et al. 1991), were employed for flexible pavement cases, which are consistent with those employed for JPCP cases. The ANN architectures were optimized by varying the number of hidden layers and neurons per hidden layer, containing randomly initialized weight per node connection. Separate ANN models were developed and optimized according to different critical pavement responses and superload types, i.e., the seven parent class types shown in Table 4 and Table 5. A 10-fold cross-validation technique was also used here for reliable prediction evaluation of ANN models. The evaluation metrics utilized included the coefficient of determination, R^2 , AAE, and RMSE, as previously described in equations 8 to 10.

Development of ANN-Based Surrogate Models

Table 20 provides essential information related to ANN modeling for flexible pavements under superloads, using the database from the LET-based analysis. The nondimensional variable, denoted as the nucleus segment load/road segment weight, is presented in Table 20. This variable is defined as the ratio of the nucleus segment loadings, which represent the mechanistic inputs accounting for the wide variation in dimensions of superload properties, to the weight of the top surface layer possessing the same area as the nucleus segment, as described by equation 20.

$$\text{Nucleus segment load/road segment weight} = \frac{\sum \text{Tire loads in nucleus segment area}}{a_n \times h_t \times \gamma_t} \quad (20)$$

where a_n is the section area of a nucleus segment, ft^2 ; h_t is the thickness of a top layer, ft; and γ_t is the unit weight of a top layer, pcf.

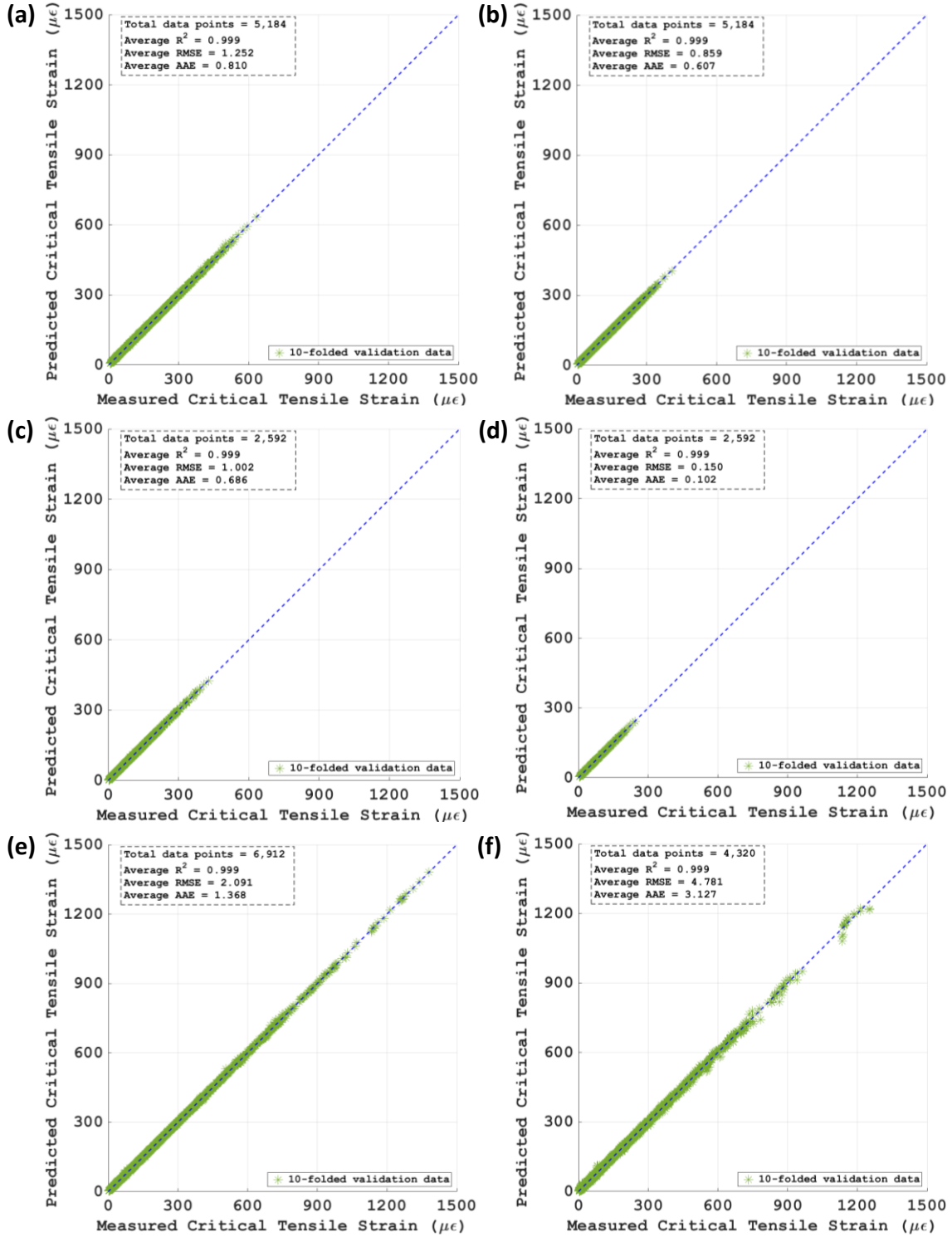
Table 20. Details of multilayer ANN modeling for flexible pavements under superloads

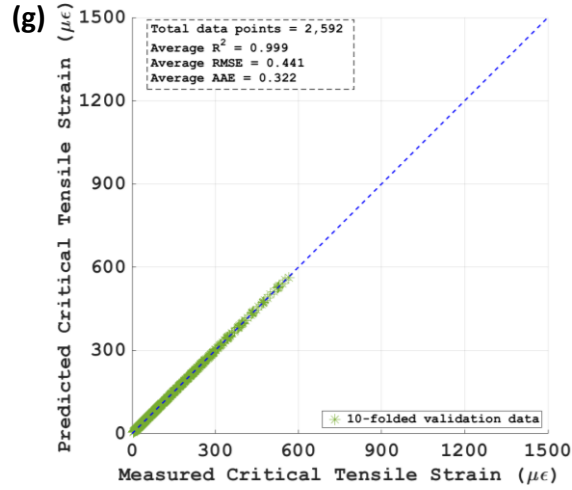
Multilayer ANN models for flexible pavements under superloads			
Explanatory variables	(1) Independent variables: Thickness of AC, base, subbase layers, modulus of elasticity of AC, base, subbase layers, and subgrade, axle weight, tire pressure (2) Nondimensional variables: Nucleus segment load/road segment weight		
Target variables	(1) Critical tensile strain at the bottom of the AC layer (2) Critical vertical strain at the mid-depth of the AC layer (3) Critical vertical strain at the mid-depth of the base layer (4) Critical vertical strain at the mid-depth of the subbase layer (5) Critical vertical strain at 6 in. below the top of the subgrade		
ANN algorithms	(1) Levenberg-Marquardt, (2) Bayesian Regularization, (3) BFGS Quasi-Newton, (4) Resilient Backpropagation, and (5) Scaled Conjugate Gradient		
Learning rate	0.005		
Distribution function	Gaussian distribution	Distribution function	Hyperbolic tangent
No. of hidden layers	1 to 3	No. of hidden layers	3 to 9

Source: Koh et al. 2024

Performance Evaluation and Architecture Optimization of ANN-Based Surrogate Models

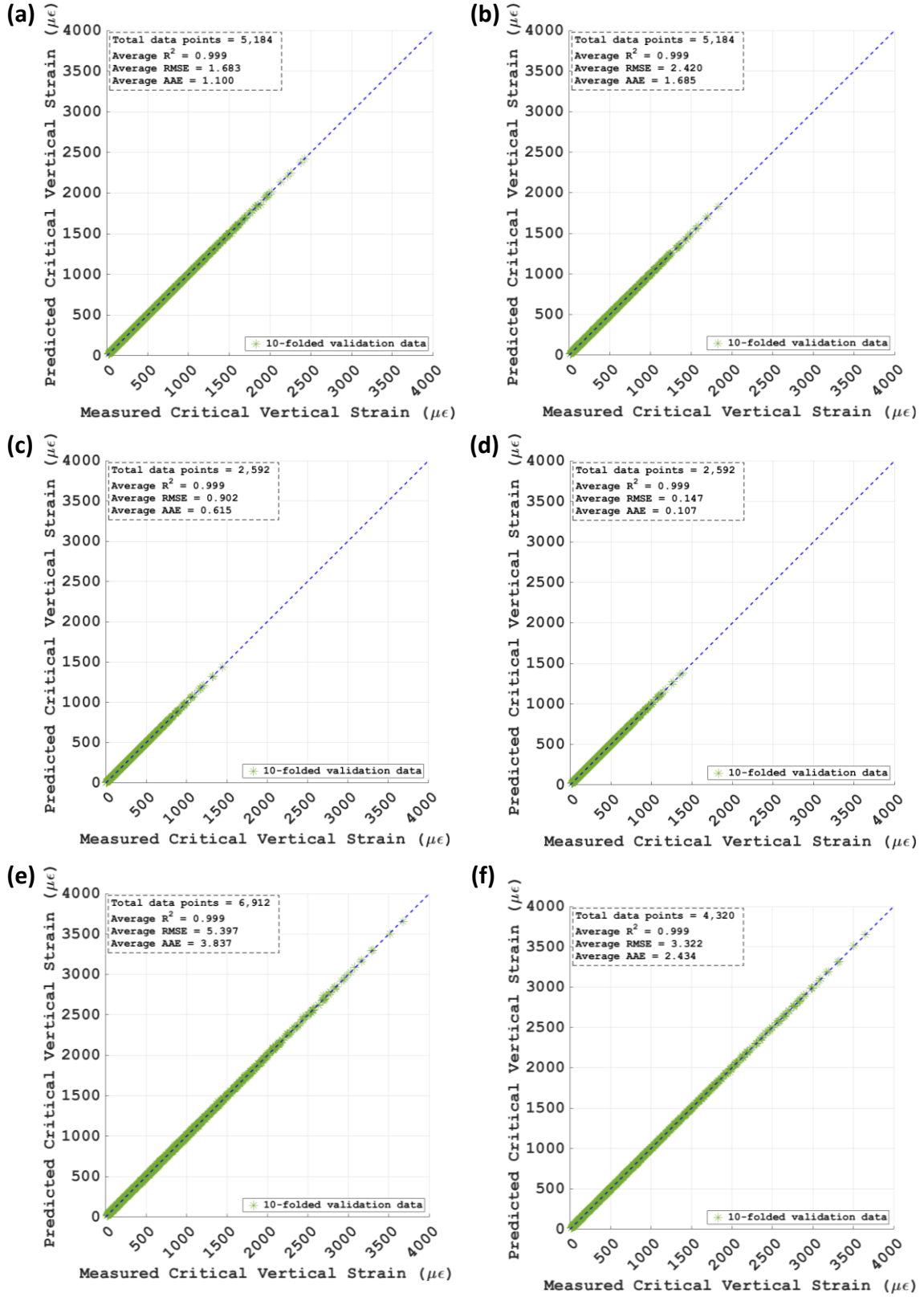
A total of 35 ANN models, dependent on 7 distinct superload parent types and 5 critical pavement response types, were developed. The prediction performance evaluation of partial ANN models, developed based on the Bayesian Regularization algorithm and architectures featuring two hidden layers and seven neurons per hidden layer, is shown in Figure 41 and Figure 42. These graphs indicate that the ANN models developed for the prediction of both critical pavement response types exhibited exceptional predictive accuracies, as evidenced by (1) R^2 values equal to or greater than 0.999, (2) AAE values equal to or less than 3.837, and (3) RMSE values equal to or less than 5.397. These results affirm the remarkably high accuracy levels achieved by each ANN model in predicting critical pavement responses of flexible pavements when subjected to a single pass of various types of superloads.

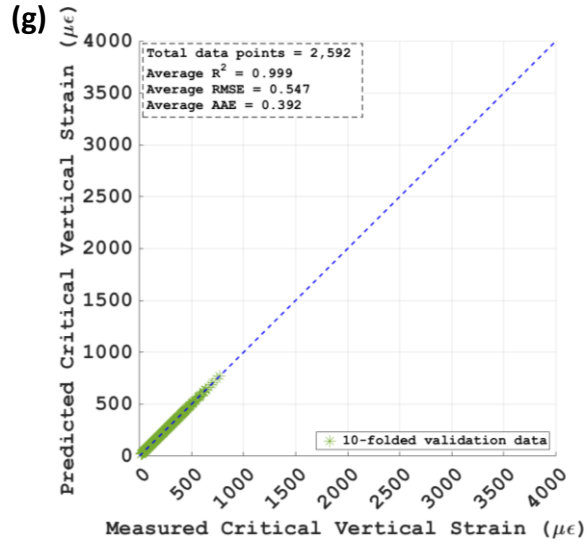




Koh et al. 2024, Reprinted with permission from Elsevier, © 2024

Figure 41. ANN model performances predicting the critical horizontal tensile strain at the bottom of the AC layer when subjected to IoHs including (a) grain carts, (b) manure tankers, (c) agricultural trailers, and (d) agricultural trucks, and when subjected to SHLs including (e) single-row modular, (f) dual-row modular, and (g) drop-deck

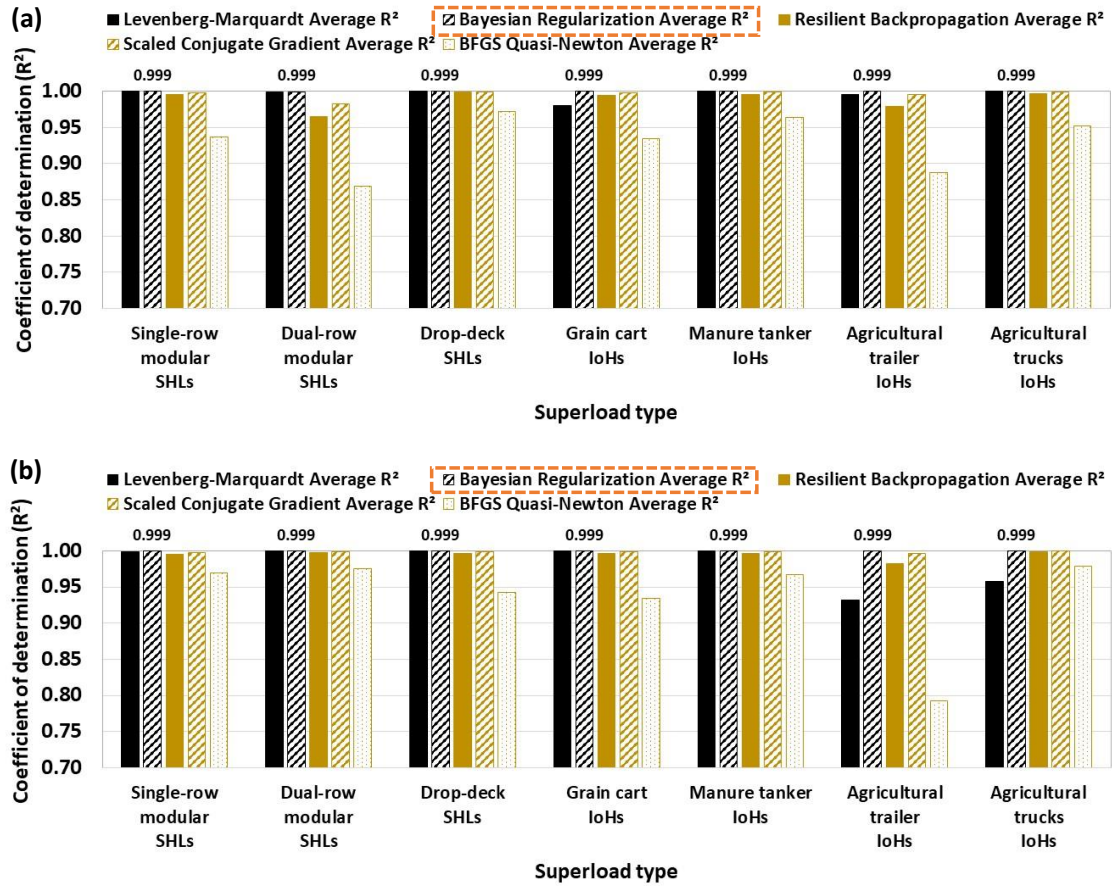




Koh et al. 2024, Reprinted with permission from Elsevier, © 2024

Figure 42. ANN model performances predicting the critical vertical strain at 6 in. below the top of the subgrade when subjected to IoHs including (a) grain carts, (b) manure tankers, (c) agricultural trailers, and (d) agricultural trucks, and when subjected to SHLs including (e) single-row modular, (f) dual-row modular, and (g) drop-deck

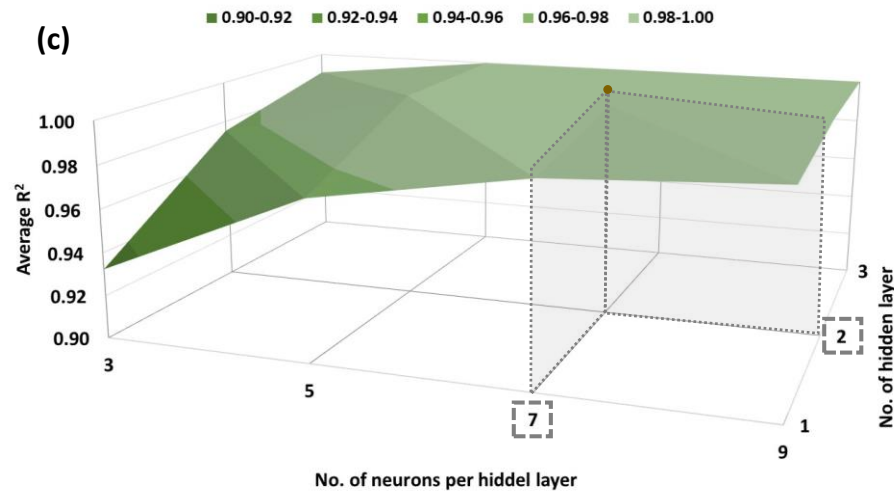
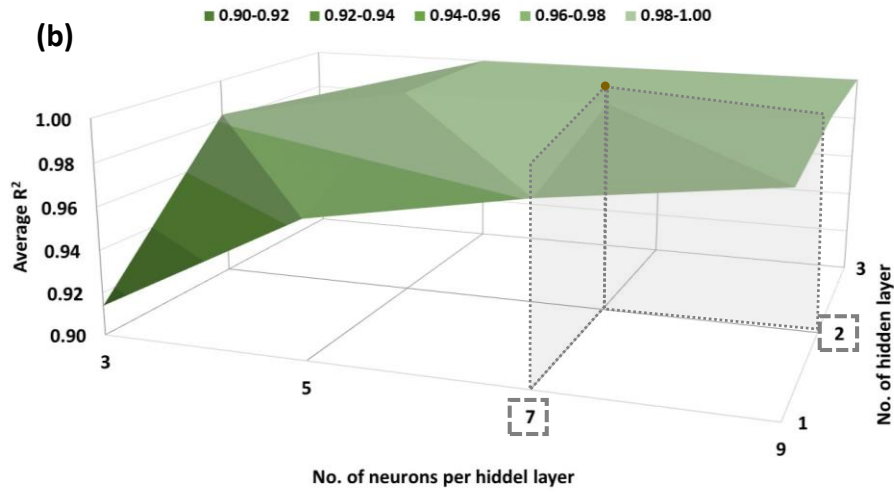
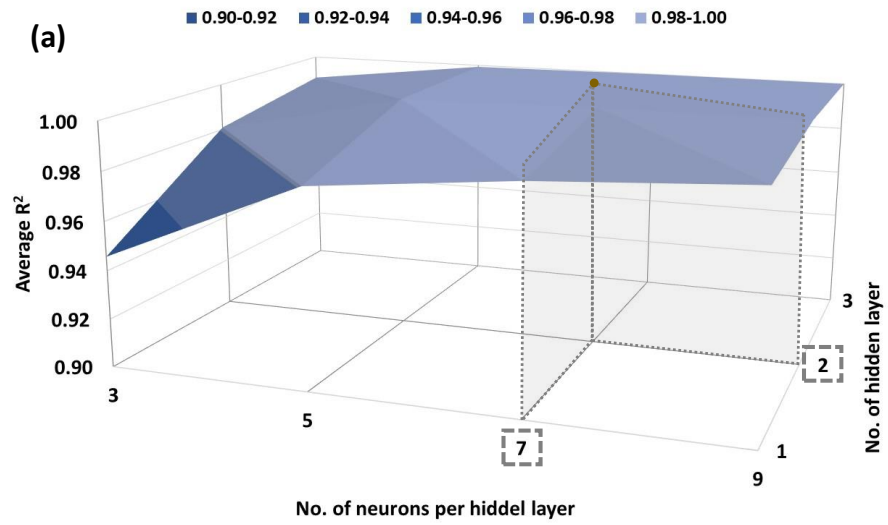
Similar to the optimized ANN-models for JPCP systems, Figure 43 shows that the Bayesian Regularization algorithm predicted the critical tensile strain at the bottom of the AC layer and critical vertical strain at 6 in. below the top of the subgrade more accurately than the other four ANN algorithms.

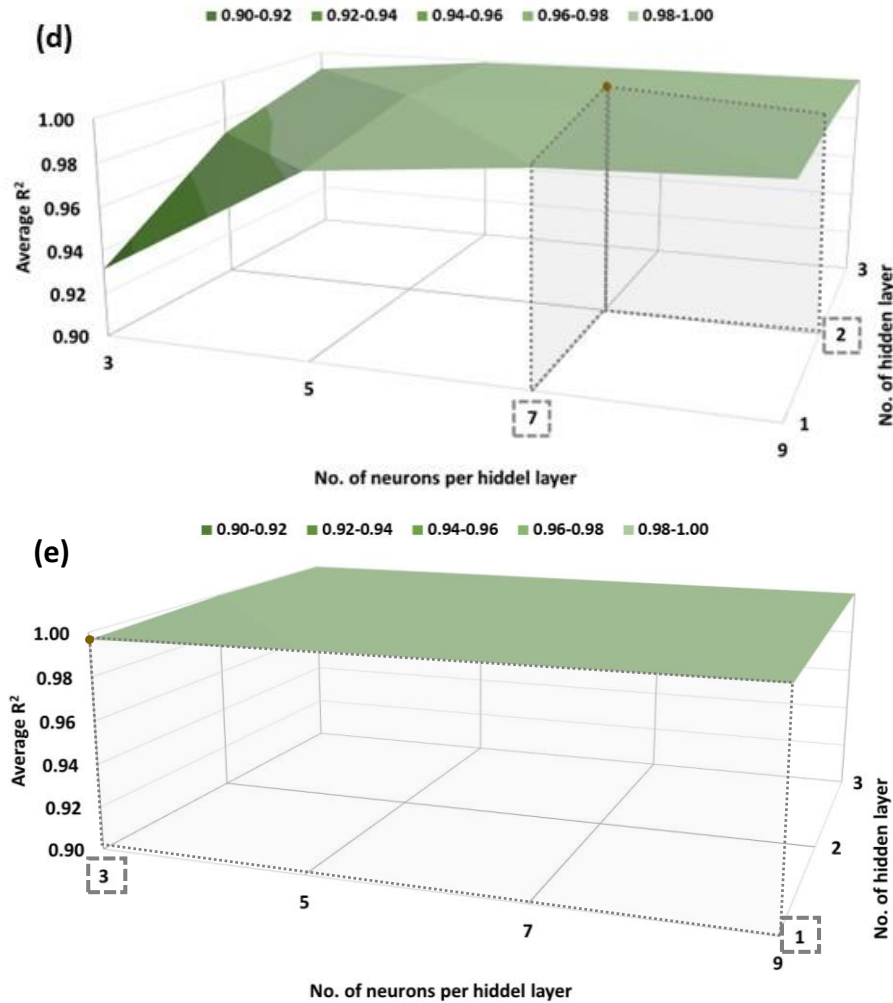


Koh et al. 2024, Reprinted with permission from Elsevier, © 2024

Figure 43. Performance evaluation of ANN models constructed with two hidden layers, seven neurons per each hidden layer, and five backpropagation algorithms when predicting (a) critical tensile strain at the bottom of the AC layer and (b) critical vertical strain at 6 in. below the top of the subgrade

Consistently, the ANN architectures featuring two hidden layers with seven neurons per hidden layer exhibited sufficient accuracy in predicting these critical pavement response types, as indicated in Figure 44, that shows the agricultural trailer case as an example among the various superload types. These findings reaffirm the reliability and efficacy of the selected ANN structures in achieving accurate predictions for critical pavement responses, particularly in the context of diverse superload scenarios.





Koh et al. 2024, Reprinted with permission from Elsevier, © 2024

Figure 44. Architecture optimization of ANN models for the agricultural trailer case constructed with the Bayesian Regularization algorithm when predicting (a) critical tensile strain at the bottom of the AC layer, critical vertical strain at (b) 6 in. below the top of the subgrade, (c) mid-depth of the subbase layer, (d) mid-depth of the base layer, and (e) mid-depth of the AC layer

Sensitivity Evaluation of ANN-Based Surrogate Models

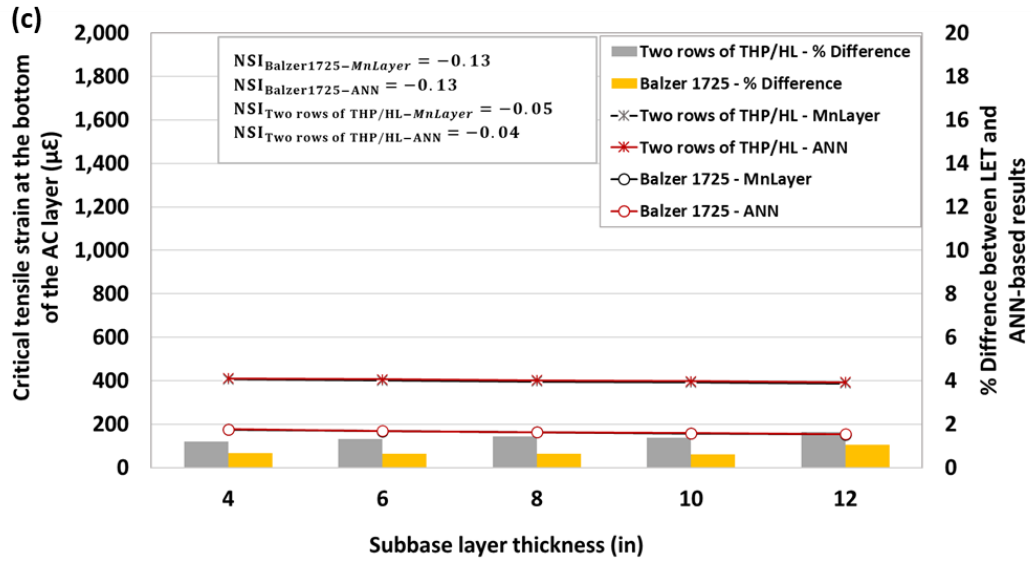
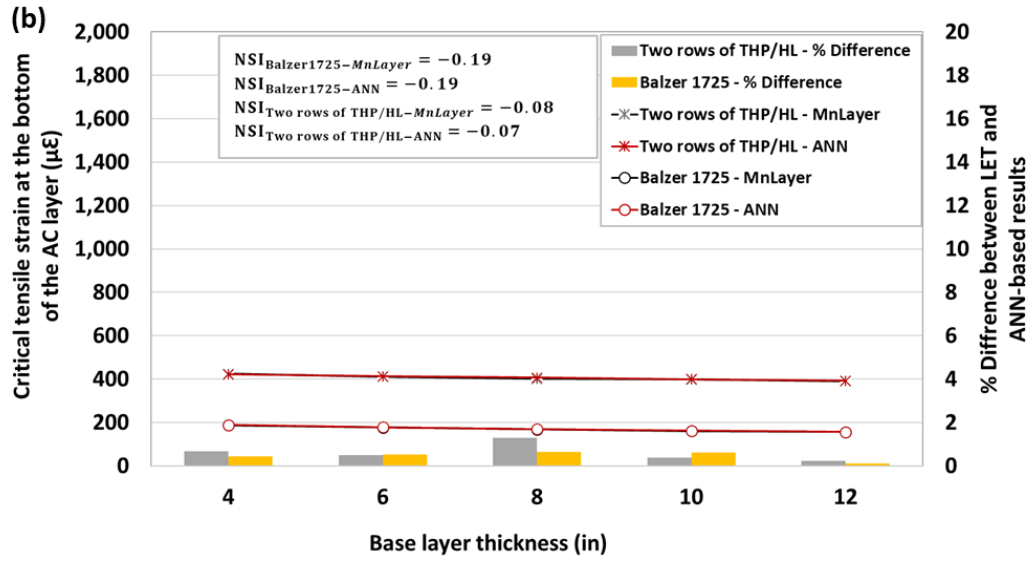
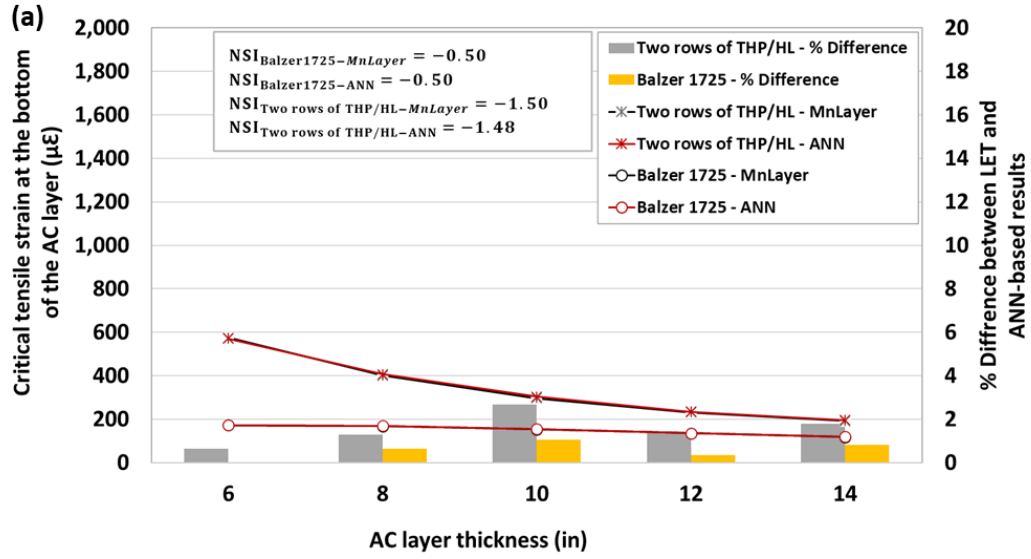
Similar to the approach taken for JPCP scenarios, the two most damage-causing superload types for bottom-up fatigue cracking and rutting were included in the OAT LSA. Table 21 provides an overview of the range encompassing each structural and loading variable considered in the sensitivity analysis for flexible pavements under superloads. It is noteworthy that the sensitivity analysis matrix excluded the modulus of elasticity for each layer because the research team's database only provides the four combinations of moduli representing the four seasons.

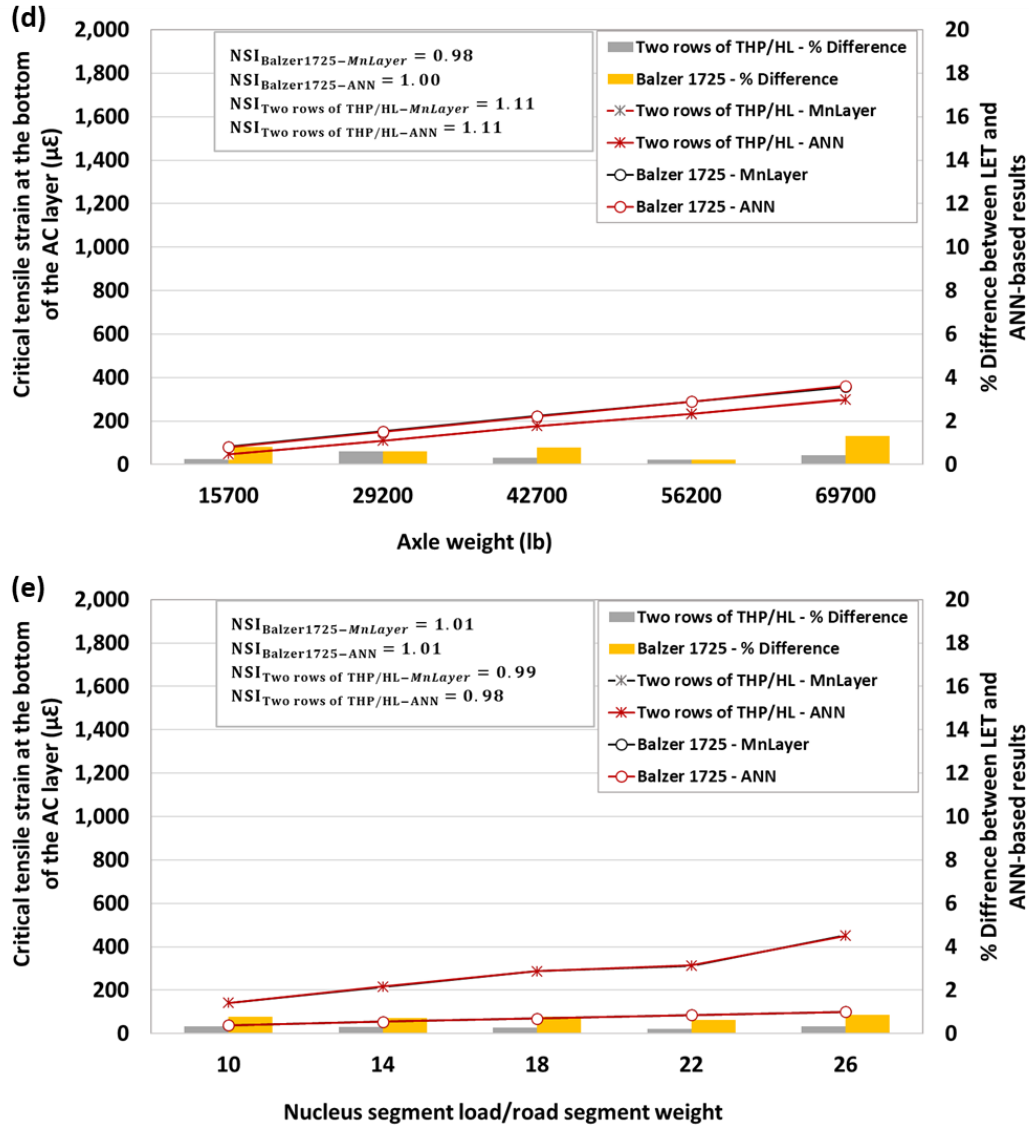
Table 21. Explanatory variable ranges for sensitivity analysis of flexible pavements under superloads

Category	Explanatory variables		Min.	Base line	Max.	Base case
Flexible pavement structural variables	Thickness of AC layer	in.	6	10	14	8
	Thickness of base layer	in.	4	8	12	8
	Thickness of subbase layer	in.	4	8	12	6
	Modulus of elasticity	psi	Moduli combination for the fall season			
Loading variables	Superload type (parent type)		Balzer1725 (grain cart – IoH)		Two rows of THP/HL (dual-row modular – SHL)	
	Axle weight	lb	15,700	42,700	69,700	65,200: Balzer1725 98,900: two rows of THP/HL
	$\frac{\text{Nucleus segment load}}{\text{road segment weight}}$	-	10	18	26	43: Balzer1725 28: two rows of THP/HL

Source: Koh et al. 2024

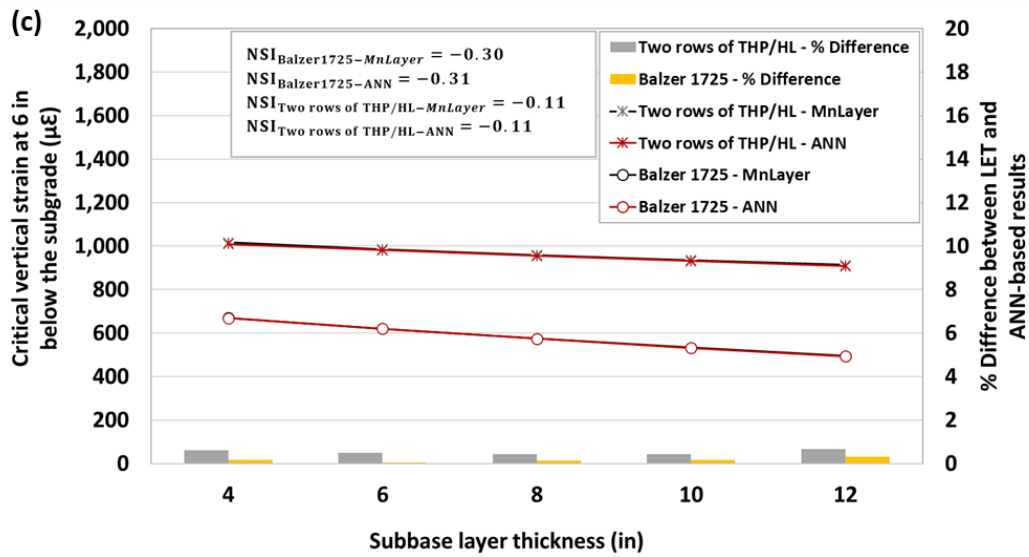
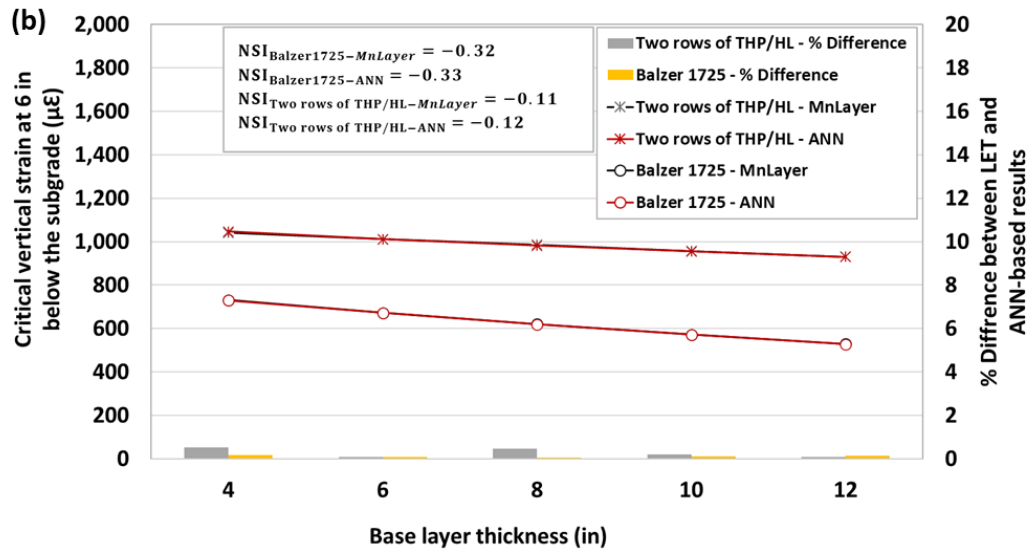
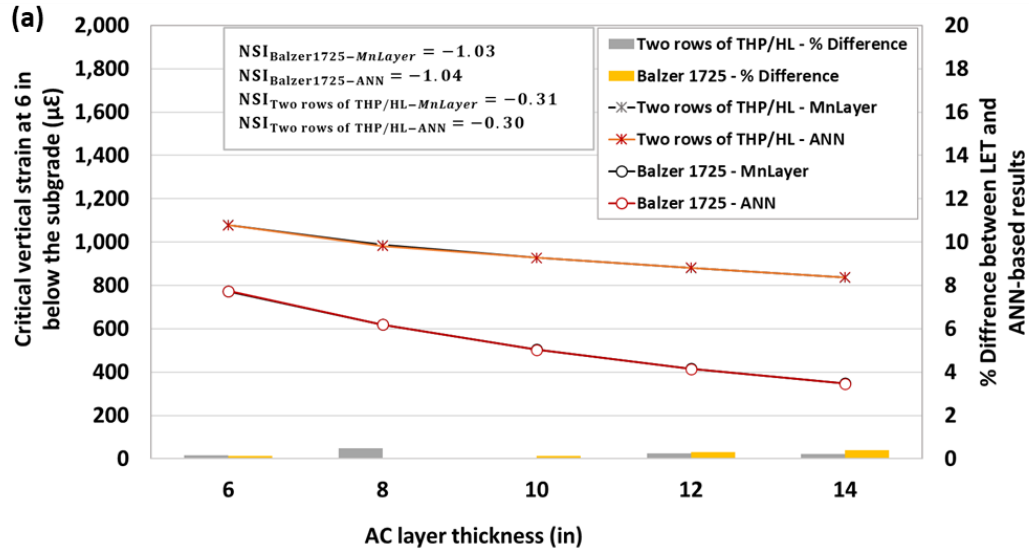
Sensitivity analysis results for the critical tensile strain at the bottom of the AC layer and the critical vertical strain at 6 in. below the top of the subgrade are shown in Figure 45 and Figure 46, respectively.

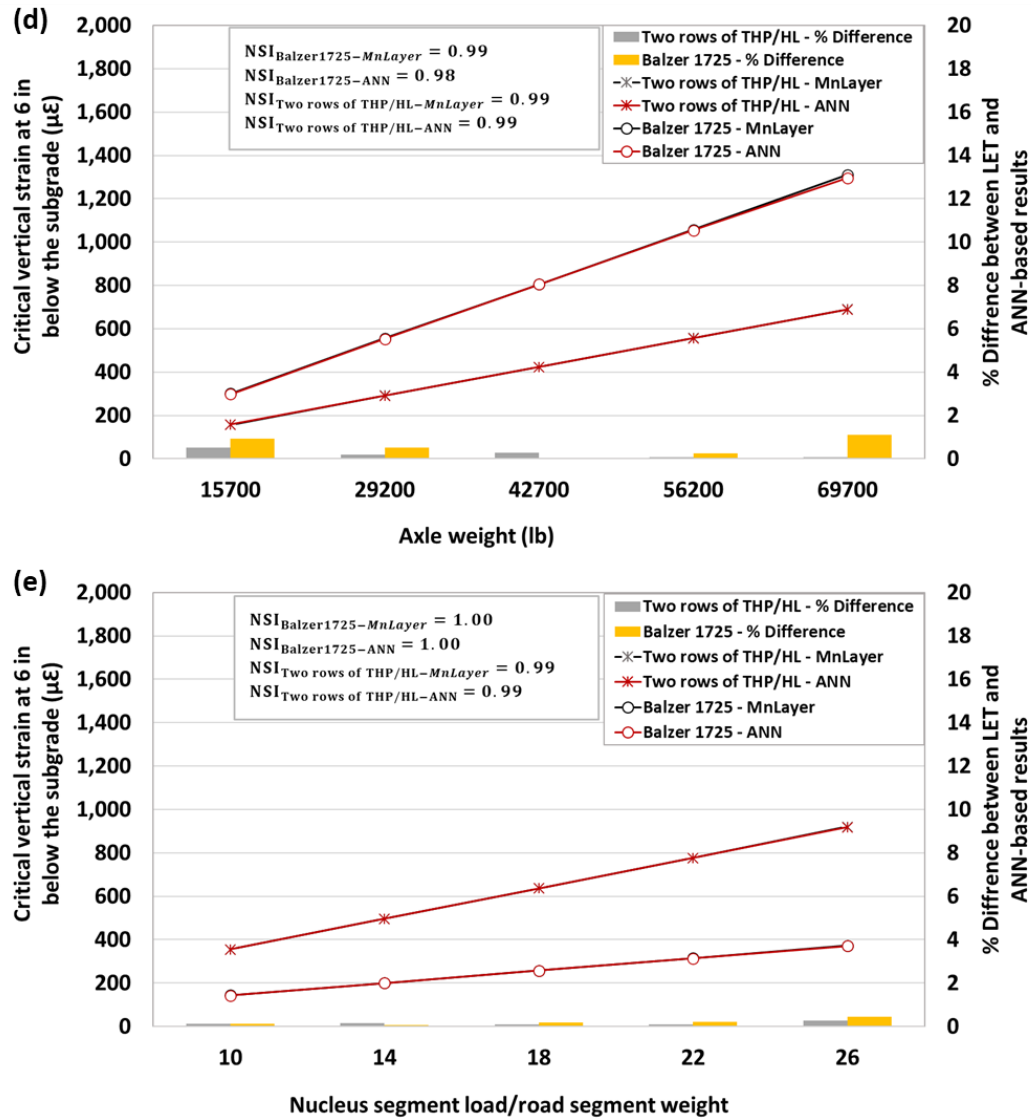




Koh et al. 2024, Reprinted with permission from Elsevier, © 2024

Figure 45. Sensitivity analysis results for the critical tensile strain at the bottom of AC layer when varying the flexible pavement structural variables including (a) AC layer thickness, (b) base layer, and (c) subbase layer, and when varying the loading variables including (d) axle weight and (e) $\frac{\text{Nucleus segment load}}{\text{road segment weight}}$





Koh et al. 2024, Reprinted with permission from Elsevier, © 2024

Figure 46. Sensitivity analysis results for the critical vertical strain at 6 in. below the top of the subgrade when varying the flexible pavement structural variables including (a) AC layer thickness, (b) base layer, and (c) subbase layer, and when varying the loading variables including (d) axle weight and (e) $\frac{\text{Nucleus segment load}}{\text{road segment weight}}$

The magnitudes of critical pavement responses predicted by the ANN models closely align with those derived from MnLayer, exhibiting differences of less than 5%. The NSIs, calculated using equation 14 for each variable, indicate that both critical pavement responses were mostly either very sensitive or sensitive to the AC layer thickness and two loading variables, while sensitive or low sensitive to the base and subbase layer thickness. The sensitivity analysis results for flexible pavements are summarized in Table 22.

Table 22. Summary of sensitivity analysis results for flexible pavements under superloads

Category	Explanatory variables	Critical pavement response type	Balzer1725 (grain cart)		Two rows of THP/HL (dual-row modular)	
			NSI	SL	NSI	SL
Flexible pavement structural variables	Thickness of AC layer	Tensile strain at bottom of AC layer	-0.50	VS	-1.48	VS
		Vertical strain at 6 in. below the top of subgrade	-1.04	VS	-0.30	S
	Thickness of base layer	Tensile strain at bottom of AC layer	-0.19	S	-0.07	LS
		Vertical strain at 6 in. below the top of subgrade	-0.33	S	-0.12	S
	Thickness of subbase layer	Tensile strain at bottom of AC layer	-0.13	S	-0.04	LS
		Vertical strain at 6 in. below the top of subgrade	-0.31	S	-0.11	S
Loading variables	Axle weight	Tensile strain at bottom of AC layer	1.00	VS	1.11	VS
		Vertical strain at 6 in. below the top of subgrade	0.98	VS	0.99	VS
	Nucleus segment load road segment weight	Tensile strain at bottom of AC layer	1.01	VS	0.98	VS
		Vertical strain at 6 in. below the top of subgrade	1.00	VS	0.99	VS

Source: Koh et al. 2024

Summary and Key Findings

This chapter provided mechanistic-based flexible pavement analysis results using LET-based analysis and corresponding flexible pavement damage and LCCA evaluations. The main objectives of this chapter were to (1) characterize the superloads traveling flexible pavement systems, (2) conduct mechanistic-based evaluations of flexible pavement damage, (3) perform LCCA to determine RDACs, and (4) develop AI-based surrogate models tailored to each superload category. Further discussion on each objective is given in the subsequent lists.

- **Characterization of superloads for flexible pavement systems**
 - LET-based analysis using MnLayer was conducted to determine the nucleus segment of each superload as a mechanistic-based loading input.
- **Evaluation of potential flexible pavement damages subjected to superloads**
 - A total of 24,660 LET-based analyses related to damage ratios of total rutting and bottom-up fatigue cracking of various flexible pavement structures under superloads

varying their payload levels from 0% to 100% were performed by applying the nucleus segment of each superload type as a loading input.

- Grain cart IoHs and single-row modular and dual-row modular SHLs caused relatively higher total rutting and bottom-up fatigue cracking in flexible pavements than other superload types at a payload level of 50% or more.
- With respect to the total rutting ratio of flexible pavements, the 50th percentile results of the damage ratio generated by manure tankers, agricultural trailers, and agricultural trucks carrying a 50% payload level reached approximately one or less, while the total rutting ratio from grain carts carrying 50% payload levels still exceeded one, representing higher total rutting than that from a class 9 truck. On the other hand, single-row and dual-row modular SHLs mostly exhibited total rutting ratios higher than those from IoHs, both exceeding one when carrying 50% payload levels or more.
- With respect to bottom-up fatigue damage ratios of flexible pavements, IoHs and SHLs carrying 50% payload levels are still likely to exceed values of 8 and 34 average damage ratios, exceeding even the 400 and 100 values of average damage ratios for single-row modular SHLs and grain carts, respectively, when carrying 100% payload levels.

- **LCCA for flexible pavements under superloads**

- For the flexible pavement performance under superloads exhibiting accumulated bottom-up fatigue cracking that governs flexible pavement performance and life cycle more than total rutting damage in all superload cases, the RDACs due to a single pass of a superload were obtained by performing multivariate LCCA that included multiple factors such as traffic load, pavement structure, material, and treatment type.
- Two types of SHLs, dual-row modular and single-row modular, and grain carts IoHs, as the superloads with relatively high tire weights, yielded the highest RDACs, meaning that the RDACs tend to be highly influenced by the tire weight of the superload. When payload levels were reduced from 100% to 75%, most of the RDACs were reduced by more than 50% for flexible pavements with an 8 in. thick AC layer, an 8 in. thick base layer, and a 6 in. thick subbase layer. RDACs also depend highly on the travel time of superloads made on flexible pavements in addition to the payload level, mainly due to the RSL, discount rate, and pavement service life.
- RDAC results from different flexible structures subjected to superloads show that average RDACs tended to dramatically decrease as the AC layer thickness increases. The reduction rates of average RDACs of flexible pavements under single-row modular SHLs, the most bottom-up fatigue crack-causing superload type, were 66%, 87%, 94%, and 98%, respectively, when the AC layer thickness increased from 6 in. to 8 in., 10 in., 12 in., and 15 in. The material properties of AC, including air voids in the HMA mixture, V_a , and effective asphalt content, V_b , were also chosen as the multivariate LCCA factors, with results confirming that relatively significant RDAC reductions were made in the flexible pavement when both V_a and V_b decreased to 4% and 8%, respectively.
- Four treatment types, including functional rehabilitation, minor structural rehabilitation, major structural rehabilitation, reconstruction, and the corresponding treatment costs per lane-mile, were adopted to estimate the potential appropriate permit fee level of superloads depending on the type of pavement treatment. In the case of a single pass of single-row modular SHLs, transporting a 50% payload level, the PWVs of RDACs can be converted from future reconstruction, major structural rehabilitation, minor structural

rehabilitation, and functional rehabilitation to be \$2,671, \$1,622, \$1,068, and \$839, respectively.

- Since the 100% payload level of each superload in this study was determined from the specifications of transportation capacity of commercial superloads, their tire and axle weights tended to far exceed the state's overweight permit limit. Accordingly, since RDACs under superloads loaded with a 100% payload level may appear more excessive than expected, reference to RDAC results for superloads having 75%, 50%, or lower payload levels is recommended, using engineering judgment in cases where the superload as a target in practice has relatively low tire or axle weight.
- **AI-based prediction model development for flexible pavements under superloads**
 - A total of 35 ANN models based on 7 different parent types of superload and 5 critical pavement response types were developed based on a data matrix consisting of inputs and outputs from MnLayer.
 - Similar to the JPCP cases, the ANN-based prediction models based on the Bayesian Regularization algorithm with architectures optimized with two hidden layers and seven neurons per hidden layer were shown to provide sufficiently high accuracy in predicting critical tensile strain at the bottom of the AC layer and critical vertical strain at the mid-depth of each layer and 6 in. below the top of the subgrade.
 - OAT LSA results indicate that both critical pavement responses were either very sensitive or sensitive to the AC layer thickness and two loading variables, and sensitive or low sensitive to the base and subbase layer thickness.

CHAPTER 6. MECHANISTIC QUANTIFICATION OF SUPERLOAD IMPACTS ON GRANULAR ROADS

To transport substantial loads of heavy agricultural and industrial commodities, a diverse array of transportation vehicles with significant payload capacities routinely uses not only state or interstate highways but also county roads or municipal roads, including granular roads designed for low-volume traffic. IoHs and SHLs, exhibiting relatively slow-moving behavior and featuring vehicle widths that exceed lane-width regulations, often use granular roads designed and constructed for low-volume traffic so as not to interrupt busy highway traffic. The primary objectives of this chapter encompass (1) the quantification of a representative structural distress of granular roads, specifically total rutting, (2) the assessment of total rutting damage-associated treatment costs, and (3) the development of optimized ANN-based models for predicting critical road responses within each layer concerning the total rutting damage of granular roads under diverse superload conditions. These objectives were grounded in the LET-based granular road analysis using MnLayer.

Characterization of Superloads: Nucleus Segment

Methodology

As illustrated in Figure 30 within the flexible pavement chapter, the increase rates of vertical strain at the top of the subgrade according to incremental tire loading, directly beneath the initial tire loading point, were calculated as part of the critical road response type selected for determining nucleus segments. During the identification of nucleus segments, the anticipation of vertical strain overlapping due to multiple tire loads at a specific depth necessitated the selection of a granular road with the thickest layers above the subgrade (specifically, 16 in. of top granular layer). This choice was made to effectively represent the sufficiently overlapped vertical strain at the top of the subgrade, as depicted in Figure 29. The determination of the number of tire loads within a nucleus segment, along both traffic and lane-width directions, involved calculating the incremental tire loads required to achieve a rate of change of less than 5% for vertical strains at the top of the subgrade, precisely beneath the initial loading point for both directions. In conjunction with the nucleus segment approach, a superposition method was again employed for the analysis of granular roads. This method was utilized to streamline computational efforts when applying superload loading inputs, as illustrated in Figure 31.

Nucleus Segments of Superloads

The number of tire loads in a nucleus segment along both traffic and lane-width directions for every superload type were derived and summarized in Table 23. Note that superloads carrying a payload at a 100% level were employed for the determination of nucleus segments, and the nucleus segment with the largest number of tire loads between the nucleus segments derived over four seasons was conservatively chosen and is listed in Table 23.

Table 23. Number of tire loads in a nucleus segment of different superload types

Name of IoH	No. of tires in nucleus segment (lane-width, traffic)	Name of SHL	No. of tires in nucleus segment (lane-width, traffic)
Kinze 1051	(1, 1)	Goldhofer THP/SL-S	(4, 1)
Kinze 1305 flotation	(1, 1)	Goldhofer THP/ET	(4, 1)
Kinze 1305 row crop	(4, 1)	Goldhofer PST/ES-E	(4, 1)
Balzer 1725	(1, 1)	Goldhofer THP/UT	(5, 1)
Balzer 2550	(1, 1)	Goldhofer THP/SL-L	(8, 1)
J&M 1151	(1, 1)	Goldhofer THP/HL-L	(8, 1)
GEA EL48-4D 4350	(1, 1)	Goldhofer THP/SL	(8, 1)
GEA EL48-6D 6100	(1, 1)	Goldhofer THP/HL	(8, 1)
GEA EL48-8D 7900	(1, 1)	Two rows of Goldhofer THP/SL-S	(1, 1)
Balzer 6800 magnum	(1, 1)	Two rows of Goldhofer PST/ES-E	(1, 1)
Balzer 9500 magnum	(1, 1)	Two rows of Goldhofer THP/UT	(4, 1)
NUHN QT Quad Tanks	(1, 1)	Two rows of Goldhofer THP/HL	(8, 1)
J&M 555 wagon	(1, 1)	Goldhofer THP/HL + outrigger	(4, 1)
J&M 755 wagon	(1, 1)	Kalyn Siebert 13 Axle Trailer	(2, 1)
Terragator 2505	(1, 1) from front axle	Guy M. Turner dual lane 200 ton	(4, 1)
Terragator TG7300C	(1, 1) from front axle	Guy M. Turner 19 Axle trailer 125 ton	(3, 1)
Terragator TG8400C	(1, 1)		
Case 340B	(1, 1)		

Source: Koh et al. 2023a

As a result, given that the counts of tire loads within nucleus segments for all superloads on granular roads, as detailed in Table 23, were observed to be equal to or less than those for flexible pavements listed in Table 17, a conservative decision was made to adopt the nucleus segments derived from flexible pavement cases as the mechanistic loading inputs for superloads applied to granular road systems.

Mechanistic Analysis for Potential Damage Evaluation: LET-Based Analysis

Methodology

An extensive examination of LET-based granular road analysis was conducted to evaluate potential rutting damage across various superload scenarios. The MnLayer software was once

again utilized to acquire critical vertical strains at the mid-depth of the top granular layer and 6 in. below the top of the subgrade that are correlated with total rutting. Nucleus segments, as specified in Table 17, were systematically employed as mechanistic loading inputs in the LET-based analysis models, which were developed in accordance with the numerical investigation matrix outlined in Table 24.

Table 24. Comprehensive analysis matrix for LET-based granular road analysis

Number of layers (type of layer)		
2 (granular layer, subgrade)		
Thickness (in.)		
Granular layer	6, 8, 10, 12, 14, 16	
Modulus of elasticity (psi)		
Season	Granular layer	Subgrade
Spring	30,000	5,000
Fall	70,000	10,000
Summer	70,000	10,000
Winter	100,000	17,000
Poisson's ratio: 0.35		
Traffic loadings		
IoH: 18 types × 4 payload levels = 72 types		
SHL: 16 types × 4 payload levels = 64 types		
FHWA class 9 truck (reference): 1 type		
Total analysis cases: 3,288 cases		

Source: Koh et al. 2023a

The damage ratio concept was once again employed to quantify the total rutting damages of granular roads under superloads. Transfer functions for both unbound layers and foundation soil, as outlined in the MEPDG (AASHTO 2015) and the latest version of AASHTOWare Pavement ME Design software (2.6.2) (AASHTO 2022), were used for the calculation of permanent and plastic deformation at the mid-depth of the top granular layer and 6 in. below the top of the subgrade, as presented in equation 21. The total permanent vertical deformation resulting from the passage of a superload was determined by combining all plastic deformations from each layer and comparing the total to that induced by a class 9 truck to calculate the damage ratio. Similar to the flexible pavement cases, the water content for granular material and fine-grained material was selected to be 10% and 15.7%, respectively, based on Iowa local data (Cetin et al. 2019, Ceylan et al. 2009).

$$\Delta_{p(soil)} = \beta_{s1} k_{s1} \varepsilon_v h_{soil} \left(\frac{\varepsilon_0}{\varepsilon_r} \right) e^{-\left(\frac{\rho}{n} \right)^\beta} \quad (21-1)$$

$$\log \beta = -0.61119 - 0.017638 W_c \quad (21-2)$$

$$\rho = 10^9 \left(\frac{C_0}{(1 - (10^9)^\beta)} \right)^{\frac{1}{\beta}} \quad (21-3)$$

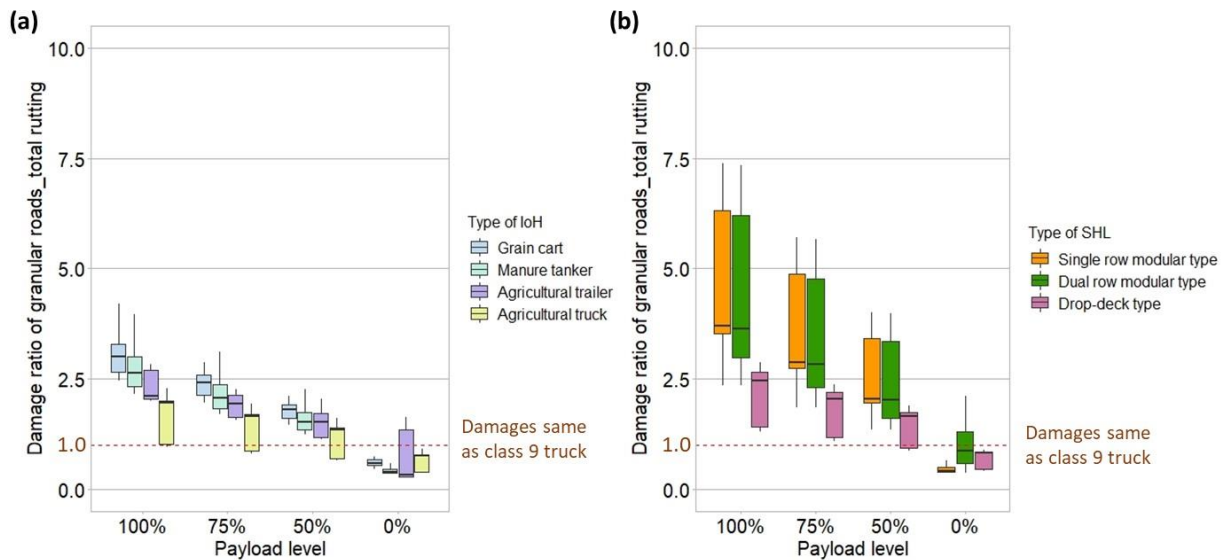
$$C_0 = \ln\left(\frac{a_1 M_r^{b_1}}{a_9 M_r^{b_9}}\right) \quad (21-4)$$

$$\frac{\varepsilon_0}{\varepsilon_r} = \frac{\left(e^{(\rho)^\beta} \times a_1 E_r^{b_1}\right) + \left(e^{\left(\frac{\rho}{10^9}\right)^\beta} \times a_9 E_r^{b_9}\right)}{2} \quad (21-5)$$

where $\Delta_{p(soil)}$ is the permanent or plastic deformation for the layer/sublayer, in.; n is the number of axle-load repetitions; ε_0 is the intercept determined from repeated load permanent deformation laboratory tests, in./in.; ε_r is the resilient strain imposed in laboratory tests to obtain material properties ε_0 , β , and ρ , in./in.; ε_v is the average vertical resilient or the elastic strain in the layer/sublayer and calculated by the structural response model, in./in.; h_{soil} is the thickness of the unbound layer/sublayer, in.; k_{s1} is the global calibration coefficient ($k_{s1} = 1.673$ for granular materials and 1.35 for fine-grained materials from the MEPDG; $k_{s1} = 0.965$ for granular materials and 0.675 for fine-grained materials from AASHTOWare Pavement ME Design software); β_{s1} is the local calibration constant for the rutting in the unbound layers (1.0 for the global calibration); W_c is the water content, %; M_r is the resilient modulus of the unbound layer or sublayer, psi; a_1 and a_9 are the regression constants ($a_1 = 0.15$, $a_9 = 20.0$), and b_1 and b_9 are the regression constants ($b_1 = 0.0$, $b_9 = 0.0$).

Damage Ratio Analysis

Figure 47 and Table 25 present a comprehensive set of 3,288 LET-based analysis results, depicting the total rutting ratio of granular roads under various superload types and payload levels. In instances where payload levels equal or exceed 50%, most types of SHLs and IoHs exhibit a greater potential for inducing total rutting compared to FHWA class 9 trucks, across both transfer function applications. Notably, grain carts as an IoH and single-row modular and dual-row modular as SHLs demonstrate a higher potential to generate significant total rutting than other superload types, even exceeding 3.1, 4.6, and 4.5 of averaged total rutting ratios, respectively, when carrying a 100% of payload level. A significant reduction in the total rutting ratio, approaching one, was observed when the payload level for both IoHs and SHLs is decreased from 100% to 50%.



Koh et al. 2023a, Reprinted with permission from Sage Publications, Inc., © 2023

Figure 47. Linear graphs for total rutting ratio of granular roads under (a) IoHs and (b) SHLs

Table 25. Averaged damage ratios of granular roads under superloads

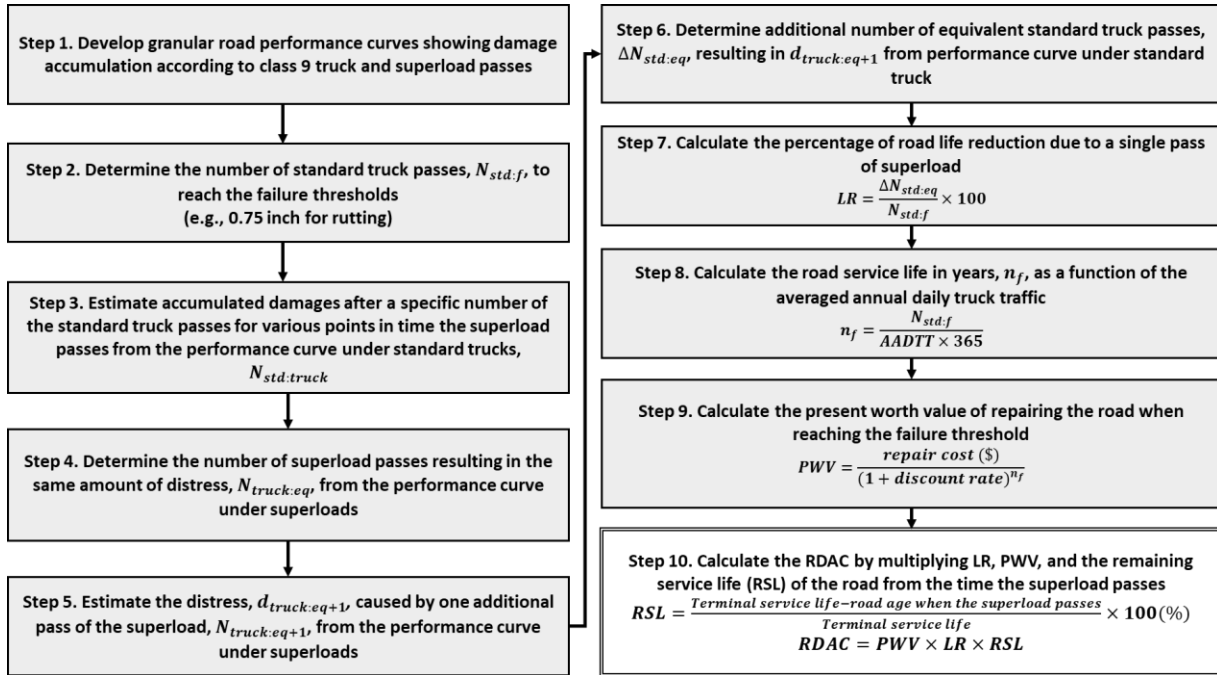
Reference	Payload level		100% payload	75% payload	50% payload	0% payload
Transfer functions from MEPDG	Total rutting ratio	IoH – 18 types (critical type)	2.6 (Grain cart: 3.1)	2.1 (Grain cart: 2.5)	1.6 (Grain cart: 1.9)	0.6 (Agricultural trailer: 0.7)
		SHL – 16 types (critical type)	4.1 (Single-row modular: 4.6)	3.2 (Single-row modular: 3.5)	2.3 (Single-row modular: 2.5)	0.7 (Dual-row modular: 1.0)
Transfer functions from AASHTO Ware Pavement ME software, ver. 2.6.2	Total rutting ratio	IoH – 18 types (critical type)	2.6 (Grain cart: 3.1)	2.1 (Grain cart: 2.5)	1.6 (Grain cart: 1.9)	0.6 (Agricultural trailer: 0.7)
		SHL – 16 types (critical type)	4.2 (Single-row modular: 4.7)	3.3 (Single-row modular: 3.6)	2.3 (Single-row modular: 2.6)	0.7 (Dual-row modular: 1.0)

Source: Koh et al. 2023a

LCCA for Mechanistic-Based RSL and Permit Fee Decision

Methodology

The RDACs related to the total rutting of granular roads under diverse superload types and payload levels were calculated utilizing methodologies consistent with those employed for JPCP and flexible pavement systems. Figure 48 delineates the procedure steps and provides detailed explanations elucidating the process of determining the RDAC for a granular road subjected to a single pass of a superload. Multivariate RDACs, varying with road structure, traffic load, and treatment type, were intensively calculated to establish a mechanistic foundation for determining permit fees associated with each type of superload. It is noteworthy that, while the maintenance period for granular roads can be decided based on the failure threshold related to total rutting, practical maintenance practices for granular roads, such as grading, soil stabilization, and dust control, have traditionally been conducted on an annual basis under the direction of a county engineer (FHWA 2015, Skorseth and Selim 2000).



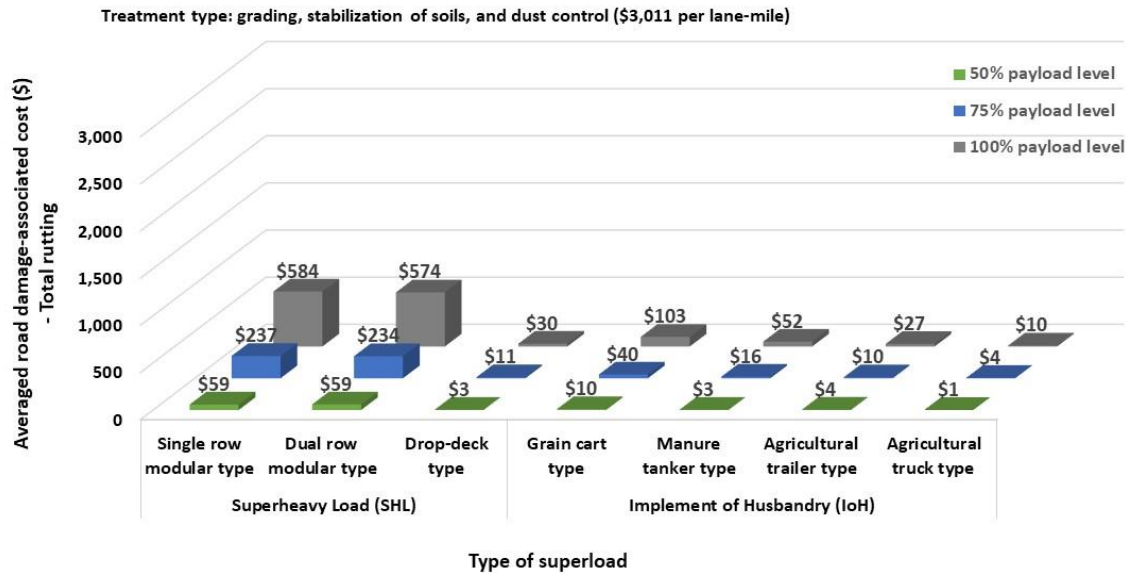
Koh et al. 2023a, Reprinted with permission from Sage Publications, Inc., © 2023

Figure 48. Detailed steps for LCCA to determine RDAC of granular road under superload

Multivariate LCCA Results: RDAC Assessment

Multivariate RDAC Assessment Case I. RDAC According to Traffic Loading

Similar to the RDAC results observed in flexible pavement cases, granular roads featuring an 8 in. thick top granular layer subjected to single-row modular SHLs exhibited the highest RDACs. Following were dual-row modular SHLs and grain carts, as illustrated in Figure 49.

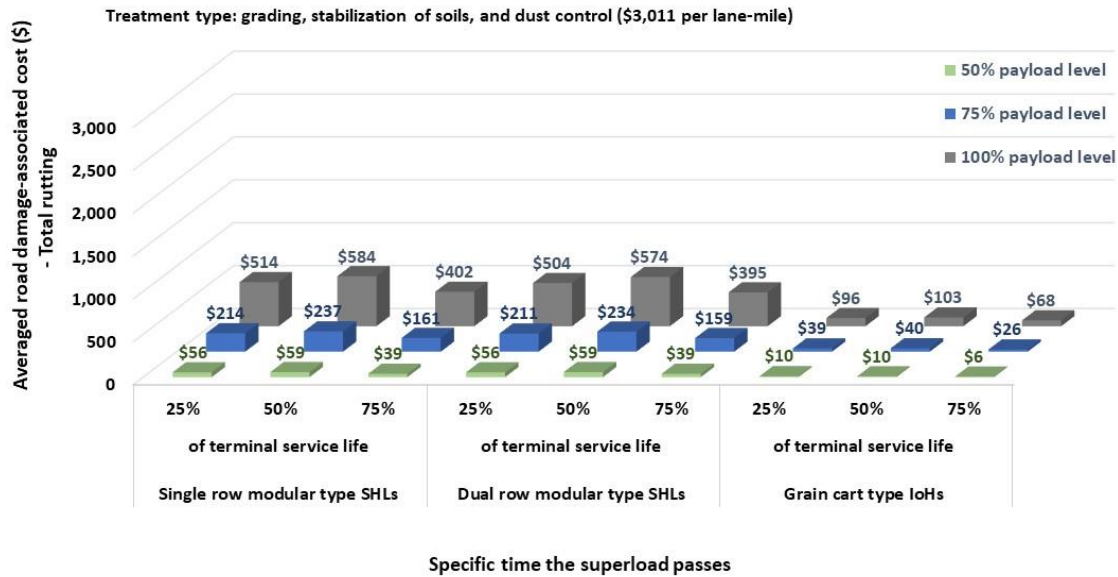


Koh et al. 2023a, Reprinted with permission from Sage Publications, Inc., © 2023

Figure 49. RDACs related to the total rutting due to a single pass of superload traveling at 50% of terminal service life of granular road

For RDAC calculation, a treatment cost per lane-mile representing the annual maintenance cost converted from the six-year-based gravel road maintenance costs ($\$18,065/6 = \$3,011$) was chosen, following a suggestion from the *Gravel Roads Construction and Maintenance Guide* (FHWA 2015, Skorseth and Selim 2000). As a result of the LCCA, using the nucleus segment approach, RDACs concerning total rutting displayed a proportional relationship to the tire weight of the superload. RDAC values exhibited a reduction of more than half when the superload payload level was decreased from 100% to 75%. Specifically, the potential RDACs stemming from single-row modular SHLs decreased significantly by 59% and 90% when the payload levels were reduced from 100% to 75% and from 100% to 50%, respectively.

Examining the relationship between RDAC and the travel time of superloads, as depicted in Figure 50, RDAC values with respect to the varying travel time of superloads on granular roads with an 8 in. thick top granular layer did not demonstrate the same proportionality observed in flexible pavement cases. This disparity is attributed to the distinct performance curve shapes for total rutting of granular roads, characterized by a logarithmic curve, in contrast to the bottom-up fatigue cracking of flexible pavements, which exhibits an exponential curve. Analyzing the logarithmic performance curves for total rutting of granular roads under superloads and a general class 9 truck, it was observed that relatively higher RDACs were derived at 50% of the terminal service life, with the highest accumulated total rutting difference between the general class 9 truck and superloads identified at approximately 50% of the terminal service life.

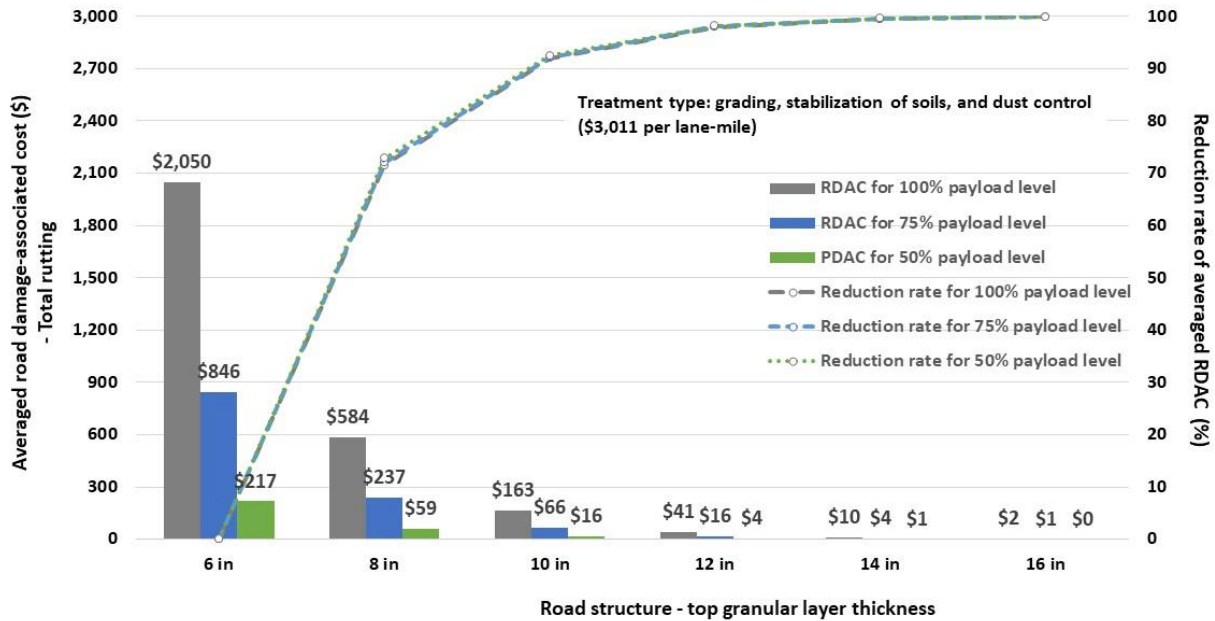


Koh et al. 2023a, Reprinted with permission from Sage Publications, Inc., © 2023

Figure 50. RDACs related to the total rutting due to a single pass of the three most damage-causing types of superload traveling at a varying time on granular road

Multivariate RDAC Assessment Case II. RDAC According to Granular Road Structures

To assess the impact of road structure on RDAC values, the reduction rate of RDACs with respect to the top granular layer thickness as a main structural factor was determined. Figure 51 shows the reduction rate of RDACs as the top granular layer thickness increases, focusing on a single pass of the single-row modular SHL, which produced the highest RDAC for total rutting of granular roads. The reduction rates of averaged RDACs remained consistent across three different payload levels, calculated as 72%, 92%, 98%, 99.5%, and 99.9%, respectively, as the top granular layer thickness increased from 6 in. to 8 in., 10 in., 12 in., 14 in., and 16 in. Note that the reduction rate of averaged RDAC for each road structure was calculated relative to a granular road with a 6 in. thick top granular layer as the reference road structure. Remarkably, granular roads with a sufficiently thick top granular layer, possibly 14 in. or more, generated RDACs close to \$0 even when subjected to a critical superload type.



Koh et al. 2023a, Reprinted with permission from Sage Publications, Inc., © 2023

Figure 51. RDACs related to the total rutting due to a single pass of single-row modular SHL traveling at 50% of terminal service life of road structures with different top granular layer thickness

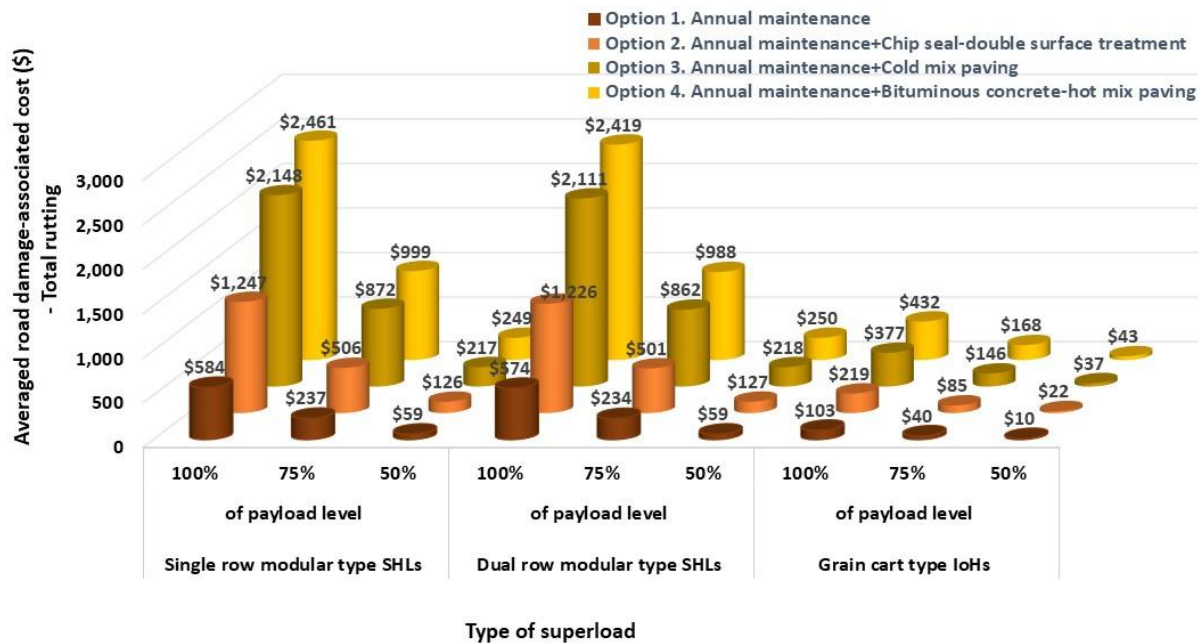
Multivariate RDAC Assessment Case III. RDAC According to Treatment Types for Conversion to Asphalt-Surfaced Pavements

A total of four options, including one dealing only with annual maintenance cost and three having different future paving options after six years of maintenance, converted into one-year-based paving costs combined with annual maintenance cost suggested by the *Gravel Roads Construction and Maintenance Guide* (FHWA 2015, Skorseth and Selim 2000), were set to be annual treatment costs to be applied to the RDAC calculation for this study as follows:

- Option 1. Annual maintenance cost: total annual treatment cost = $\$18,065/6 = \$3,011$
- Option 2. Annual maintenance cost + chip seal-double surface treatment: total annual treatment cost = $\$18,065/6$ (annual maintenance cost) + $\$20,533/6$ (one-year-based paving cost) = $\$6,433$
- Option 3. Annual maintenance cost + cold mix: total annual treatment cost = $\$18,065/6$ (annual maintenance cost) + $\$48,390/6$ (one-year-based paving cost) = $\$11,076$
- Option 4. Annual maintenance cost + bituminous concrete-hot mix: total annual treatment cost = $\$18,065/6$ (annual maintenance cost) + $\$58,080/6$ (one-year-based paving cost) = $\$12,691$

In Figure 52, RDAC results are presented for various treatment types applied to granular roads featuring an 8 in. thick top granular layer, specifically addressing the three superload types that cause the most total rutting. A single pass of single-row modular SHLs or dual-row modular

SHLs transporting a 50% payload level, for example, exhibited a high potential for inducing RDACs of around \$249, \$217, \$126, and \$59, derived from the treatments designated as option 4, option 3, option 2, and option 1, respectively.



Koh et al. 2023a, Reprinted with permission from Sage Publications, Inc., © 2023

Figure 52. RDACs of granular road for different treatment types and payload levels due to a single pass of the three most total rutting-causing types of superload

Development of AI-Based Prediction Models

Methodology

This section presents the development and optimization of ANN-based models designed to predict critical road responses related to total rutting of granular roads. Specifically, the models focus on critical vertical strains at the mid-depth of the top granular layer and 6 in. below the top of the subgrade of granular roads under a single pass of various superloads. The development process utilized an LET-based granular road analysis database compiled from previous sections of this chapter, covering various nucleus segments and payload levels associated with different superload types. Figure 53 provides a schematic representation outlining the primary steps involved in ANN modeling for granular roads under superloads.

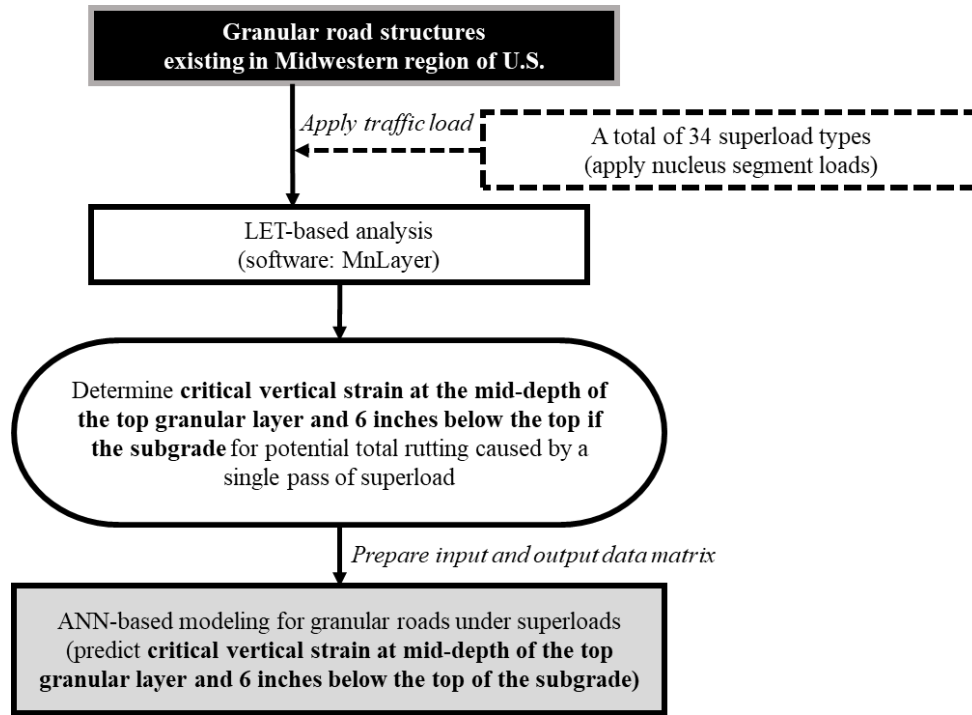


Figure 53. Overall steps for ANN modeling for granular roads under different superloads

Note that in the above figure, the gray-colored box indicates the main step of this chapter.

A database was prepared including the inputs and outputs of LET-based granular road analysis to develop ANN-based models. This database adheres to the experimental matrix outlined in Table 24, encompassing all necessary inputs and outputs extracted from the MnLayer software. This organized data matrix serves as the fundamental basis for the development and optimization of ANN models. The incorporation of diverse superload types and payload levels ensures a thorough examination of scenarios involving total rutting damage in granular roads under various superloads.

The same set of five backpropagation algorithms, viz., Levenberg-Marquardt (Levenberg 1944, Marquardt 1963), Bayesian Regularization (MacKay 1992), BFGS Quasi-Newton (Broyden 1970a, Broyden 1970b, Fletcher 1970, Goldfarb 1970, Shanno 1970), Resilient Backpropagation (Riedmiller and Braun 1993), and Scaled Conjugate Gradient (Johansson et al. 1991), previously applied to ANN models for JPCPs and flexible pavements, was again employed in the development of ANN-based models for granular roads under superloads. The architectures of ANN models were also optimized by adjusting the number of hidden layers and neurons per hidden layer. Separate ANN models were developed and optimized based on different critical road response and superload types, corresponding to the seven parent class types listed in Table 4 and Table 5. To ensure reliable prediction evaluation of the ANN models, a 10-fold cross-validation technique was implemented and the coefficient of determination, R^2 , AAE, and RMSE were used as the evaluation metrics.

Development of ANN-Based Surrogate Models

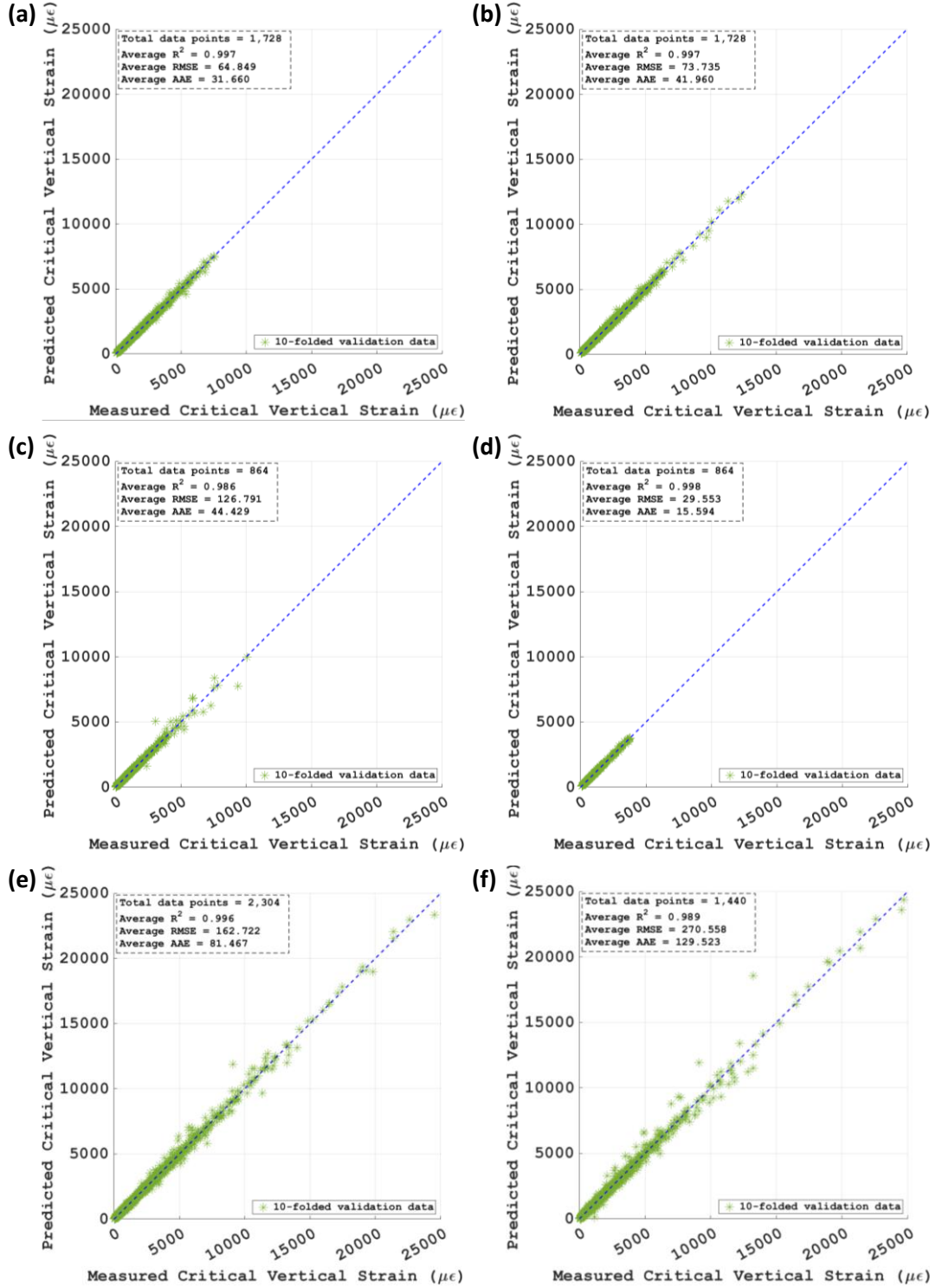
In Table 26, detailed information regarding the multilayer ANN modeling for granular roads under superloads is outlined, including the database from the comprehensive LET-based granular road analysis. The nondimensional variable, denoted as the nucleus segment load/road segment weight described in the previous equation 20, is also used as one of explanatory variables like with the ANN models for flexible pavements.

Table 26. Details of multilayer ANN modeling for granular roads under superloads

Multilayer ANN models for granular roads under superloads			
Explanatory variables	(1) Independent variables: Thickness of top layer, modulus of elasticity of top layer and subgrade, axle weight, tire pressure (2) Nondimensional variables: Nucleus segment load/road segment weight		
Target variables	(1) Critical vertical strain at the mid-depth of the top granular layer (2) Critical vertical strain at 6 in. below the top of the subgrade		
ANN algorithms	(1) Levenberg-Marquardt, (2) Bayesian Regularization, (3) BFGS Quasi-Newton, (4) Resilient Backpropagation, and (5) Scaled Conjugate Gradient		
Learning rate	0.005		
Distribution function	Gaussian distribution	Distribution function	Hyperbolic tangent
No. of hidden layers	1 to 3	No. of hidden layers	2 to 6

Performance Evaluation and Architecture Optimization of ANN-Based Surrogate Models

A total of 14 ANN models were developed and optimized, aligning with 7 parent types of superloads and 2 target variables for granular roads. As illustrative instances, Figure 54 showcases Bayesian Regularization algorithm-based ANN models featuring two hidden layers and six neurons per hidden layer, predicting the critical vertical strain at 6 in. below the top of the subgrade during a single pass of diverse superload types. Remarkably, all seven ANN models exhibited R^2 values greater than 0.98, RMSE values equal to or less than 270, and AAE values less than 130, indicating exceptional prediction accuracies.



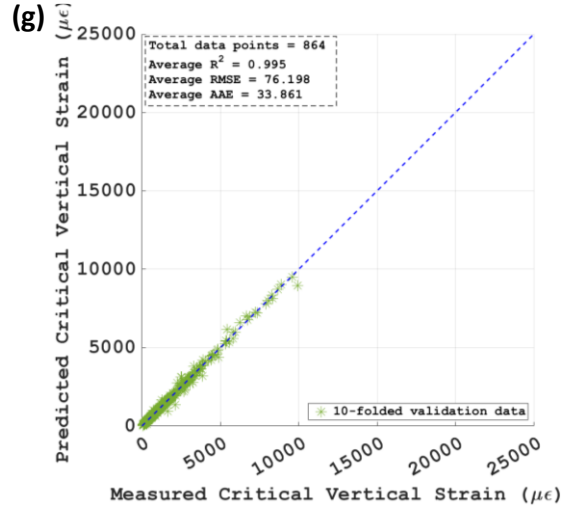


Figure 54. ANN model performances predicting the critical vertical strain at 150 mm below the top of the subgrade when subjected to IoHs including (a) grain carts, (b) manure tankers, (c) agricultural trailers, and (d) agricultural trucks, and when subjected to SHLs including (e) single-row modular, (f) dual-row modular, and (g) drop-deck types

The accuracy of predicting the critical vertical strain at 6 in. below the top of the subgrade, presented as R^2 values, from various backpropagation algorithm-based ANN models with two hidden layers and six neurons per hidden layer was derived, as shown in Figure 55.

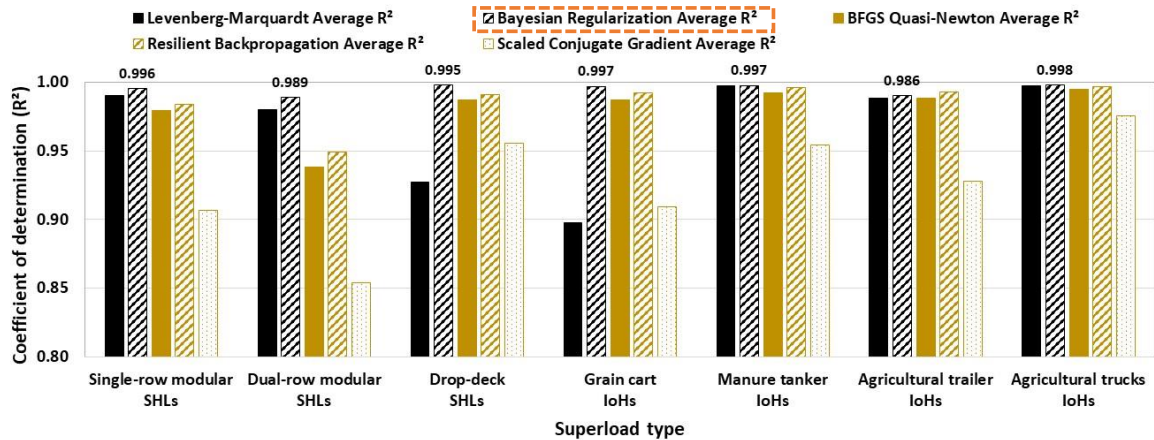


Figure 55. Performance evaluation of ANN models constructed with two hidden layers, six neurons per each hidden layer, and five backpropagation algorithms when predicting critical vertical strain at 6 in. below the top of the subgrade

The Bayesian Regularization algorithm-based ANN models provided the highest precision accuracies among the five algorithms, similar to the JPCP and flexible pavement cases. Then, the ANN model architectures, constructed with a Bayesian Regularization algorithm to predict critical vertical strain at the mid-depth of the top granular layer and 6 in. below the top of the subgrade, were optimized in terms of the number of hidden layers and corresponding neurons.

Consequently, it can be roughly confirmed from Figure 56 that two hidden layers and six neurons per hidden layer were enough to provide high prediction accuracies, in which the R^2 values were derived to be more than 0.99 for both road response types. Note that, for the critical vertical strain at the mid-depth of the top granular layer, the identical set of five backpropagation algorithms was employed as in the case of 6 in. below the top of the subgrade, confirming that the Bayesian Regularization algorithm consistently demonstrated the highest predictive accuracy for each superload parent type.

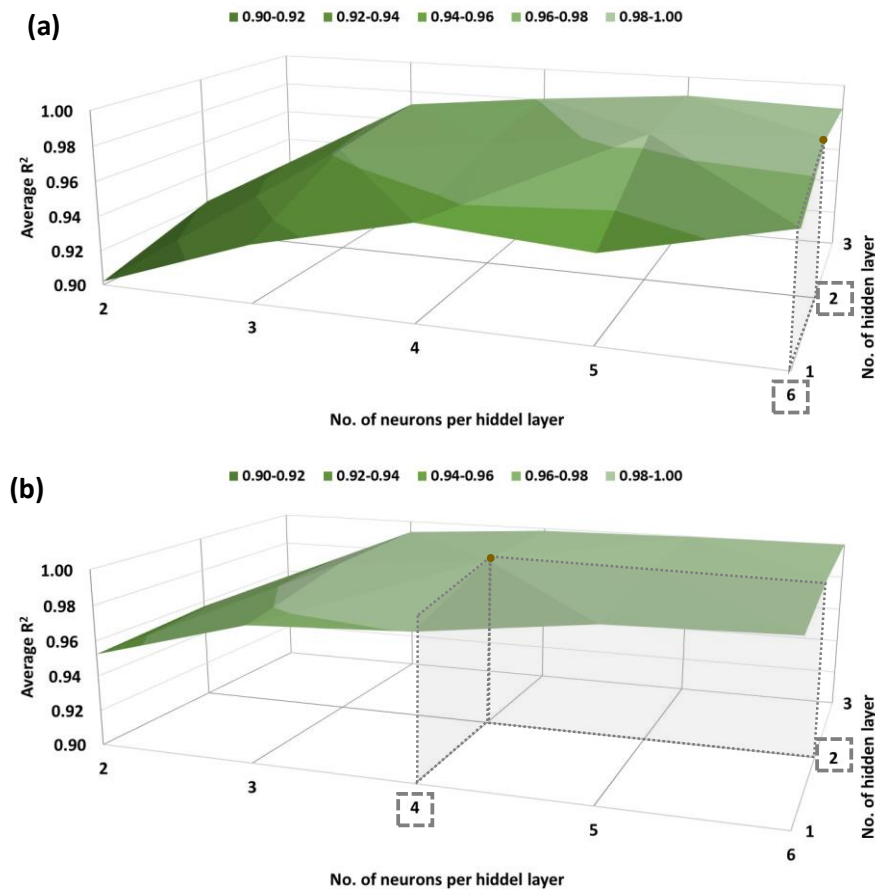


Figure 56. Architecture optimization of ANN models for dual-row modular SHL case constructed with the Bayesian Regularization algorithm when predicting critical vertical strain at (a) 6 in. below the top of the subgrade and (b) mid-depth of the top granular layer

Summary and Key Findings

This chapter provided mechanistic-based granular road analysis results using LET-based analysis and corresponding total rutting damage and LCCA evaluations. The main objectives of this chapter were to (1) characterize the superloads traveling granular road systems, (2) conduct mechanistic-based evaluations of total rutting damage, (3) perform LCCA to determine the RDAC, and (4) develop AI-based surrogate models tailored to each superload category. Further discussion on each objective is given in the subsequent lists.

- **Characterization of superloads for granular road systems**
 - LET-based analysis using MnLayer was conducted to determine the nucleus segment of each superload traveling on granular road systems as a mechanistic-based loading input.
 - Considering that the tire load counts within nucleus segments for all superloads on granular roads were found to be equal to or less than those for flexible pavements, a conservative decision was made to utilize the nucleus segments derived from flexible pavement cases as the mechanistic loading inputs for superloads applied to granular road systems.
- **Evaluation of potential total rutting damage of granular roads subjected to superloads**
 - A total of 3,288 LET-based analyses related to the total rutting ratio of various granular road structures under superloads while varying their payload levels from 0% to 100% were also performed by applying the nucleus segment of each superload type as a loading input.
 - A single pass of grain carts among IoHs and single-row modular and dual-row modular among SHLs are likely to generate greater total rutting than other superload types, even exceeding 3.1, 4.6, and 4.5 of averaged total rutting ratios, respectively, when carrying 100% payload levels. When the payload levels of all types of superloads were reduced from 100% to 50%, significant reductions in the total rutting ratio, reaching approximately one, were made, meaning they produced similar total rutting to a general class 9 truck.
- **LCCA for granular roads under superloads**
 - From granular road performance under superloads showing accumulated total rutting, a main structural distress type of granular roads, RDACs due to a single superload pass were obtained by performing multivariate LCCA using multiple factors such as traffic load, granular road structure, and treatment type.
 - A single pass of a single-row modular SHLs exhibited the highest RDAC for granular roads having an 8 in. thick top granular layer, followed by dual-row modular SHLs and grain carts, showing that, using the nucleus segment approach, RDACs related to total rutting also tended to be proportional to the tire weight of the superload. When the superload payload levels were reduced from 100% to 75%, the RDACs were reduced by more than half. The highest potential RDACs from single-row modular SHLs decreased significantly by 59% and 90% when the payload levels were lowered from 100% to 75% and from 100% to 50%, respectively. With respect to the relationship between the superload travel time and RDAC, it was confirmed from logarithmic performance curves that relatively higher RDACs were derived when the superloads traveled at approximately 50% of terminal road service life, where the largest difference between accumulated total rutting between superloads and general class 9 trucks occurred at 50% of terminal service life.
 - The RDAC results for the various granular road structures subjected to superloads show that average RDACs tended to decrease significantly with increasing the thickness of the top granular layer. The reduction rates of averaged RDACs of granular roads under a single pass of single-row modular SHLs were calculated to be 72%, 92%, 98%, 99.5%, and 99.9%, respectively, when the top granular layer thickness increased from 6 in. to 8 in., 10 in., 12 in., 14 in., and 16 in. When the top granular layer thickness was increased

by up to 14 in. or more, RDACs neared \$0 even when subjected to the most total rutting-causing SHL.

- Four treatment options were considered in determining annual treatment costs for RDAC calculation, including the first option dealing only with annual maintenance cost, and three other options having annual maintenance cost combined with one-year-based paving options after six years of maintenance, including chip seal-double surface treatment, cold mix, and bituminous concrete-hot mix. In the case of a single pass of a single-row modular or dual-row modular SHL transporting a 50% payload level, the PWVs of RDACs were derived from the four treatment options to be \$59, \$126, \$217, and \$249, respectively.
 - As noted from the previous chapters, since the RDACs under superloads carrying a 100% payload level may appear much higher than expected, engineering judgment is needed to properly refer to LCCA results from this study. Note that this study only deals with the structural distress in calculating the RDAC, so higher RDACs can be derived when considering functional distress, such as loose aggregate or washboarding, which may govern the terminal service lives of granular roads.
- **AI-based prediction model development for granular roads under superloads**
 - A total of 14 ANN-based surrogate models for predicting critical road responses for granular roads under various superload types were developed and optimized. These models demonstrated exceptional predictive accuracies. Bayesian Regularization algorithm-based ANN models were found to achieve the highest prediction accuracies among the five backpropagation algorithms tested. Furthermore, optimization of the ANN architectures revealed that two hidden layers, each with six neurons, can deliver sufficiently high prediction accuracies for both types of critical road responses.
 - These findings pave the way for more informed decision-making in granular road design and maintenance, particularly when dealing with superload traffic. The ANN models developed in this study provide sufficient potential to be employed in granular road design software such as AASHTOWare Pavement ME Design in the future.

CHAPTER 7. FORENSIC INVESTIGATION OF IOWA COUNTY ROADS AND HIGHWAYS

Mechanistic-based pavement and granular road analysis results employing FEM and LET approaches necessitate data validation through in situ field data collection and analysis. This can be achieved by installing data acquisition systems at pavement or granular road systems with structures similar to those employed for computational analysis in the preceding chapters. To identify road sections suitable for instrumentation with data acquisition systems and ensure alignment with the road structures addressed in computational analyses, forensic investigations were conducted at various Iowa locations. These investigations encompassed a total of 18 road sections, including AC-surfaced pavements, PCC-surfaced pavements, and granular roads, as detailed in Table 27. The specific items of the forensic investigation are outlined in the same table, providing essential information for determining the JPCP, full-depth flexible pavement, and granular road selected for field instrumentation. Note that the necessary components of forensic investigation from the FHWA's distress identification manual (Miller and Bellinger 2014) and the *Gravel Pavement Surface Evaluation and Rating (PASER) Manual* (Walker 2002) were employed. Further details on the field instrumentation activities will be given in the subsequent section.

Table 27. Items and locations for forensic investigations

Investigation items	
(1) Geographical coordinates, (2) traffic volume and vehicle types, (3) design features of road section, (4) surface and subsurface conditions, (5) topography, (6) presence of a permanent WIM system near the road section, and (7) availability of external power sources	
Location	Road type (name of the road section)
Union County	(1) One AC-surfaced pavement section (Rea Road) (2) Two PCC-surfaced pavement sections (Cherry and North Osage streets) (3) One granular road section (Osage Street)
Keokuk County	(1) One PCC-surfaced pavement section (170th Street) (2) One granular road section (120th Avenue)
Monona County	(1) Two AC-surfaced pavement sections (K45 and E60) (2) One PCC-surfaced pavement section (E60) (3) Four granular road sections (Filbert Avenue, 295th Street, Linden Avenue, and 133rd Street)
Tama County	(1) One AC-surfaced pavement section (V18) (2) Four granular road sections (190th, 200th, 220th, and 240th streets)
Total	18 sites (4 AC-surfaced pavement sections, 4 PCC-surfaced pavement sections, and 10 granular road sections)

Forensic Investigation for Potential Instrumentation Sites

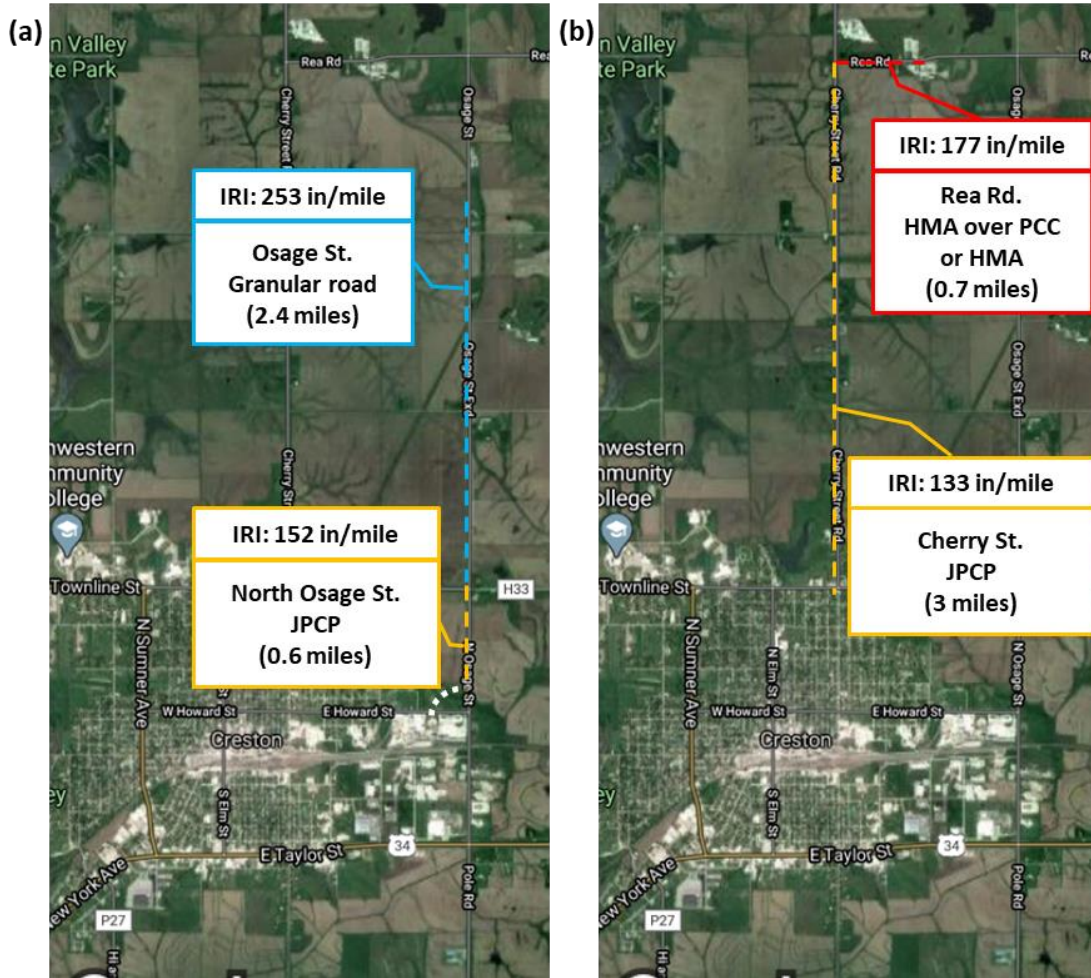
Forensic Investigation in Union County

The forensic investigation took place, from May 7 to 9, 2020, on Osage Street (granular road) and North Osage Street (PCC-surfaced pavement), which share a continuous route, as well as Rea Road (AC-surfaced pavement) and Cherry Street (PCC-surfaced pavement), sharing another continuous route in Union County, Iowa. Thorough identification of topography, distress, design features, and daily traffic was conducted, accompanied by the measurement of the international roughness index (IRI) for each road section utilizing a high-speed profiler (SSI, Inc. 2023), as shown in Figure 57.



Figure 57. High-speed profiler used for IRI measurement

Figure 58 depicts the location and brief information of each road section involved in the forensic investigations. It is important to note that the primary objective of the forensic investigations is to find potential field instrumentation sites for the installation of necessary sensors within the pavement and granular road systems. That is, factors crucial for the effective operation of the remote sensing system, such as the availability of an external power source, the presence of superload or overweight vehicle traffic, and the severity of distress in the existing road section, hold greater significance in this study compared to historical data about the road section.



© Google 2024

Figure 58. Locations of forensic investigation sites in Union County: (a) Osage and North Osage streets and (b) Rea Road and Cherry Street

Collecting information pertaining to the type of distress and its severity from forensic investigation sites is essential to pre-record the existing distress in road sections and identify additional distress in pavements and granular roads caused by superload traffic. This visual investigation serves as a logical support for quantifying the impact of superloads on specific types and structures of road systems by comparing road conditions before and after the passage of a superload. The distress type and severity, along with the design features, of each investigated road section are depicted and summarized in Figure 59.



Figure 59. Summary of the forensic investigation results conducted in Union County at (a) Osage Street, (b) North Osage Street, (c) Cherry Street, and (d) Rea Road

Since it is also imperative to investigate the type and volume of traffic, with particular attention to the presence of a superload traveling the road section, the research team conducted a traffic survey for each road section to investigate the traffic type and volume over a designated hour. Note that the traffic type and volume presented in Table 28 reflect data collected for a specific hour and not the averaged traffic volume of a road section typically represented by annual average daily traffic (AADT) or AADTT.

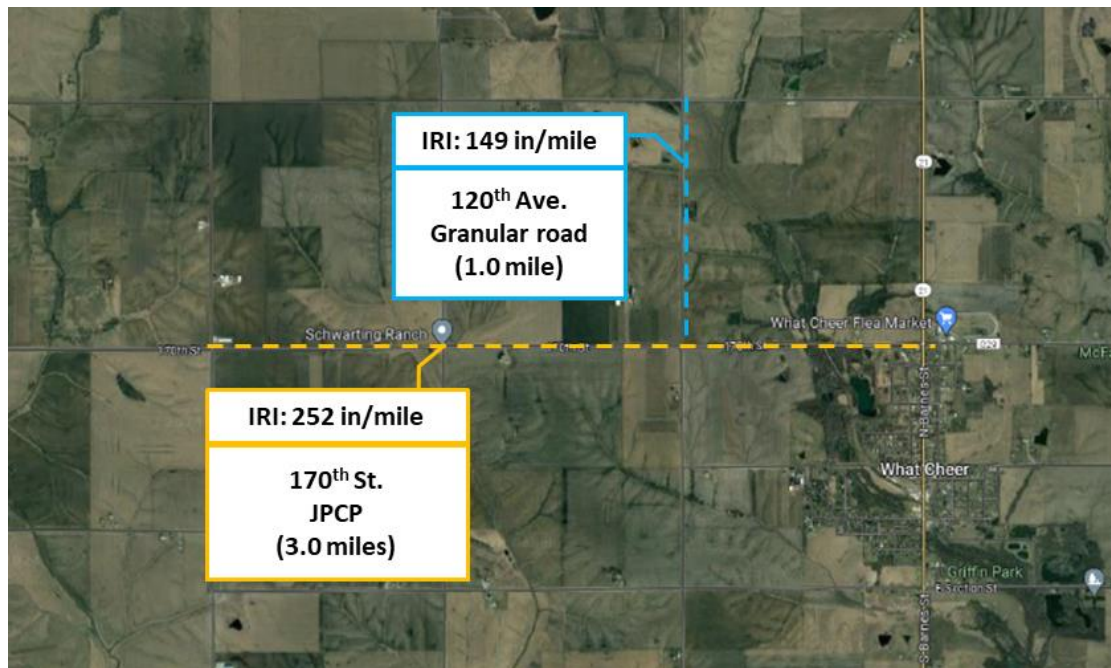
Table 28. Traffic type and volume for a specific hour surveyed on May 7, 2020

Road name	Direction	Time	FHWA classification class 1–5	FHWA classification class 6–13	IoH	SHL
Osage Street	South bound	11:00 a.m. to 12:00 p.m.	7	0	1	0
	North bound	11:00 a.m. to 12:00 p.m.	3	1	1	0
North Osage Street	South bound	11:00 a.m. to 12:00 p.m.	34	16	2	0
	North bound	11:00 a.m. to 12:00 p.m.	49	21	0	0
Cherry Street	South bound	9:30 a.m. to 10:30 a.m.	74	8	1	0
	North bound	9:30 a.m. to 10:30 a.m.	80	2	1	1
Rea Road	East bound	9:30 a.m. to 10:30 a.m.	18	1	0	1
	West bound	9:30 a.m. to 10:30 a.m.	19	0	0	0

As can be seen in Table 28, a single SHL traveled both Cherry Street and Rea Road at approximately 10 a.m. on May 7, 2020. Notably, this specific SHL, identified as a modular SHL with dollies, engaged in continuous round trips on these two road sections for three consecutive days, from May 7 to May 9. Details of these travels and the corresponding distress investigations are introduced in a subsequent section near the end of this chapter. While the three road sections, including North Osage Street, Cherry Street, and Rea Road, encountered relatively high traffic volumes, all four road sections had a low volume of IoH and SHL traffic, the main traffic targets of this study. All four road sections were located where external power could be supplied from utility poles, but there was no permanent WIM system in the vicinity. More detailed information on the forensic investigation conducted in Union County can be found in Appendix A.

Forensic Investigation in Keokuk County

The forensic investigation in Keokuk County was conducted on April 1, 2021, over approximately 3 mi of 170th Street (PCC-surfaced pavement) and 1 mi of 120th Avenue (granular road). A comprehensive investigation was undertaken, encompassing the meticulous examination of topography, distress, design features, and daily traffic patterns, and the IRI was also measured for each road section. Figure 60 provides a visual representation and concise details of the location of each road section involved in the forensic investigations. As previously detailed, this study placed heightened emphasis on factors crucial to the efficient operation of the remote sensing system, notably considering including the availability of an external power source, the presence of superload traffic, and the severity of distress within the existing road section.



© Google 2024

Figure 60. Locations of forensic investigation sites in Keokuk County: 170th Street and 120th Avenue

Distress type and severity data were gathered from both 170th Street and 120th Avenue to document the prevailing conditions of the pavement and granular road. Figure 61 illustrates and summarizes the distress type, severity, and design features for each scrutinized road section. The severity of distress observed in the JPCP section of 170th Street was high, indicating that it may not have been the most suitable section for installation and monitoring of the data acquisition system.

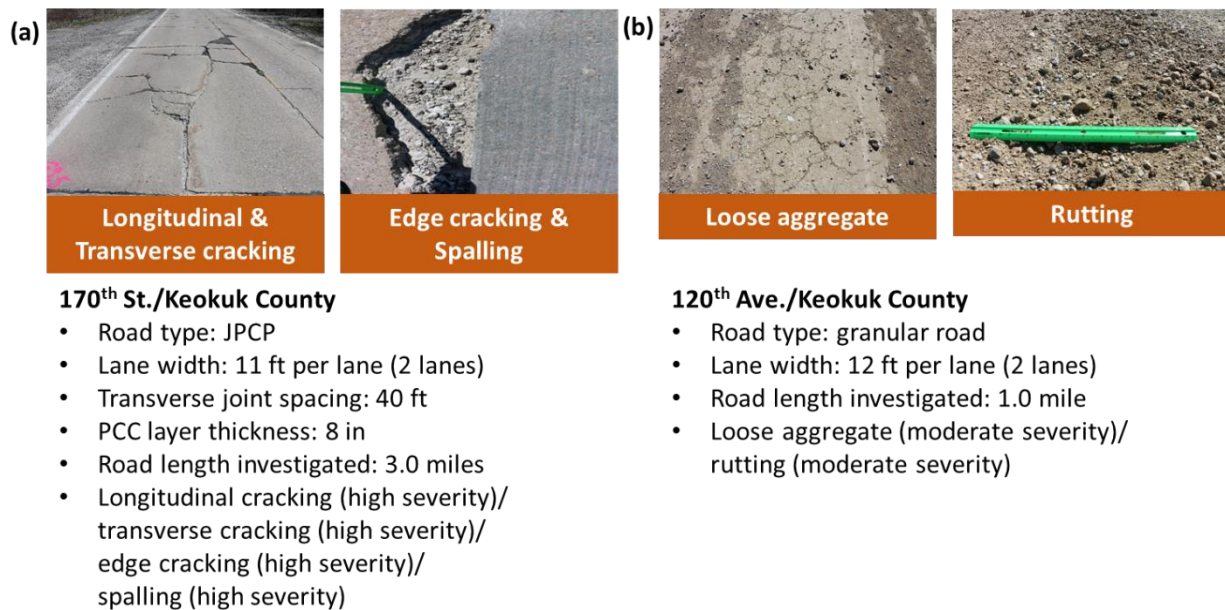


Figure 61. Summary of the forensic investigation results conducted in Keokuk County at (a) 170th Street and (b) 120th Avenue

The type and volume of traffic were again investigated, with a specific focus on identifying the presence of superloads traveling on the road sections. The research team carried out a traffic survey for each road segment, scrutinizing traffic type and volume over a designated hour, as outlined in Table 29.

Table 29. Traffic type and volume for a specific hour surveyed on April 1, 2021

Road name	Direction	Time	FHWA classification class 1–5	FHWA classification class 6–13	IoH	SHL
170th Street	East bound	3:00 p.m. to 4:00 p.m.	16	3	1	0
	West bound	3:00 p.m. to 4:00 p.m.	12	2	1	0
120th Avenue	South bound	3:00 p.m. to 4:00 p.m.	3	0	1	0
	North bound	3:00 p.m. to 4:00 p.m.	4	0	0	0

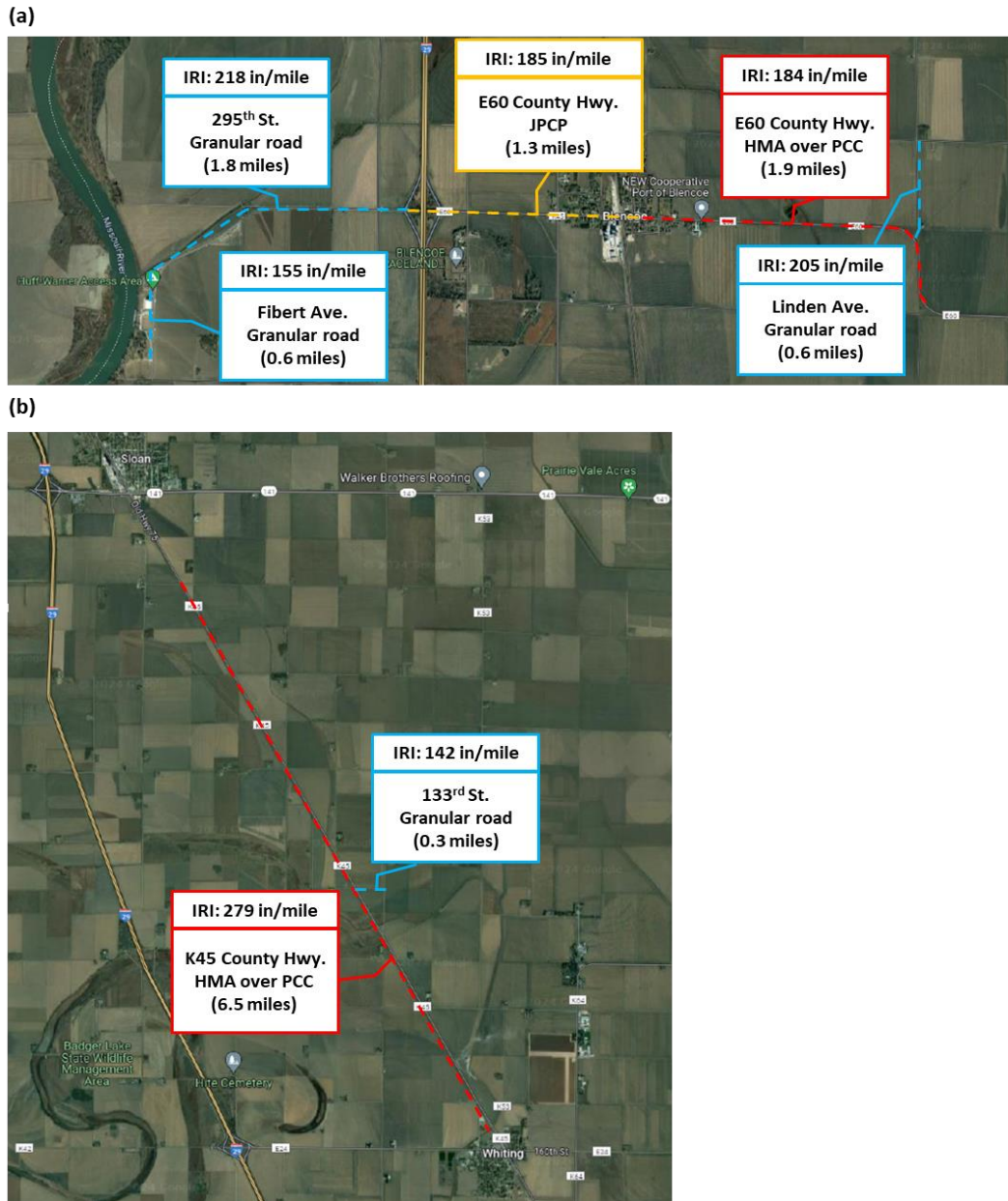
Notably, no SHL traffic was recorded on either 170th Street or 120th Avenue between 3 p.m. and 4 p.m. on April 1, 2021, while two IoHs were counted on 170th Street and one IoH was observed on 120th Avenue during the same period. Since both road sections experienced relatively low traffic volumes, both sections were deemed unsuitable for field instrumentation due to a lack of high distress severity and low traffic volume particularly related to superload

traffic. Absence of a permanent WIM system in the vicinity and the scarcity of utility poles from which the data acquisition system could draw an external power source further contributed to this determination. For a more detailed account of the forensic investigation conducted in Keokuk County, refer to Appendix A.

Forensic Investigation in Monona County

The Monona County engineer informed the research team about two JPCP reconstruction projects, offering an opportunity for the team to strategically install sensors in sync with the upcoming reconstruction activities. One project involved extending a highway, replacing the existing granular road (295th Street) with a JPCP section featuring an 8 in. PCC layer thickness, with reconstruction scheduled for around October 2021. The second project entailed replacing the existing composite pavement of a county highway (K45) with a JPCP section featuring an 8 in. PCC layer thickness, with reconstruction set to occur around July 2021. The prospect of installing data acquisition systems in conjunction with these reconstruction projects was of paramount importance. It allowed the research team to strategically place necessary sensors in the newly constructed JPCP systems, enabling the collection of JPCP response data in accordance with traffic and environmental conditions without causing damage to the existing road sections.

To further study roadways in Monona County, the research team conducted forensic investigations on a total of seven road sections, including two sections of county highways with AC-surfaced pavement (K45 and E60), one county highway section with PCC-surfaced pavement (E60), and four granular road sections (Filbert Avenue, 295th Street, Linden Avenue, and 133rd Street). This investigation took place from April 28 to 30, 2021. Figure 62 shows the location and brief information of each road section involved in the forensic investigations.



© Google 2024

Figure 62. Locations of forensic investigation sites in Monona County: (a) Filbert Avenue, 295th Street, E60, and Linden Avenue and (b) K45 and 133rd Street

Despite the impending JPCP reconstructions at (1) E60 and 295th Street and (2) K45, the research team conducted a comprehensive field investigation to document existing distress types and severity across these seven road sections. Figure 63 provides a visual representation and summary of the distress types, severity levels, and design features for each road segment.



Figure 63. Summary of the forensic investigation results conducted in Monona County at (a) Filbert Avenue, (b) 295th Street, (c) E60 (JPCP), (d) E60 (composite pavement), (e) K45, and (f) 133rd Street

The composite pavement section of K45 exhibited high severity in almost all types of distress that can be seen in the composite pavement system, underscoring the imperative need for JPCP reconstruction along this 6.5 mi stretch of road.

It is essential to highlight that the planning of the two JPCP reconstruction projects was strategically oriented toward accommodating a substantial volume of both truck and IoH traffic, stemming from the fact that these road sections play a crucial role as a farm-to-market route. To help comprehensively understand the traffic type and volume for each road segment, the research team conducted a one-hour traffic investigation for each road section. Table 30 shows that, despite a minimal volume of IoH traffic recorded between 4:02 p.m. and 5:02 p.m. on April 29, 2021, K45, planned for JPCP reconstruction, experienced a notable volume of other types of traffic, particularly truck traffic. Notably, utility poles lined the entirety of K45, especially at intersections such as those with 133rd Street or 140th Street, providing access to an external power supply. It is also noteworthy that the WIM system is located 8 mi north of K45.

Table 30. Traffic type and volume for a specific hour surveyed on April 29, 2021

Road name	Direction	Time	FHWA classification class 1–5	FHWA classification class 6–13	IoH	SHL
Filbert Avenue	South bound	12:20 p.m. to 1:20 p.m.	4	2	1	0
	North bound	12:20 p.m. to 1:20 p.m.	9	4	0	0
295th Street	East bound	12:20 p.m. to 1:20 p.m.	6	4	1	0
	West bound	12:20 p.m. to 1:20 p.m.	9	4	0	0
E60 (JPCP)	East bound	12:20 p.m. to 1:20 p.m.	13	4	1	0
	West bound	12:20 p.m. to 1:20 p.m.	8	3	0	0
E60 (composite)	East bound	12:20 p.m. to 1:20 p.m.	19	11	1	0
	West bound	12:20 p.m. to 1:20 p.m.	8	6	1	0
Linden Avenue	South bound	2:20 p.m. to 3:20 p.m.	5	0	1	0
	North bound	2:20 p.m. to 3:20 p.m.	1	0	0	0
K45	South bound	4:02 p.m. to 5:02 p.m.	30	21	1	0
	North bound	4:02 p.m. to 5:02 p.m.	22	12	0	0
133rd Street	East bound	4:02 p.m. to 5:02 p.m.	3	2	2	0
	West bound	4:02 p.m. to 5:02 p.m.	6	1	1	0

Forensic Investigation in Tama County

Following the forensic investigation in Monona County, the research team had decided to use K45 located there as the JPCP site for installing a remote sensing system. However, because challenges were encountered while searching for a full-depth flexible pavement section for remote sensing system installation, multiple visits and communications with other counties were necessary.

The Tama County engineer provided valuable information, indicating the presence of a potential full-depth flexible pavement and thus providing an opportunity for the research team to install its

sensing system. The full-depth flexible pavement section, reconstructed in 2004 and comprised of 6.5 in. of AC layer over a fly ash-treated subgrade, spans a length of 7 mi along V18. Given that V18 intersects with several granular roads exhibiting good road conditions, such as 190th, 200th, 220th, and 240th streets, and other streets, the research team made the decision to strategically place core data loggers at one of these intersections. This approach allowed for the use of one core data-collecting system to manage the sensors installed in both the full-depth flexible pavement and the granular road. Consequently, the forensic investigations conducted in Tama County were specifically focused on identifying an optimal intersection site for installation of a remote-sensing system capable of efficiently managing both the full-depth flexible pavement and granular road sections through a unified core data-collecting system.

On July 7, 2022, the research team conducted forensic investigations on a total of five road sections, including one full-depth flexible pavement county highway section (V18) and four granular road sections (190th, 200th, 220th, and 240th streets). Figure 64 depicts the location and brief information about each road section involved in this forensic investigation.



© Google 2024

Figure 64. Locations of forensic investigation sites in Tama County: V18 and 190th, 200th, 220th, and 240th streets

Given that neither V18 nor other granular road sections were scheduled for any treatment activities in the near future, the research team had to plan for damages to both the existing full-depth flexible pavement and granular road by cutting a portion of each road section to install the required sensors in these road systems. Since the potential sensor installation sites had to be in good condition to mitigate the impact of existing distress on pavement response measurements when subjected to superloads, the research team conducted a distress survey on those five road sections to identify the optimum site for installing the remote-sensing system. Figure 65 shows a visual representation and summary of distress types, severity levels, and design features for each road segment.



Figure 65. Summary of the forensic investigation results conducted in Tama County at (a) V18 and (b) 190th, (c) 200th, (d) 220th, and (e) 240th streets

The full-depth flexible pavement section of V18 exhibited highly severe longitudinal and transverse cracking, and while corresponding treatment had been implemented to address these distresses along the entirety of the highway, certain sections of V18, such as the one intersecting with 190th Street, displayed only moderate severity for the same types of distress. All granular road sections investigated demonstrated overall good road conditions.

During the forensic investigation, the research team found several livestock and agricultural farms located along V18 and four granular road sections that seemed to hold significant importance as a farm-to-market route. To collect information regarding the traffic type and volume for each road segment, the research team conducted one-hour traffic investigations for each road section.

Table 31 shows that, despite an overall low volume of traffic recorded on July 7, 2022, across the five road sections in Tama County, the presence of several IoHs and trucks transporting agricultural products and livestock was observed. Also, utility poles spanned the entirety of V18, particularly located at intersections with all four granular road sections, serving to provide a source of external power. No permanent WIM system was found near the road sections of interest. Given the absence of alternative sites suitable for field instrumentation on full-depth flexible pavement, V18 and a granular road sharing an intersection emerged as an optimal location for the team's potential field instrumentation sites.

Table 31. Traffic type and volume for a specific hour surveyed on July 7, 2022

Road name	Direction	Time	FHWA classification class 1–5	FHWA classification class 6–13	IoH	SHL
V18	South bound	11:10 a.m. to 12:10 p.m.	11	4	1	0
	North bound	11:10 a.m. to 12:10 p.m.	13	6	4	1
190th Street	East bound	11:10 a.m. to 12:10 p.m.	3	1	2	0
	West bound	11:10 a.m. to 12:10 p.m.	2	1	2	0
200th Street	East bound	11:10 a.m. to 12:10 p.m.	1	0	1	0
	West bound	11:10 a.m. to 12:10 p.m.	3	2	0	0
220th Street	East bound	12:40 p.m. to 1:40 p.m.	2	0	0	0
	West bound	12:40 p.m. to 1:40 p.m.	0	1	0	0
240th Street	South bound	12:40 p.m. to 1:40 p.m.	1	1	0	0
	North bound	12:40 p.m. to 1:40 p.m.	2	1	1	0

Forensic Investigation of Road Conditions According to Superload Traffic

This section provides additional detailed information about the three round trips conducted by a modular SHL with dollies during three consecutive days, specifically between May 7 and 9, 2020, traveling both Cherry Street (JPCP) and Rea Road (composite pavement) in Union County. Figure 66 shows the travel route taken by the SHL over the three days, between 9:00 a.m. and 10:00 a.m. The SHL commenced its operation from the north end of Creston through Cherry Street and arrived at the Central Iowa Power Cooperative (CIPCO) located near Rea Road. Note that the main objective of the investigation was to identify the additional distress induced by three round trips of an SHL on both Cherry Street and Rea Road.



© Google 2020

Figure 66. Travel route in Union County taken by a modular SHL during three consecutive days

A modular SHL equipped with six additional axles of dollies and transporting a huge engine block traveled north on Cherry Street. It then turned right to get onto Rea Road, eventually arriving at CIPCO to unload the engine block. After unloading, the empty SHL returned to Creston without any cargo. This travel routine occurred once per day, and the exact same activity was repeated for the subsequent two days, each time transporting the same engine block weighing 445,554 lb. Figure 67 and Table 32 provide a detailed representation of the vehicle configuration and loading information of the SHL that traveled the road sections for three consecutive days. The SHL was configured with dollies placed in the middle portion of its modules to ensure that the axle weights remained below 20 kips.

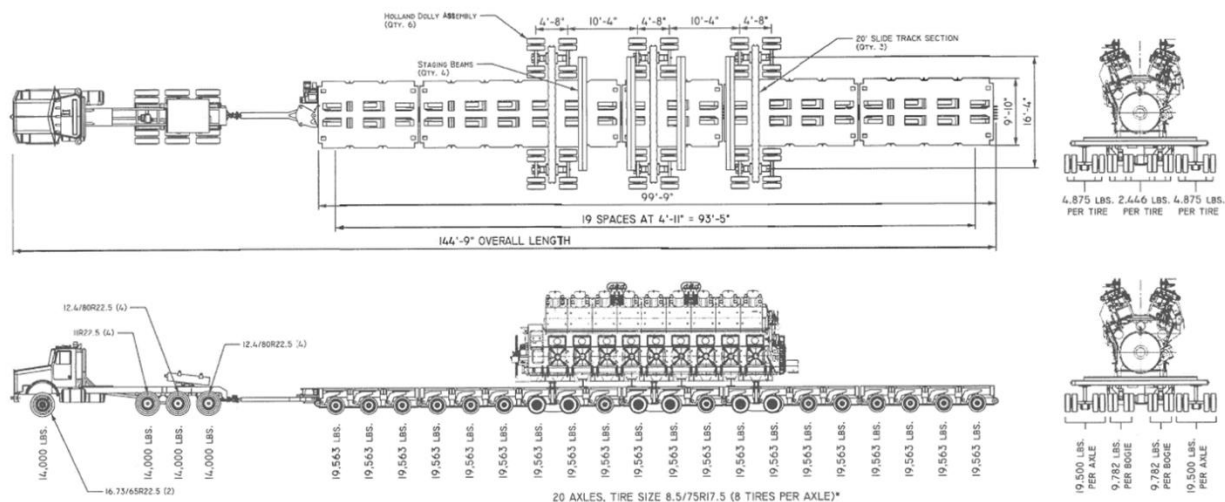


Figure 67. Body configuration of modular SHL with dollies that traveled road sections in Union County

Table 32. Loading information of modular SHL with and without an engine block

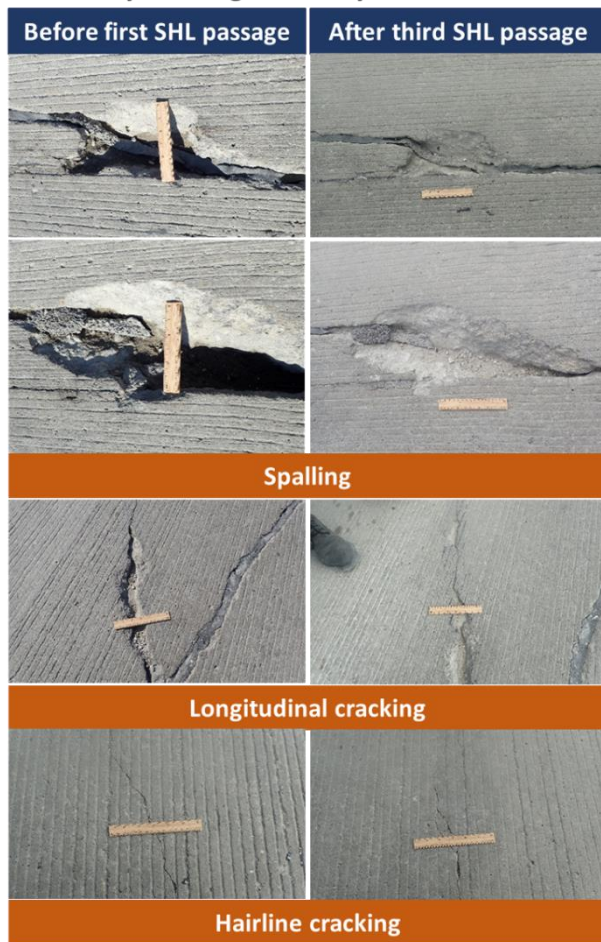
Date of travel	Cargo	No. of axles	GVW (lb)	Axle weight (lb)	Axle spacing
May 7, 2020	Engine block	20	630,854	19,563	4 ft 11 in.
	Empty	20	194,000	7,500	4 ft 11 in.
May 8, 2020	Engine block	20	630,854	19,563	4 ft 11 in.
	Empty	20	194,000	7,500	4 ft 11 in.
May 9, 2020	Engine block	20	630,854	19,563	4 ft 11 in.
	Empty	20	194,000	7,500	4 ft 11 in.
Weight of engine block	445,554 lb				
Travel time	9:00 a.m. to 11:00 a.m.				

The section of Cherry Street through which the SHL traveled featured a JPCP structure, comprised of a 10 in. thickness of PCC layer over a 6 in. modified subbase. For the section of Rea Road through which the SHL traveled, the initial 0.1 mi was characterized by a structure

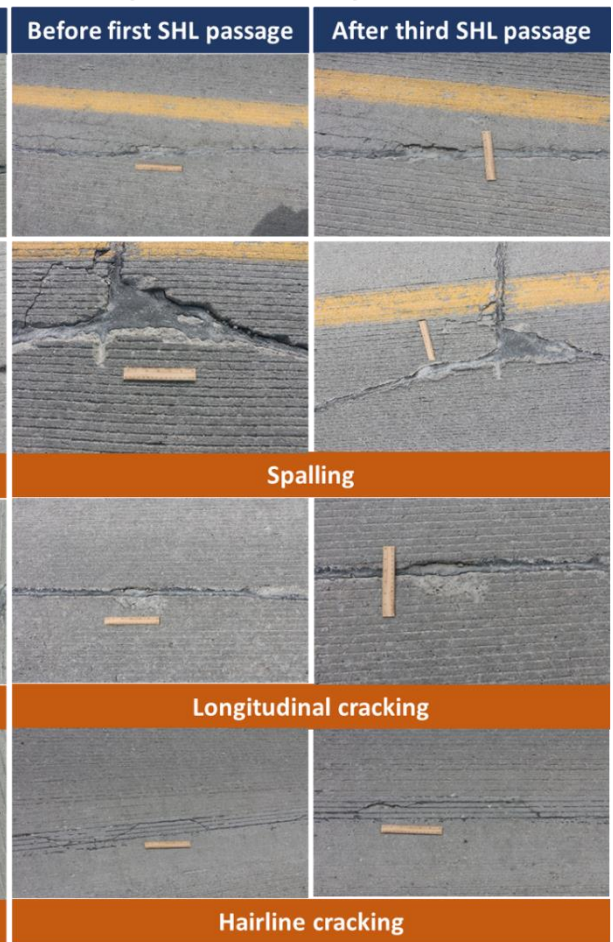
consisting of 4 in. of HMA overlay over a PCC layer, and the remaining 0.6 mi stretch was comprised of 4 in. of HMA overlay over an AC layer. A thorough investigation was conducted before and after the SHL passages on two specific 500 ft sections of Cherry Street, each exhibiting different preexisting severity levels of distress, and on the entire 0.7 mi length of Rea Road, as shown in Figure 66. The representative types of distress found in each investigated section before the passage of the SHL were compared with those observed in the exact same locations after the three round trips of the SHL.

Figure 68 provides visual comparisons through photographs, illustrating the severity of the representative distress before the first passage of the SHL and after the third passage of the SHL at several locations within each investigated section. This visual representation allows for a direct observation of the impact of the superload on the pavement systems. Notably, the figure reveals that there was no significant increase in the representative distress across all three investigated sections, despite being subjected to three passes of a loaded SHL and three passes of an unloaded SHL. This visual observation suggests that the pavement systems exhibited resilience, indicating that a limited number of SHL passes may not result in a dramatic impact on their condition.

(a) Cherry St. – high severity section



(b) Cherry St. – low severity section



(c) Rea Rd. – whole section

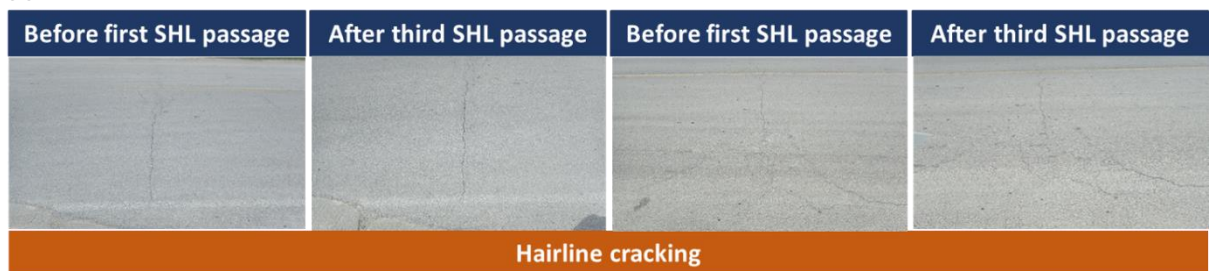


Figure 68. Distress severity survey at (a) Cherry Street - high severity section, (b) Cherry Street - low severity section, and (c) Rea Road before the first passage of SHL and after the third passage of SHL

Summary and Key Findings

Since mechanistic-based analysis employing FEM and LET approaches necessitated validation through in situ field data collection and analysis, forensic investigations were conducted across various road sections in Iowa, encompassing AC-surfaced pavements, PCC-surfaced pavements,

and granular roads, to identify suitable sites for instrumentation with data acquisition systems. The main items for forensic investigations that served as significant factors in determining proper sites for installing the data acquisition systems were (1) geographical coordinates, (2) traffic volume and vehicle types, (3) design features of the road section, (4) surface and subsurface conditions, (5) topography, (6) presence of a permanent WIM system near the road section, and (7) availability of external power sources. Further discussion on the forensic investigations conducted as part of this chapter is provided in the subsequent lists.

- **Forensic investigation in Union County**

- Investigations were conducted on Osage Street, North Osage Street, Rea Road, and Cherry Street.
- Thorough identification and documentation of topography, distress, design features, and traffic counts were performed.
- Distress levels of moderate severities for the JPCP sections, low severity for the composite pavement section, and high severity for the granular road section were identified.
- Low superload traffic was counted; utility poles existed along the road sections; no permanent WIM system existed in the vicinity.
- A modular SHL equipped with six additional axles of dollies and transporting a huge engine block traveled Cherry Street and Rea Road for three consecutive days.

- **Forensic investigation in Keokuk County**

- Investigations were conducted on 170th Street and 120th Avenue.
- Thorough identification and documentation of topography, distress, design features, and traffic counts were performed.
- Distress levels of high severity for the JPCP section and moderate severity for the granular road section were identified.
- Low superload traffic was counted; scarcity of utility poles; no permanent WIM system existed in the vicinity.

- **Forensic investigation in Monona County**

- Investigations of road sections, including Filbert Avenue, 295th Street, E60, K45, and 133rd Street, were conducted before two JPCP reconstruction projects.
- Thorough identification and documentation of topography, distress, design features, and traffic counts were performed.
- Distress levels of low severity for the JPCP section, high severities for the composite pavement sections, and low to moderate severities for the granular road sections were identified.
- Several IoHs were counted; utility poles line the entirety of K45, especially at intersections with 133rd Street and 140th Street; permanent WIM system located 8 mi from K45.
- Strategic planning was made for field instrumentation in alignment with JPCP reconstruction on K45.

- **Forensic investigation in Tama County**
 - Investigations were conducted focusing on full-depth flexible pavement (V18) and granular roads (190th, 200th, 220th, and 240th streets) for identifying potential sites for data acquisition system installation.
 - Thorough identification and documentation of topography, distress, design features, and traffic counts was conducted.
 - Distress levels of high severity for the full-depth flexible pavement section, but moderate severity for certain sections were identified such as near the intersection with 190th Street. Low to moderate severities for the granular road sections were identified.
 - Several IoHs and trucks transporting agricultural products and livestock were observed; utility poles line the entirety of V18; no permanent WIM system existed in the vicinity.
 - Strategic planning was made for field instrumentation on V18 as a full-depth flexible pavement section and 190th Street as a granular road section.

- **Forensic investigation of road conditions according to superload traffic in Union County**
 - A modular SHL with dollies traveled both Cherry Street (JPCP) and Rea Road (composite pavement) in Union County over three consecutive days, between May 7 and 9, 2020.
 - Investigation of distress levels before and after SHL passages was conducted.
 - A visual comparison indicated a limited impact from the SHL passes on the pavement condition.

CHAPTER 8. FIELD INSTRUMENTATION AND MONITORING

This chapter focuses on implementation of field instrumentation and in situ data monitoring and analysis across three types of road systems: JPCP, full-depth flexible pavement, and granular road. Mechanical pavement and granular road response measurement from instrumented sensors and data acquisition systems is one of the most reliable approaches to bridging the gap between mechanistic models and roads with in situ conditions. Mechanistic models can be validated using long-term performance-monitoring data collected from the field from a specific site with material-specific properties. Direct measurement of pavement and granular road responses related to each structural distress type from the in situ data acquisition system can also help establish mathematical correlations between strains or stresses within the road structure and environmental, traffic, and boundary conditions.

The objectives of this chapter's activities were to install remote-sensing systems and collect data on pavement and granular road responses, taking into account environmental conditions and traffic loadings, to verify mechanistic-based pavement and granular road analysis results. The process of installing remote-sensing systems on-site for JPCP, full-depth pavement, and granular road sections required meticulous planning, including identifying precise locations and depths for sensor installation for measuring critical pavement or granular road responses. Seamless communication with county engineers and construction managers was also essential for coordinating construction scheduling, and attention had to be paid to safety measures such as traffic control during on-site installations.

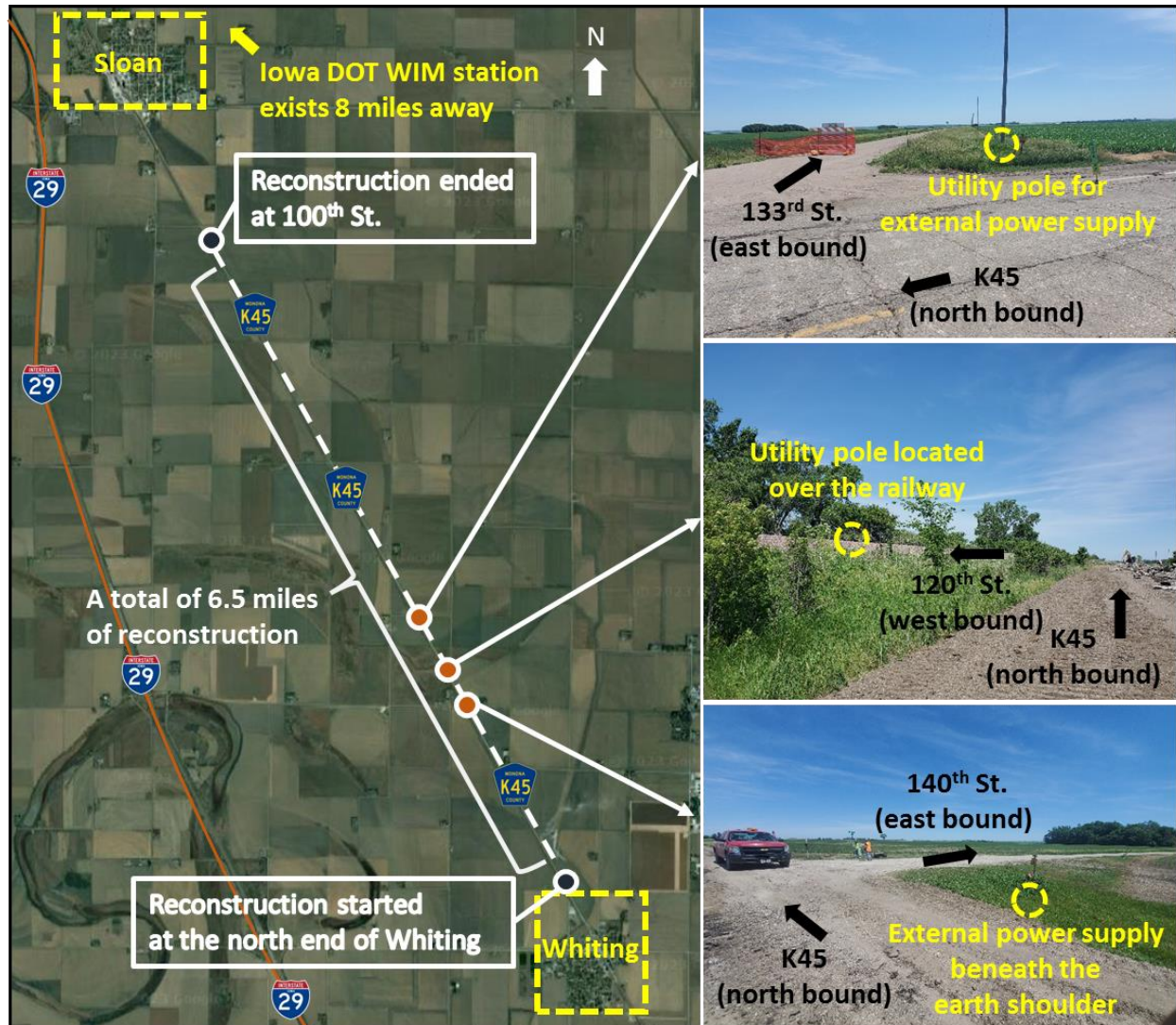
Field Instrumentation and Monitoring at JPCP Section

This section introduces detailed steps and methodologies used for the remote data acquisition system installation, including a P-WIM system and other necessary sensors such as strain gauges, thermistors, and moisture sensors, in conjunction with the JPCP reconstruction project carried out in Monona County, Iowa, during the second half of 2021. This section also outlines the number and types of sensors utilized, aimed at measuring pavement responses associated with structural distress, particularly fatigue cracking, in a reconstructed JPCP section. Environmental factors such as temperature and water content, along with traffic loads, were considered in the in situ data analysis. Utility and durability of the sensors and other components of the data acquisition system were also assessed. Long-term performance monitoring was conducted to quantify the performance of the JPCP over time.

Site Condition

Field instrumentation involving the installation of sensors, data loggers, and power components was carried out on a reconstructed JPCP road section located in Monona County, Iowa, to evaluate JPCP performance under environmental and traffic loads. The selection of the instrumentation site was based on a forensic investigation of several potential Iowa sites described in the previous chapter. Key factors considered by the research team in selecting the field instrumentation site included (1) JPCP reconstruction schedule, (2) frequencies of truck, IoH, or SHL traffic, (3) proximity to a WIM system, (4) availability of an external power supply



(e.g., utility pole) from the earth shoulder near the sensor installation spot, and (5) absence of traffic obstruction signs such as a traffic lights or stop signs. Detailed information about K45 in Monona County, identified as the optimal field instrumentation site for the study where a JPCP reconstruction was planned, is provided in Figure 69 and Table 33.



© Google 2024

Figure 69. Site information for K45

Table 33. Summary of road section information under JPCP reconstruction

Question	Answer	
	Before reconstruction	After reconstruction
Road section name	Partial K45 road section from the north end of Whiting to 100th Street	
Road type	Composite pavement (HMA overlay on PCC pavement)	JPCP
No. of lanes	Two lanes (one per each direction)	Two lanes (one per each direction)
Width of lane	12 ft per lane	12 ft per lane
Length of road section under reconstruction	6.5 mi	
Thickness of paving layer	HMA overlay: 3 in. to 8 in. PCC layer: 5 in. to 8 in.	PCC layer: 8 in.
AADT	597	-
Primary vehicles	Resident vehicle, truck, IoH	Resident vehicle, truck, IoH
Averaged pavement condition index (PCI)	66.85	-
Averaged IRI (in./mi)	119	-
Major failure type	 <p>Alligator cracking, longitudinal cracking, block cracking, rutting, patch deterioration</p>	 <p>No failure found</p>

Following the forensic investigation, a partial road section of K45 stretching from the north end of Whiting to 100th Street, with multiple types of high severity distresses was found to be a critical road section that had experienced heavy traffic, both from resident vehicles and overweight vehicles transporting agricultural products. Due to convenient accessibility to an external power supply, two locations near the intersections of K45 (composite pavement) with 133rd and 140th streets (granular roads) were selected as candidates for potential instrumentation locations.

Field Instrumentation Plan

Since the JPCP reconstruction on K45 was scheduled to take place between June and October 2021, all components of the data acquisition system required advanced preparation, and pre-testing and installation work were imperative and had to be completed before or during this period. Since the stages of JPCP reconstruction typically do not proceed according to an exact schedule, it was necessary to thoroughly plan and execute required activities for each stage in sync with a construction schedule prone to unexpected changes.

To evaluate the JPCP performance under environmental and traffic loads, with a particular focus on fatigue cracking, a range of sensors and components were prepared, including strain gauges for measuring strain at the top and bottom of the PCC slab, and thermistors and moisture sensors for monitoring temperature and water content, respectively, in each layer. Corresponding data loggers, as well as auxiliary components such as modems, ethernet networking for remote control, power components, and enclosures, were also prepared. A P-WIM system equipped with a pair of piezoelectric sensors and a traffic counter was also prepared to collect load data produced by traffic passing through the remote-controlled sensor installation section after the JPCP reconstruction. Table 34 provides an overview of the embedded sensor types, the P-WIM system, and their brief specifications, as well as other components of the data acquisition system installed on the earth shoulder near the sensor installation site.

Table 34. Brief specifications of data acquisition system components for JPCP

Component type*	Model	Description	Number	Location
Strain gauge	CEST350 (BDI 2022a)	Embeddable strain transducer	4	Top of PCC slab
			4	Bottom of PCC slab
Thermistor	TS-EM (BDI 2024a)	Embeddable temperature sensor	4	Top of PCC slab
			4	Bottom of PCC slab
Moisture sensor	TEROS12 (METER Group 2024)	Volumetric water content, temperature, and electrical conductivity sensor	6	Top of soil layers
Data logger	STS-CDL-01 (BDI 2019)	Core data logger	1	Enclosure
	STS4-16-TE4 (BDI 2020)	16-channel data logger for strain gauges and thermistors	1	Enclosure
	ZL6 (METER Group 2023)	6-channel data logger for moisture sensors	1	Enclosure
Ethernet/modem	DCM-MC7354	Cellular wireless modem with a Verizon data plan	1	Enclosure
Power component	PW-AC-10A24	24V 10A power system	1	Enclosure
Enclosure	ENC-UB-36B2	Aluminum enclosure Size: 36 in. (H) × 30.5 in. (W) × 13.3 in. (D)	1	Earth shoulder
P-WIM system	TRS unit (IRD 2023a)	Traffic recording system (TRS) collecting traffic volume, speed, weight, and classifications	1	Earth shoulder
	MSI-BL-CLS2 (IRD 2023b)	2.4 m length sensors	2	Surface of JPCP

* Minor components of the data acquisition system are not listed here.

A CEST350 strain gauge developed by Bridge Diagnostics, Inc. (BDI) is a strain transducer with a 4 in. gauge length and a full Wheatstone bridge configuration, facilitating the measurement of high-frequency dynamic responses up to 250 Hz, as depicted in Figures 70a and 70b. It was imperative to measure high-frequency strain responses of at least up to 50 Hz to properly capture the dynamic responses induced by high-speed passing traffic loads. Thermistors also developed by BDI were deployed to monitor the temperatures at both the top and bottom of the PCC slab to account for temperature gradient and curling effects contributing to fatigue cracking, as shown in Figure 70c. Preparations were also made to install moisture sensors, specifically TEROS12 units from METER Group, to monitor static water content and temperature within each soil layer of the road section. Figure 70d illustrates the arrangement for data collection from strain gauges and thermistors, employing a 16-channel data logger, STS4-16-TE4, manufactured by BDI, while moisture sensor data were gathered using a 6-channel ZL6 data logger developed by METER Group. All collected data were stored and processed in the central STS-CDL-01 data logger. A wireless modem was included to facilitate remote system control and data transmission from the field. Since the data acquisition system was intended to measure JPCP responses over long periods, establishing a consistent power supply was a priority for maintaining data collection and monitoring. The data acquisition system was designed to incorporate an internal power system capable of delivering a 24V 10A alternating current power output, complete with alternating current surge protection, circuit breakers, load terminals, and proper grounding, thereby ensuring reliable power distribution from an external power source. The overall configuration of the data acquisition system is outlined in Figure 70e. A P-WIM system for collecting traffic data in conjunction with the high-frequency dynamic response measurement from the remote data acquisition system is shown in Figure 70f. Comprehensive details regarding the P-WIM system, including installation procedures and data collection protocols, are elaborated in Appendix B.

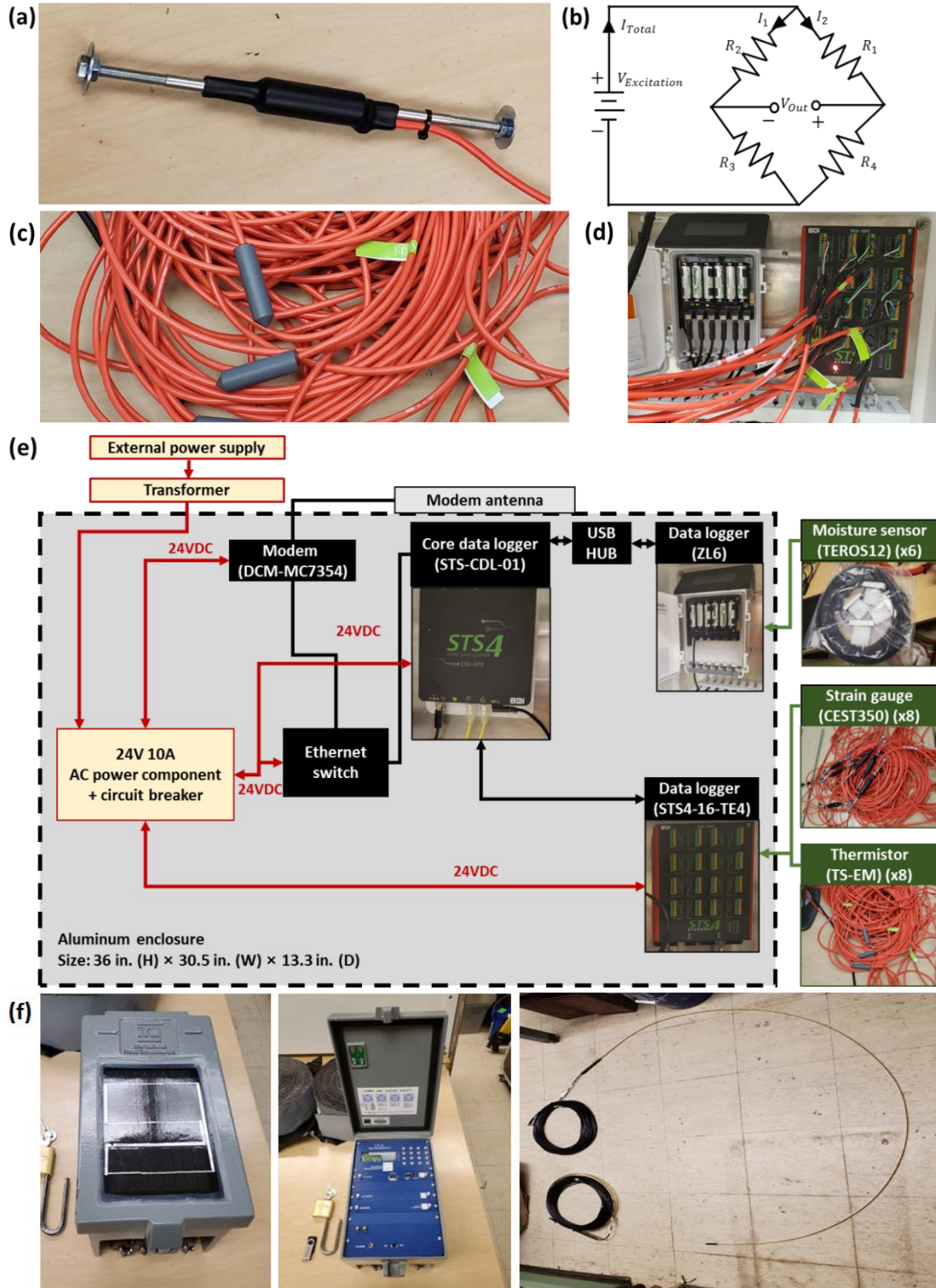


Figure 70. Major components of the data acquisition system: (a) strain gauge based on (b) Wheatstone bridge circuit, (c) thermistor, (d) STS4-16-TE4 (right) and ZL6 (left), and the (e) overall configuration of the remote data acquisition system operating in conjunction with the (f) P-WIM system

All sensors, data loggers, and the in situ data monitoring software, STS-LIVE (BDI 2024b), were pre-tested in the laboratory to ensure their performance and reliability before moving them to the construction field, as shown in Figure 71a. This testing encompassed examination and calibration of all sensors, including strain gauges, thermistors, and moisture sensors. It was ensured that the entire system operated properly without any malfunctions in any of its components, as depicted in Figures 71b to 71d.

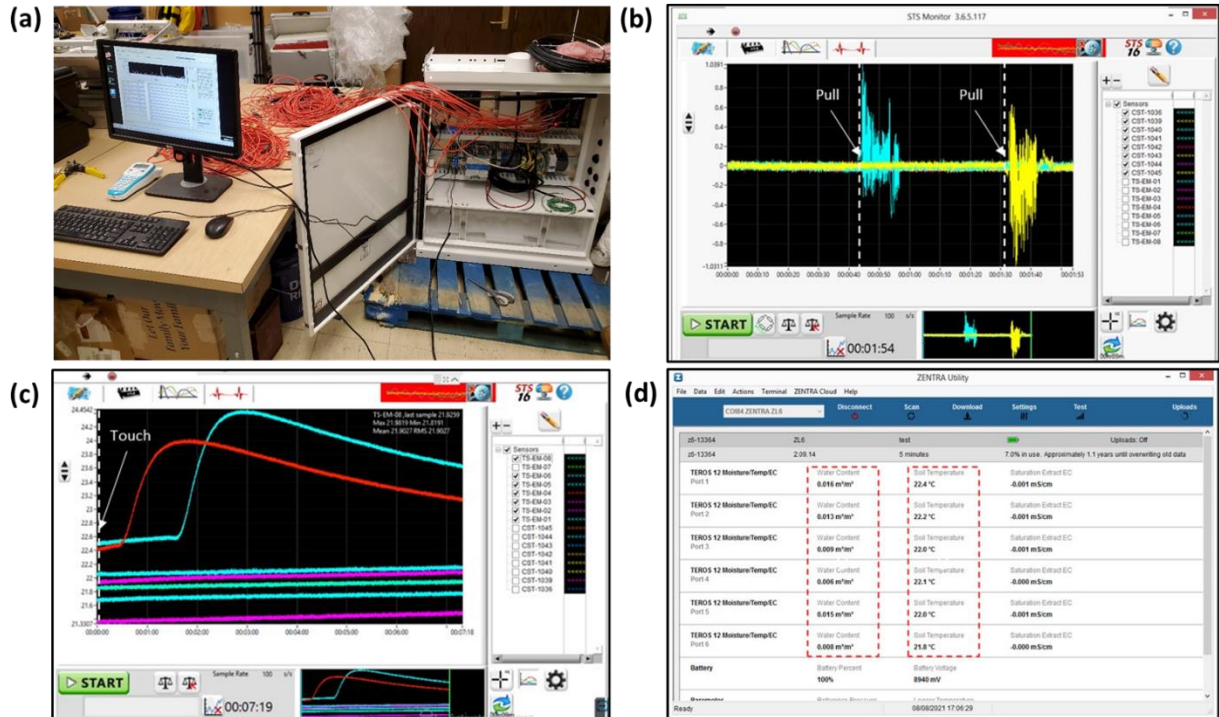


Figure 71. Pre-testing of the data acquisition system in the (a) laboratory, focusing particularly on the sensors: (b) strain gauges, (c) thermistor, and (d) moisture sensors

Repeated environmental and traffic load-induced stresses or strains at both the top and the bottom of the PCC slab have potential to exacerbate slab curvature, potentially leading to fatigue failure such as top-down and bottom-up fatigue cracking (Ceylan et al. 2016). The sensor installations listed in Table 34 were strategically planned at precise locations depicted in Figure 72 to evaluate the fatigue damage of the JPCP section caused and intensified by superloads and the curling effect induced by daily and seasonal temperature gradients within the PCC slab. Note that this study specifically focused on evaluating transverse fatigue cracking that would govern JPCP performance under superload traffic conditions, as indicated in the preceding section. As discussed in Chapter 4, critical stresses occurring at the top and the bottom of the PCC slab are more likely to manifest near a slab's edge or corner in the case of general trucks or IoHs. On the other hand, since SHLs, characterized by a large number of tires per axle, have significant potential to generate critical stresses either at the edge or at the center of the lane, four sensor trees were strategically placed, with each sensor tree installed at specific locations identified through computational analysis, revealing horizontal and vertical locations where critical pavement responses could occur due to superload traffic.

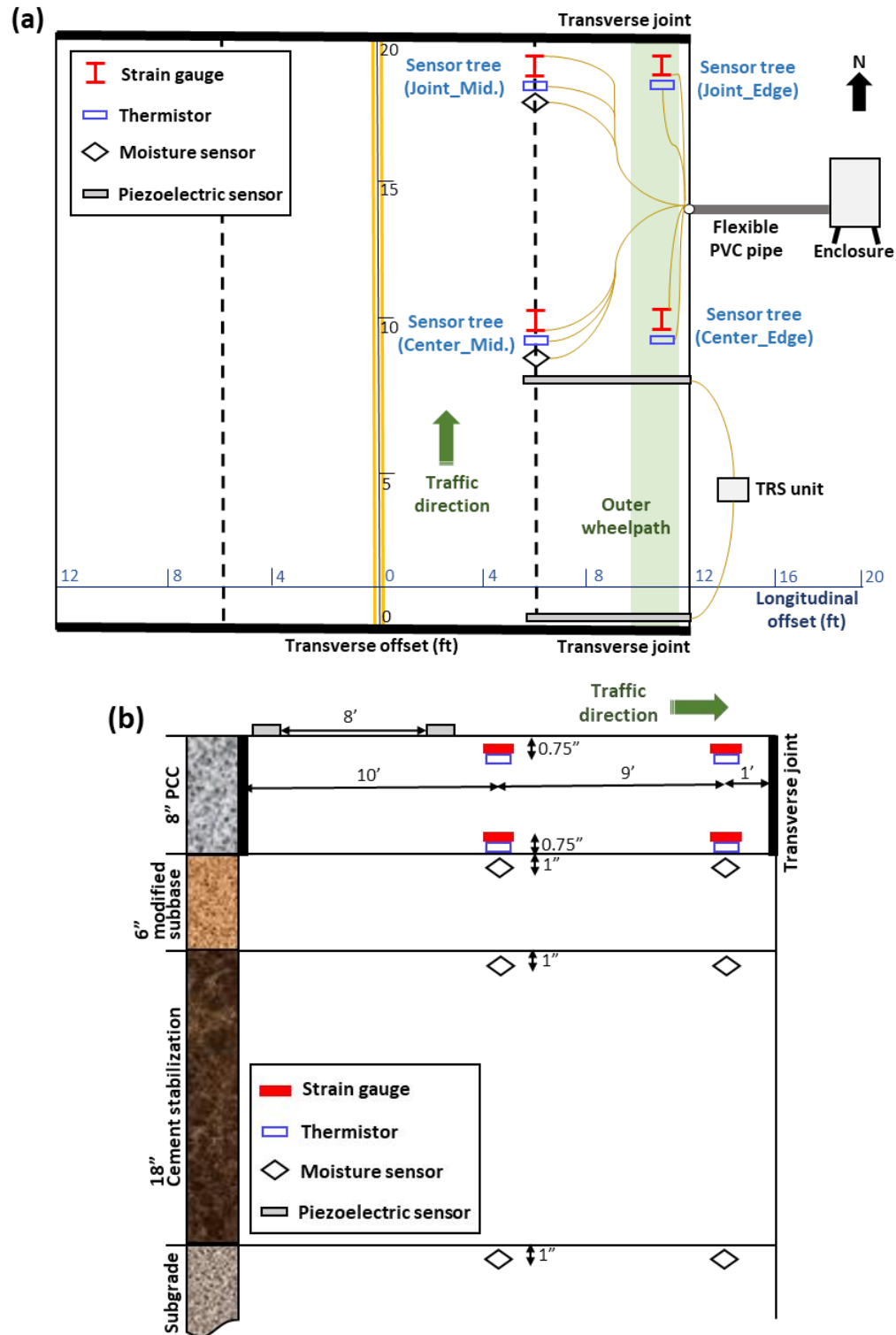


Figure 72. Sensor installation plan for JPCP section: (a) plane view and (b) cross-sectional view

Field Instrumentation in Reconstructed JPCP Section

The reconstruction of K45, spanning a total of 6.5 mi, commenced in June 2021. As illustrated in Figure 73, the reconstruction process involved the excavation and removal of the existing composite pavement road, followed by the establishment of gradation activities for each soil layer. By approximately June 28, 2021, the subgrade soil was completely exposed, so pre-testing of soil layers was conducted accordingly.



Figure 73. JPCP reconstruction process: (a) excavation of existing composite pavement, (b) removal and (c) gradation, to (d) expose the subgrade soil

In conjunction with the compaction and gradation activities for each soil layer, necessary pre-testing for each layer was conducted at two specific locations: the intersections of K45 with 133rd and 140th streets, where external power supplies were accessible. Three types of pre-testing: lightweight deflectometer (LWD) testing, dynamic cone penetration (DCP) testing, and sand-cone testing, were carried out on each soil layer to determine layer properties such as modulus of elasticity, California bearing ratio (CBR), resilient modulus, unit weight, and water content, properties that can play a crucial role in future studies on calibrating computational JPCP models using field data. At both intersections, 15 LWD and 5 DCP tests were conducted on 5 adjacent PCC slab sections, with the PCC slab section positioned in the middle where the sensors were installed, as shown in Figure 74.

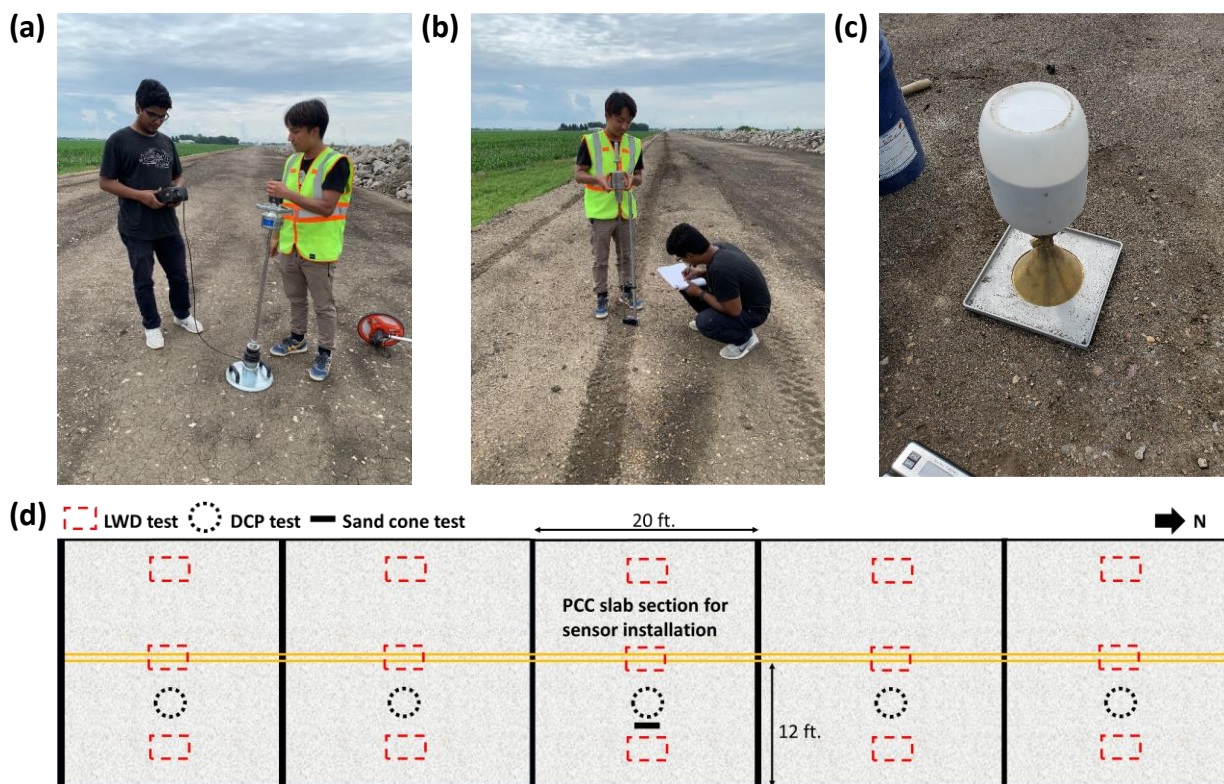


Figure 74. Pre-testing of each soil layer: (a) LWD test, (b) DCP test, and (c) sand cone test, and their (d) testing spots

Sand-cone testing was also performed once at each planned instrumentation site. The results of the pre-testing are summarized in Table 35.

Table 35. Summary of pre-testing results for each soil layer in two potential field instrumentation sections

Soil layer	Averaged modulus of elasticity (psi)	Averaged CBR (%)	Averaged resilient modulus (psi)	Averaged dry unit weight (pcf)	Averaged water content (%)
K45 section near 133rd Street					
Modified subbase layer	8,356	42.6	28,136	106	7.9
Cement stabilized layer	7,487	16.4	15,259	123	11.2
Subgrade	1,690	3.5	5,599	142	11.4
K45 section near 140th Street					
Modified subbase layer	7,196	46.2	29,428	104	6.3
Cement stabilized layer	6,068	18.0	16,197	118	17.5
Subgrade	1,794	2.1	4,106	112	19.6

Note: Pre-testing results were averaged from all testing results for each testing type and site.

Analysis of the pre-testing results revealed that the subgrade soils at both sections exhibited CBR values (%) of less than 5, indicating poor strength for supporting the JPCP (Schaefer et al. 2008). On the other hand, the modified subbase layers at both sections demonstrated CBR values (%) exceeding 40, indicating that the subbase layers had good strength to support the PCC layer (Schaefer et al. 2008). Following a forensic investigation and careful consideration of the pre-testing outcomes, it was confirmed that the two potential field instrumentation sites exhibited similar structural and material properties, so the section near 133rd Street, which featured a visible utility pole for an external power supply, was selected as the designated sensor-instrumentation site.

Before installing the sensor trees on the soil layers, a series of preparatory activities shown in Figure 75 was undertaken. These activities involved (1) coring holes down to the top of the subgrade using a coring probe truck to install the sensor trees, (2) installing a wooden structure to provide support for the enclosure at the earth shoulder, and (3) pre-assembling the sensor trees and organizing strain gauges and thermistors at precise heights by affixing these sensors to carbon fiber rods. Carbon fiber rods were used to minimize the effect of rod-temperature changes on the thermistors.

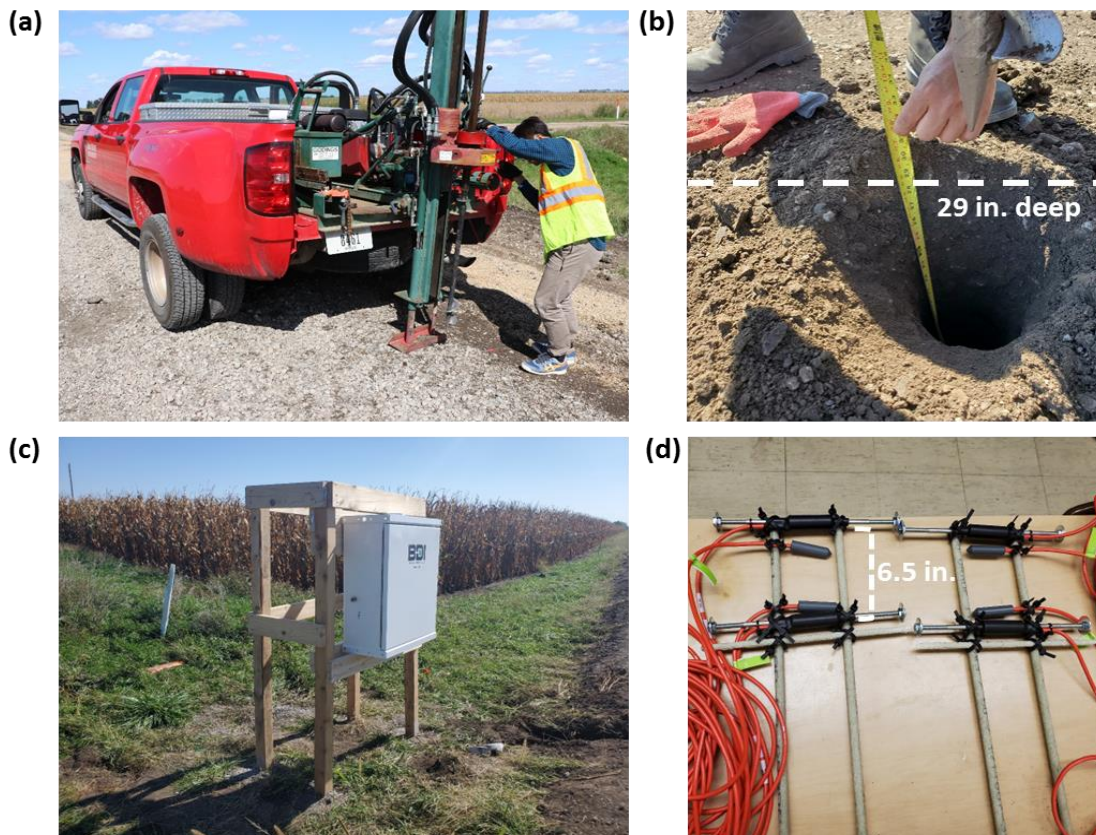


Figure 75. Activities prior to PCC paving: (a) coring holes using a coring probe truck (b) down to the subgrade surface, (c) installing wooden structure and enclosure at the earth shoulder, and (d) building sensor trees

On October 12, 2021, three days before the PCC paving commenced, sensor installation was performed. Initially, moisture sensors were positioned atop each soil layer, followed by installation of sensor trees containing strain gauges and thermistors into four pre-drilled holes. Sets of strain gauges and thermistors were then affixed to the top and bottom of the carbon fiber rods, ensuring a spacing of approximately 6.5 in. so as not to exceed the 8 in. thickness of the PCC slab. All sensor cables were then routed through flexible polyvinyl chloride (PVC) pipes embedded along the excavated path from the road edge to the earth shoulder where the enclosure was located, protecting them from potential damage caused by a two-track concrete paver and traffic loads. On the day of PCC paving, pre-placement of concrete over the sensor trees was performed to protect the sensors from the impact of concrete dropped by the two-track concrete paver. Following paving, texturing, and curing procedures, an external power supply was connected to the data acquisition system by installing an on-site transformer and meter. Upon completion of the installation process, it was confirmed that the system operated normally and could be remotely controlled while measuring JPCP responses under environmental and traffic loads. The overall steps of the data acquisition system installation process are illustrated in Figure 76.

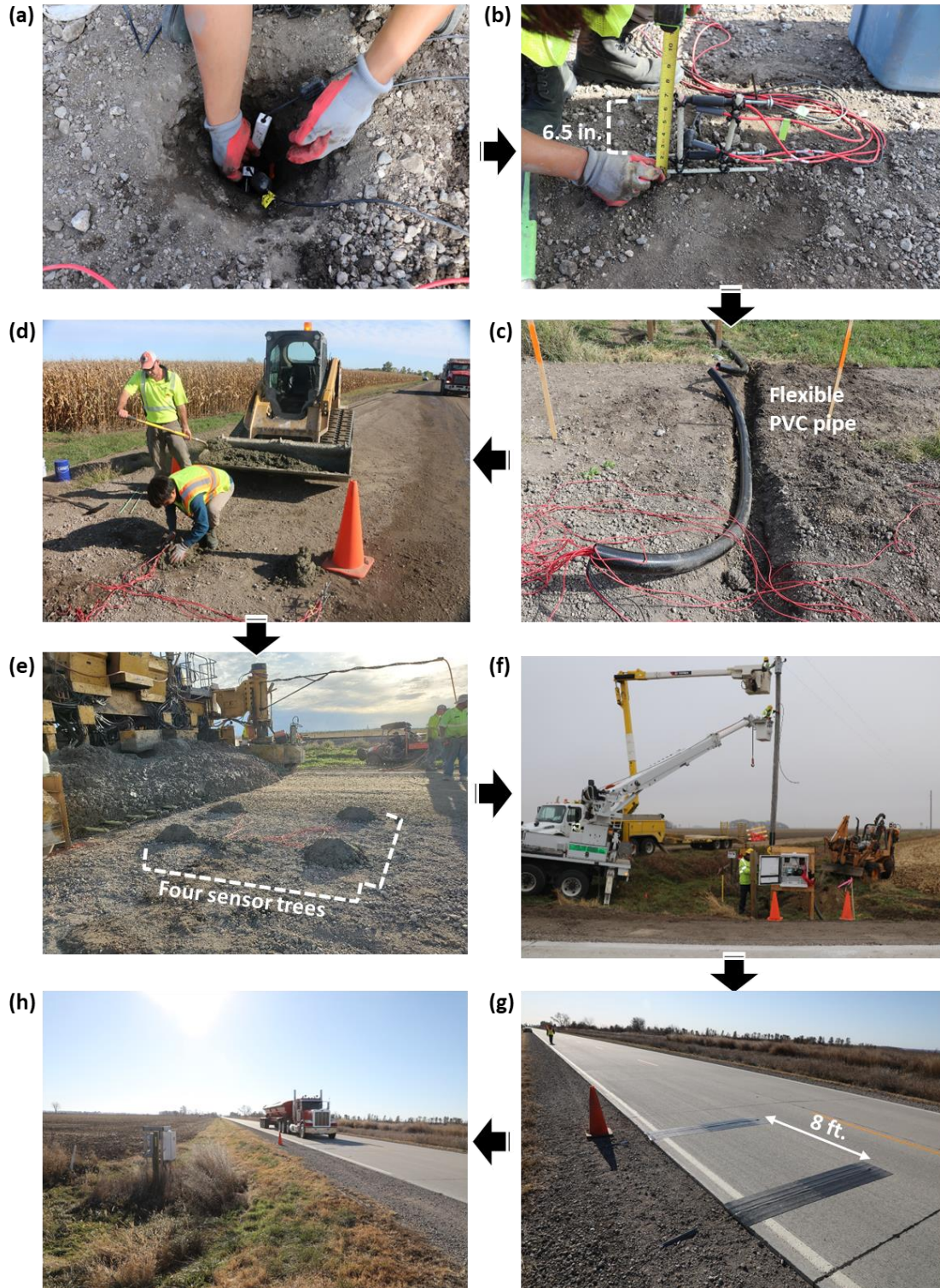


Figure 76. Overall steps of the data acquisition system installation: (a) installing moisture sensors and (b) sensor trees, (c) protecting sensor cables through flexible PVC pipe, (d) pre-placing concrete over sensor trees, (e) PCC paving, (f) connecting the external power supply, (g) installing P-WIM system, and (h) collecting the field data

It is important to highlight that, although the thickness of the PCC layer in the JPCP was intended to be 8 in., the actual thickness of the PCC layer was observed to be 8.5 in. upon examination of the concrete coring specimens. This discrepancy in PCC layer thickness was a crucial factor to consider in accurately constructing FEM-based models to verify the in situ data.

JPCP Performance Monitoring

In accordance with the sensor-installation plan delineated in Figure 72, all sensors were labeled and connected to their corresponding channels on the data loggers to prepare them for collecting long-term data. This section summarizes the results from analysis of field data collected on December 19, 2021, the same year the data acquisition system was installed, as well as on June 19, 2022. The field data, particularly concerning JPCP responses obtained through the remote sensing system during passage of a representative general class 9 truck, an IoH, and an SHL, underwent validation via comparative analysis with the FEM-based results, employing mechanistic models developed with a structure identical to that of the JPCP road section instrumented for field data collection.

Figure 77 depicts the one-day-based strain and temperature data in the PCC slab after noise elimination from data collected on December 19, 2021, and June 19, 2022. It is noteworthy that the data for December 19, 2021, were collected at a 100 Hz rate, while the data for June 19, 2022 were collected at a 50 Hz rate because it was confirmed that the 100 Hz measurement collected an excessive amount of data, and that the 50 Hz data measurement was sufficient to capture traffic-load data. All data points were collected 24-7, and the system was remotely controlled while it transmitted data. It can easily be seen in Figure 77 that the time-dependent temperature and strain in the PCC slab of the JPCP section collected during the winter season (i.e., data for December 19, 2021) seem very reasonable, i.e., the JPCP structure exhibited a positive temperature gradient for its PCC slab in the daytime (around 2 to 3 p.m.), resulting in tensile strain at the bottom of the PCC slab and compressive strain at the top of the PCC slab due to the downward curling effect, neglecting the initial compressive strain caused by concrete curing. Additionally, data collected during the spring season (i.e., data for June 19, 2022) indicates that, as expected, temperatures in the PCC slab increased dramatically, and the corresponding strains in the PCC slab were shown to exhibit behavior somewhat different from that in the winter season. Due to the increased internal temperature throughout the PCC slab, all strain gauges exhibited higher compressive-strain values than those measured in the winter season, and even the strain values measured at the bottom of the PCC slab showed some compressive strain during the daytime, even though the gradients of compressive strain were lower than those at the top of PCC slab.

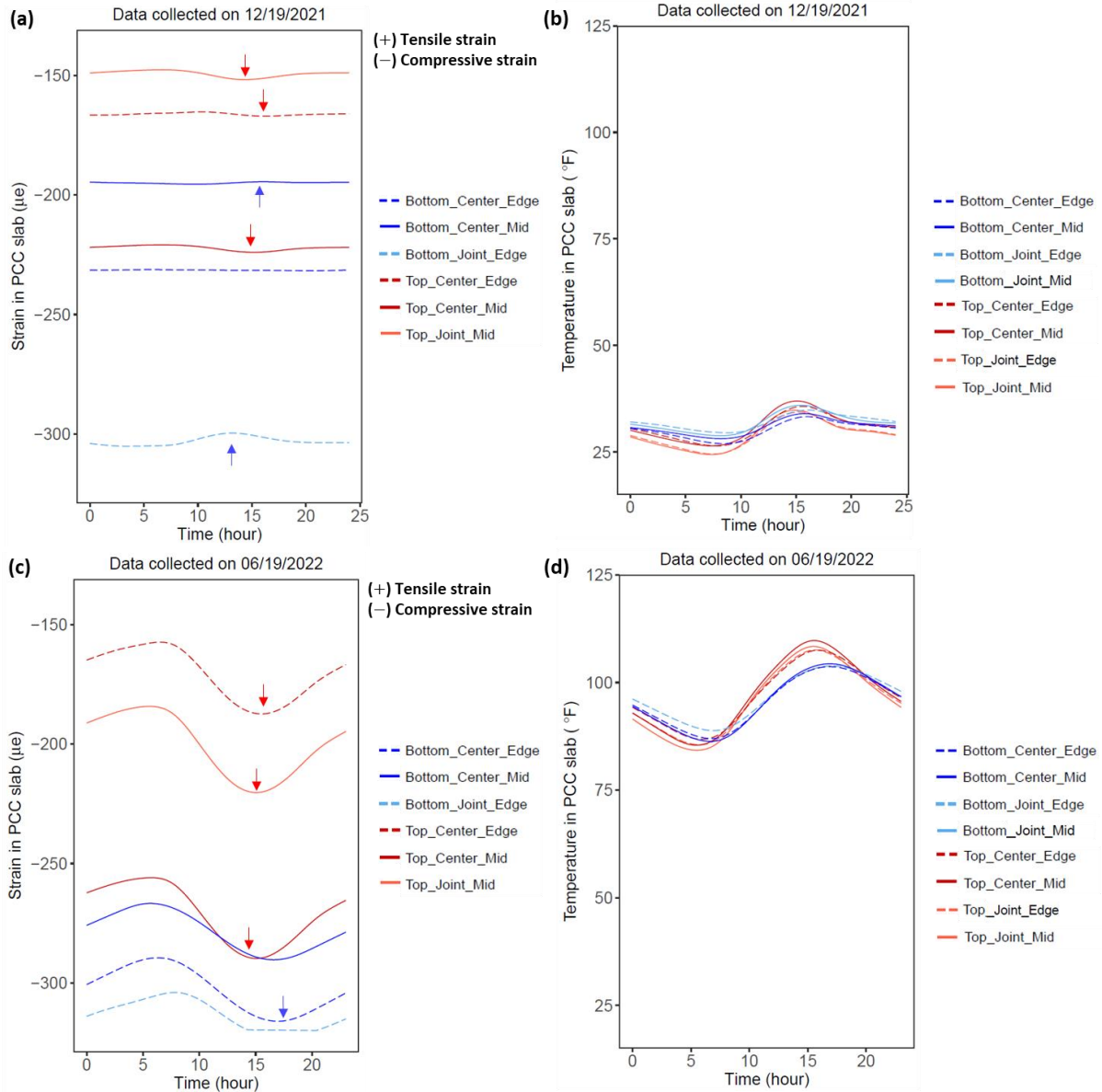


Figure 77. In situ JPCP data collected on December 19, 2021 including (a) strain and (b) temperature in the PCC slab, and on June 19, 2022 including (c) strain and (d) temperature in the PCC slab

Volumetric water content and temperature data recorded at the top of each soil layer by TEROS12 sensors are depicted in Figure 78 for the same two days. Except for the measured water content from the modified subbase layer located down the center of the PCC slab, most water content values were shown to be the highest at the subgrade and tended to decrease toward the upper layer for the two seasonal data collections. It was also observed that, during the winter season, the temperature of the subgrade layer was higher compared to that of other soil layers, attributable to the lower air temperature. Conversely, in the spring season, the modified subbase layer exhibited a higher temperature relative to other lower soil layers, likely due to the elevated air temperature.

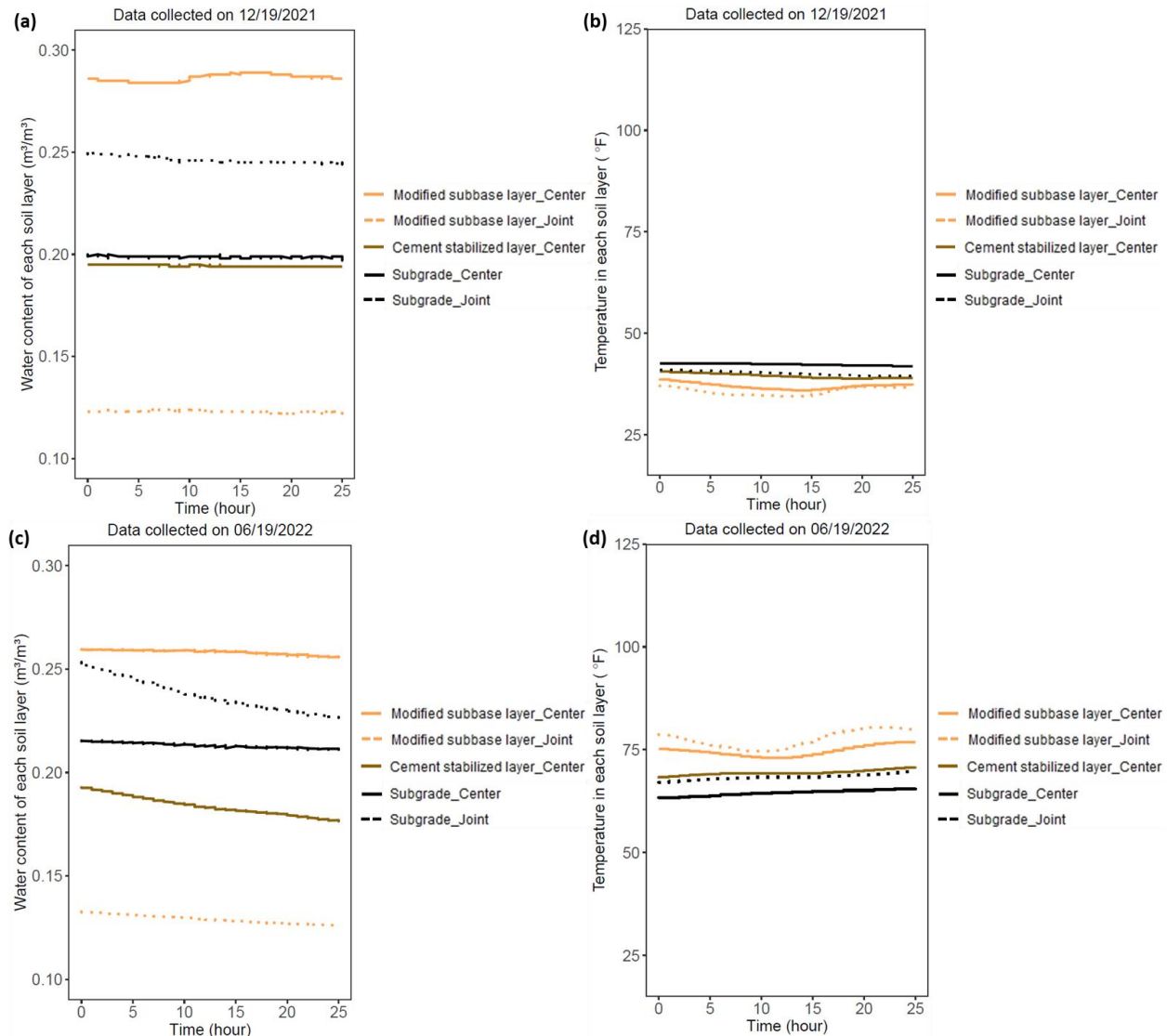
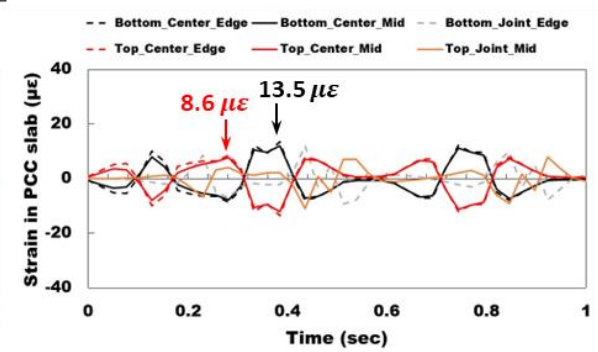
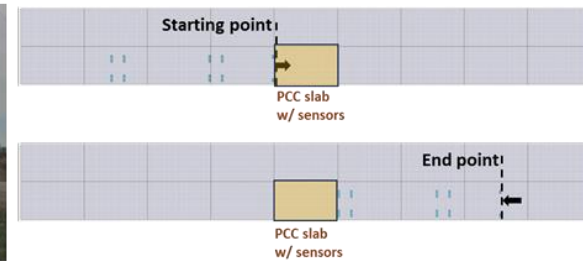
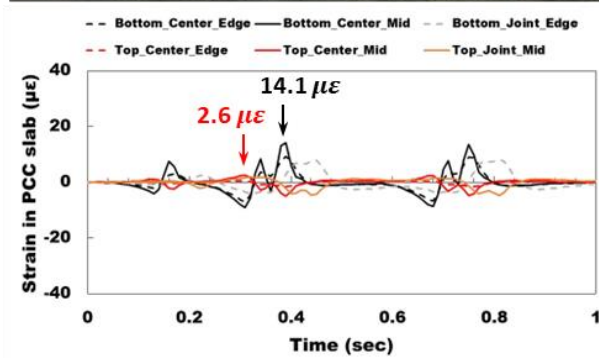
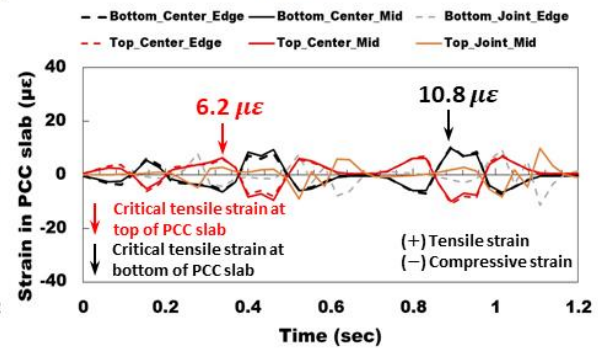
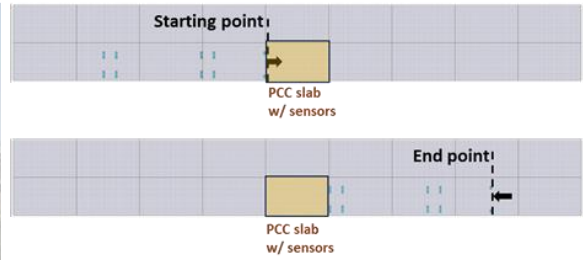
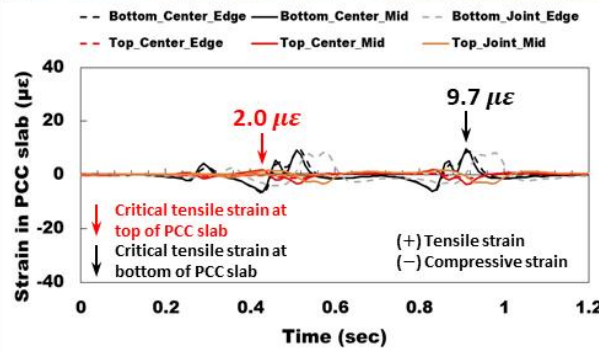


Figure 78. In situ JPCP data collected on December 19, 2021 including (a) water content and (b) temperature in soil layers, and on June 19, 2022 including (c) water content and (d) temperature in soil layers

Measuring the critical tensile strain or stress generated from traffic loads is critical when evaluating traffic impact on JPCP structural damage, especially fatigue cracking, over its service life (ARA, Inc. 2004a). Strain gauges and data loggers were able to capture dynamic strains in the PCC slab when subjected to different traffic loads comprised of different numbers of axles, even superload vehicles, while the P-WIM system collected necessary traffic loading information, including GVW, vehicle class, speed, axle weight, and axle spacing. Strain variations and critical tensile strain caused by a single pass of four transportation vehicle types: a class 9 truck with GVW close to the permit limit (i.e., 80 kips), a class 9 truck having about 12% higher GVW than the permit limit, a drop-deck SHL, and an agricultural truck IoH, were measured at a 50 Hz rate after removing noise and the initial compressive strain generated by concrete curing, as shown in Figure 79.



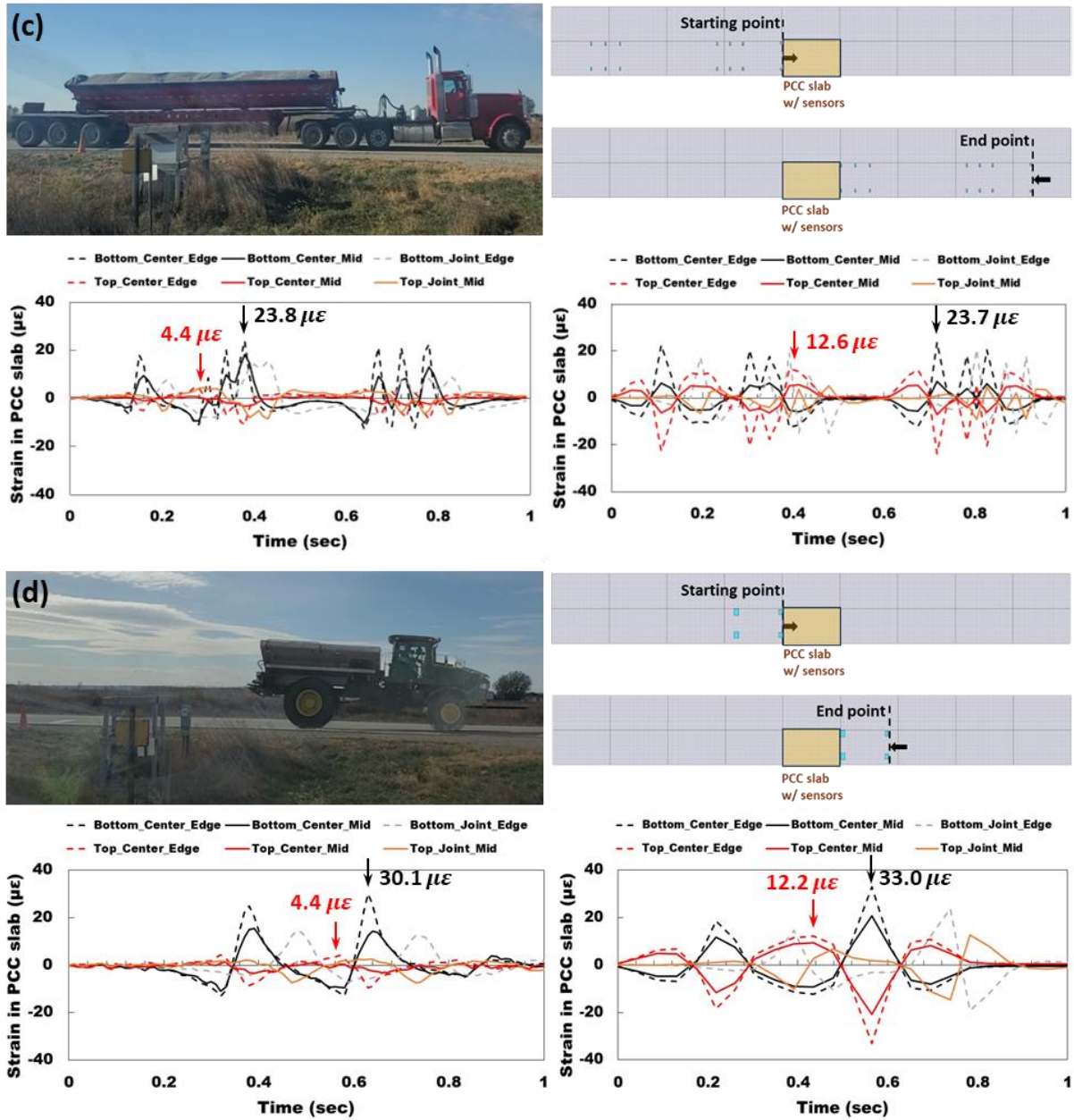


Figure 79. Sets of figures of transportation vehicles (top-left), FEMs (top-right), in situ JPCP strain data (bottom-left), and FEM-based analysis results (bottom-right) for (a) class 9 truck, (b) overweight class 9 truck, (c) drop-deck SHL, and (d) agricultural truck

Note that the authors selected a class 9 truck with a GVW 12% higher than the existing permit limit among all the traffic measured on-site, in accordance with Iowa Senate File 2376, effective in January 2023, which explicitly allows gross weights of permitted vehicles to exceed the gross weights in Iowa Code section 321.463 by up to 12% (i.e., 90 kips for class 9 truck).

To verify field data, computational analysis results derived from the FEM-based rigid pavement analysis program, ISLAB 2005, were also incorporated into Figure 79. FEM-based JPCP models

with the same structural and environmental conditions as K45 were developed, with a particular focus on the period from October to November 2023, during which vehicles traveled over the field instrumented road section. Detailed information on the FEMs is summarized in Table 36. As previously noted, upon inspection the actual thickness of the PCC layer in the JPCP was found to be 8.5 in., exceeding the planned thickness of 8 in. To accurately represent the JPCP structures, the FEMs were adjusted to reflect the measured thickness of 8.5 in. for the PCC layer.

Table 36. Summary of FEM information implementing K45 and traffic loads

JPCP structural properties for a period from October to November 2023				
PCC layer	Elastic modulus (psi)	4,000,000	Averaged temperature difference between top and bottom of PCC layer (°F)	-1.6 (varied over time when selected vehicles pass)
	Thickness (in.)	8.5	CTE (10 ⁻⁶ in./in./°F)	4.3
	Transverse joint spacing (ft)	20	LTE at transverse joints (%)	90
	Poisson’s ratio	0.2	Mesh size (in.)	6
Soil layers	Composite modulus of subgrade reaction* (psi/in.)			352
Selected traffic load properties collected from October to November 2023				
Vehicle type	GVW (kip)	Axle weight (kip)		Axle spacing (ft) from the front-most axle to the rear-most axle
Class 9 truck	76.3	10.3 (steering), 14.0/17.7 (front tandem), 16.9/17.4 (rear tandem)		18.0, 4.3, 35.1, 4.1
Overweight class 9 truck	89.8	14.7 (steering), 19.0/19.4 (front tandem), 18.4/18.3 (rear tandem)		12.1, 4.6, 34.3, 4.4
Drop-deck SHL	192.2	27.1 (steering), 16.0/31.5/30.3 (front tridem), 30.3/28.7/28.3 (rear tridem)		13.1, 4.6, 4.5, 33.7, 5.1, 5.0
Agricultural truck	63.2	23.9 (front single), 39.3 (rear single)		15.5

* In situ pre-testing results were utilized to calculate the composite modulus of subgrade reaction.

It can be easily recognized that for the various vehicle types shown in Figure 79, the maximum positive peak-tensile strains collected from the bottom of the PCC slab can be regarded as the critical pavement responses related to bottom-up fatigue cracking, while the maximum positive tensile strains obtained from the top of the PCC slab are indicative of critical pavement responses associated with top-down fatigue cracking. By comparing in situ critical pavement response data with those obtained from FEM-based analysis results, it was confirmed that the strain-variation trends depicted in Figure 79a for a class 9 truck, Figure 79b for an overweight class 9 truck, and Figures 79c and 79d for superloads, exhibited notable similarities between in situ data and FEA results. The critical tensile strains collected in situ from the bottom of the PCC slab exhibited magnitudes remarkably like those from the FEA results. In contrast, substantial gaps in the magnitude of critical tensile strains when compared to the FEA results were shown from the top of the PCC slab; for example, 6.2 $\mu\epsilon$ of critical tensile strain at the top of the PCC slab was obtained from FEA while 2.0 $\mu\epsilon$ was measured in situ when subjected to the 80 kips class 9 truck loading.

To investigate the reason for the lower magnitude of critical tensile strains at the top of the PCC slab collected in situ, an MIRA ultrasonic tomograph (ACS Group 2018) displayed in Figure 80 was used at the field instrumentation site to capture the exact locations of strain gauges that could potentially affect the magnitudes of tensile strains.

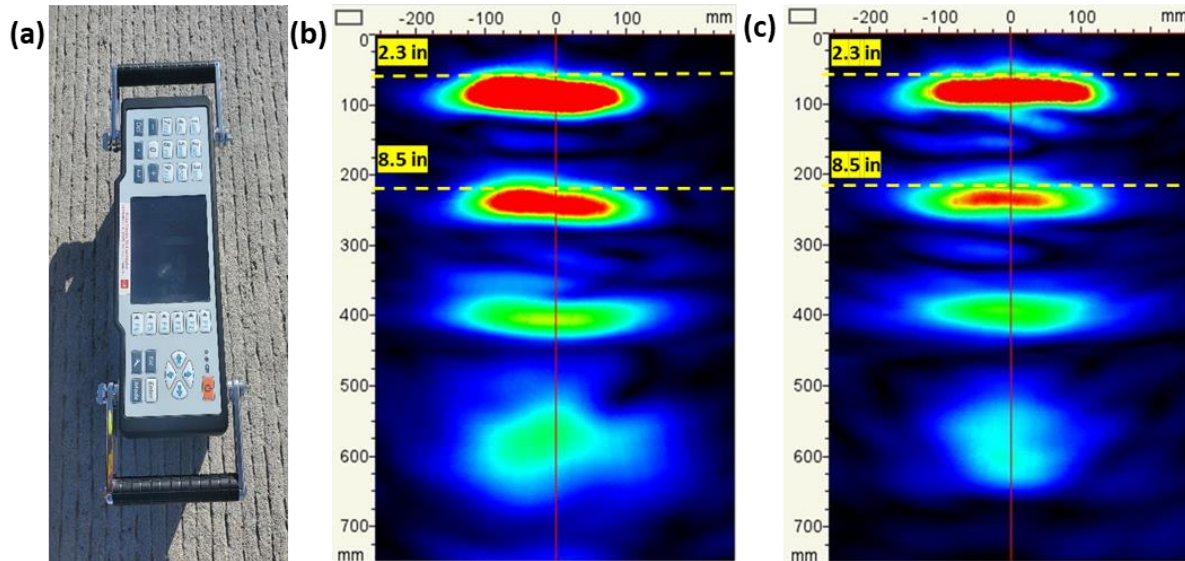


Figure 80. (a) MIRA ultrasonic tomograph and images of sensor trees embedded at (b) Center_Edge and (c) Center_Mid

Upon examination, while it was confirmed that the strain gauges intended to be located at the bottom of the PCC slab were positioned at the appropriate depths, aligning with the lowest part of the slab, it was discovered that the strain gauges intended to be located at the top of the slab were located approximately 2.3 in. below the JPCP surface. A possible reason for this discrepancy was attributed to the weight of the concrete falling from the concrete paver during concrete paving, possibly leading to the strain gauges at the top of the sensor trees being lowered. To address this issue, the authors conducted post-processing to linearly increase the tensile strains collected at a depth of 2.3 in. below the top of the PCC slab to account for traffic and temperature gradient impacts (Huang 2004). This adjustment assumed that the strain gauges were located near the JPCP surface, as depicted in Figure 81a. As a result of this corrective measure, Figure 81b indicates that the scaled field data, including critical tensile strain at the top and bottom of the PCC slab when subjected to class 9 trucks and superloads, could be verified as reliable in situ data compared with the FEA results, revealing a notably high degree of similarity, with a coefficient of determination R^2 of approximately 0.98.

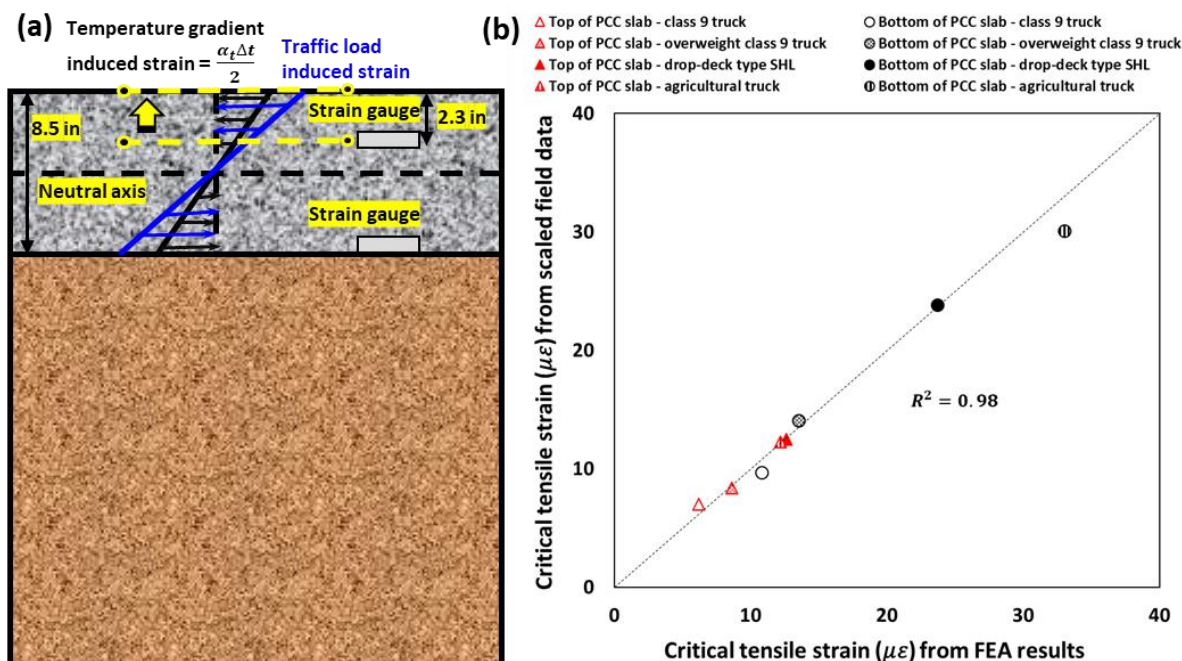


Figure 81. (a) Schematic drawing of field data scaling and the (b) verification of field data using FEM-based analysis results

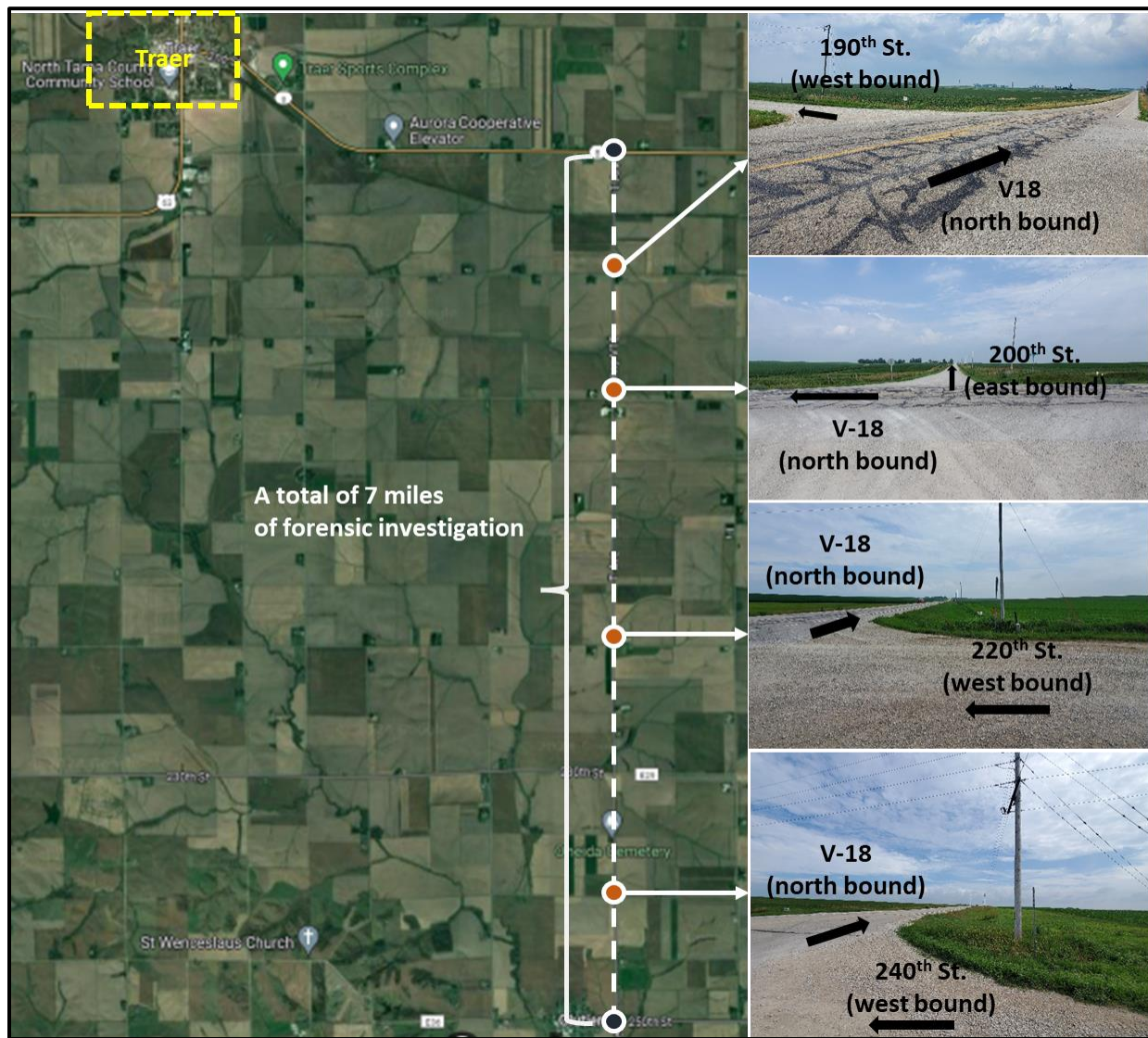
Field Instrumentation and Monitoring at Flexible Pavement Section

In September 2022, a remote data acquisition system was installed at V18, characterized as a full-depth flexible pavement, located near its intersection with 190th Street in Tama County, Iowa. This system included a P-WIM system along with various other sensors, such as strain gauges, soil compression sensors, pressure cells, thermistors, and moisture sensors. This section provides an overview of the quantity and type of sensors employed, focusing on measuring pavement responses related to structural distress, notably bottom-up fatigue cracking and rutting, within a full-depth flexible pavement section. The analysis of in situ data accounted for environmental factors such as temperature and water content, in conjunction with the impact of traffic loads.

Site Condition

To install the sensors within the pavement structure, since a minimal portion of the full-depth flexible pavement required cutting and excavation at designated locations for sensor installation, it was necessary to obtain approval from the county engineer to ensure authorization for damaging the existing pavement. The research team considered several key factors when selecting the sensor installation site, including (1) choice of a section with a full-depth flexible pavement structure, (2) frequent truck, IoH, or SHL traffic, (3) accessibility to an external power source from the earth shoulder near the designated sensor installation spot, and (4) absence of traffic obstructions such as traffic lights or stop signs. As a result, the research team received approval from the Tama County engineer to cut a 4 ft × 4 ft area of V18 near the intersection


with 190th Street for sensor installation purposes, and to repair the damaged section under the guidance and support of the county engineer following sensor installation. Detailed information about V18 in Tama County, identified as the optimal field instrumentation site for the full-depth flexible pavement system, is provided in Figure 82 and Table 37.



© Google 2024

Figure 82. Site information for V18

Table 37. Summary of V18 information

Question	Answer
Road section name	V18
Road type	Full-depth flexible pavement (reconstructed in 2004)
No. of lanes	Two lanes (one per each direction)
Width of lane	11 ft per lane
Length of road section under forensic investigation	7 mi
Thickness of paving layer	HMA layer: 6.5 in.
AADT	740
Primary vehicles	Resident vehicle, truck, IoH
Averaged PCI	-
Averaged IRI (in./mi)	151
Major failure type	 <p>Alligator cracking, longitudinal cracking, transverse cracking</p>

Based on site investigation and communication with the county engineer, a particular section of V18 near 190th Street, featuring a utility pole in close proximity to both V18 and 190th Street, was identified as an appropriate site for installing the data acquisition system. It was also discovered through an Iowa One Call investigation that there was minimal interference from embedded internet and telephone cables and water pipes in V18 near 190th Street compared to other intersections, so that the excavation required for sensor installation would be unlikely to cause damage to existing underground facilities in this area.

It is notable that the road condition of 190th Street and the distance from the utility pole to 190th Street, characterized as a granular road, were also crucial factors for selecting the field instrumentation site. This was because it was planned so that the sensors installed in both the full-depth flexible pavement and the granular road could share a single core data logger housed within a single enclosure installed at the intersection to reduce costs associated with additional enclosures, data loggers, modems, and other related components. The quantity and type of sensors installed on 190th Street will be discussed in detail later in this chapter.

Field Instrumentation Plan

Unlike the field instrumentation conducted on the reconstructed JPCP section, scheduling for field instrumentation at the full-depth flexible pavement site was more flexible since the main procedure of field instrumentation on V18 was partial cutting and installation of sensors within the full-depth flexible pavement system that could be arranged at any time in coordination with the Tama County engineer. The sensor installation and operation of the data acquisition system took place on September 21, 2022, contingent upon the availability of the county engineer and staff. Before the sensor installation, preparatory steps included an underground facility investigation conducted by Iowa One Call and installation of wooden supports at the earth shoulder near the utility pole located at the intersection of V18 and 190th Street, completed by August 18, 2022. All components of the data acquisition system underwent thorough preparation and pre-testing in advance of the main installation phase.

A comprehensive array of sensors and components were readied to evaluate the performance of the full-depth flexible pavement system under environmental and traffic loads, with specific focus on bottom-up fatigue cracking and rutting. These included strain gauges for measuring strain at both the top and bottom of the AC layer, thermistors and moisture sensors for monitoring temperature and water content in each layer, soil compression sensors for measuring vertical displacement at 6 in. below the top of the subgrade, and a pressure cell for collecting vertical pressure at the top of the subgrade. Note that strain gauges were also installed at the top of the AC layer in case there might be a need to evaluate top-down fatigue cracking in future studies. Corresponding data loggers, as well as auxiliary components such as modems, ethernet networking for remote control, power components, and enclosures, eventually shared with the sensors installed in the granular road, were also prepared. A P-WIM system equipped with a pair of piezoelectric sensors and a traffic counter was also prepared to collect load data generated by traffic passing through the remote-controlled sensor installation section.

Table 38 provides a comprehensive overview of the embedded sensor types, the P-WIM system, and their brief specifications, along with other components of the data acquisition system installed on the earth shoulder near the sensor installation site.

Table 38. Brief specifications of data acquisition system components for flexible pavement

Component type*	Model	Description	Number	Location
Strain gauge	AST350 (BDI 2022b)	Embeddable strain transducer	4	Top of AC layer
			6	Bottom of AC layer
Soil compression sensor	SCS-010F (BDI 2022c)	Vertical displacement in unbound aggregate material	2	6 in. below the top of subgrade
Earth pressure cell	ER-3500 (GEOKON 2023)	Semiconductor type transducer for dynamic pressure measurement	1	Top of subgrade
Thermistor	TS-EM (BDI 2024a)	Embeddable temperature sensor	2	Top of AC layer
			2	Bottom of AC layer
Moisture sensor	TEROS12 (METER Group 2024)	Volumetric water content, temperature, and electrical conductivity sensor	3	Top of soil layers
Data logger	STS-CDL-01 (BDI 2019)	Core data logger	1	Enclosure
	STS4-16-TE4 (BDI 2020)	16-channel data logger for strain gauges and thermistors	2	Enclosure
	ZL6 (METER Group 2023)	6-channel data logger for moisture sensors	1	Enclosure
Ethernet/modem	DCM-ICB600CD	Cellular wireless modem with a Verizon data plan	1	Enclosure
Power component	PW-AC-10A24	24V 10A power system	1	Enclosure
Enclosure	ENC-UB-36B2	Aluminum enclosure Size: 36 in. (H) × 30.5 in. (W) × 13.3 in. (D)	1	Earth shoulder
P-WIM system	TRS unit (IRD 2023a)	TRS collecting traffic volume, speed, weight, and classifications	1	Earth shoulder
	MSI-BL-CLS2 (IRD 2023b)	2.4 m length sensors	2	Surface of pavement

* Minor components of the data acquisition system are not listed here. Data loggers, modem, power component, and enclosure were shared with sensors installed on granular road section.

The AST350 strain gauge developed by BDI, specifically designed for asphalt applications, features a 6 in. gauge length and a full Wheatstone bridge configuration to facilitate the measurement of high-frequency dynamic responses, as shown in Figure 83a. A soil-compression sensor, also developed by BDI, was deployed to monitor vertical displacement at 6 in. below the top of the subgrade to account for rutting damage, as depicted in Figure 83b. An ER-3500 earth pressure cell developed by GEOKON was also prepared to monitor dynamic vertical pressure at the top of the subgrade, as shown in Figure 83c. Other sensors and components are identical to

the ones used in JPCP field instrumentation. Figure 83d illustrates the arrangement of strain gauges, thermistors, soil compression sensors, and an earth pressure cell connected to a 16-channel STS4-16-TE4 data logger manufactured by BDI, and moisture sensors were connected to a 6-channel ZL6 data logger developed by METER Group. All collected data were subsequently stored and processed in the central data logger, STS-CDL-01, as in the case of JPCP instrumentation. A wireless modem was included to facilitate remote system control and data transmission from the field. Given the system's intended purpose of measuring full-depth flexible pavement responses over extended periods, ensuring the presence of a consistent power supply was necessary, so the data acquisition system was designed with an internal power system capable of delivering a 24V 10A alternating current power output, complete with alternating current surge protection, circuit breakers, load terminals, and proper grounding, thereby ensuring reliable power distribution from the external power source. The overall configuration of the data acquisition system is illustrated in Figure 83e.

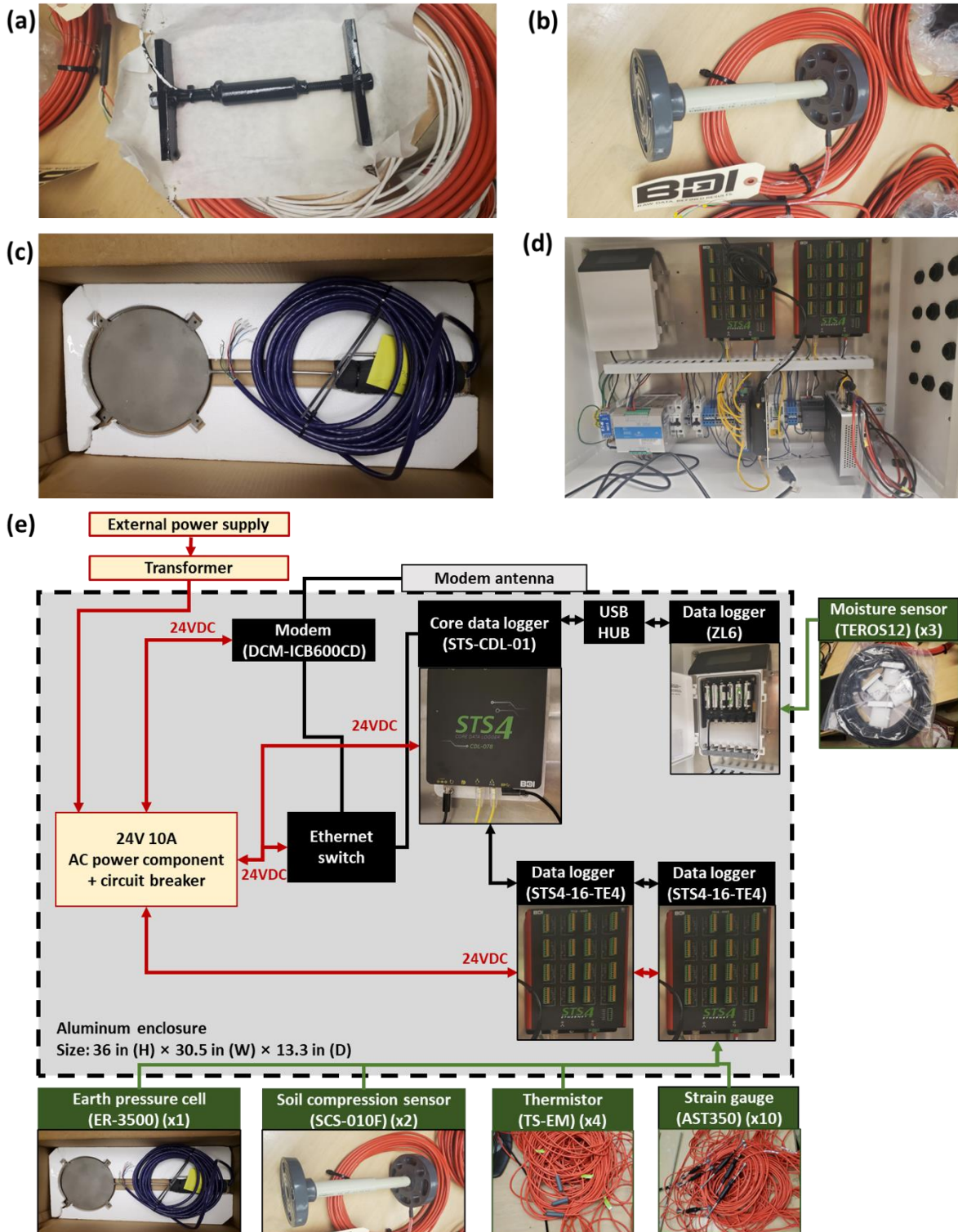


Figure 83. Major components of the data acquisition system: (a) strain gauge, (b) soil compression sensor, (c) earth pressure cell, (d) STS4-16-TE4 (right) and ZL6 (left), and the (e) overall configuration of the remote data acquisition system

To evaluate the impact of superloads on bottom-up fatigue and rutting damages, sensors detailed in Table 38 were strategically installed at the precise locations shown in Figure 84.

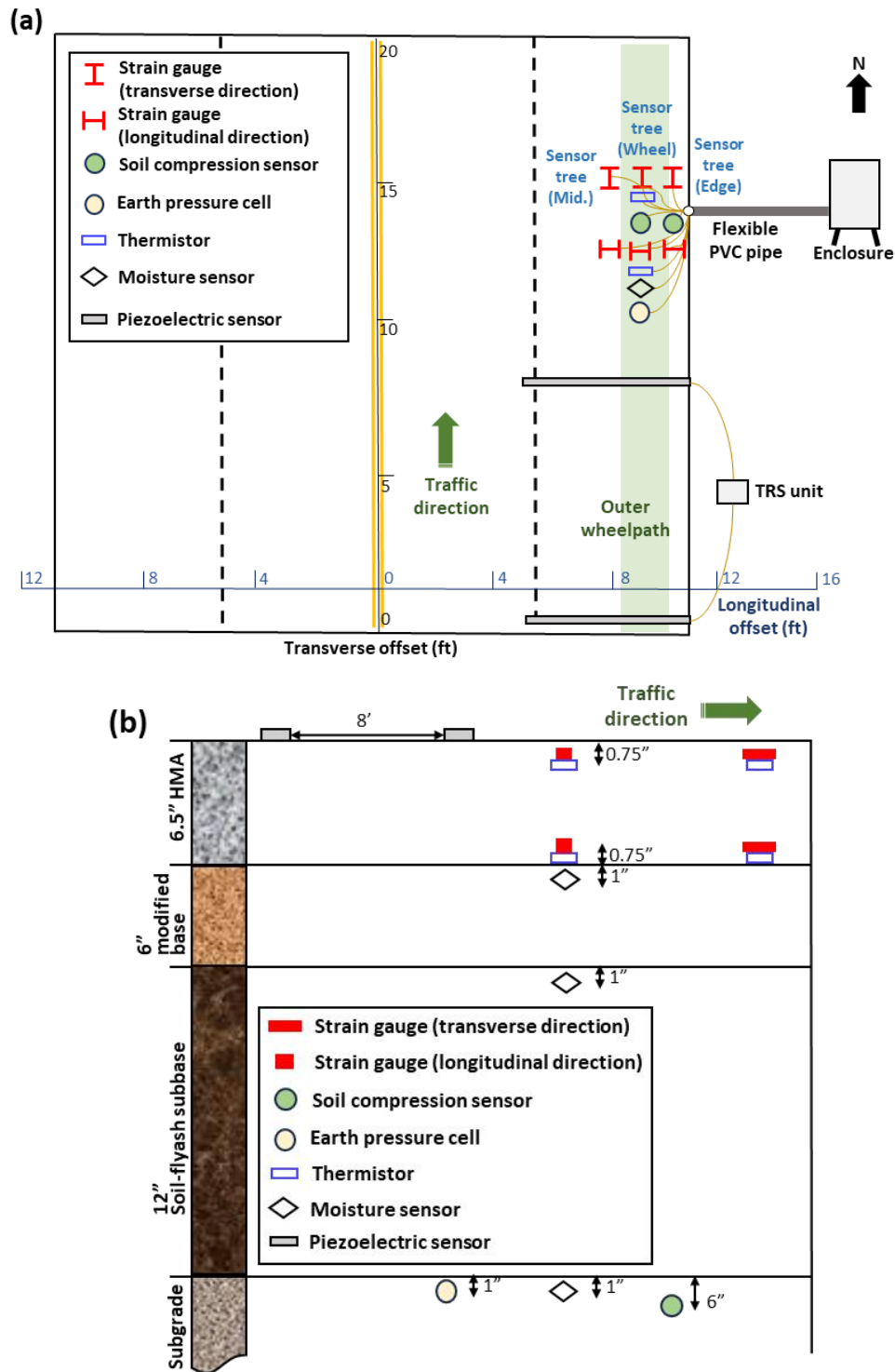


Figure 84. Sensor installation plan for full-depth flexible pavement section: (a) plane view and (b) cross-sectional view

As described in Chapter 5, critical tensile strains at the bottom of the AC layer and critical vertical strains at 6 in. below the top of the subgrade are predominantly generated either directly beneath the tire loading point or between two successive tire loading points, so six sensor trees were installed along the potential wheel path line and two additional lines that could potentially generate critical pavement responses in both longitudinal and transverse directions. These locations were selected based on the computational analysis results derived from Chapter 5, which identified locations where critical pavement responses were likely to occur due to superload traffic.

Field Instrumentation in Full-Depth Flexible Pavement Section

Preparatory activities were undertaken prior to excavating a portion of V18 near 190th Street. These included (1) installing a wooden structure to support the enclosure at the earth shoulder, (2) conducting an investigation of underground facilities via Iowa One Call, (3) building sensor trees using carbon fiber rods to affix strain gauges and thermistors, to be installed at specified depths within the AC layer, and (4) arranging for an excavator to conduct trench cutting and subsequent backfilling operations, as shown in Figure 85.

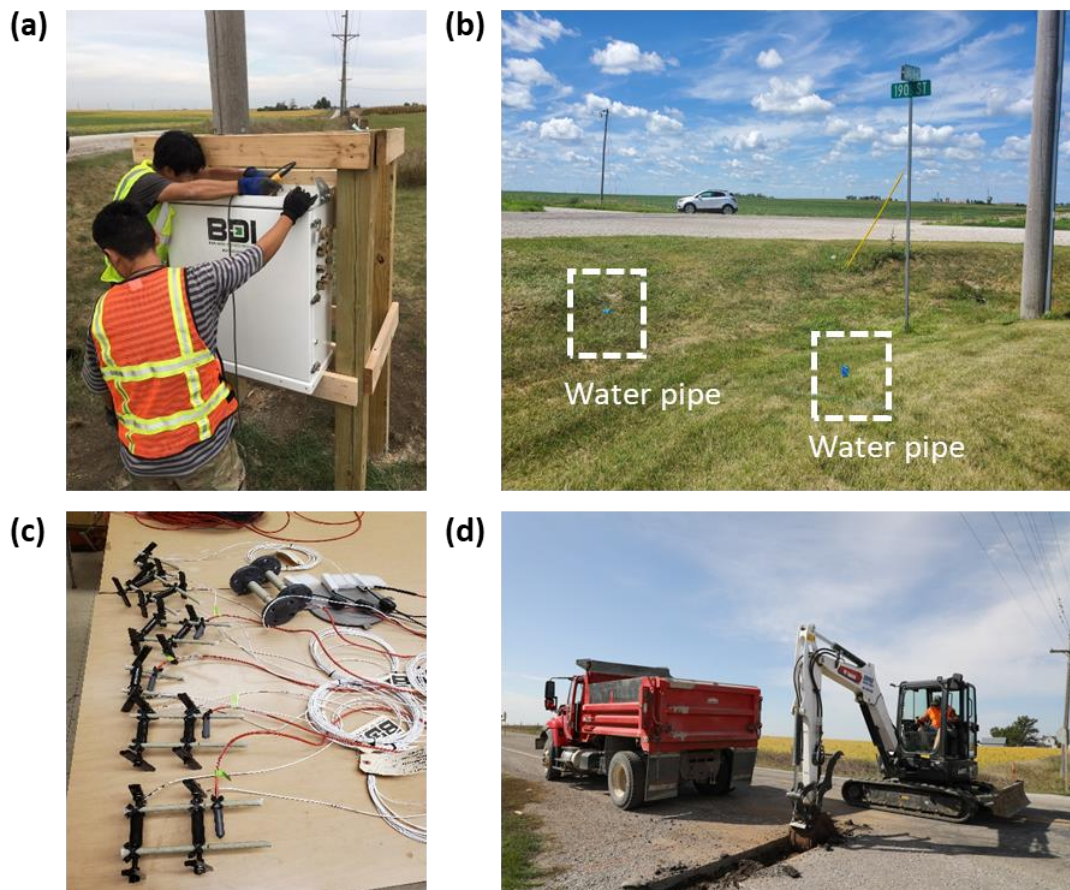


Figure 85. Activities prior to data acquisition system installation: (a) installing a wooden structure, (b) investigating underground facilities via Iowa One Call, (c) preparing sensor trees, and (d) arranging an excavator

The main field instrumentation activities for the full-depth flexible pavement were executed on September 21, 2022. This involved excavating a 4 ft × 4 ft area of V18 near the intersection with 190th Street, installing sensors, connecting these sensors to data loggers pre-located at the earth shoulder, and repairing the damaged road. To initiate the field instrumentation, the county engineer and their team took charge of traffic control to ensure safety. The excavator then proceeded to excavate the pre-cut 4 ft × 4 ft portion of the flexible pavement, as well as the route from the edge of the road to the earth shoulder where the enclosure was installed. Upon excavating down to the subgrade, an LWD test was conducted to measure the elastic modulus of the subgrade, approximately 9,200 psi. Note that LWD testing could not be conducted on the base and subbase layers because the excavation was carried out all the way down to the subgrade at once, after which all sensors were installed at the specified depths and locations as planned. To protect them from traffic loads, sensor cables were routed through flexible PVC pipes embedded along the excavated path, leading to the enclosure where they were connected to the data loggers. Following confirmation that the sensors and system were functioning correctly, the excavated route and damaged road were backfilled and repaired using asphalt materials provided by the county engineer. Upon completion of the installation process, it was verified that the system operated normally and could be remotely controlled while measuring the full-depth flexible pavement responses under environmental and traffic loads. The external power supply was later activated following the installation of the meter and transformer on-site, enabling continuous collection of pavement response data over time. The P-WIM system was also installed on-site to begin collecting traffic data. Detailed information about the P-WIM system, covering installation procedures and data collection protocols, is available in Appendix B.

The overall steps of the data acquisition system installation process are depicted in Figure 86. It is important to note that although the reported thickness of the AC layer was 6.5 in., the actual thickness observed during excavation was 6 in., so a 6 in. AC layer was included in the LET-based models when validating the in situ data, as discussed in the following section.



Figure 86. Steps of the data acquisition system installation: (a) pre-cutting a portion of the road, (b) trench cutting for the PVC pipe route, (c) excavating the designated portion of the road, (d) installing the sensors, (e) protecting sensor cables through flexible PVC pipe, (f) repairing the damaged road, (g) connecting the external power supply, and (h) installing P-WIM system

Full-Depth Flexible Pavement Performance Monitoring

This section provides the in situ data analysis results, encompassing horizontal strain of the AC layer, vertical displacement at 6 in. below the top of the subgrade, and temperature and water content within each soil layer, collected on June 2, 2023, and on November 2, 2023.

Furthermore, the field data, with a specific focus on the horizontal strain at the bottom of the AC layer and vertical strain at 6 in. below the top of the subgrade, acquired through a remote sensing system during the passage of a representative general class 9 truck and IoH, underwent validation through comparative analysis with LET-based results. These analyses employed mechanistic models developed with a flexible pavement structure identical to the road section instrumented for field data collection.

Figure 87 depicts collected strain and temperature data after noise removal in the AC layer over 24 hours on June 2, 2023, and November 2, 2023. The data from both days were collected at a frequency of 50 Hz, with the system being remotely controlled during data collection and transmission. Notably, it can be confirmed from Figure 87 that the time-dependent strain in the AC layer of the full-depth flexible pavement section collected on both June 2 and November 2 exhibited trends somewhat different than expected. While the overall time-dependent temperature collected on November 2 was observed to be lower than that collected on June 2, with daytime temperatures measured higher than nighttime, as expected, the time-dependent tensile strains collected on June 2 were found to be higher between 12 a.m. to 9 a.m. compared to those between 1 p.m. and 4 p.m. The same trend was observed in the data collected on November 2, contrary to expectations. These discrepancies can be attributed to the partial cutting and subsequent repair of the AC layer that resulted in the creation of construction joints and introduced additional boundary conditions near the installed sensors. As a result, the horizontal strain responses to temperature variations were observed to follow a trend markedly different from the anticipated behavior. This underscores a limitation of in situ data analysis for full-depth flexible pavement, particularly due to the limited number of full-depth flexible pavement sections available in Iowa, making it challenging at present to find road sections undergoing full-depth flexible pavement reconstruction. Still, the in situ data remain valuable for validating LET-based analysis results, despite acknowledging the influence of construction joints on pavement responses when subjected to superloads.

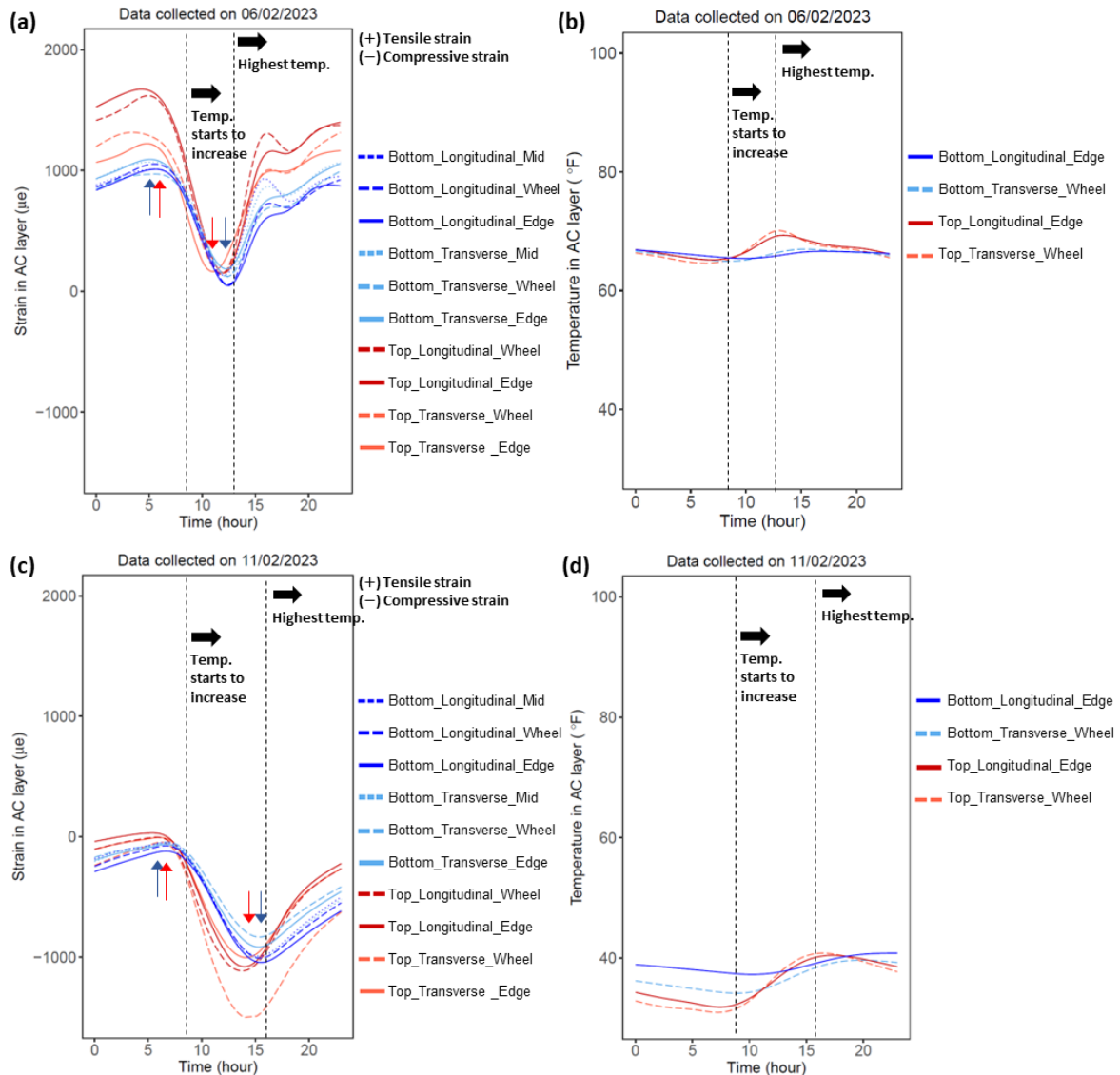


Figure 87. In situ full-depth flexible pavement data collected on June 2, 2023 including (a) strain and (b) temperature in the AC layer, and on November 2, 2023 including (c) strain and (d) temperature in the AC layer

The analysis of vertical displacement, measured at 6 in. below the top of the subgrade for a 24-hour period on both June 2 and November 2, 2023, is presented in Figure 88. It was observed that the subgrade soil underwent increased compression, resulting in higher vertical displacement during periods of elevated temperature in daytime. The overall vertical displacements recorded on November 2 were also lower compared to those on June 2, attributed to the higher resilient modulus of the subgrade in November, consistent with the expectations of the research team.

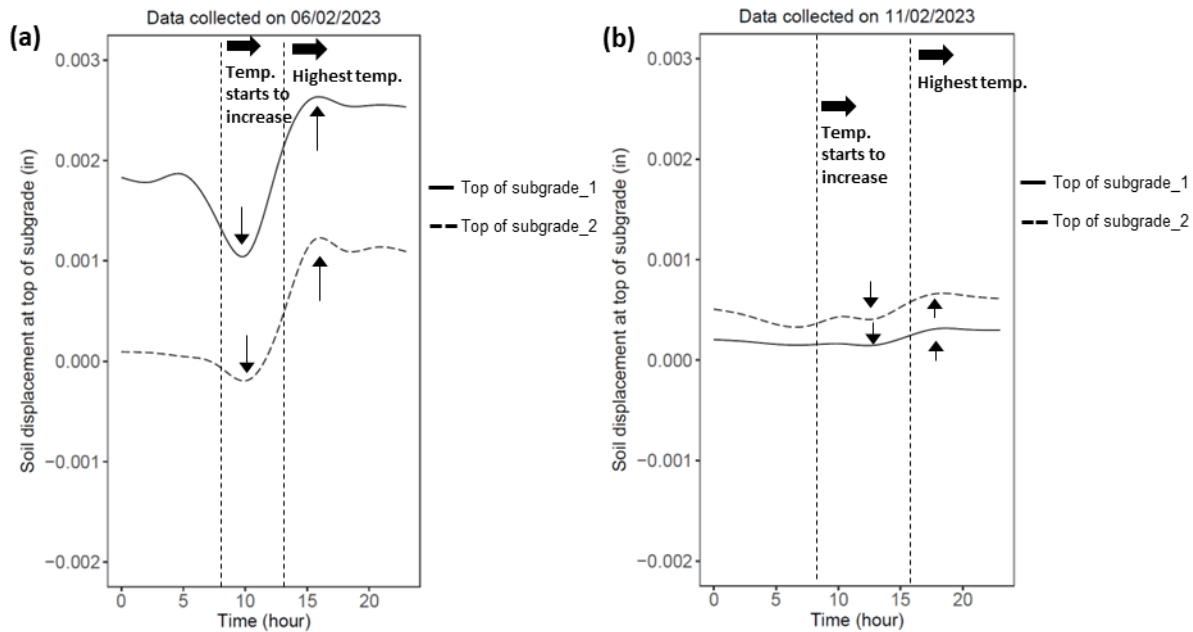


Figure 88. In situ vertical displacement data measured at 6 in. below the top of the subgrade collected on (a) June 2, 2023, and (b) on November 2, 2023

The volumetric water content and temperature data recorded at the top of each soil layer by TEROS12 sensors are depicted in Figure 89 for the same two days. An interesting observation was made on June 2, where precipitation began around 1 p.m., leading to a significant increase in water content values across all soil layers, with the most pronounced increase observed in the subgrade. It was also noted that the overall temperatures of the soil layers collected on November 2 were lower compared to those recorded on June 2, as expected. During the daytime, the temperatures of the subgrade were also observed to be the lowest among the three soil layers, consistent with expectations.

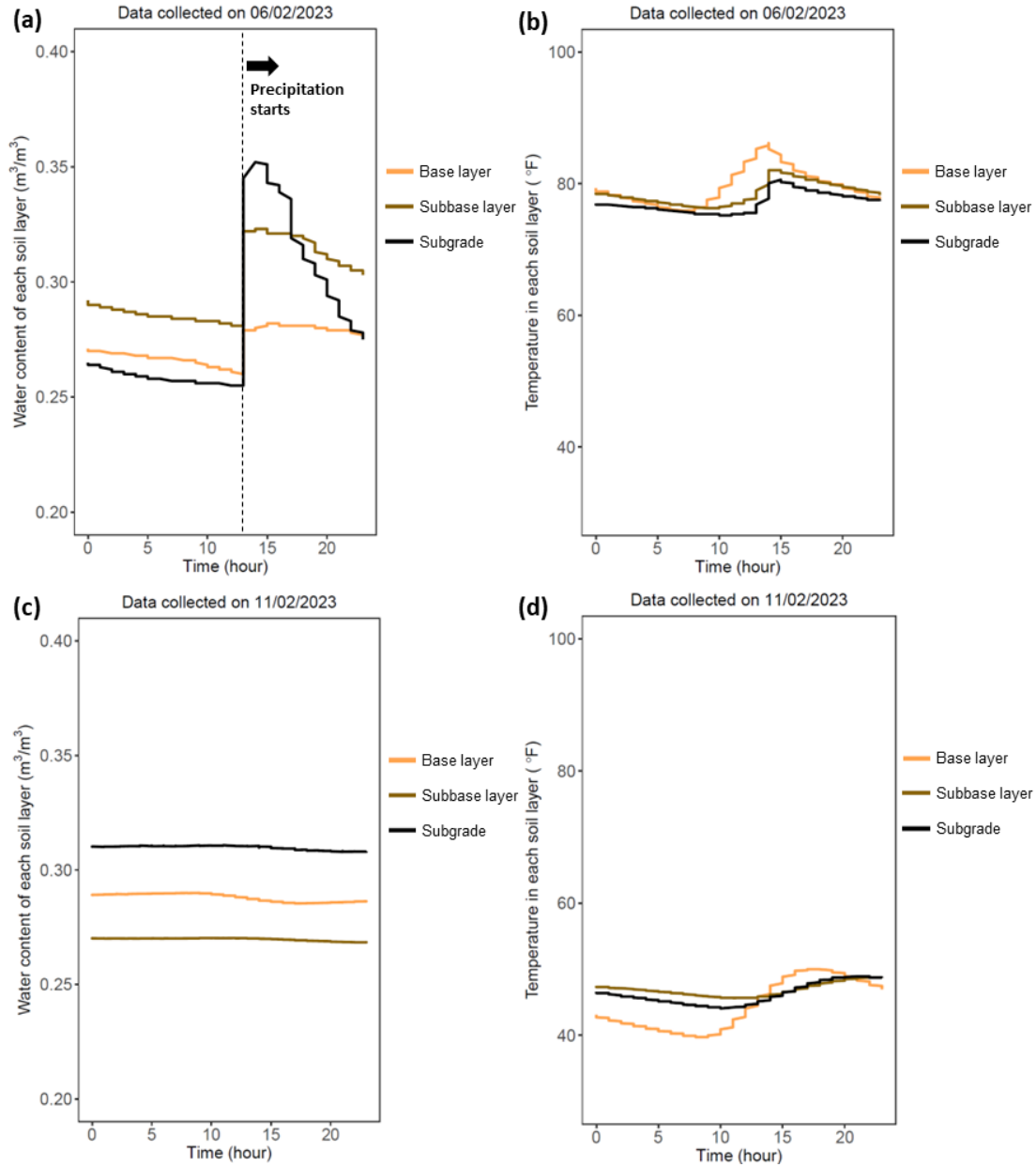


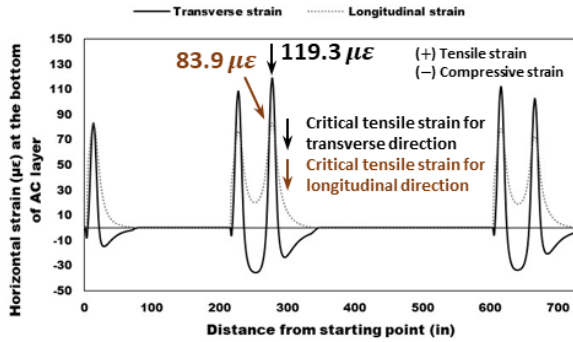
Figure 89. In situ full-depth flexible pavement data collected on June 2, 2023 including (a) water content and (b) temperature in soil layers, and on November 2, 2023 including (c) water content and (d) temperature in soil layers

The strain gauges embedded in the AC layer and the soil compression sensors installed in the subgrade effectively captured dynamic horizontal strain and vertical displacement, respectively, in response to various traffic loads. Simultaneously, the P-WIM system gathered essential traffic-loading data, including GVW, vehicle class, speed, axle weight, and axle spacing. Critical tensile strain at the bottom of the AC layer and critical vertical strain at 6 in. below the top of the subgrade, induced by a single pass of a class 9 truck with a GVW of 74 kips, and an agricultural truck IoH with a GVW of 55 kips, were recorded at a 50 Hz rate after noise removal, as depicted in Figure 90 and Figure 91, respectively.

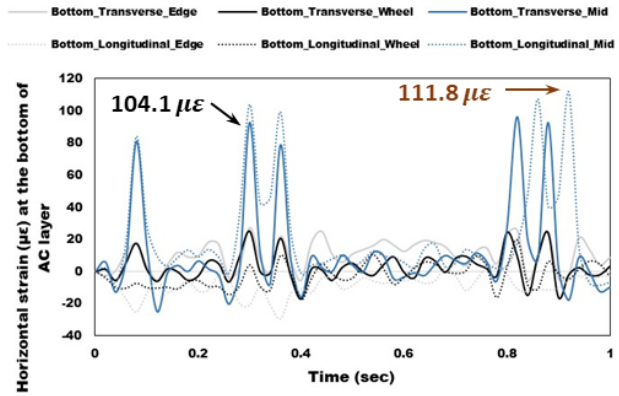
(a)



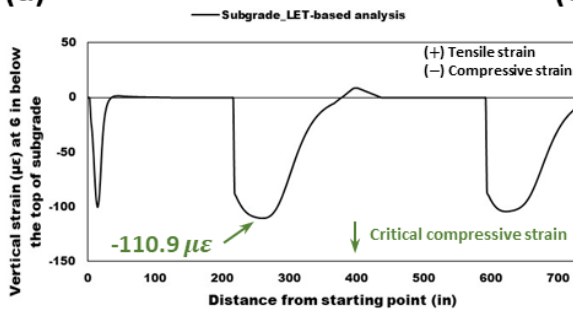
(b)



(c)



(d)



(e)

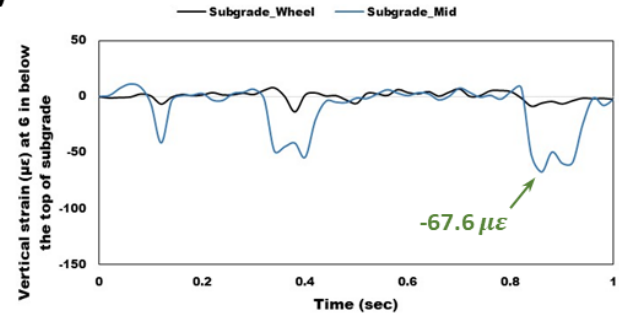


Figure 90. Pavement response of the sensor installation section to the (a) passage of a class 9 truck, exhibiting the resulting horizontal strain at the bottom of the AC layer through (b) LET-based analysis and (c) in situ AC layer strain data, and the resulting vertical strain at 6 in. below the top of the subgrade via (d) LET-based analysis and (e) in situ subgrade strain data

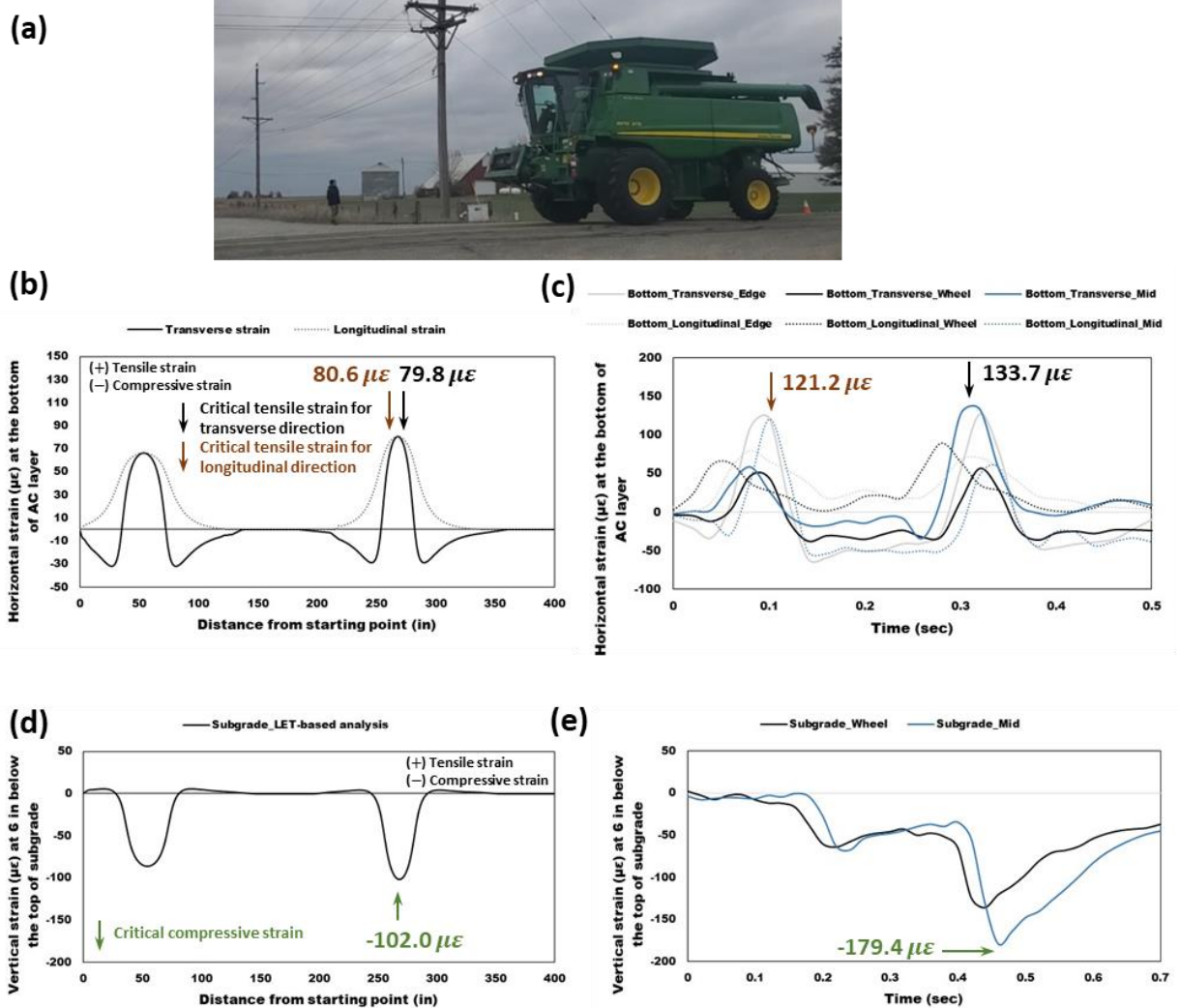


Figure 91. Pavement response of the sensor installation section to the (a) passage of an agricultural truck, exhibiting the resulting horizontal strain at the bottom of the AC layer through (b) LET-based analysis and (c) in situ AC layer strain data, and the resulting vertical strain at 6 in. below the top of the subgrade via (d) LET-based analysis and (e) in situ subgrade strain data

To validate the field data, computational analysis results from the LET-based pavement analysis program MnLayer are also shown in Figure 90 and Figure 91. Applying the structural conditions of V18, LET-based flexible pavement models were developed; detailed information for these LET-based analysis models is summarized in Table 39.

Table 39. Summary of LET-based model information implementing V18 and traffic loads

Structural properties of full-depth flexible pavement				
AC layer	Elastic modulus (psi)	500,000	Thickness (in.)	6
Base layer	Elastic modulus (psi)	35,000	Thickness (in.)	6
Subbase layer	Elastic modulus (psi)	30,000	Thickness (in.)	12
Subgrade	Elastic modulus (psi)*	9,200	Thickness (in.)	∞
All layers	Poisson's ratio			0.35
Selected traffic load properties collected from October to November 2023				
Vehicle type	GVW (kip)	Axle weight (kip)		Axle spacing (ft) from the front-most axle to the rear-most axle
Class 9 truck	73.7	7.3 (steering), 16.4/17.7 (front tandem), 16.8/15.5 (rear tandem)		17.6, 4.3, 28.2, 4.3
Agricultural truck	55.3	33.2 (front single), 22.1 (rear single)		16.7

* In situ pre-testing result was utilized for calculating elastic modulus of the subgrade.

As previously mentioned, upon in situ inspection, the actual thickness of the AC layer at the excavation section was found to be 6 in., lower than the 6.5 in. thickness indicated in the V18 reconstruction design drawing from 2004. To accurately represent the flexible pavement structures in MnLayer, the thickness of other soil layers, including the modified base and soil-fly ash subbase, were adjusted to 6 in. and 12 in., respectively, based on the 2004 reconstruction plan and measurements conducted by the research team during the excavation. The modulus of elasticity of the subgrade was derived from the LWD testing result, while the modulus of elasticity of other layers was based on general values for the fall season (Table 18) previously used for mechanistic-based analysis.

It is evident from Figure 90 and Figure 91 that the maximum positive horizontal strains collected from the bottom of the AC layer, observed for the general class 9 truck and the agricultural truck, respectively, signify critical pavement responses linked to bottom-up fatigue cracking. The maximum negative vertical strains measured at 6 in. below the top of the subgrade indicate critical pavement responses associated with rutting damage. Upon comparison of the in situ critical pavement response data with those obtained from LET-based analysis results, notable discrepancies were observed between the critical strains depicted in Figure 90 and Figure 91 for the class 9 truck and the agricultural truck, respectively. For example, when the flexible pavement section was subjected to a class 9 truck, the critical tensile strains measured in situ at the bottom of the AC layer were recorded at 104.1 $\mu\epsilon$ and 111.8 $\mu\epsilon$ for the transverse and longitudinal directions, respectively. In comparison, the LET-based analysis yielded values of 119.3 $\mu\epsilon$ and 83.9 $\mu\epsilon$ for the transverse and longitudinal directions, respectively. These differences were further accentuated during the agricultural truck passage, where the in situ critical tensile strains at the bottom of the AC layer were measured at 133.7 $\mu\epsilon$ and 121.2 $\mu\epsilon$ for the transverse and longitudinal direction, respectively, while the LET-based analysis indicated values of 79.8 $\mu\epsilon$ and 80.6 $\mu\epsilon$ for the same directions. Similar inconsistencies were observed in the case of vertical strain in the subgrade.

Several factors may contribute to these inconsistencies. One possible reason is that the formation of construction joints during the road damage and repair process may impact the magnitude of pavement responses. Inaccuracies in the modulus of each layer and the traffic load data collected from the P-WIM system, as well as deviations in the passage of traffic, and whether it passed directly above the sensor-tree locations, could also play a role. Despite these discrepancies, since the in situ pavement response and traffic data remain valuable as empirical data, the scaling factors calculated through comparison between mechanistic-based analysis results and in situ data were incorporated in the prototype tool, as will be detailed in a later chapter, offering users the flexibility to decide whether to scale the pavement response data based on the in situ data. While the scaling factors have currently been calculated for specific scenarios involving a limited range of vehicles traveling on a flexible pavement with a 6 in. AC layer thickness, their application could lead to the development of a more advanced analysis tool for superloads if further research obtains in situ data from diverse road sections subjected to various types of superloads.

Field Instrumentation and Monitoring at Granular Road Section

Site Condition


A portion of 190th Street in Tama County, Iowa, characterized as a granular road, required excavation to install sensors for collecting road response and environmental data, near its intersection with V18. As described in the previous chapter, the 190th Street site was chosen as a potential site for field instrumentation due to the presence of a utility pole at its intersection with V18, ensuring a consistent external power supply and minimal disruption to underground facilities during trench cutting. A visual evaluation of 190th Street indicated that the road was in good condition without any notably severe distress, another critical factor in its selection as the field instrumentation site. Approval was obtained from the Tama County engineer to excavate a 4 ft × 4 ft area of 190th Street near the intersection and to conduct trench cutting from the edge of the granular road to the earth shoulder, as well as to repair the damaged section under the guidance and support of the county engineer following the sensor installation. Detailed information regarding 190th Street in Tama County, identified as the optimal field instrumentation site for the granular road system, is provided in Figure 92 and Table 40.



© Google 2024

Figure 92. Site information for 190th Street

Table 40. Summary of 190th Street information

Question	Answer
Road section name	190th Street
Road type	Granular road
No. of lanes	Two lanes (one per each direction)
Width of lane	9 ft per lane
Length of road section under forensic investigation	2 mi
Thickness of top layer	Top granular layer: 8 in.
AADT	-
Primary vehicles	Resident vehicle, truck, IoH
Averaged PCI	-
Averaged IRI (in./mi)	178
Major failure type	 <p>None</p>

Prior to the installation of sensors, Iowa One Call investigated the existing underground facilities that included internet cables, phone cables, and water pipes, near the intersection of 190th Street. The investigation confirmed that the excavation and trench cutting activities were unlikely to cause damage to the existing underground facilities in the area. The distance from the utility pole to 190th Street was also deemed manageable in that the lengths of sensor cables could reach the data loggers located on the earth shoulder. As previously mentioned, the sensors installed in both the full-depth flexible pavement and the granular road were designed to share a single core data logger housed within a single enclosure installed at the same intersection. This approach aimed to reduce costs associated with additional enclosures, data loggers, modems, and other related components.

Field Instrumentation Plan

After completing the sensor installation and subsequent repair of the damaged section with asphalt patching treatment for the full-depth flexible pavement section, the field instrumentation plan for the granular road section was prepared and shared with the county engineer, outlining the excavation plan down to the subgrade and the strategic installation of sensors within the granular road system. Sensor installation was performed on November 1, 2022, based on the availability of the county engineer and the excavator. All necessary preparations including installation of wooden supports and the enclosure housing data loggers, modem, and other components, had already been completed during field instrumentation for the full-depth flexible pavement. Therefore, the research team focused solely on ensuring thorough preparation and pre-testing of sensors in advance of the main installation phase.

To evaluate the performance of the granular road system under environmental and traffic loads, with particular focus on rutting damage, installation of sensors for granular road, including soil-compression sensors, pressure cells, thermistors, and moisture sensors, was planned for mid-depth of the top granular layer and 6 in. below the top of the subgrade. All sensors were integrated with the data loggers previously deployed for the sensors installed in the flexible pavement section. Unlike JPCP or flexible pavement with paved surfaces, due to adhesion issues, the granular road surface posed challenges for fixing the piezoelectric sensors of the P-WIM system using mastic tapes. As a solution, the research team opted to analyze specific vehicles passing over both V18 and 190th Street as a single route by reviewing video recordings, while the piezoelectric sensors were installed exclusively in V18. This approach enabled the analysis of granular road response data when subjected to traffic passing over both road sections.

Table 41 provides brief information about the embedded sensor types and their specifications, along with other components of the data acquisition system located at the earth shoulder. Note that the components of the data acquisition system listed in Table 41, excluding the sensors, remain consistent with those detailed in Table 38.

Table 41. Brief specifications of data acquisition system components for granular road

Component type*	Model	Description	Number	Location
Soil compression sensor	SCS-010F (BDI 2022c)	Vertical displacement at each layer	1	Mid-depth of top layer
			2	6 in. below the top of subgrade
Earth pressure cell	ER-3500 (GEOKON 2023)	Semiconductor type transducer for dynamic pressure measurement	1	Mid-depth of top layer
			1	6 in. below the top of subgrade
Thermistor	TS-EM (BDI 2024a)	Embeddable temperature sensor	2	Mid-depth of top layer
			2	6 in. below the top of subgrade
Moisture sensor	TEROS12 (METER Group 2024)	Volumetric water content, temperature, and electrical conductivity sensor	1	Mid-depth of top layer
			2	6 in. below the top of subgrade
Data logger	STS-CDL-01 (BDI 2019)	Core data logger	1	Enclosure
	STS4-16-TE4 (BDI 2020)	16-channel data logger for strain gauges and thermistors	2	Enclosure
	ZL6 (METER Group 2023)	6-channel data logger for moisture sensors	1	Enclosure
Ethernet/modem	DCM-ICB600CD	Cellular wireless modem with a Verizon data plan	1	Enclosure
Power component	PW-AC-10A24	24V 10A power system	1	Enclosure
Enclosure	ENC-UB-36B2	Aluminum enclosure Size: 36 in. (H) × 30.5 in. (W) × 13.3 in. (D)	1	Earth shoulder

* Minor components of the data acquisition system are not listed here. Data loggers, modem, power component, and enclosure were shared with sensors installed on full-depth flexible pavement section.

As listed in Table 41, soil compression sensors and thermistors developed by BDI, an earth pressure cell developed by GEOKON, and moisture sensors developed by METER Group, all previously introduced in the flexible pavement case, were also prepared for field instrumentation in the granular road section. These sensors, shown in Figures 93a to 93d, were interconnected with the data loggers shared with those installed in the full-depth flexible pavement section. All data collected from both the granular road and flexible pavement were intended to be stored and processed in the central data logger, STS-CDL-01. A wireless modem and an internal power system capable of delivering a 24V 10A alternating current power output were also shared for

data collection in the granular road section. The overall configuration of the data acquisition system is illustrated in Figure 93e.

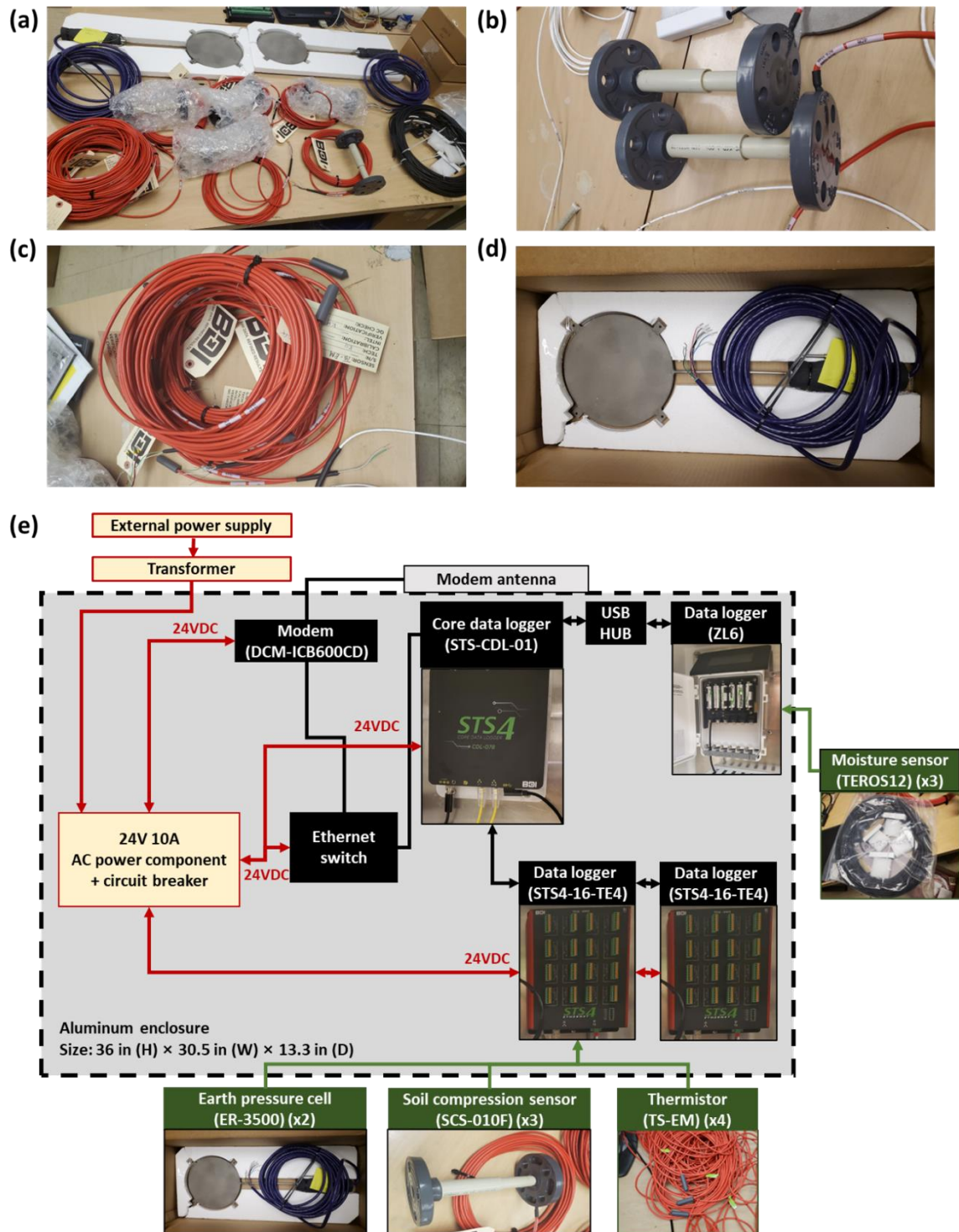


Figure 93. (a) Sensors of the data acquisition system including (b) soil compression sensors, (c) thermistors, (d) earth pressure cell, and the (e) overall configuration of the remote data acquisition system

The sensors, especially the soil compression sensors, were planned to be installed at precise locations along the potential wheel path line, as illustrated in Figure 94, to measure critical vertical strains at 6 in. below the top of the subgrade and at mid-depth of the top granular layer.

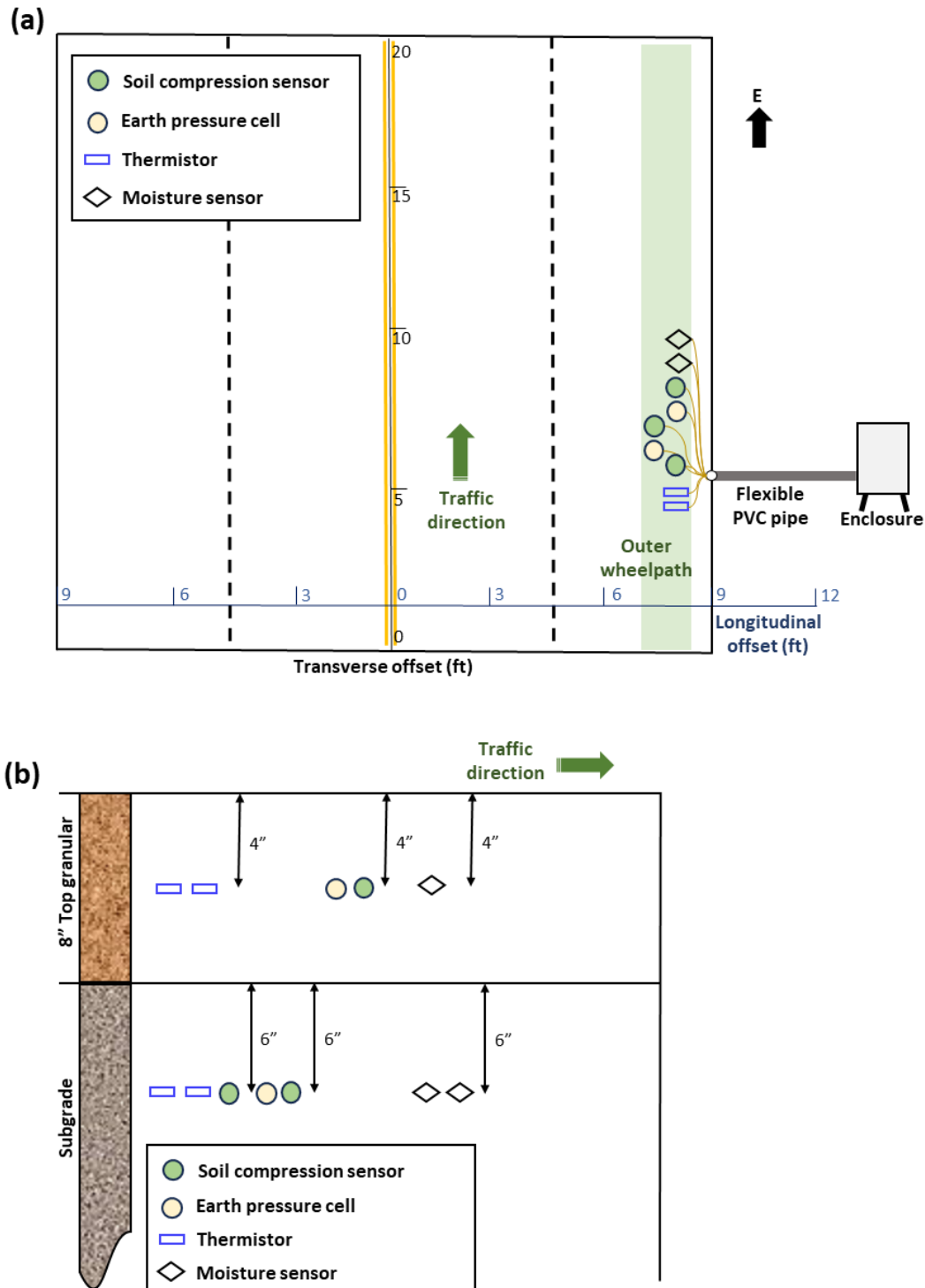


Figure 94. Sensor installation plan for granular road section: (a) plane view and (b) cross-sectional view

These locations were carefully chosen based on the findings of the computational analyses outlined in Chapter 6, which identified locations prone to experiencing critical vertical strains when subjected to superload traffic.

Field Instrumentation in Granular Road Section

All sensors were prepared and pre-tested prior to deploying them in the field, where the data loggers, modem, and other components had been previously installed in the flexible pavement section during its instrumentation. An excavator was engaged to execute excavation, trench cutting, and subsequent backfilling operations. Primary field instrumentation activities for the granular road section were carried out on November 1, 2022. This encompassed excavating a 4 ft × 4 ft area of 190th Street near its intersection with V18, installing sensors, connecting them to data loggers at the earth shoulder, then backfilling and compacting the damaged road. Traffic control was managed by the county engineer and their team to ensure safety throughout the field instrumentation process. During traffic control, the excavator proceeded with excavation of the designated area of the granular road and the route from the road edge to the earth shoulder where the enclosure was located. Upon excavating down to the subgrade, an LWD test was conducted to determine the elastic modulus of the subgrade, yielding a value of approximately 11,400 psi. Additionally, LWD testing performed on the top granular surface revealed an elastic modulus value of around 76,100 psi. After these tests, all sensors were installed at their predetermined depths and locations, with sensor cables carefully routed through flexible PVC pipes embedded along the excavated path to safeguard them from traffic loads. These cables were then connected to the data loggers housed within the enclosure, after which the excavated area and route were backfilled and compacted by the excavator. Upon completion of the installation process, it was verified that the system operated normally and could be remotely controlled while measuring both granular road and full-depth flexible pavement responses within a single data processing system. A continuous external power supply was provided to ensure ongoing collection of response data from both types of roads.

The overall steps of the sensor installation process in the granular road section are delineated in Figure 95. It is pertinent to mention that, during excavation, the thickness of the top granular layer was determined to be 8 in., so an 8 in. thickness of the top granular layer was provided to the LET-based models discussed in the following section when validating the in situ data.



Figure 95. Steps of the sensor installation: (a) trench cutting for the PVC pipe route, (b) excavating the designated area of the road, (c) installing the sensors, (d) protecting sensor cables through flexible PVC pipe, (e) backfilling and compacting the damaged road, and (f) activating the external power supply

Granular Road Performance Monitoring

The in situ data collected on June 4, 2023, and on November 4, 2023, including vertical displacement, temperature, and water content at 6 in. below the top of the subgrade and at mid-depth of the top granular layer, were thoroughly analyzed to evaluate performance of the data acquisition system. The vertical strain at these locations during the passage of a representative general class 9 truck and an IoH was also subjected to comparative analysis with LET-based results. These analyses employed mechanistic models developed for a granular road structure

identical to that of 190th Street. Figure 96 presents the vertical displacement and temperature data recorded in each layer over a 24-hour period, after removing noise from the data collected on June 4 and November 4, 2023.

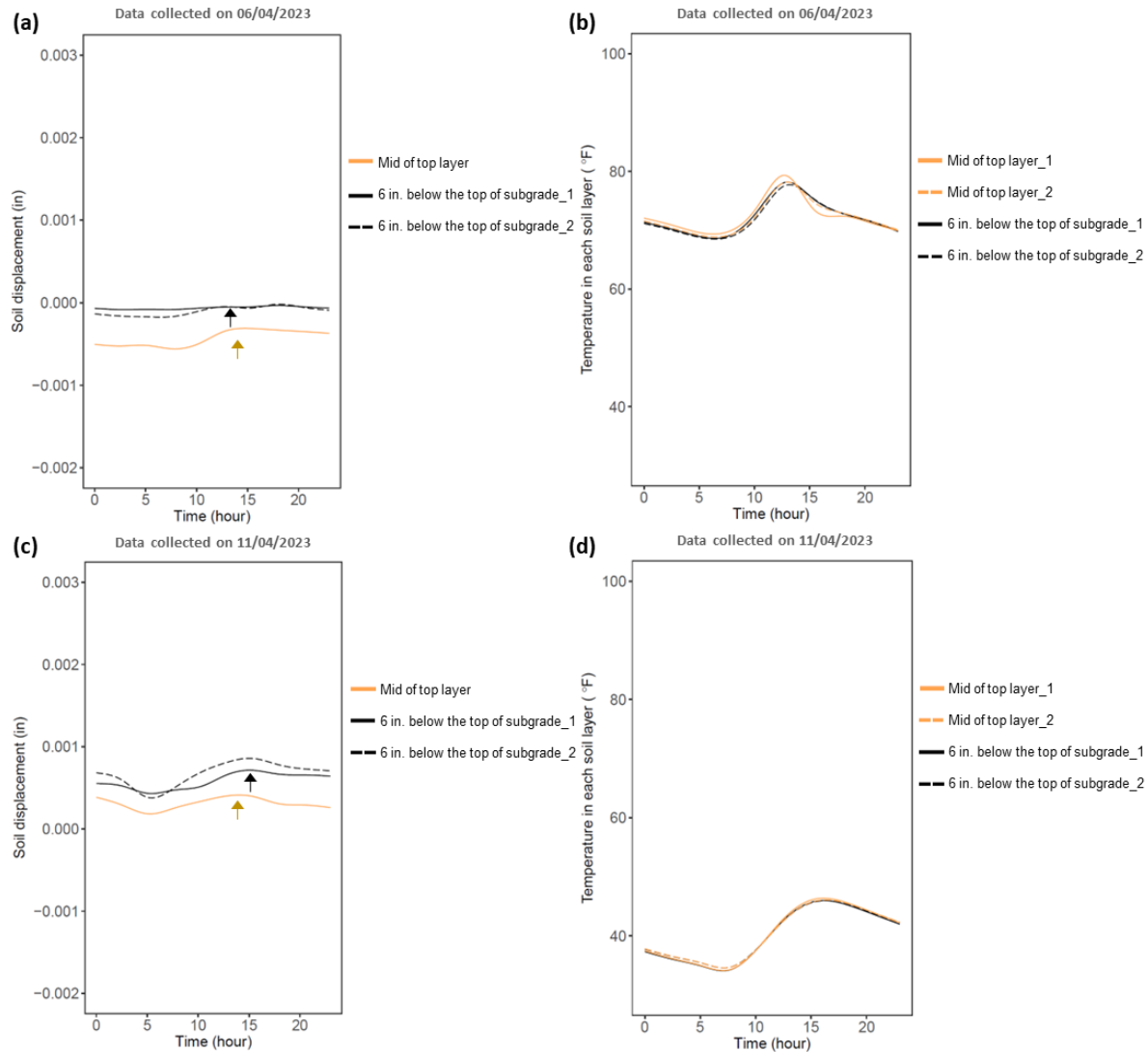


Figure 96. In situ granular road data including (a) vertical displacement and (b) temperature collected on June 4, 2023, and (c) vertical displacement and (d) temperature collected on November 4, 2023

The data were collected at a frequency of 50 Hz, using remote control of the system during data collection and transmission. The overall time-dependent temperature collected on November 4 was lower than that collected on June 4, with daytime temperatures measured higher than nighttime temperatures, as expected. The subgrade and top granular layer also exhibited increased compression during periods of elevated daytime temperatures, resulting in higher vertical displacement. Overall, the subgrade experienced higher compressive displacement than the top granular layer due to the lower elastic modulus of the subgrade measured on site, consistent with anticipated behavior.

Figure 97 shows the volumetric water content and temperature data obtained from TEROS12 sensors within each layer for the same two days. The temperature data collected from both the thermistors and moisture sensors demonstrated consistent reliability, as evidenced by their similar readings and trends over time at the same installation depth.

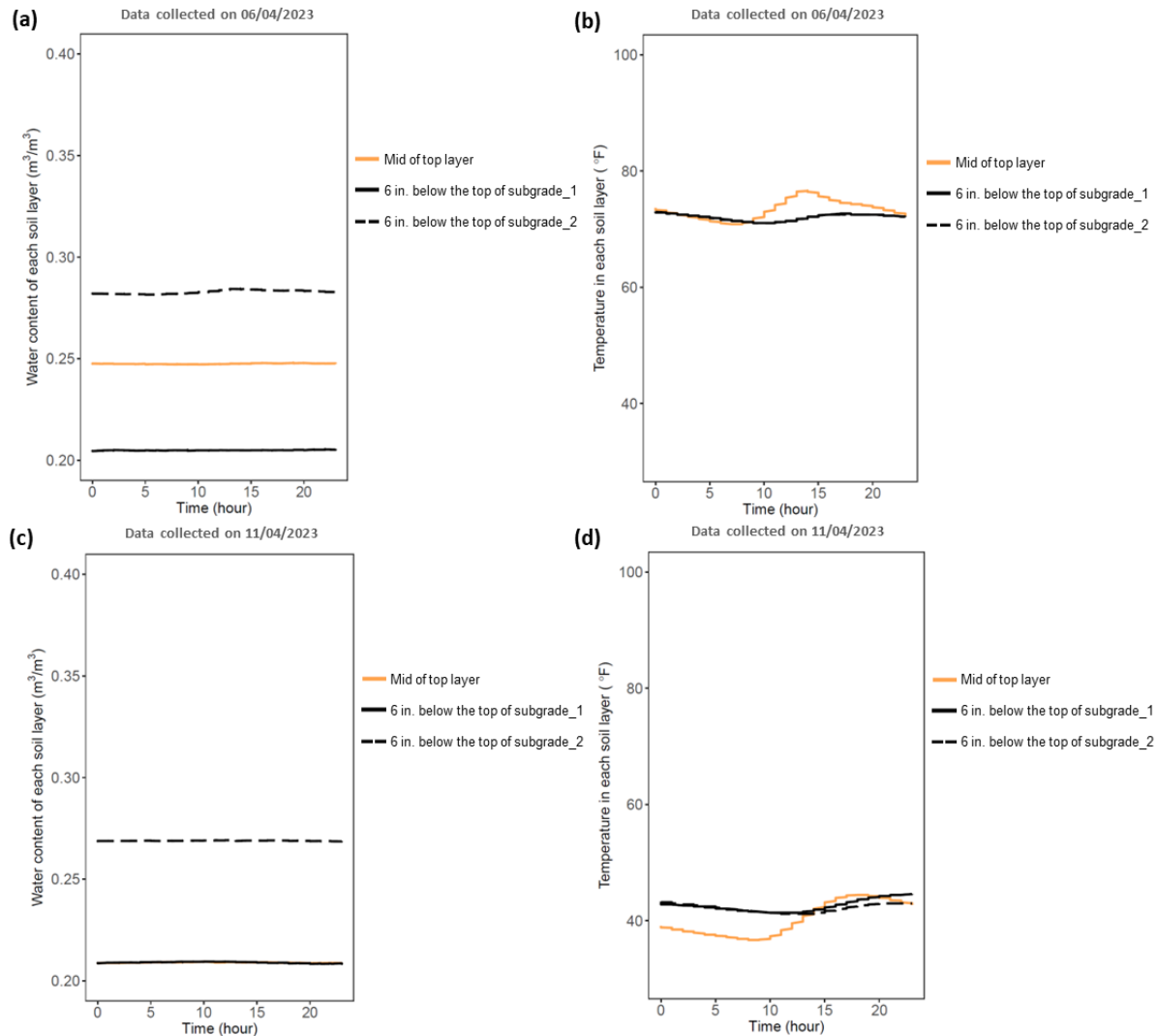


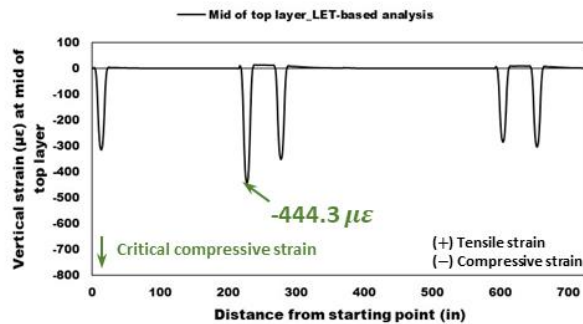
Figure 97. In situ granular road data collected on June 4, 2023 including (a) water content and (b) temperature in each layer, and on November 4, 2023 including (c) water content and (d) temperature in each layer

Soil compression sensors placed in both the top granular layer and the subgrade were able to capture the dynamic vertical displacement resulting from diverse traffic loads. The analysis for in situ data verification focused solely on vehicles traveling on both V18, where the P-WIM system was installed, and 190th Street regarded as a single route. Critical vertical strains at 6 in. below the top of the subgrade and at the mid-depth of the top granular layer, induced by a single pass of a class 9 truck with a GVW of 71 kips and an agricultural truck IoH with a GVW of 55 kips, were recorded at a frequency of 50 Hz, as shown in Figure 98 and Figure 99, respectively.

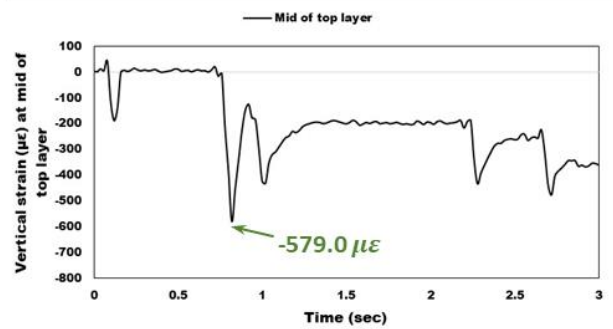
(a)



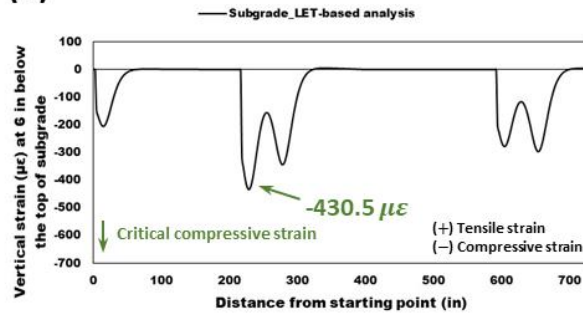
(b)



(c)



(d)



(e)

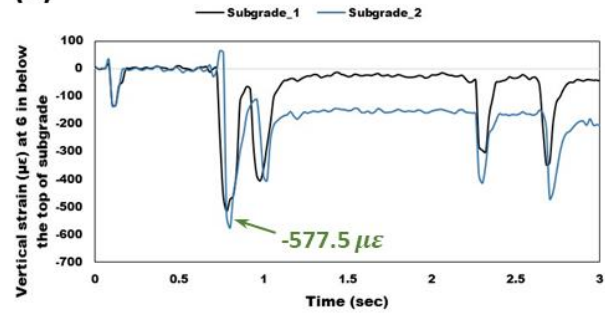


Figure 98. Granular road response of the sensor installation section to the (a) passage of a class 9 truck, exhibiting the resulting vertical strain at the mid-depth of the top granular layer through (b) LET-based analysis and (c) in situ strain data, and the resulting vertical strain at 6 in. below the top of the subgrade via (d) LET-based analysis and (e) in situ strain data

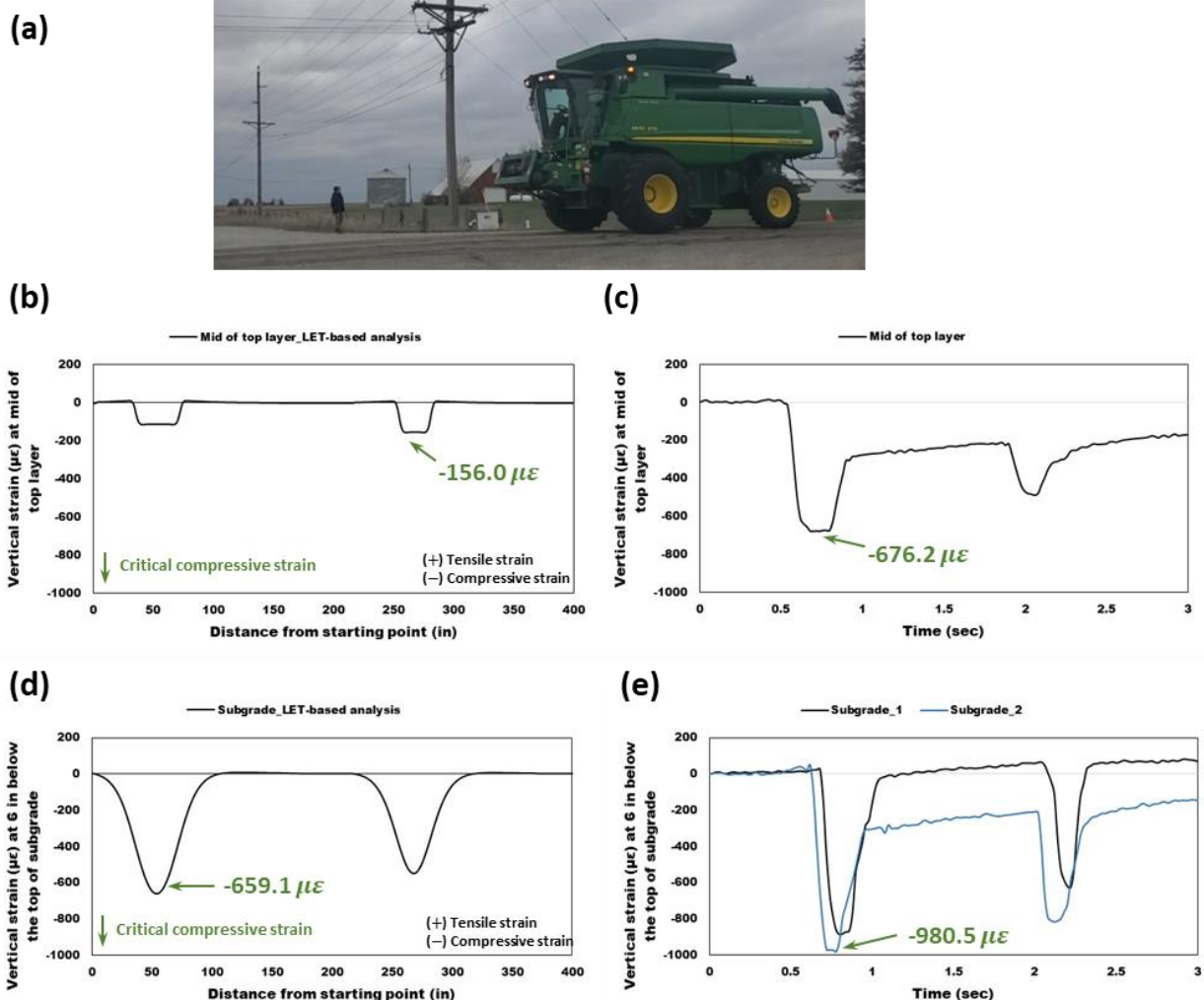


Figure 99. Granular road response of the sensor installation section to the (a) passage of an agricultural truck, exhibiting the resulting vertical strain at the mid-depth of the top granular layer through (b) LET-based analysis and (c) in situ strain data, and the resulting vertical strain at 6 in. below the top of the subgrade via (d) LET-based analysis and (e) in situ strain data

To validate the field data, computational analysis results derived from MnLayer were also analyzed with the results shown in Figure 98 and Figure 99, utilizing LET-based granular road models reflective of the structural properties of 190th Street. Detailed information of these LET-based analysis models is presented in Table 42. The thickness of the top granular layer and the modulus of elasticity of each layer were applied to the models based on on-site measurements and results of LWD testing, respectively.

Table 42. LET-based model information implementing 190th Street and traffic loads

Structural properties of granular road				
Top granular layer	Elastic modulus (psi)*	76,100	Thickness (in.)	8
Subgrade	Elastic modulus (psi)*	11,400	Thickness (in.)	∞
All layers	Poisson's ratio			0.35
Selected traffic load properties collected from October to November 2023				
Vehicle type	GVW (kip)	Axle weight (kip)		Axle spacing (ft) from the frontmost axle to the rearmost axle
Class 9 truck	71.4	13.1 (steering), 18.7/14.8 (front tandem), 12.0/12.8 (rear tandem)		16.4, 4.2, 28.9, 4.1
Agricultural truck	55.3	33.2 (front single), 22.1 (rear single)		16.7

* In situ pre-testing result was utilized for calculating elastic modulus of each layer.

Figure 98 and Figure 99 reveal that the maximum negative vertical strains measured at the mid-depth of the top granular layer and 6 in. below the top of the subgrade reflect critical road responses associated with rutting damage. A comparison of the in situ critical vertical strain data with those derived from LET-based analysis results revealed notable discrepancies for both the class 9 truck and the agricultural truck. For example, when subjected to a class 9 truck, the critical compressive vertical strains measured in situ at the mid-depth of the top layer and 6 in. below the top of the subgrade were recorded at 579.0 $\mu\epsilon$ and 577.5 $\mu\epsilon$, respectively. In contrast, the LET-based analysis results reflected significantly lower critical compressive vertical strain values of 444.3 $\mu\epsilon$ and 430.5 $\mu\epsilon$ at these respective locations. These differences were further pronounced during the agricultural truck passage, where the in situ critical compressive vertical strains within the top granular layer and subgrade were measured at 676.2 $\mu\epsilon$ and 980.5 $\mu\epsilon$, respectively, while the LET-based analysis reflected values of 156.0 $\mu\epsilon$ and 659.1 $\mu\epsilon$, respectively, for the same layers. One potential explanation for these differences lies in the formation of construction joints during the road damage and repair process, possibly impacting the magnitude of granular road responses, akin to the flexible pavement cases, and inaccurate measurement of the modulus of each layer or the traffic load data collected from the P-WIM system might also contribute to inconsistent outcomes. Despite these discrepancies, the in situ granular road response and traffic data remain valuable as empirical data.

Summary and Key Findings

The utilization of sensors and data acquisition systems for Iowa road systems represents a highly reliable approach for bridging the gap between mechanistic models and in situ road conditions. This chapter introduced procedures and methodologies involved in installing remote data acquisition systems, encompassing sensors, data loggers, modems, and power components, across JPCP, full-depth flexible pavement, and granular road sections. During the second half of 2021, a singular data acquisition system was installed in the reconstructed JPCP on K45 in Monona County, Iowa, and subsequently, during the latter half of 2022, another data acquisition

system was installed in the existing full-depth flexible pavement and granular road on V18 and 190th Street, respectively, in Tama County, Iowa. The collected performance-monitoring data from these three road sections, coupled with traffic load data from the P-WIM system, underwent thorough analysis and validation using mechanistic-based analysis results. This rigorous process served to evaluate the utility and reliability of the data acquisition system while quantifying the performance of various road systems throughout their service life, especially when subjected to superload traffic. Further discussion on the activities conducted as part of this chapter is given in the subsequent lists.

- **Field instrumentation and monitoring of JPCP section**

- A detailed installation plan was implemented, outlining precise installation locations for various components of the data acquisition system such as the P-WIM system, strain gauges, thermistors, moisture sensors, and other components. This plan was designed to evaluate the performance of JPCP under environmental impact and traffic loads by collecting in situ data at a frequency of higher than 50 Hz, sufficient for capturing traffic-load data.
- The analysis of JPCP performance monitoring data included observations for specific days in December 2021 and June 2022. The data collected in December was found to be reasonable in that the JPCP structure exhibited daytime behavior in which there was a positive temperature gradient in its PCC slab resulting in the tensile strain at the bottom of the PCC slab and a compressive strain at the top of the PCC slab due to the downward-curling effect. The data collected in June was found to be somewhat different from that of December in that the strain values measured at the bottom of the PCC slab also showed some compressive strain during the daytime, although the gradients of compressive strain were lower than those at the top of the PCC slab.
- The volumetric water content and temperature data obtained from the moisture sensors were deemed reasonable, aligning well with the seasonal temperatures and the characteristics of each soil layer.
- In situ critical tensile strains collected at the bottom of the PCC slab exhibited remarkable similarities in magnitude to those obtained from FEA results. However, notable gaps in critical tensile strain magnitudes were observed at the top of the PCC slab compared to the FEA results due to inadvertently lowered depth of in situ strain gauges at the top of the PCC slab relative to their planned locations. Following precise depth measurements of the strain gauges in the field using the MIRA ultrasonic tomograph, post-processing adjustments were implemented, linearly increasing the critical tensile strains at the top of the PCC slab. This theoretical adjustment yielded remarkably close resemblance between the scaled field data and FEA outcomes, achieving an R^2 value of approximately 0.98.

- **Field instrumentation and monitoring of flexible pavement section**

- A detailed installation plan was also made for a full-depth flexible pavement section to install various components of the remote data acquisition system at the exact locations, including the P-WIM system, strain gauges, soil compression sensors, earth pressure cell, thermistors, moisture sensors, and other components. The data acquisition system was intended to evaluate the performance of full-depth flexible pavement under environmental impact and traffic loads by collecting in situ data at a 50 Hz rate. Notably, the data acquisition system, except for the sensors embedded in the flexible pavement

structure, was shared with the sensors installed in the granular road section, thereby reducing the overall cost of field instrumentation.

- Examination of flexible pavement performance monitoring data involved observations for November and June 2023. The overall time-dependent temperature of the AC layer in November was measured lower than that collected in June, with daytime temperatures measured higher than for nighttime, as expected. However, an unexpected observation emerged regarding the time-dependent tensile strains within the AC layer on both days, indicating higher values during periods of decreasing temperatures, contrary to expectations. These discrepancies can be attributed to the partial cutting and subsequent repair of the AC layer when installing the sensors, resulting in the creation of construction joints and introduction of additional boundary conditions near the installed sensors.
 - Vertical displacements measured at 6 in. below the top of the subgrade revealed that the subgrade soil underwent increased compression, resulting in higher vertical displacement during periods of elevated temperature in daytime. Overall vertical displacements recorded in November were lower compared to those in June, attributable to the higher resilient modulus of the subgrade in November and consistent with the research team's expectations.
 - The volumetric water content and temperature data obtained from the moisture sensors were reasonable, aligning well with expectations.
 - Comparison of in situ critical pavement response data with those obtained from LET-based analysis results revealed notable discrepancies for the class 9 truck and the agricultural truck, possibly due to the formation of construction joints during the road damage and repair process that might impact the magnitude of pavement responses. Inaccuracies in the modulus of each layer and the traffic load data collected from the P-WIM system, as well as deviations in the passage of traffic, could also play a role. Despite these discrepancies, since the in situ pavement response and traffic data remain valuable as empirical data, the scaling factors calculated through comparison between mechanistic-based analysis results and in situ data were incorporated in the prototype tool to be detailed in a later chapter, offering users the flexibility to decide whether or not to scale the pavement response data based on the in situ data.
- **Field instrumentation and monitoring of granular road section**
 - Another sensor installation plan was developed for a granular road section to install pre-prepared sensors, including soil-compression sensors, earth-pressure cell, thermistors, and moisture sensors, at precise depths and locations. The main data-processing components of the data acquisition system, including data loggers, modem, and power components, were shared with the sensors embedded in the flexible pavement section.
 - The overall time-dependent temperature collected in November 2023 was lower than that collected in June 2023, with daytime temperatures measuring higher than nighttime temperatures as expected. The subgrade and top granular layer also exhibited increased vertical compression during periods of elevated daytime temperatures, resulting in higher vertical displacement. The subgrade experienced higher compressive displacement than the top granular layer due to the lower elastic modulus of the subgrade measured on-site, consistent with anticipated behavior.

- The volumetric water content and temperature data obtained from the moisture sensors were also found to be reasonable.
- Upon comparison of in situ critical vertical strains at both locations, i.e., mid-depth of the top granular layer and 6 in. below the top of the subgrade, with those obtained from LET-based analysis results, notable discrepancies were observed between the class 9 truck and the agricultural truck. The same reasoning as with flexible pavements may explain this discrepancy, i.e., the formation of construction joints during the road damage and repair process may impact the magnitude of granular road responses. While inaccurate traffic load data collected from the P-WIM system could also influence the magnitude of granular road responses, the in situ road response and traffic data still remain valuable as empirical data.

CHAPTER 9. DEVELOPMENT OF USER-FRIENDLY PROTOTYPE TOOL FOR QUANTIFYING SUPERLOAD IMPACTS ON IOWA ROAD INFRASTRUCTURE

Integration of Superload and M-E Road Analysis Techniques into RISAT

RISAT, a user-friendly prototype tool, incorporates ANN-based models developed for two distinct pavement types, JPCPs and flexible pavements. These models were utilized to quantify potential pavement damages, associated treatment costs, and reductions in road service life resulting from diverse superload scenarios. Note that the granular road type was excluded from the RISAT, a decision made because solely assessing RDACs and service life reductions based on rutting damage, a main structural distress type, was deemed insufficient. Further investigation into additional functional distresses such as loose aggregate or washboarding that might govern the service life of granular roads is needed for a future study.

RISAT is a macro-enabled Visual Basic for Applications (VBA)-based Microsoft Excel automation tool comprised of a navigation panel and several sub-tools. The research team had prior experience in developing VBA-based automation tools, such as Iowa Pavement Analysis Techniques (IPAT) (Citir et al. 2021) and Pavement Structural Analysis Tool (PSAT) for Iowa local roads (Citir et al. 2023). These tools were primarily designed to handle conventional vehicle classes as defined by the FHWA. Drawing upon these skills and experiences proved instrumental in the development of RISAT to quantify the impact of the superload traffic on road infrastructure.

The main navigation panel of RISAT enables users to navigate through different sub-tools by selecting the pavement and superload types they wish to analyze among two road types (i.e., JPCP and flexible pavement) and seven superload parent types (i.e., grain cart, manure tanker, agricultural trailer, agricultural truck, single-row modular SHL, dual-row modular SHL, and drop-deck SHL). Each sub-tool produces mechanistic-based outputs derived from ANN-based prediction models, each developed specifically for the respective pavement and superload type. The sub-tools also partially incorporate empirical-based response data from in situ measurements to scale the resulting critical road responses. In RISAT, the main structural damages considered are bottom-up and top-down fatigue damage for JPCPs and bottom-up fatigue and rutting damage for flexible pavements. The methodology for calculating potential damages, associated treatment costs, and reductions in service life for each road subjected to different types of superloads follows the approach outlined in Chapters 4 and 5.

Figure 100 and Figure 101 illustrate the overall flowchart of the RISAT for analyzing JPCPs and flexible pavements, respectively, employing ANN-based prediction models.

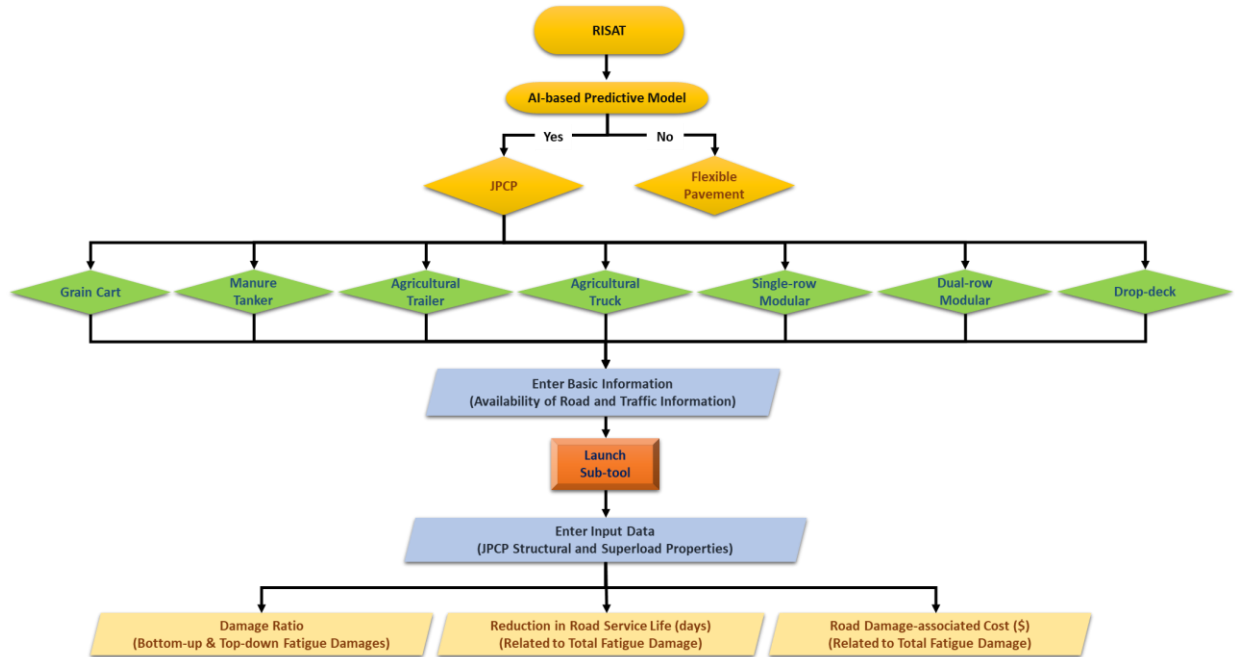


Figure 100. Flowchart of RISAT employing ANN-based prediction models for JPCP analysis under various superload types

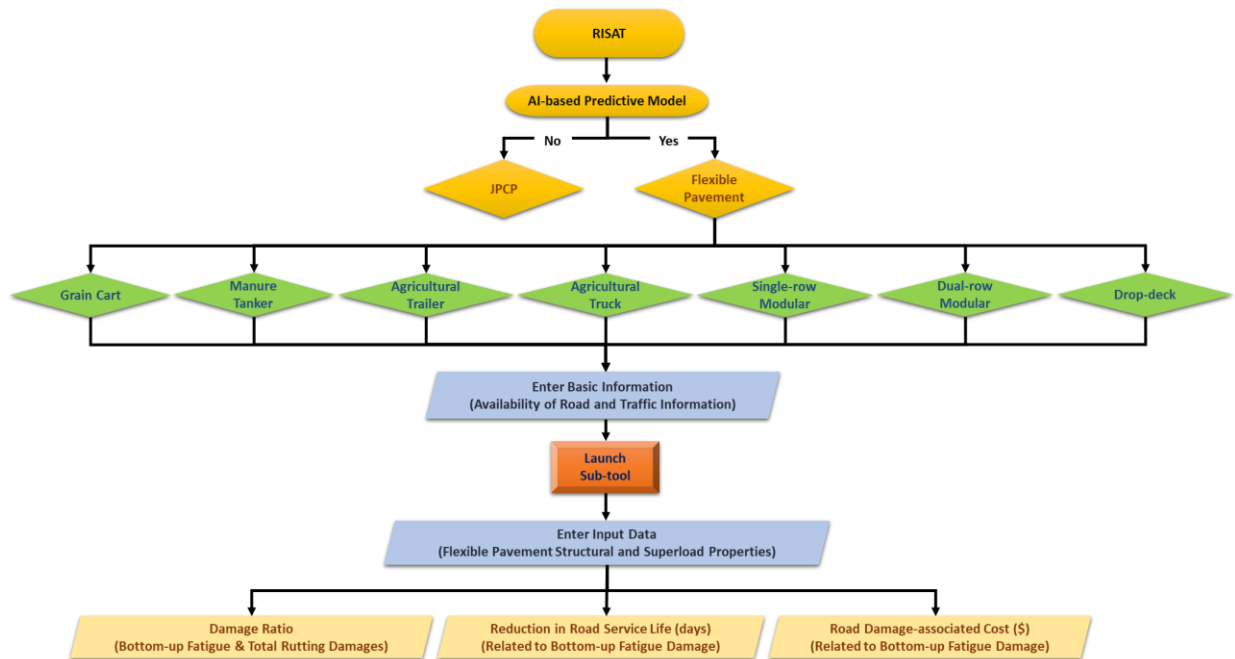


Figure 101. Flowchart of RISAT employing ANN-based prediction models for flexible pavement analysis under various superload types

The inputs required for the navigation panel and sub-tools, along with the outputs achievable from each sub-tool, are summarized in Table 43 for analyzing JPCPs and in Table 44 for analyzing flexible pavements.

Table 43. Input and output variables in RISAT when analyzing JPCPs

Navigation panel				
Input*	Questions regarding whether users have the information related to the pavement system			
	Questions regarding whether users have the information related to the superload traffic			
	Project Name: Description of the road		COUNAME: County Name	
	PROJECT_NO: Number (ID) of the project		BPRJ: Beginning of the project	
	EPRJ: Ending of the project		CONYR: Year of the construction	
Output	Link to the respective sub-tools			
Sub-tools				
Input*	Pavement system			
	Thickness of PCC layer	Modulus of elasticity of PCC layer	CTE of PCC layer	
	Temperature gradient of PCC layer	Transverse joint spacing	Transverse joint LTE	
	Modulus of elasticity of subgrade		Shoulder type	
	Superload configuration			
	Axle number	Axle weight	Tire pressure	
	Number of tires per axle	Tire width	Axle spacing	
	Tire spacing	Outer tire spacing: Distance between leftmost tire and the rightmost tire of a superload		
	Additional information for M-E analysis			
	Superload travel year	AADTT	Number of lanes	
	Length of the section	Treatment cost	Discount rate	
	Output	N_f (number of repetitions to failure) related to bottom-up fatigue damage		
		Damage ratio related to bottom-up fatigue cracking		
N_f (number of repetitions to failure) related to top-down fatigue damage				
Damage ratio related to top-down fatigue cracking				
RDAC		Service life reduction		

* Minor input variables are not listed here

Table 44. Input and output variables in RISAT when analyzing flexible pavements

Navigation panel			
Input*	Questions regarding whether users have the information related to the pavement system		
	Questions regarding whether users have the information related to the superload traffic		
	Project Name: Description of the road		COUNAME: County Name
	PROJECT_NO: Number (ID) of the project		BPRJ: Beginning of the project
	EPRJ: Ending of the project		CONYR: Year of the construction
Output	Link to the respective sub-tools		
Sub-tools			
Input*	Pavement system		
	Thickness of AC layer	Air voids of AC	Effective binder contents of AC
	Thickness of base layer	Water contents of base layer	Thickness of subbase layer
	Water contents of subbase layer	Water contents of subgrade	Seasonal-based combination of modulus of elasticity
	Superload configuration		
	Axle number	Axle weight	Tire pressure
	Number of tires per axle	Tire width	Axle spacing
	Tire spacing	Outer tire spacing: Distance between leftmost tire and the rightmost tire of a superload	
	Additional information for M-E analysis		
	Superload travel year	AADTT	Number of lanes
	Length of the section	Treatment cost	Discount rate
	Output	N_f (number of repetitions to failure) related to bottom-up fatigue damage	
Damage ratio related to bottom-up fatigue cracking			
N_f (number of repetitions to failure) related to rutting damage			
Damage ratio related to rutting			
RDAC		Service life reduction	

* Minor input variables are not listed here

The navigation panel asks users to provide basic information when they have their own information related to structural properties of the pavement system and loading properties of the superload traffic. Users are also invited to input basic information about the road section and project if they wish to do so. Within each sub-tool accessed through the navigation panel, users must enter all the input variables related to the chosen pavement and superload type. These variables encompass structural properties of the pavement system, loading properties of the superload, and other relevant information. Note that RISAT includes recommendation values and plausible ranges for most input variables within each input cell intended to guide users and prevent them from entering unreasonable values for each input variable.

After providing these inputs, users obtain outputs such as N_f , damage ratio, RDAC, and reduction in service life. For JPCPs, all outputs are calculated and presented based on two approaches; the first relies on the specified modulus of each layer provided by the user, while the second approach is based on averaged values of each output derived from the four seasonal moduli of each layer listed in Table 8 in Chapter 4. For flexible pavements, all outputs are derived based on two approaches: the first approach applies the specific seasonal-based moduli

of each layer listed in Table 18 in Chapter 5, while the second approach is based on the yearly based outputs from applying the effective modulus of each month to the output calculation. The difference in output derivation approaches between JPCP and flexible pavement systems is attributable to inconsistent trends in the modulus of each layer within JPCPs and flexible pavements across different seasons.

Features of RISAT

This section describes the RISAT interface and provides comprehensive details regarding each component comprising both the navigation panel and the sub-tools. The RISAT is developed in the form of a Microsoft Excel macro-enabled worksheet (.xlsm), requiring Excel 2016, 2019, or 2021, as well as VBA, to run the tool. Upon launching the RISAT software (RISAT.xlsm), users will encounter the navigation panel, providing access to the Artificial Intelligence-based Models, the primary approach utilized in developing predictive models, as shown in Figure 102a. The navigation panel will then offer users the option to select their preferred road type between JPCP and flexible pavement as depicted in Figure 102b. Users can then select a specific superload type from the drop-down list shown in Figure 102c. The first list offers the options IoH and SHL, while the subsequent list provides choices for superload subtypes such as grain cart, manure tanker, agricultural trail, and agricultural truck for IoH or single-row modular, dual-row modular, and drop-deck for SHL. If users select both road and superload types, they will be prompted with questions regarding whether they have their own information related to the structural properties of the pavement system and the loading properties of superload traffic. Even if users provide no detailed information, RISAT provides recommended values and plausible ranges for most input variables, allowing users to apply these recommended input values if they choose, as shown in Figure 102d. As a final step in use of the navigation panel, the tool prompts users to enter basic information about the road section and project if they wish, as illustrated in Figure 102e. All the basic information entered by users in this step will be transferred to the sub-tool and displayed accordingly. Clicking on LAUNCH TOOL will prompt users to open the sub-tool specifically developed for each road and superload type.

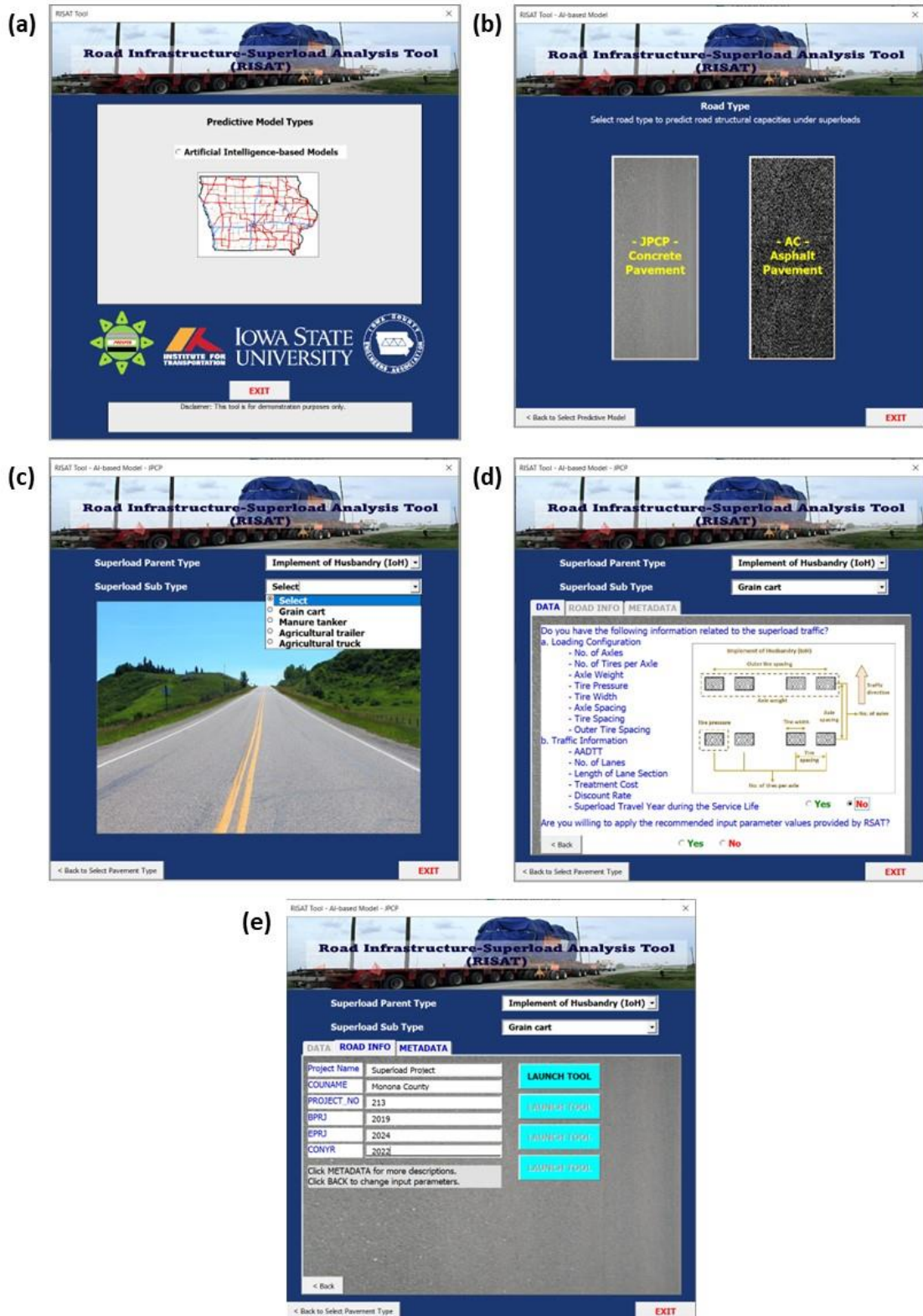


Figure 102. Interface of the navigation panels of RISAT: (a) predictive model selection, (b) road type selection, (c) superload type selection, (d) question, and (e) basic information input

RISAT incorporates a total of 14 sub-tools, categorized under 2 road types and 7 superload types, and the navigation panel guides users to their desired sub-tool following their selection. Once users have navigated to the designated sub-tool, as exemplified in Figure 103, they are prompted to input data necessary to conduct an analysis for a specific pavement type under a specific superload category.

Road Infrastructure-Superload Analysis Tool (RISAT)

Project Name:
County Name:
Project No.:
EPCL:
Construction Year:

Pavement system

Layer properties	JPCP system	
	US unit	SI unit
Thickness (ft/inch)	8.0	2.03
Modulus of elasticity (ksi/MPa)	4,000,000	27,579
Coefficient of thermal expansion (in/in/°F)	4.3	7.7
Temperature gradient (°F/inch)	0	-0.7
Transverse joint spacing (ft/inch)	20	6
Transverse joint L/E (ft)	80	80
Modulus of elasticity (ksi/MPa)	15,000	90
Poisson's ratio	0.18	0.18
Composite modulus of subgrade reaction (ksi/inch)	119.2	0.031

Shoulder type: Full-depth tied PCC shoulder

Superload configuration

Superload type	Implement of Husbundry				Grain Cart								
	Axle weight	Tire pressure	No. of tires per axle	Tire width	Axle spacing	Tire spacing	Outer tire spacing						
1	45000	278.01	35.6	0.25	2	35.7	0.81	78	1.98	126	3.20	126	3.20
2	45000	278.01	35.6	0.25	2	35.7	0.81	78	1.98	126	3.20	126	3.20
3	45000	278.01	35.6	0.25	2	35.7	0.81	78	1.98	126	3.20	126	3.20

Additional information for M-E analysis

Items	JPCP system
Construction year	2012
Superload travel year	2013
AADTT	1000
Number of lanes	2
Length of section (mile)	10
Treatment cost (\$)	220000
Discount rate (%)	3.5

Estimation of damage ratio

Calculate bottom-up fatigue damage ratio	Damage ratio	JPCP system	
		Specified modulus-based	Yearly-based
N_f		5.28E-04	8.90E-04
		1.19E+08	6.63E+08
Calculate top-down fatigue damage ratio		1.69E+09	1.07E+10
		2.37E+07	7.60E+11

Estimation of RDAC and service life reduction

Calculate Road Damage-Associated Cost (RDAC)	RDAC (\$)	JPCP system	
		Specified modulus-based	Yearly-based
Service life reduction (days)		29	148
		1	1

Data scaling option: No data scaling

Legend

- user input
- either predicted/computed outputs or unit conversion
- macro-based button that users should click to calculate
- toggle button that users should click to choose an option

Diagram: Implement of Husbundry (left)

Outer tire spacing: 126 in (3.20 m)
Axle weight: 45,000 lb (20,400 kg)
Tire pressure: 278.01 psi (19.2 MPa)
Tire width: 35.6 in (0.91 m)
Tire spacing: 78 in (1.98 m)
No. of tires per axle: 2
No. of axles: 3

Buttons: EXPORT RESULTS, CLEAN, GO BACK TO MAIN TOOL

Figure 103. A sub-tool of the RISAT designed for JPCP analysis under the grain cart category

The sub-tools feature cells color-coded as green, white, orange, and yellow. Green cells are designated for user input, while white cells serve as outputs or facilitate unit conversion. Orange cells are embedded with macros to trigger specific functionalities, and yellow cells contain toggle buttons for users to select options. It is important to note that only green, orange, and yellow cells are editable, allowing users to click and modify their contents as needed.

Regarding the sub-tools designed for JPCP analysis, Figure 104 provides details for each component presented to the users. Figure 104a displays basic project and road information transferred from the input panel of the navigation panel, as depicted in Figure 102e. If users have already entered this information in the navigation panel, it is unnecessary to re-enter it in the sub-tool. Figure 104b indicates the pavement structural properties required for accurate pavement

analysis. Note that users should input the modulus of elasticity of the subgrade to automatically calculate the composite modulus of subgrade reaction. Users can also select shoulder type from options such as full-depth tied PCC shoulder (70% LTE), full-depth tied PCC shoulder (50% LTE), HMA shoulder, and granular shoulder, utilizing the same approaches applied for the mechanistic-based analysis described in Chapter 4 (see Figure 8). As depicted in Figure 104c, most input variables have recommended input ranges and values provided by the research team for user reference. Should users input values outside a recommended range, a warning message will prompt them to re-enter values within the suggested input range. Upon entering JPCP structural properties, a schematic drawing representing the JPCP structure will be generated as in Figure 104d, illustrating the thickness of the PCC layer over the subgrade, transverse joint spacing, and LTE. Users are then required to input loading properties of the superload, as demonstrated in Figure 104e. In the axle number cells, users are asked to number the axles sequentially from one up to the total number of axles the superload has, starting from the steering axle to the last axle. Axle weight and tire pressure cells require users to input the axle weight and tire pressure for each axle, from the steering axle to the last axle. The number of tires per axle must be entered for each axle, along with the tire width for tires on each axle. Axle spacing and tire spacing also require user input. Users may input the average tire spacing for each axle if tire spacing varies between tires within an axle. The outer tire spacing refers to the total length from the outer edge of the leftmost tire to the outer edge of the rightmost tire within an axle. All property values of input variables are automatically converted from US units to SI units, with both sets of values displayed in the sub-tools for user convenience. Figure 104f delineates additional information requisite for M-E analysis, encompassing the year of travel for the superload on the road section, AADTT, number of lanes on the road section, length of the road section, future rehabilitation or reconstruction treatment cost, and discount rate. These details are pivotal for performing LCCA to calculate RDAC and the reduction in JPCP service life. Users are also afforded the option to scale the results of mechanistic-based analysis using in situ data collected from the remote data acquisition system described in Chapter 8. If users opt for data scaling based on in situ data, the mechanistic-based data will be scaled accordingly. Conversely, selecting no data scaling will result in outputs derived solely from mechanistic-based analysis results, so users will obtain outputs such as N_f and damage ratio related to bottom-up and top-down fatigue damages, as well as RDAC and reduction in service life of JPCP when subjected to a single pass of the superload.

(a) **Road Infrastructure-Superload Analysis Tool (RISAT)**

Project Name:	Superload Project
County Name:	Monona County
Project No:	213
BPRJ:	2019
EPRJ:	2024
Construction Year:	2022

(b) **Pavement system**

Layer properties		JPCP system	
		US unit	SI unit
PCC Layer	Thickness (US unit: inch)(SI unit: mm)	8.0	203
	Modulus of elasticity (US unit: psi)(SI unit: Mpa)	4,000,000	27,579
	Coefficient of thermal expansion (US unit: $10^{-6}/^{\circ}\text{F}$)(SI unit: $10^{-6}/^{\circ}\text{C}$)	4.3	7.7
	Temperature gradient (US unit: $^{\circ}\text{F}/\text{inch}$)(SI unit: $^{\circ}\text{C}/\text{mm}$)	0	-0.7
	Transverse joint spacing (US unit: feet)(SI unit: m)	20	6
	Transverse joint LTE (%)	90	90
Subgrade (based on Westergaard theory)	Modulus of elasticity (US unit: psi)(SI unit: Mpa)	13,000	90
	Poisson's ratio	0.35	0.35
	Composite modulus of subgrade reaction (US unit: psi/in)(SI unit: Mpa/m)	115.2	0.031
Shoulder type	Select shoulder type	Full-depth tied PCC shoulder (70% LTE)	

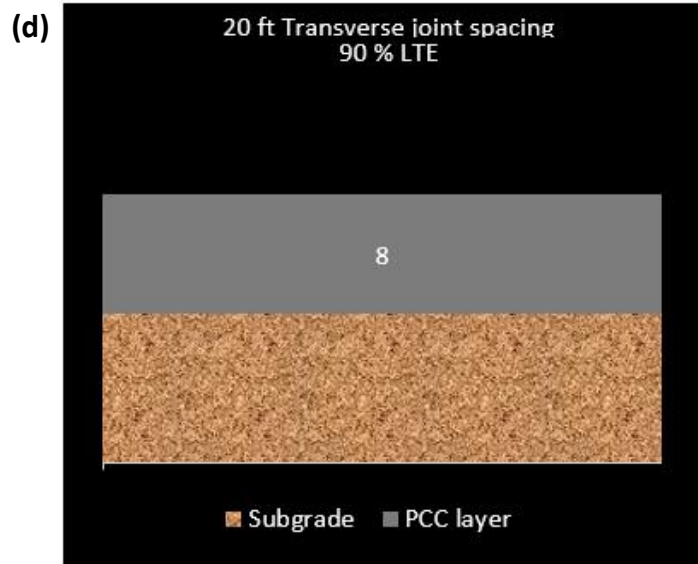
Choose an option
 Full-depth tied PCC shoulder (70% LTE)
 Full-depth tied PCC shoulder (50% LTE)
 HMA shoulder
 Granular shoulder

(c) **Pavement system**

Layer properties		JPCP system	
		US unit	SI unit
PCC Layer	Thickness (US unit: inch)(SI unit: mm)	8.0	203
	Modulus of elasticity (US unit: psi)(SI unit: Mpa)	4,000,000	27,579
	Coefficient of thermal expansion (US unit: $10^{-6}/^{\circ}\text{F}$)(SI unit: $10^{-6}/^{\circ}\text{C}$)	4.3	7.7
	Temperature gradient (US unit: $^{\circ}\text{F}/\text{inch}$)(SI unit: $^{\circ}\text{C}/\text{mm}$)	0	-0.7
	Transverse joint spacing (US unit: feet)(SI unit: m)	20	6
	Transverse joint LTE (%)	90	90
Subgrade (based on Westergaard theory)	Modulus of elasticity (US unit: psi)(SI unit: Mpa)	13,000	90
	Poisson's ratio	0.35	0.35
	Composite modulus of subgrade reaction (US unit: psi/in)(SI unit: Mpa/m)	115.2	0.031
Shoulder type	Select shoulder type	Full-depth tied PCC shoulder (70% LTE)	

Input range:
6 to 15

 Recommendation:
8



[illegible]

(f)	Additional information for M-E analysis		Data scaling option	
	Information for M-E analysis		JPCP system	No data scaling
	Items	Construction year	2022	Choose an option
		Superload travel year	2023	Data scaling based on in-situ data
		AADTT	1000	No data scaling
		Number of lanes	2	
		Length of section (mile)	10	
		Treatment cost (\$)	220000	
		Discount rate (%)	5.5	

(g)

Estimation of damage ratio			
Fatigue cracking			JPCP system
Calculate bottom-up fatigue damage ratio	N_f	Specified modulus-based	5.28E+04
		Yearly-based	8.90E+04
	Damage ratio	Specified modulus-based	1.19E+06
		Yearly-based	6.63E+08
Calculate top-down fatigue damage ratio	N_f	Specified modulus-based	1.69E+09
		Yearly-based	1.07E+10
	Damage ratio	Specified modulus-based	2.37E+07
		Yearly-based	7.40E+11

Estimation of RDAC and service life reduction			
RDAC and service life reduction			JPCP system
Calculate Road Damage-Associated Cost (RDAC)	RDAC (\$)	Specified modulus-based	29
		Yearly-based	148
	Service life reduction (days)	Specified modulus-based	1
		Yearly-based	2

Figure 104. Details of sub-tool components of RISAT: (a) basic project and road information, (b) pavement structural properties, (c) recommended input range and value, (d) schematic drawing depicting pavement structure, (e) loading properties of the superload, (f) additional information for M-E analysis, and (g) analysis results

Users can access additional information, including developer details, research documentation (final report), and the analysis and design specifications and criteria utilized to develop the M-E JPCP models. These resources are accessible via the About, Documentation, and Quick Information buttons, respectively, as depicted in Figure 105a. Users also have the option to generate an output Excel file in the same folder where the RISAT is located, generating a table

summarizing the outputs by clicking the EXPORT RESULTS button. To clear all input variable cells entered by users, users click the CLEAN button. Users can also return to the navigation tool interface by selecting the GO BACK TO MAIN TOOL button, as illustrated in Figure 105b.

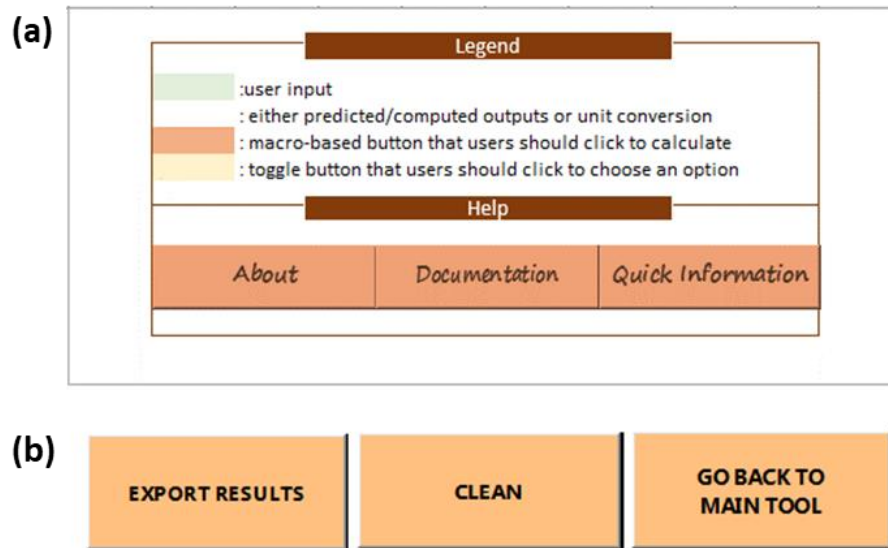


Figure 105. Additional functions of sub-tool: (a) buttons for accessing developer details, research documentation, and analysis and design specifications and criteria and (b) buttons for exporting results, cleaning cells, and going back to the navigation panel

When users choose flexible pavement analysis from the navigation panel, they will be directed to the corresponding sub-tool for flexible pavements. Figure 106 presents an overview of the features of the flexible pavement analysis sub-tool, exemplified for flexible pavement under single-row modular SHL. Much like the JPCP sub-tools, only cells highlighted in green, orange, and yellow are editable, allowing users to click on these cells and modify their contents as needed.

CHAPTER 10. REPAIR, REHABILITATION, AND FUNDING ALTERNATIVES

Investigation into repair and rehabilitation alternatives and funding alternatives yielded several practical options for addressing the impact of superloads on Iowa's highways and county roads. Leveraging insights from the literature review conducted in Chapter 2, combined with findings from forensic investigations, field instrumentation, and numerical analyses, the project team identified strategies aimed at extending the service life of the road infrastructure heavily traveled by superloads. Repair and rehabilitation alternatives encompass a range of techniques, including but not limited to the following:

- Pavement resurfacing, patching, and joint repairs are options to address localized damages and distresses, thereby enhancing pavement performance and durability in anticipation of potential superload traffic. Implementation of a structured maintenance program is pivotal in preemptively addressing existing damages and distresses, preventing their escalation into critical failure points under superload traffic. Such a program encompasses activities including patching potholes, repairing cracks, and maintaining proper drainage to mitigate water-induced damage (Danz et al. 2020). Absence of regular maintenance exacerbates the progression of cracking under continuous passage of superloads or heavy-haul trucks, leading to further propagation of existing cracks, and repeated superload loading cycles can potentially induce fatigue within the pavement material, weakening its resilience to crack growth. Inadequate maintenance practices such as deficient drainage systems, inadequate surface sealing, or delayed repairs can amplify crack propagation. Neglecting timely interventions allows cracks to widen and deepen, thereby compromising overall structural integrity of the pavement. As evidenced by the findings of this study, fatigue cracking emerges as a critical factor predisposing pavement systems to failure, so it is imperative to conduct routine pavement repair and rehabilitation initiatives to effectively counteract fatigue-related distresses and uphold pavement longevity when facing the impact of superload traffic.
- Implementation of structural enhancements, such as designing the top surface layer with a thickness sufficient to withstand the traffic loading conditions of superloads is another option. According to the analysis results derived from this study, especially the LCCA findings, it is recommended that top surface layers exceeding 8 in. in thickness be implemented across all three road system types: JPCP, flexible pavement, and granular road. This adjustment is deemed essential for markedly mitigating pavement and granular road damages that can potentially be induced by superloads. However, it should be noted that this recommendation for the thickness of top layers is based on LCCA results aimed at reducing superload traffic-induced treatment costs only, and this recommendation does not reflect a mandatory requirement for paved or unpaved road design. Conducting full-depth reclamation (FDR) also presents an additional approach for bolstering the structural integrity of pavement systems against superloads. FDR involves pulverizing existing pavement and incorporating a stabilizing agent such as cement or lime to form a new base layer with a higher modulus; this has been identified as a critical factor in mitigating fatigue-related damages for JPCPs and fatigue and rutting-related damages for flexible pavements when subjected to superloads. Such comprehensive rehabilitation strategies offer definitive solutions for fortifying structural integrity of road systems against the challenges posed by superload traffic.

- Utilization of innovative and advanced materials such as high-performance concrete and asphalt mixes can enhance the modulus of pavement and granular road systems, a critical factor in fortifying the road systems against extremely heavy loading conditions associated with superloads.
- Utilization of granular road stabilization techniques, including techniques such as adding cement or lime to the granular material, applying geotextiles, or using chemical stabilizers, improve the strength and stability of granular road systems when subjected to superload traffic.

Funding alternatives to offset damage to Iowa's pavements and granular roads resulting from superload traffic have also been identified. These alternatives include the following:

- Implementing special permits or fees for superload traffic significantly induces additional damages and distresses on road infrastructure. Imposing special permits or fees for superloads exceeding standard weight and size limits can generate revenue specifically directed to repair and rehabilitation activities. Based on the RDACs calculated in the LCCA sections of this study, a mechanistic basis for determining such special permit fees can be established. This entails considering various factors that include superload type and payload levels, structural properties of road systems, and other pertinent variables. Certain types of superloads such as modular SHLs, often boast exceptionally high payload capacities as specified in their product manuals or specifications, and to safeguard against substantial damage to road systems, careful consideration must be given to permitting transportation of such payloads.
- Implementing contracts for pavement or granular road construction incentivize contractors to achieve specific performance metrics such as minimizing pavement distresses or extending service life despite the extended number of superload traffic instances. Such contracts can ultimately mitigate the necessity for subsequent repair and rehabilitation efforts resulting from superload traffic.
- Securing additional federal and state funding specifically for repair and rehabilitation of roads facing high volumes of superload traffic is another option. Exploring public-private partnerships (PPPs) may also offer a viable avenue for infrastructure maintenance. Through PPPs, collaboration with private entities frequently using the roads can be leveraged to access private investment and expertise while sharing associated risks and responsibilities.

CHAPTER 11. CONCLUSIONS

Overall Conclusions

In contrast to conventional vehicle types outlined in the FHWA vehicle classification scheme, specialized transportation vehicles, referred to as superloads in this study, present unique challenges to predicting their impacts on road infrastructure due to their ability to carry exceptionally heavy payloads, in addition to their own weight, such as agricultural and industrial products including excavators and wind towers. With the growing sizes of farms and the energy industry, modern superloads transport a significant amount of heavy agricultural and industrial products over not only state or interstate highways but also county and municipal roads, encompassing both granular roads and paved roads. The number of tires and axle configuration (e.g., single-axle, tandem-axle, tridem-axle, and quad-axle), as well as their loadings, are considered major factors in predicting pavement and granular road damages caused by superloads, particularly as they become more common with the current trend of using these high-efficiency and large-scale transportation vehicles to transport heavy agricultural commodities or industrial products. Superloads can be distinguished from general vehicle types not only by their high GVW and axle loadings that may exceed the dimensions of the state's permit limit but also by their non-standardized configurations of tires and axles, including a wide range of dimensions with respect to number, spacing, and loading. Such non-standardized loading configurations are known to be a major factor often responsible for unexpected damage to pavement and granular road systems, especially in the Midwestern region of the United States.

After conducting M-E analysis with comprehensive tasks, including numerical analysis, LCCA, AI-based predictive modeling, forensic investigations, and field data analysis from instrumented remote data acquisition systems, a thorough analysis to evaluate the impact of superloads on Iowa's road infrastructure, encompassing JPCPs, flexible pavements, and granular roads was successfully performed. The culmination of these efforts has resulted in the development of RISAT, a user-friendly prototype tool that allows users to easily calculate structural damages, associated treatment costs, and the reduction in service life for paved road systems, thereby facilitating informed decision-making and efficient management of road infrastructure.

The superloads investigated in this study encompassed 18 types of IoHs and 16 types of SHLs commonly used in the Midwestern region of the United States. This total of 34 types of superloads and an FHWA class 9 truck (reference vehicle), with payload levels of 100%, 75%, 50%, and 0% that each superload can carry, were included in this study to quantify their impacts on pavement and granular road systems. Experimental matrices were meticulously developed to conduct FEA for JPCPs and LET-based analysis for flexible pavements and granular roads, encompassing a diverse range of road structures commonly found in Iowa. A comprehensive total of approximately 33,000 cases of JPCPs, 25,000 cases of flexible pavements, and 3,300 cases of granular roads were subjected to numerical analysis, allowing for a thorough analysis of the structural road damages and associated treatment costs induced by each superload type on the respective road systems. Valuable insights into the potential damages and counteracting strategies associated with each road system were derived through this extensive numerical exploration. Following the collection of a database from mechanistic-based numerical

investigations, ANN-based prediction models were subsequently developed and optimized for each road and superload type. These models demonstrated outstanding accuracy in forecasting critical pavement or granular road responses for representative structural distresses. This underscores the reliability of the RISAT that employs these ANN-based models to calculate and present pavement damages along with associated treatment costs. Note that this study focused on full-depth flexible and rigid pavements as well as granular roads and did not cover composite pavements such as HMA overlay over PCC, PCC overlay over HMA, and others.

Conclusions for JPCP Cases

The quantification of superload impacts on JPCPs was conducted and described using both mechanistic and empirical methodologies described in Chapters 4, 7, and 8. The core findings are summarized as follows:

- **Characterization of superloads for JPCP systems**
 - FEA was conducted to meticulously determine critical loading locations of superloads related to bottom-up and top-down fatigue cracking as mechanistic-based loading inputs.
 - The study identified all critical loading locations of different superload types, considering axle configuration, trailer type, and transverse joint LTE.
- **Evaluation of potential JPCP damages subjected to superloads**
 - The study performed 32,880 cases of FEA related to damage ratios of bottom-up and top-down fatigue cracking of various JPCP structures under superloads.
 - Grain cart IoHs induced significant fatigue-related cracking in JPCP slabs, surpassing other IoH types. Grain carts and manure tankers at all payload levels except 0% exhibited fatigue damage ratios greater than one. Agricultural trailers and agricultural trucks also exhibited relatively lower damage ratios, even lower than one for some JPCP models when carrying a 50% payload or lower. Overall, most IoHs except for grain carts caused fatigue damage similar to that by FHWA class 9 trucks when carrying a 50% payload level.
 - Modular SHLs exhibited greater fatigue-related cracking compared to drop-deck SHLs, impacting JPCP integrity. Drop-deck SHLs caused similar or even lesser fatigue damages than FHWA class 9 trucks at all payload levels, while modular SHLs are likely to cause significant fatigue damages greater than those for FHWA class 9 trucks for payload levels of 50% or more.
 - Different shoulder alternatives, including granular shoulders, full-depth PCC shoulders, and partial-depth HMA shoulders, had similar critical loading locations for various superload categories. Critical tensile stresses within the PCC slab of JPCPs under IoHs are significantly reduced when full-depth PCC shoulders are used, while SHLs exhibit relatively small reductions of critical tensile stresses when paved shoulders are used. This is mainly related to axle-loading positions.
- **LCCA for JPCPs under superloads**
 - Significant insights were gained through LCCA, shedding light on the economic implications of superload-induced damages on JPCP service life.

- Dual-row modular SHLs emerged as the primary contributor to JPCP service life reduction, followed by grain cart IoHs and single-row modular SHLs, emphasizing the need for payload-level optimization.
 - Payload level reduction of superloads significantly mitigated both service life reductions and RDACs, reflecting the potential for cost-effective mitigation strategies.
 - RDACs tended to decrease significantly as PCC layer thickness increased, while the RDACs decreased only slightly as the transverse joint spacing decreased.
 - The influence of management factors on RDACs such as treatment type and discount rate underscored the importance of considering such factors in pavement management decisions.
- **AI-based prediction model development for JPCPs under superloads**
 - A total of 14 ANN-based prediction models were developed for predicting critical pavement responses tailored to 7 different superload categories and 2 different critical pavement response types.
 - The models, optimized with the Bayesian Regularization algorithm, two hidden layers, and seven neurons per hidden layer, exhibited high accuracy in predicting critical tensile stress at both the bottom and top of PCC slabs, enhancing predictive capabilities for pavement performance under superload conditions.
- **Installation of sensors and data acquisition system**
 - Based on the forensic investigation results, strategic planning was made for field instrumentation in coordination with JPCP reconstruction on K45 in Monona County, Iowa.
 - A remote data acquisition system comprised of a P-WIM system, strain gauges, thermistors, moisture sensors, and other components was successfully installed on a reconstructed JPCP section of K45, facilitating real-time pavement response data monitoring.
 - Upon completion of the installation process, it was confirmed that the system operated normally and could be remotely controlled while measuring JPCP responses under environmental conditions and traffic loads.
- **Analysis of JPCP performance-monitoring data**
 - Analysis of data collected during specific periods, including December 2021 and June 2022, provided valuable insights regarding both environmental and traffic-related impacts on JPCP behavior.
 - Observations revealed significant differences in strain values between December 2021 and June 2022, highlighting the dynamic nature of JPCP response to environmental conditions.
 - The in situ temperature and volumetric water content data collected from thermistors and moisture sensors underscored the reliability of the data acquisition system.
 - In situ critical tensile strains collected at the bottom of the PCC slab, when subjected to a class 9 truck, agricultural truck, and drop-deck SHL, exhibited remarkable similarity in magnitude to those obtained from FEA results. However, notable gaps in critical tensile-strain magnitudes were observed at the top of the PCC slab compared to FEA results due

to the inadvertently lowered depth of in situ strain gauges at the top of the PCC slab relative to their planned locations.

- Post-processing adjustments to in situ critical tensile strains at the top of the PCC slab, based on FEA outcomes, ensured data accuracy and facilitated close resemblance between field data and FEM analysis.

These comprehensive conclusions underscore the multifaceted approach used to understand superload impacts on JPCPs, incorporating mechanistic analysis, empirical data collection, economic evaluation, and advanced modeling techniques. The integration of field instrumentation and monitoring further enhanced the reliability and applicability of research findings in real-world JPCP management practices.

Conclusions for Flexible Pavement Cases

The evaluation of superload impacts on flexible pavements described in Chapters 5, 7, and 8 was undertaken utilizing both mechanistic and empirical methodologies. The core findings are outlined as follows:

- **Characterization of superloads for flexible pavement systems**

- A nucleus segment concept was adopted as an identification method for determining the minimum loading group per each type of superload that produced the maximum critical pavement responses close to those that occur when the pavement is subjected to the whole loading configuration.
- The study conducted LET-based analysis to determine the nucleus segment of each superload as a mechanistic-based loading input.

- **Evaluation of potential flexible pavement damages subjected to superloads**

- The study performed 24,660 LET-based analyses related to damage ratios of total rutting and bottom-up fatigue cracking of various flexible pavement structures under superloads.
- The research revealed that grain carts among IoHs and single-row modular and dual-row modular types among SHLs cause relatively higher total rutting and bottom-up fatigue cracking in flexible pavements.
- For total rutting damages, the 50th percentile results of the damage ratio generated by manure tankers, agricultural trailers, and agricultural trucks carrying 50% payload level reached approximately one or less, while the total rutting ratio from grain carts carrying 50% payload levels exceeded one, representing higher total rutting than that from a class 9 truck. On the other hand, single-row and dual-row modular types of SHLs exhibited total rutting ratios mostly higher than those from IoHs, both exceeding one when carrying 50% payload levels or more.
- For bottom-up fatigue damages, IoHs and SHLs carrying 50% payload levels are still likely to exceed values of 8 and 34 average damage ratios, exceeding even the 400 and 100 values of average damage ratios for single-row modular SHLs and grain carts, respectively, when carrying 100% payload levels.

- **LCCA for flexible pavements under superloads**
 - The study calculated RDACs resulting from a single pass of a superload through multivariate LCCA, considering factors such as traffic load, flexible pavement structure, AC material, and treatment type.
 - Two types of SHLs, dual-row modular and single-row modular, and grain carts as an IoH exhibited the highest RDACs, with RDACs significantly influenced by the superload tire weight and travel time on flexible pavements.
 - RDAC results from different flexible structures subjected to superloads show that RDACs tended to dramatically decrease as AC layer thickness increased.
 - The influence of material properties of AC and management factors on RDACs underscored the importance of considering these factors in flexible pavement management decisions.
- **AI-based prediction model development for flexible pavements under superloads**
 - The study developed 35 ANN models based on 7 different superload parent types and 5 critical pavement response types, yielding sufficiently high accuracy in predicting critical tensile strain for bottom-up fatigue cracking and critical vertical strain for total rutting.
 - The ANN models, optimized with the Bayesian Regularization algorithm and architectures of two hidden layers and seven neurons per layer, exhibited high accuracy in predicting critical flexible pavement responses under various superload conditions.
- **Installation of sensors and data acquisition system**
 - Based on the forensic investigation results, the research team established a detailed installation plan for a remote data acquisition system on a full-depth flexible pavement section located on V18 in Tama County, Iowa.
 - This system consisted of a P-WIM system, strain gauges, soil-compression sensors, an earth pressure cell, thermistors, moisture sensors, and other components. The system was successfully installed on V18, facilitating real-time flexible pavement response data monitoring.
 - Upon completion of the installation process, it was confirmed that the system operated normally and could be remotely controlled while measuring flexible pavement responses under both environmental conditions and traffic loads.
- **Analysis of flexible pavement performance monitoring data**
 - Monitored flexible pavement performance data revealed that temperature variations, vertical displacements, and volumetric water content collected from each sensor aligned well with expectations.
 - The researchers noted discrepancies between in situ tensile strain data within the AC layer and LET-based analysis results, attributing them to construction joints and inaccuracies in the AC layer's modulus and traffic load data.
 - Upon comparison of in situ critical pavement response data with those obtained from LET-based analysis results, notable discrepancies were observed for a class 9 truck and agricultural truck. One possible reason for this is the formation of construction joints during the road damage and repair process that may have impacted the magnitude of pavement responses. Inaccuracies in the modulus of each layer and the traffic load data

collected from the P-WIM system as well as deviations in the passage of traffic could also play a role. Despite these discrepancies, the in situ pavement response and traffic data remain valuable as empirical data.

- The study incorporated scaling factors calculated through comparison between mechanistic-based analysis results and in situ data into a prototype tool, providing users with flexibility in scaling pavement response data.

These conclusions collectively provide insights into the mechanistic quantification of superload impacts on flexible pavements and the effectiveness of field instrumentation and monitoring in capturing pavement performance data. The findings also contribute to the development of AI-based prediction models for enhanced prediction of flexible pavement performance under superload traffic.

Conclusions for Granular Road Cases

The impact of superloads on granular roads was described in Chapter 6, 7, and 8. The fundamental outcomes are summarized as follows:

- **Characterization of superloads for granular road systems**
 - The study conducted LET-based analysis to determine the nucleus segment as a mechanistic-based loading input of each superload traveling on granular road systems.
- **Evaluation of potential granular road damages subjected to superloads**
 - The study performed 3,288 cases of LET-based analyses related to the total rutting ratio of various granular road structures under superloads, varying payload levels from 0% to 100%.
 - The researchers identified grain carts among IoHs and single-row modular and dual-row modular types among SHLs as causing greater total rutting than other superload types.
 - When the payload levels of all types of superloads were reduced from 100% to 50%, significant reductions in the total rutting ratio, reaching approximately one, were identified.
- **LCCA for granular roads under superloads**
 - The study obtained RDACs through multivariate LCCA, considering factors such as traffic load, road structure, and treatment type.
 - RDACs showed significant reductions when superload payload levels were lowered, with RDACs proportional to superload tire weight. RDACs also decreased significantly with increasing top granular layer thickness, indicating the effectiveness of a thicker top granular layer in reducing RDACs when experiencing superload traffic.
- **AI-based prediction model development for granular roads under superloads**
 - The team developed 14 ANN-based surrogate models for predicting critical vertical strains for total rutting damages under various superload types, achieving exceptional predictive accuracies.

- Bayesian Regularization algorithm-based ANN models demonstrated the highest prediction accuracies, with optimal architectures comprised of two hidden layers with six neurons each.
- **Installation of sensors and data acquisition system**
 - The researchers developed a sensor installation plan for a granular road section located on 190th Street in Tama County, Iowa, near V18, where sensors for the full-depth flexible pavement study were installed.
 - The team installed the sensors, including soil-compression sensors, an earth pressure cell, thermistors, and moisture sensors, at exact depths and locations within the granular road section. The main data-processing components of the data acquisition system, including data loggers, modem, and power components, were shared with the sensors embedded in the flexible pavement section.
- **Analysis of granular road performance monitoring data**
 - Overall, time-dependent temperatures, volumetric water contents, and vertical displacements at the subgrade and top granular layer aligned with anticipated behavior.
 - Upon comparison of in situ critical vertical strains with those obtained from LET-based analysis results, notable discrepancies were observed for a class 9 truck and agricultural truck, and the same reason given for the field instrumentation of the full-depth flexible pavement may explain this discrepancy. The in situ granular road response and traffic data still remain valuable as empirical data.

These conclusions offer valuable insights into the mechanistic quantification of superload impacts on granular roads and the effectiveness of field instrumentation and monitoring in capturing pavement performance data. The AI-based prediction models developed for granular roads provided sufficiently high accuracies in predicting the critical road responses related to total rutting damages when subjected to various types of superloads.

Conclusions for Development of Prototype Tool: RISAT

- The study developed the RISAT, integrating ANN-based models for JPCPs and flexible pavements to quantify potential pavement damages, treatment costs, and service life reductions resulting from various superload scenarios.
- RISAT is a macro-enabled VBA-based Microsoft Excel-based automation tool featuring a navigation panel and sub-tools.
- The navigation panel allows users to select pavement and superload types for analysis, guiding them through various sub-tools that provide mechanistic-based outputs derived from ANN-based prediction models, incorporating in situ empirical-based response data to scale critical pavement responses.
- RISAT deals with the main structural damages such as bottom-up and top-down fatigue damages for JPCPs, and bottom-up fatigue and rutting damages for flexible pavements.
- Users can easily input pavement structural and loading properties for a chosen pavement and superload type to obtain the damage ratio, RDAC, and reduction in service life of JPCPs or flexible pavements under various superload scenarios.

- The RISAT prototype tool offers a comprehensive solution for quantifying superload impacts on Iowa road infrastructure, providing engineers and planners with valuable insights for informed decision-making in pavement design and maintenance.

CHAPTER 12. RECOMMENDATIONS FOR IMPLEMENTATION AND FUTURE RESEARCH

This study developed the RISAT, which is designed to assist Iowa county engineers in evaluating the impact of superloads on Iowa road infrastructure in terms of structural damages, RDACs, and reduction in service life. RISAT comprehensively incorporates the findings of this study, encompassing both theoretical frameworks and practical applications for JPCPs and flexible pavements exposed to various superload scenarios. The tool offers a wide range of options for estimating damages and associated treatment costs, considering diverse pavement structures and superload loading configurations. It also offers options for applying various treatment types for future repair or rehabilitation and incorporates a discount rate reflective of the current US economic conditions, facilitating accurate determination of RDACs. These estimations can enable county engineers to quickly make informed decisions regarding repair and rehabilitation plans for each road section under their jurisdiction, as well as determining appropriate permit fees or weight permits for superloads traveling on Iowa roads. Figure 108 demonstrates the integration of the Microsoft Excel-based RISAT into Iowa county's pavement asset management procedures.

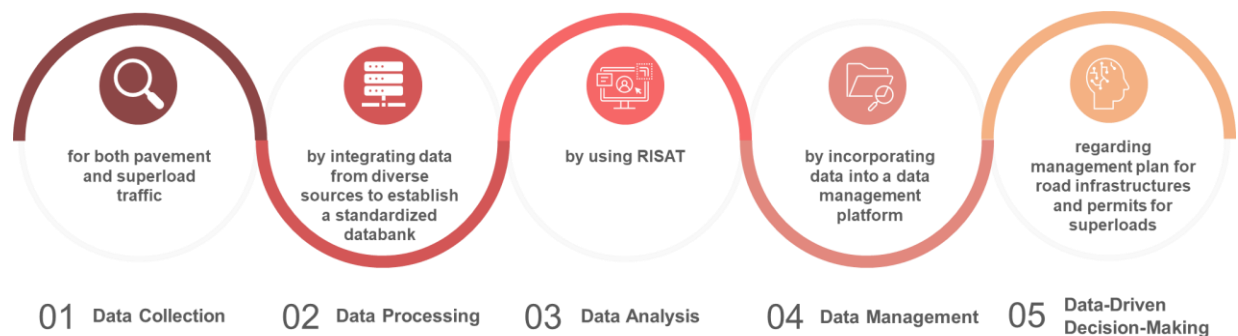


Figure 108. Integration of RISAT into pavement asset management protocols

Each procedure is delineated in the following recommended steps:

- **Step 1: Data collection**
Conduct data collection of county pavement inventory data, including construction history, structural damages, and maintenance activities, employing cost-effective methodologies. Collect superload traffic data, including frequency of annual superload passages and their respective loading configurations (such as axle weights, GVWs, and tire weights) for each road section, utilizing permanent and portable traffic counters and WIM systems, or automatic traffic recorders (ATRs) as economically viable approaches. Alternatively, deploy traffic counting systems or video-based traffic monitoring systems with additional funding and labor resources.
- **Step 2: Data processing**
Integrate superload traffic data with AADT and AADTT data per road section to contextualize the impact of superloads within overall traffic patterns. Segment and

summarize collected data to pinpoint events such as structural damages and distress data along linear features like pavement management sections. Employ dynamic processing techniques to assign linear measures (e.g., milepost, latitude, and longitude) to individual pavement sections while incorporating superload traffic data into the processing framework. Integrate data from diverse sources while preventing duplication or overlap, especially distinguishing between heavy-haul trucks and superloads necessitating distinct categorization, thus establishing a standardized databank for streamlined analysis.

- **Step 3: Data analysis with RISAT**

Utilize the Microsoft Excel-based RISAT to analyze processed data and evaluate the impact of superloads on Iowa road infrastructure. Leverage RISAT to evaluate structural damages, RDACs, and reductions in service life for various pavement types and superload configurations.

- **Step 4: Data management**

Incorporate processed and analyzed data into a data management platform or software tailored to Iowa county's practices, ensuring compatibility with existing data management systems to facilitate seamless integration and accessibility for county engineers and stakeholders. Implement robust data storage and retrieval mechanisms to maintain data integrity and support ongoing analysis and decision-making processes. Establish protocols for updating and maintaining superload traffic data to ensure its relevance and accuracy over time.

- **Step 5: Data-driven decision-making**

Utilize insights gleaned from RISAT analyses, emphasizing structural damages and associated treatment costs, to prioritize resource allocation for pavement preservation and rehabilitation efforts. Utilize outcomes from RISAT for various pavement structures and superload types to make informed decisions regarding repair and rehabilitation plans, as well as determine appropriate permit fees or weight restrictions for superloads traveling on Iowa road infrastructure. Continuously monitor and evaluate the impact of superload traffic on pavement conditions, adjusting strategies and policies as needed to mitigate adverse effects and ensure long-term infrastructure sustainability.

The forthcoming phase(s) of this endeavor will yield guidelines designed to address the needs of county engineers in fully implementing the recommended steps described above, while also enhancing the capabilities of RISAT. These guidelines are organized into five distinct categories related to each step:

- **Step 1: Enhance data collection practices with advanced technology and strategy**

To ensure consistent and reliable updates across Iowa counties' roads, it is imperative to develop and implement standardized data-collection protocols. These protocols may utilize low-cost data collection tools tailored for local road agencies, enabling more frequent gathering of pavement performance data and establishing a comprehensive and dependable database. With such tools in place, local road agencies can accurately record geographical coordinates, structural characteristics, and environmental conditions for each road section,

using standardized metadata to minimize errors during data transfer and ensure database integrity when road alignments change. Adoption by local agencies of recommendations from the Iowa Highway Research Board (IHRB) project entitled “Development of a Smartphone-Based Road Performance Data Collection Tool” (Yang et al. 2023) is highly encouraged. The project’s research team has been actively developing standardized, nonproprietary collection tools, including a smartphone-based road performance data collection tool and a smart vehicle black box, both equipped with automatic vehicle location (AVL) technology. For the collection of superload traffic data, exploration of advanced technologies such as a remote sensing system with WIM technology or AI-based vehicle detection and tracking systems is required. Training programs aimed at regular review and update of traffic data, including accurate categorization of superload traffic related to other vehicle types, are essential to ensure alignment with evolving best practices.

- **Step 2: Develop automated algorithms or tools for data processing**

Develop automated algorithms or tools to streamline data processing and updates. Enhance integration capabilities to incorporate additional data sources when road alignment or traffic volume changes. Implement rigorous quality-control measures to ensure data accuracy and reliability. Exploring cloud-based solutions offers potential for scalable and efficient data processing, and fostering collaboration with academic institutions or research organizations can provide access to advanced data processing techniques, thereby enriching research endeavors.

- **Step 3: Integrate IPAT and PSAT capabilities into RISAT**

Expand the capabilities of RISAT to include functionalities of other pavement and operational management tools, specifically IPAT and PSAT developed from IHRB projects entitled “Development of Iowa Pavement Analysis Techniques (IPAT)” (Citir et al. 2021) and “Development of Pavement Structural Analysis Tool (PSAT) for Iowa Local Roads” (Citir et al. 2023), respectively. This integration will elevate the tool to a comprehensive solution for analyzing paved-road systems, extending beyond superloads to encompass all types of traffic, including vehicles classified by the FHWA. Collaboration with key stakeholders, including the Iowa DOT, county engineers, and industry experts, is also essential to enhance the robustness of RISAT by addressing real-world challenges and incorporating solutions into updated versions of the tool. Regular performance evaluations and updates of RISAT to account for changes in road alignments or treatment costs, as well as rapidly evolving superload types and configurations would be required.

- **Step 4: Add WIM data to RISAT and integrate the tool into a geographic information system (GIS) platform**

Incorporate WIM data sourced from the Iowa DOT Motor Vehicle Division and Office of Systems Planning (OSP) (Iowa DOT 2018) into RISAT, alongside video-recorded traffic data. Integrate the tool seamlessly into the GIS platform to enhance its functionality and usability. These two approaches will establish robust data management systems tailored to Iowa counties’ specific needs, addressing superload issues on Iowa road infrastructure and ensuring efficiency and accuracy in data processing. Establishing protocols for data backup and recovery to mitigate the risk of data loss and ensure operational continuity and providing

ongoing training and support for staff involved in data management activities to optimize utilization of the integrated system would be important.

- **Step 5: Develop a total package for repair and rehabilitation solutions for lifetime pavement resilience, considering traffic conditions of each road section in Iowa**

Formulate a total package of repair and rehabilitation solutions aimed at enhancing pavement resilience throughout its lifetime, with due consideration to the traffic conditions, including FHWA classified vehicles and superloads, prevalent in each road section across Iowa. By incorporating insights from data collected through RISAT and other integrated tools, such as WIM data and GIS platforms, tailor-made solutions can be devised to address specific challenges faced by different road segments. These solutions will not only focus on mitigating structural road damages but also on optimizing maintenance strategies to prolong pavement service life under varying traffic conditions.

Future research topics have been identified and prioritized to not only support the full implementation of outcomes from this study but also to facilitate transparent and rational decision-making in the management of Iowa's pavement and granular road assets. These often face public requests for increased axle or gross weight limits on commercial vehicles. The topics are as follows:

- **Evaluation of increased legal loads and their impact on Iowa pavement service life**

The implementation of Iowa's new all systems overweight permit brings significant changes to transportation regulations, allowing increased weight allowances on designated roads. County engineers are tasked with identifying permitted routes by 2025, necessitating thorough evaluations of road capabilities. Rigorous M-E investigations are essential to assess the impact of increased weight allowances, requiring comprehensive data collection on pavement history and structural design. Despite the complexities, effective approaches for pavement preservation are crucial for prudent road asset management amidst evolving legislative frameworks. While this research study, TR-781, addressed superload impacts, further study is needed to evaluate the effects of overweight traffic permitted by the new permit and refine methodologies to meet updated challenges.

- **Impact quantification of heavy agricultural vehicles on Iowa's granular roads**

Granular roads, comprising a substantial portion of Iowa's secondary road network, serve as vital conduits for agricultural transportation but face accelerated degradation, exacerbated by heavy agricultural vehicles. Current maintenance practices, often reactive and underfunded, fail to address the significant deterioration caused by these vehicles. To comprehensively assess their impact, a systematic analysis of various factors is essential, including material qualities, drainage, and traffic patterns. M-E methodologies offer a systematic approach to quantify these effects, facilitating informed decision-making for granular road preservation and management. While this research study, TR-781, addressed superload impacts, additional study is needed to fully understand the effects of heavy agricultural vehicles on granular roads, incorporating both structural and functional deteriorations.

- **Impact of superloads on Iowa's composite pavement systems**

This project examined the impact of superload traffic on Iowa's pavements and granular roads, focusing mainly on full-depth flexible and rigid pavements and granular roads. A proposed Phase II would extend the study to include composite pavements, aiming to enhance the M-E analysis methodologies and tools for quantifying superload impacts on almost every type of road system existing in Iowa. By deploying remote sensing and WIM systems, a Phase II would seek to provide comprehensive insights and management tools for addressing superload traffic challenges across Iowa's road infrastructure.

- **Developing a low-cost WIM tool for enhanced OS/OW traffic management in Iowa's county roads**

The transportation landscape in Iowa has faced challenges in accurately assessing the impact of OS/OW vehicles on county roads while managing limited resources. Developing a low-cost WIM tool capable of accurately measuring both the GVW and axle weight of OS/OW traffic, supplemented by remote sensing systems with AI-based algorithms for traffic type classification, is crucial. The proposed solution aims to democratize access to crucial data for decision-making, enhance efficiency and accuracy compared to traditional methods, and facilitate proactive maintenance and infrastructure planning on Iowa county roads.

REFERENCES

- AASHTO. 2022. *AASHTOWare Pavement ME Design*. American Association of State Highway and Transportation Officials, Washington, DC. <https://me-design.com/MEDesign/?AspxAutoDetectCookieSupport=1>. Last accessed April 2024.
- AASHTO. 2015. *Mechanistic-Empirical Pavement Design Guide: A Manual of Practice*, 2nd Edition. American Association of State Highway and Transportation Officials, Washington, DC.
- ACS Group. 2018. *Ultrasonic Low-Frequency Tomograph A1040 MIRA Operation Manual*. Acoustic Control Systems – ACS Group, Saarbrücken, Germany. <https://acs-international.com/wp-content/themes/Divi-2/download/10%20A1040%20MIRA/Operation%20manual.pdf>. Last accessed April 2024.
- ARA, Inc. 2004a. Part 3. Design Analysis, Chapter 4. Design of New and Reconstructed Rigid Pavements. *Guide for Mechanistic-Empirical Design of New and Rehabilitated Pavement Structures*. Applied Research Associates, Inc., ERES Consultants Division, Champaign, IL.
- ARA, Inc. 2004b. Appendix GG-1: Calibration of Permanent Deformation Models for Flexible Pavements. *Guide for Mechanistic-Empirical Design of New and Rehabilitated Pavement Structures*. Applied Research Associates, Inc., ERES Consultants Division, Champaign, IL.
- Batioja-Alvarez, D. D., E. Y. Hajj, and R. V. Siddharthan. 2018. *Analysis Procedures for Evaluating Superheavy Load Movement on Flexible Pavements, Volume IX: Appendix H, Analysis of Cost Allocation Associated With Pavement Damage Under a Superheavy Load Vehicle Movement*. No. FHWA-HRT-18-057. Federal Highway Administration, Turner-Fairbank Highway Research Center, McLean, VA.
- BDI. 2019. *STS4: Core Data Logger*. Bridge Diagnostics, Inc., Louisville, CO. <https://bdiest.com/wp-content/uploads/2022/09/201521-Rev-B-Datasheet-Core-Data-Logger-STS4-CDL.pdf>. Last accessed April 2024.
- BDI. 2020. *STS4: 4- or 16-Channel Terminal Nodes*. Bridge Diagnostics, Inc., Louisville, CO. <https://bdiest.com/wp-content/uploads/2022/09/201611-Rev-B-Datasheet-STS4-Data-Acquisition-STS4-TE4.pdf>. Last accessed April 2024.
- BDI. 2022a. *CEST350: Concrete Embedment Strain Transducer*. Bridge Diagnostics, Inc., Louisville, CO. <https://bdiest.com/wp-content/uploads/2020/08/208781-Rev-C-Datasheet-Concrete-Embedment-Strain-Transducer-CEST350.pdf>. Last accessed April 2024.
- BDI. 2022b. *AST and VAST: Asphalt Strain Transducers*. Bridge Diagnostics, Inc., Louisville, CO. <https://bdiest.com/wp-content/uploads/2022/09/208601-Rev-D-Datasheet-Asphalt-Strain-Transducer-AST350-VAST350.pdf>. Last accessed April 2024.
- BDI. 2022c. *SCS: Soil Compression Gage*. Bridge Diagnostics, Inc., Louisville, CO. <https://bdiest.com/wp-content/uploads/2022/09/208791-Rev-C-Datasheet-Soil-Compression-Sensor-SCS.pdf>. Last accessed April 2024.
- BDI. 2024a. *Thermistor*. Bridge Diagnostics, Inc., Louisville, CO. <https://bdiest.com/wp-content/uploads/2016/01/Products-Thermistor.pdf>. Last accessed April 2024.
- BDI. 2024b. *STS-LIVE*. Bridge Diagnostics, Inc., Louisville, CO. <https://bdiest.com/product/sts-live/>. Last accessed April 2024.

- Broyden, C. G. 1970a. The Convergence of a Class of Double-Rank Minimization Algorithms 1. General Considerations. *IMA Journal of Applied Mathematics*, Vol. 6, No. 1, pp. 76–90.
- Broyden, C. G. 1970b. The Convergence of a Class of Double-Rank Minimization Algorithms: 2. The New Algorithm. *IMA Journal of Applied Mathematics*, Vol. 6, No. 3, pp. 222–231.
- Byrum, C. R., and W. Hansen. 1994. Influence Function Approach to Analysis of Jointed Portland Cement Concrete Pavement. *Transportation Research Record: Journal of the Transportation Research Board*, Vol. 1449, pp. 148–158.
- Cetin, B., S. Satvati, J. C. Ashlock, and C. Jahren. 2019. *Performance-Based Evaluation of Cost-Effective Aggregate Options for Granular Roadways*. IHRB Project TR-704. Institute for Transportation, Iowa State University, Ames, IA.
- Ceylan, H. 2014. Performance Evaluation of a Jointed Plain Concrete Pavement Using Mechanistic-Empirical Pavement Design Guide: A Case Study. Transportation Research Board 93rd Annual Meeting, January 12–16, Washington, DC.
- Ceylan, H., K. Gopalakrishnan, and S. Kim. 2009. *Characterization of Unbound Materials (Soils/Aggregates) for Mechanistic-Empirical Pavement Design Guide*. CTRE Project 06-271. Institute for Transportation, Iowa State University, Ames, IA.
- Ceylan, H., S. Kim, K. Gopalakrishnan, C. W. Schwartz, and R. Li. 2014. Sensitivity Analysis Frameworks for Mechanistic-Empirical Pavement Design of Continuously Reinforced Concrete Pavements. *Construction and Building Materials*, Vol. 73, pp. 498–508.
- Ceylan, H., S. Yang, K. Gopalakrishnan, S. Kim, P. Taylor, and A. Alhasan. 2016. *Impact of Curling and Warping on Concrete Pavement*. IHRB Project TR-668. Institute for Transportation, Iowa State University, Ames, IA.
- Citir, N., H. Ceylan, S. Kim, D. Waid, B. P. Moore, and I.-H. Cho. 2023. *Development of Pavement Structural Analysis Tool (PSAT) for Iowa Local Roads*. IHRB Project TR-762. Program for Sustainable Pavement Engineering and Research, Institute for Transportation, Iowa State University, Ames, IA.
- Citir, N., O. Kaya, H. Ceylan, S. Kim, D. Waid, and B. P. Moore. 2021. *Development of Iowa Pavement Analysis Techniques (IPAT)*. IHRB Project TR-740. Program for Sustainable Pavement Engineering and Research, Institute for Transportation, Iowa State University, Ames, IA.
- Clyne, T. R., X. Li, M. O. Marasteanu, and E. L. Skok. 2003. *Dynamic and Resilient Modulus of Mn/DOT Asphalt Mixtures*. MN/RC – 2003-09. Minnesota Department of Transportation, St. Paul, MN.
- Danz, M. E., W. R. Selbig, and N. H. Buer. 2020. Assessment of Restorative Maintenance Practices on the Infiltration Capacity of Permeable Pavement. *Water*, Vol. 12, No. 6, p. 1563.
- Dong, Q., B. Huang, X. Shu, C. Zhou, and J. Maxwell. 2014. Use of Finite Element Analysis and Fatigue Failure Model to Estimate Costs of Pavement Damage Caused by Heavy Vehicles. *Transportation Research Record: Journal of the Transportation Research Board*, Vol. 2455, No. 1, pp. 54–62.
- ERES Consultants. 1999. ISLAB2000 Finite Element Code for Rigid Pavement Analysis. Version 3.6. ERES Consultants, Champaign, IL.
- Fanous, F., B. Coree, and D. Wood. 2000. *Response of Iowa Pavements to a Tracked Agricultural Vehicle*. Center for Transportation Research and Education, Institute for Transportation, Iowa State University, Ames, IA.

- FHWA. 2015. *Gravel Roads Construction and Maintenance Guide*. Federal Highway Administration, Washington, DC.
- FHWA. 2014. *Traffic Monitoring Guide: Appendix C. Vehicle Types*. Federal Highway Administration, Washington, DC.
https://www.fhwa.dot.gov/policyinformation/tmguidetmg_2013/vehicle-types.cfm. Last accessed April 2024.
- Fletcher, R. 1970. A New Approach to Variable Metric Algorithms. *The Computer Journal*, Vol. 13, No. 3, pp. 317–322.
- GEOKON. 2023. *Instruction Manual: Model 3500 Series Earth Pressure Cells*. GEOKON, Lebanon, NH.
https://www.geokon.com/content/manuals/3500_Earth_Pressure_Cells.pdf. Last accessed April 2024.
- Goldfarb, D. 1970. A Family of Variable-Metric Methods Derived by Variational Means. *Mathematics of Computation*, Vol. 24, No. 109, pp. 23–26.
- Hajj, E. Y., R. V. Siddharthan, H. Nabizadeh, S. Elfass, M. Nimeri, S. F. Kazemi, D. Batioja-Alvarez, and M. Piratheepan. 2018. *Analysis Procedures for Evaluating Superheavy Load Movement on Flexible Pavements, Volume I: Final Report*. FHWA-HRT-18-049. Federal Highway Administration, Turner-Fairbank Highway Research Center, McLean, VA.
- Hansen, W., and Y. Wei. 2008. *PCC Pavement Acceptance Criteria for New Construction When Built-In Curling Exists*. RC-1481. Michigan Department of Transportation, Lansing, MI.
- Hiller, J. E., and J. R. Roesler. 2005. Determination of Critical Concrete Pavement Fatigue Damage Locations Using Influence Lines. *Journal of Transportation Engineering*, Vol. 131, No. 8, pp. 599–607.
- Huang, Y. H. 2004. *Pavement Analysis and Design*, 2nd Edition. Pearson Education, London, UK.
- Iowa DOT. 2018. *Intelligent Transportation Systems (ITS) and Communications Systems Service Layer Plan*. Iowa Department of Transportation, Ames, IA.
- Iowa DOT. 2019. *2019–2028 Transportation Asset Management Plan*. Iowa Department of Transportation, Ames, IA.
- Iowa DOT. 2023a. *Iowa Truck Information Guide*. Iowa Department of Transportation, Ames, IA.
- Iowa DOT. 2023b. *Open Data: Pavement*. Iowa Department of Transportation, Ames, IA.
<https://data.iowadot.gov/datasets/IowaDOT::pavement/about>. Last accessed October 2023.
- IRD. 2023b. *Piezoelectric Sensors*. International Road Dynamics, Inc., Saskatoon, SK, Canada.
<https://irdinc.com/products/axle-sensors-grout/piezoelectric-sensors-2/>. Last accessed April 2024.
- IRD. 2023a. *TRS Counters, Classifiers and WIM Data*. International Road Dynamics, Inc., Saskatoon, SK, Canada. <https://irdinc.com/products/counters-classifiers/trs-counters-classifiers-and-wim-data/>. Last accessed April 2024.
- Johansson, E. M., F. U. Dowlal, and D. M. Goodman. 1991. Backpropagation Learning for Multilayer Feed-Forward Neural Networks Using the Conjugate Gradient Method. *International Journal of Neural Systems*, Vol. 2, No. 4, pp. 291–301.
- Khazanovich, L. 2022. *NCHRP Research Report 1019: Quantifying the Effects of Implements of Husbandry on Pavements*. National Cooperative Highway Research Program, Washington, DC.

- Khazanovich, L., and Q. Wang. 2007. MnLayer: High-Performance Layered Elastic Analysis Program. *Transportation Research Record: Journal of the Transportation Research Board*, Vol. 2037, No. 1, pp. 63–75.
- Klaiber F. W., T. L. Thomas, and D. Y. Lee. 1979. *Fatigue Behavior of Air-Entrained Concrete: Phase II*. Iowa Department of Transportation, Ames, IA.
- Koh, Y., H. Ceylan, S. Kim, and I.-H. Cho. 2022a. Structural and Fatigue Analysis of Jointed Plain Concrete Pavement Top-Down and Bottom-Up Transverse Cracking Subjected to Superloads. *Transportation Research Record: Journal of the Transportation Research Board*, Vol. 2676, No. 9, pp. 76–93.
- Koh, Y., H. Ceylan, S. Kim, and I. H. Cho. 2022b. Characterizations of Super Heavy Loading Configuration for Flexible Pavement Analysis. *Proceedings of the Eleventh International Conference on the Bearing Capacity of Roads, Railways and Airfields*, CRC Press, Boca Raton, FL, pp. 370–379.
- Koh, Y., H. Ceylan, S. Kim, and I. H. Cho. 2023a. Mechanistic Basis for Permit Fee Decision of Superloads Traveling on Low-Volume Roads Using Structural Damage Evaluation. *Transportation Research Record: Journal of the Transportation Research Board*, p. 03611981231156577.
- Koh, Y., H. Ceylan, S. Kim, and I. H. Cho. 2023b. Critical Responses of Flexible Pavements under Superheavy Loads and Data-Driven Surrogate Model. *International Journal of Pavement Research and Technology*, Vol. 16, pp. 513–543.
- Koh, Y., H. Ceylan, S. Kim, and I. H. Cho. 2024. An Artificial-Intelligence Based Approach for Predicting Structural Damages of Paved-Road Systems under Superloads. *Construction and Building Materials*, Vol. 411, p. 134257.
- Korenev, B. G., and E. I. Chernigovskaya. 1962. Analysis of Plates on Elastic Foundation. *Gosstroizdat*, Moscow, Russia.
- Lee, D.-Y., F. W. Klaiber, and J. W. Coleman. 1978. Fatigue Behavior of Air-Entrained Concrete. *Transportation Research Record: Journal of the Transportation Research Board*, Vol. 671, pp. 20–23.
- Levenberg, K. 1944. A Method for the Solution of Certain Non-Linear Problems in Least Squares. *Quarterly of Applied Mathematics*, Vol. 2, pp. 164–168.
- Lim, J., A. Azary, L. Khazanovich, S. Wang, S. Kim, H. Ceylan, and K. Gopalakrishnan. 2012. *Effects of Implements of Husbandry (Farm Equipment) on Pavement Performance*. Minnesota Department of Transportation, St. Paul, MN.
- MacKay, D. J. C. 1992. A Practical Bayesian Framework for Backpropagation Networks. *Neural Computation*, Vol. 4, No. 3, pp. 448–472.
- Marquardt, D. W. 1963. An Algorithm for Least-Squares Estimation of Nonlinear Parameters. *Journal of The Society for Industrial and Applied Mathematics*, Vol. 11, No. 2, pp. 431–441.
- METER Group. 2024. *TEROS 11/12*. METER Group, Inc., Pullman, WA. http://publications.metergroup.com/Manuals/20587_TEROS11-12_Manual_Web.pdf. Last accessed April 2024.
- METER Group. 2023. *ZL6*. METER Group, Inc., Pullman, WA. http://publications.metergroup.com/Manuals/20789_ZL6_Manual_Web.pdf. Last accessed April 2024.

- Miller, J. S., and W. Y. Bellinger. 2014. *Distress Identification Manual for the Long-Term Pavement Performance Program (Fifth Revised Edition)*. FHWA-HRT-13-092. Federal Highway Administration, Turner-Fairbank Highway Research Center, McLean, VA.
- Nimeri, M., H. Nabizadeh, E. Hajj, R. V. Siddharthan, and S. Elfass. 2018. *Analysis Procedures for Evaluating Superheavy Load Movement on Flexible Pavements, Volume III: Appendix B, Superheavy Load Configurations and Nucleus of Analysis Vehicle*. FHWA-HRT-18-051. Federal Highway Administration, Turner-Fairbank Highway Research Center, McLean, VA.
- Packard, R. G., and S. D. Tayabji. 1985. New PCA Thickness Design Procedure for Concrete Highway and Street Pavements. *Proceedings of the Third International Conference on Concrete Pavement Design and Rehabilitation*, April 23–25, Purdue University, West Lafayette, IN.
- Papagiannakis, A. T. 2015. *NCHRP Report 476: Practices for Permitting Superheavy Load Movements on Highway Pavements*. National Cooperative Highway Research Program, Washington, DC.
- Phares, B., C. T. Kilaru, L. Greimann, J. Seo, and K. Freeseaman. 2017. *Study of the Impacts of Implements of Husbandry on Bridges Volume I: Live Load Distribution Factors and Dynamic Load Allowances*. IHRB Project TR-613. Bridge Engineering Center, Institute for Transportation, Iowa State University, Ames, IA.
- Prakoso, A., H. R. Chunduri, and L. F. Walubita. 2022. *Guidelines for Portable Weight-in-Motion (WIM) System Installation and Traffic Data Analysis*. Project 5-6940-01. Texas A&M Transportation Institute, College Station, TX.
- Rezaei-Tarahomi, A., H. Ceylan, O. Kaya, K. Gopalakrishnan, and S. Kim. 2019. *Implementing A Multiple-Slab Response Model for Top-Down Cracking Mode in Rigid Airport Pavements*. Federal Aviation Administration, Washington, DC.
- Riedmiller, M., and H. Braun. 1993. A Direct Adaptive Method for Faster Backpropagation Learning: The RPROP Algorithm. *Proceedings of IEEE International Conference on Neural Networks*, pp. 586–591, San Francisco, CA.
- Schaefer, V., L. Stevens, D. White, and H. Ceylan. 2008. *Design Guide for Improved Quality of Roadway Subgrades and Subbases*. IHRB Project TR-525, Center for Transportation Research and Education, Institute for Transportation, Iowa State University, Ames, IA.
- Shanno, D. F. 1970. Conditioning of Quasi-Newton Methods for Function Minimization. *Mathematics of Computation*, Vol. 24, No. 111, pp. 647–656.
- Skorseth, K., and A. A. Selim. 2000. *Gravel Roads: Maintenance and Design Manual*. Federal Highway Administration, Washington, DC.
- Souleyrette, R., T. McDonald, Z. Hans, A. Kamyab, T. Welch, and B. Storm. 2001. *Paved Shoulders on Primary Highways in Iowa: An Analysis of Shoulder Surfacing Criteria, Costs, and Benefits*. Center for Transportation Research and Education, Institute for Transportation, Iowa State University, Ames, IA.
- SSI, Inc. 2023. *SSI Inertial Profiling Systems Technical Specifications*. Surface Systems & Instruments, Inc., Auburn, CA. https://www.smoothroad.com/wp-content/uploads/2023/02/SSI-High-Speed-Profiling-System-Technical-Specifications_2023.pdf. Last accessed April 2024.
- Stone, J. R., M. Kowalsky, R. Hughes, C. K. Herrick, B. Narron, and W. Cao. 2012. *Analysis of Truck Load Weight Distribution in North Carolina*. North Carolina Department of Transportation, Raleigh, NC.

- Tirado, C., C. Carrasco, J. M. Mares, N. Gharaibeh, S. Nazarian, and J. Bendaña. 2010. Process to Estimate Permit Costs for Movement of Heavy Trucks on Flexible Pavements. *Transportation Research Record: Journal of the Transportation Research Board*, Vol. 2154, No. 1, pp. 187–196.
- TxDMV. 2024. *Super Heavy Single-Trip Permits*. Texas Department of Motor Vehicles, Austin, TX. <https://www.txdmv.gov/motor-carriers/oversize-weight-permits/super-heavy-single-trip>. Last accessed April 2024.
- Uzan, J. 2001. Jacob Uzan Layer Elastic Analysis (JULEA) Software. Technion University, Haifa, Israel.
- Vandenbossche, J. M., C. A. Donnelly, N. Buettner, S. Sen, and Z. Brody. 2021. *Effect of Superloads on Pavement Life*. FHWA-PA-2022-001-PITT WO 019. Pennsylvania Department of Transportation, Harrisburg, PA.
- Visintine, B. A., G. R. Rada, and A. L. Simpson. 2018. *Guidelines for Informing Decisionmaking to Affect Pavement Performance Measures*. FHWA-HRT-17-090. Federal Highway Administration, Turner-Fairbank Highway Research Center, McLean, VA.
- Walker D. 2002. *Gravel Pavement Surface Evaluation and Rating (PASER) Manual*. Transportation Information Center, University of Wisconsin-Madison, Madison, WI.
- Wang, S., H. Ceylan, S. Kim, K. Gopalakrishnan, L. Khazanovich, and S. Dai. 2012. Impact of Farm Equipment Loading on Rigid Pavement Performance Using Finite Element Analysis. *10th International Conference on Concrete Pavements*, July 8–12, Québec City Québec, Canada.
- Witczak, M. W., and M. M. El-Basyouny. 2004. Appendix IT-1: Calibration of Fatigue Cracking Models for Flexible Pavements. *Guide for Mechanistic-Empirical Design of New and Rehabilitated Pavement Structures*. National Cooperative Highway Research Program, Washington, DC.
- Yang, B., Y. Jiao, H. Jiang, V. A. Gorthy, M. A. A. Sourav, H. Ceylan, W. Zhang, S. Kim, C. Lin, S. Mao, D. Waid, and B. P. Moore. 2023. *Development of a Smartphone-Based Road Performance Data Collection Tool*. IHRB Project TR-777. Program for Sustainable Pavement Engineering and Research, Institute for Transportation, Iowa State University, Ames, IA.

APPENDIX A. FORENSIC INVESTIGATION DATA

Forensic Investigation Data from Union County

This appendix section includes imagery and documentation related to a forensic investigation carried out in Union County, Iowa, from May 7 to 9, 2020. This investigation covered sections of Osage Street (a granular road) and North Osage Street (featuring PCC-surfaced pavement), that form a contiguous route, as well as Rea Road (featuring AC-surfaced pavement) and Cherry Street (also featuring PCC-surfaced pavement), constituting another continuous route. The primary objectives of this forensic investigation were to assess topographical features, identify distress patterns, evaluate design characteristics, and analyze daily traffic patterns. IRI values were also measured for each road segment using a high-speed profiler. Chapter 7 extensively documents the principal findings of the forensic investigation conducted in Union County. This appendix complements the documentation by presenting additional materials such as images and surveys of distress as well as construction or reconstruction design drawings provided by the county engineer.

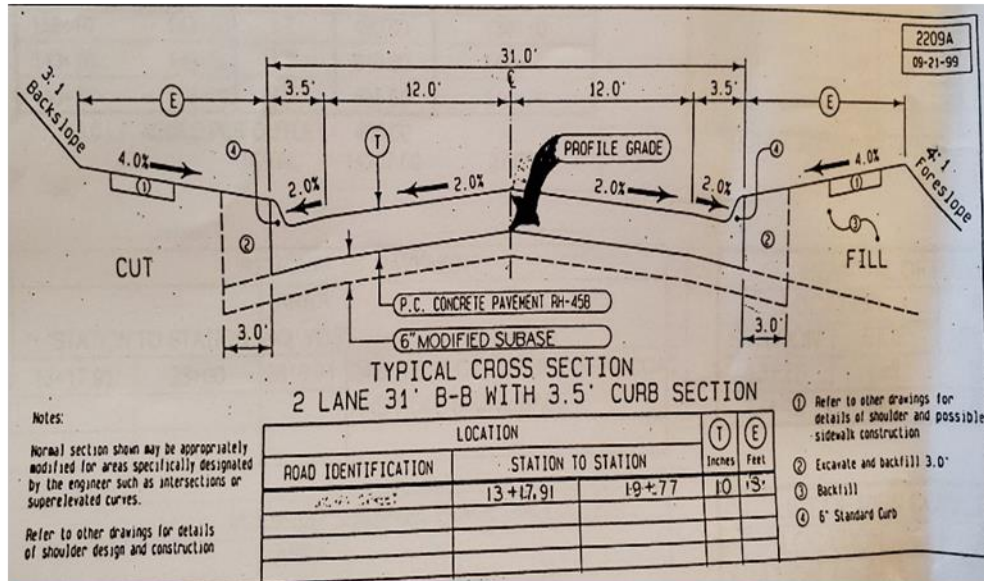
Overall distress types and features along with corresponding images captured from each road section are depicted in Figure 109. For detailed information regarding the severity of these distresses in each specific road section, refer to Chapter 7.



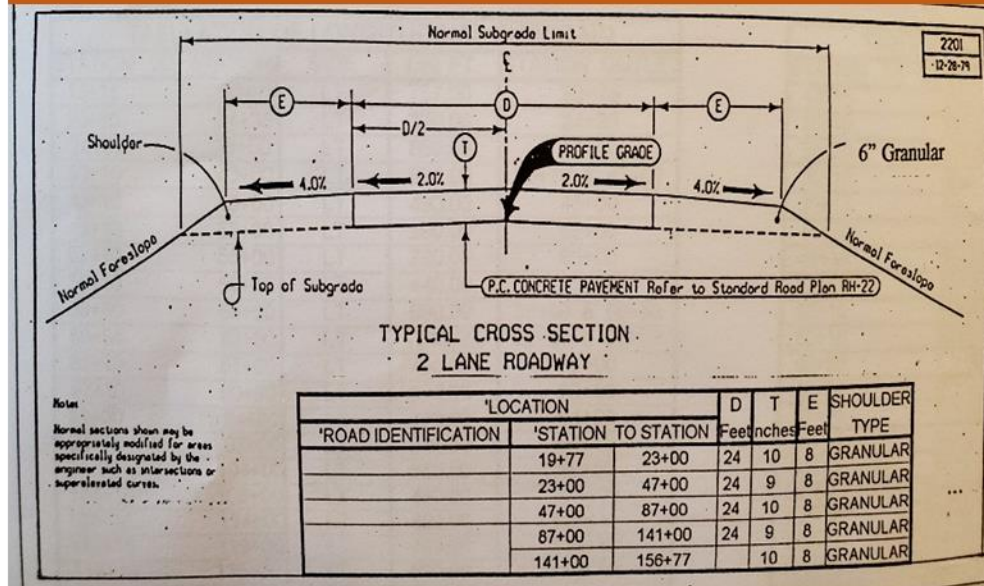
Figure 109. Representative distresses and features of each road section: (a) Osage Street, (b) North Osage Street, (c) Rea Road, and (d) Cherry Street

As detailed in Chapter 7, a modular SHL with dollies conducted three round trips over three consecutive days, specifically between May 7 and 9, 2020, traveling both Cherry Street and Rea Road in Union County. The SHL initiated its operations from the northern terminus of Creston, proceeded along Cherry Street, and concluded near Rea Road at the CIPCO facility. Figure 110 provides cross-sectional structural information for both Cherry Street and Rea Road, while Figure 111 offers a comparison of images depicting existing distress before and after the third pass of the SHL, and there was no significant visual exacerbation of these distresses overall following three SHL passages.

(a)



Cherry St. – from Sta. 13+17.91 to Sta. 19+77



Cherry St. – from Sta. 19+77 to Sta. 156+77

(b)

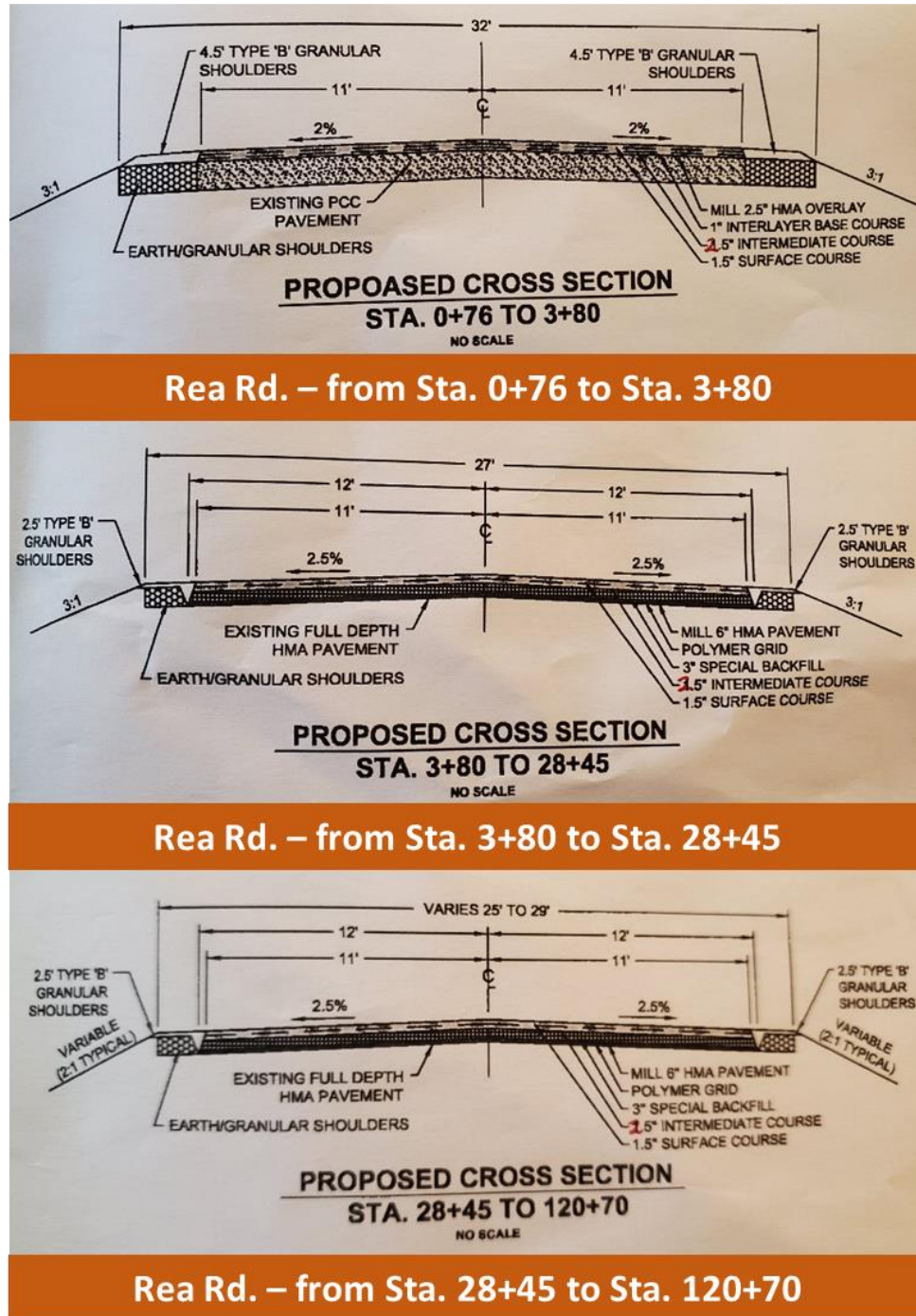


Figure 110. Cross-sectional structural information for (a) Cherry Street and (b) Rea Road

(a)





Figure 111. Comparison of distress severities before and after the third passage of the modular SHL over (a) Cherry Street and (b) Rea Road

Forensic Investigation Data from Keokuk County

Another forensic investigation was carried out in Keokuk County on April 1, 2021, over approximately 3 mi of 170th Street (PCC-surfaced pavement) and 1 mi of 120th Avenue (granular road). The primary objectives of this forensic investigation were to assess topographical features, identify distress patterns, evaluate design characteristics, and analyze daily traffic patterns. IRI values were also measured for each road segment using a high-speed profiler. Chapter 7 extensively documents the principal findings of the forensic investigation conducted in Keokuk County, and this appendix section complements this documentation by presenting additional materials such as images and surveys of distress, as well as construction or reconstruction design drawings provided by the county engineer.

Overall distress types along with corresponding images captured from each road section are depicted in Figure 112. For detailed information regarding the severity of these distresses in each specific road section, refer to Chapter 7.

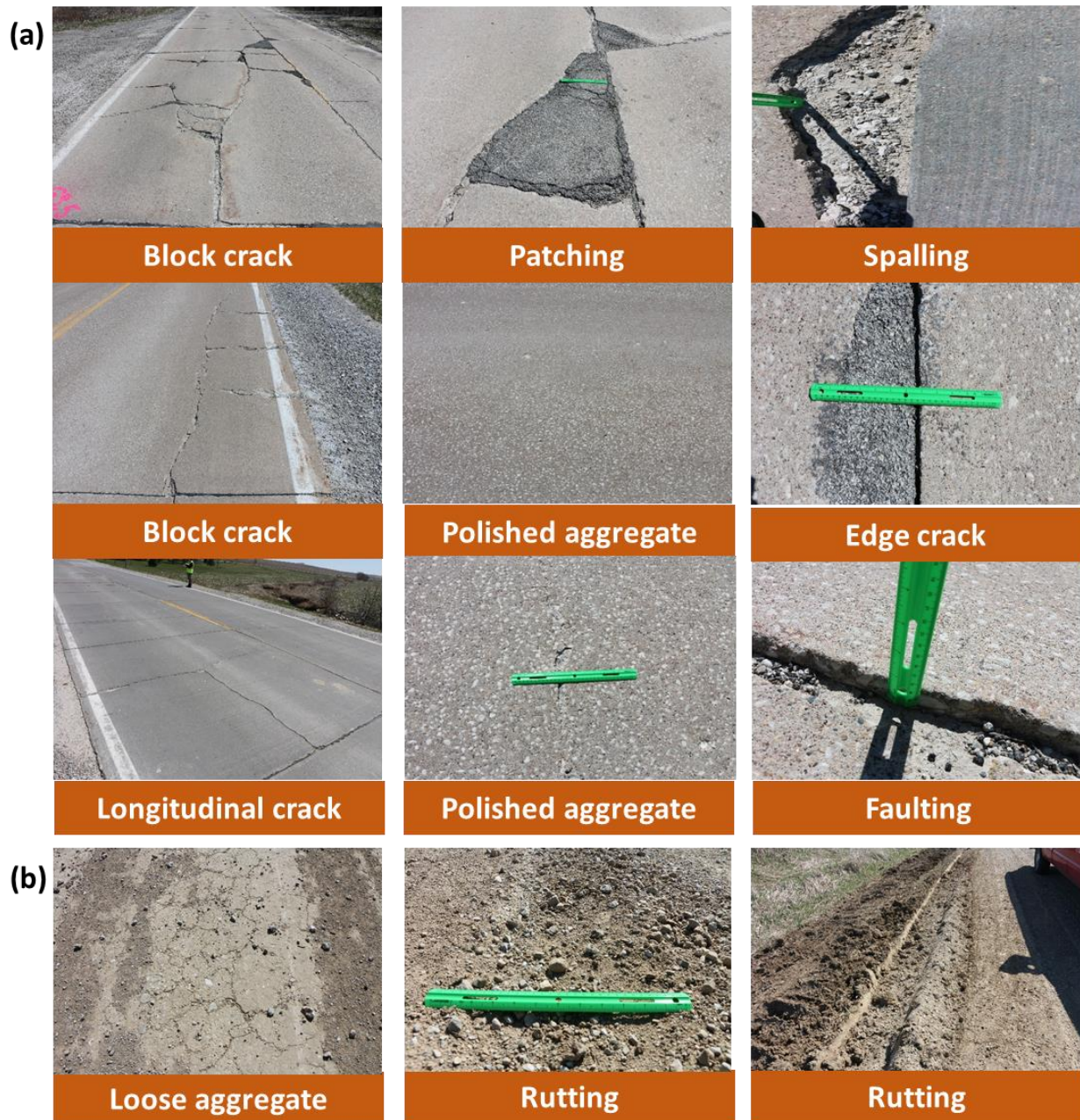
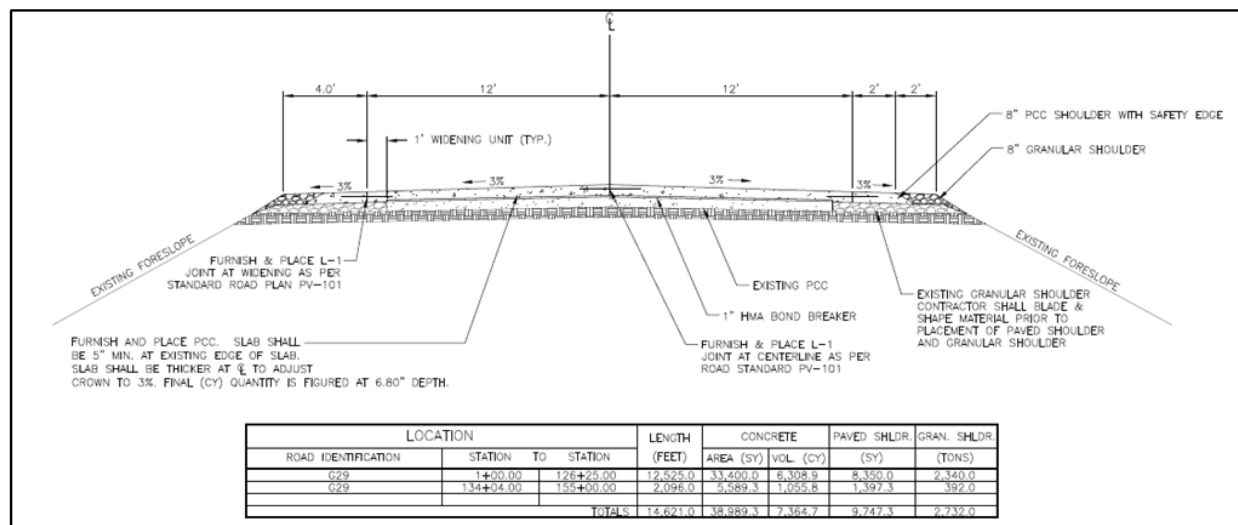
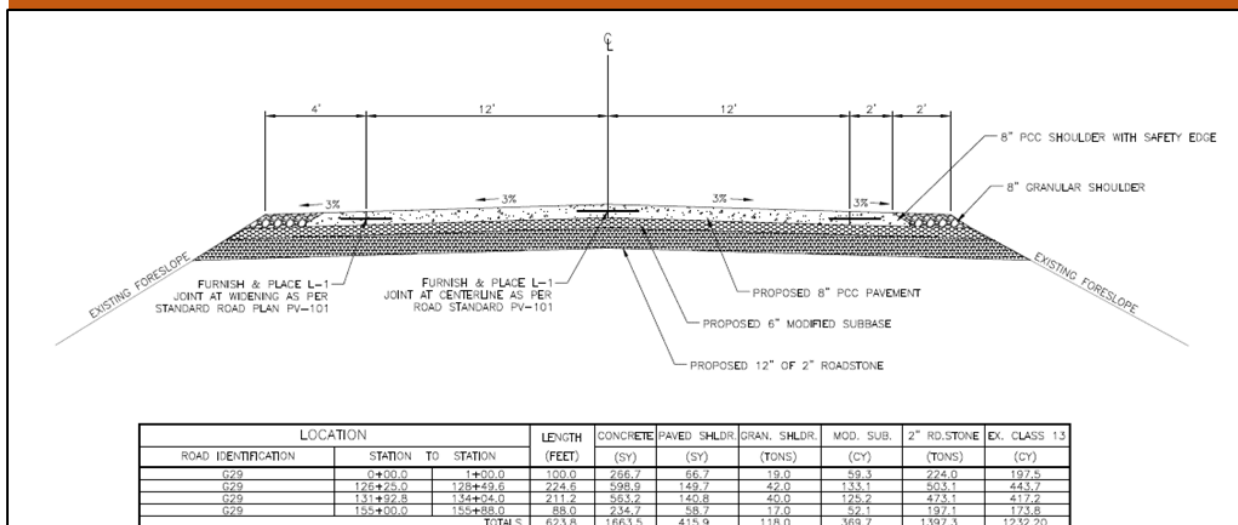


Figure 112. Representative distresses of each road section: (a) 170th Street and (b) 120th Avenue

Keokuk County's 170th Street was awaiting unbound PCC overlay activity scheduled for June 2021. While the PCC pavement with a PCC overlay was not the focus of this study, the cross-sectional structural details of the proposed unbound PCC overlay project are provided in Figure 113 for additional context.



170th St. – from Sta. 1+00 to Sta. 155+00: 5 in. PCC overlay



170th St. – from Sta. 0+00 to Sta. 1+00; Sta. 126+25 to Sta. 128+49.6; Sta. 131+92.8 to Sta. 134+04; Sta. 155+00 to Sta. 155+88: 8 in. PCC overlay

Figure 113. Proposed cross-sectional structural information of unbound PCC overlay project for 170th Street, scheduled for June 2021

Forensic Investigation Data from Monona County

Forensic investigation was also carried out in Monona County on a total of seven road sections, including two sections with AC-surfaced pavement (K45 and E60), one section with PCC-surfaced pavement (E60), and four granular road sections (Filbert Avenue, 295th Street, Linden Avenue, 133rd Street). This investigation took place from April 28 to 30, 2021. The primary objectives of this investigation were to assess topographical features, identify distress patterns,

evaluate design characteristics, and analyze daily traffic patterns and IRI. Chapter 7 extensively documents the principal findings of the forensic investigation conducted in Monona County, and this appendix section complements this documentation by presenting additional materials, such as images and surveys of distress, as well as construction or reconstruction design drawings provided by the county engineer.

It is noteworthy that two JPCP reconstruction projects were planned in Monona County. The first project aimed to extend a highway, involving replacement of the existing granular road (295th Street) with a JPCP section featuring an 8 in. PCC layer thickness, with reconstruction scheduled for approximately October 2021. The second project involved replacing the existing composite pavement (K45) with a JPCP section featuring an 8 in. PCC layer thickness, with reconstruction scheduled for around July 2021. Ultimately, K45 was chosen as a field instrumentation site for this study.

Overall distress types along with corresponding images captured from each road section are depicted in Figure 114. For detailed information regarding the severity of these distresses in each specific road section, refer to Chapter 7.

(a)



Longitudinal crack



Transverse crack



Block crack



Alligator crack



Rutting



Pothole

(b)



Transverse crack



Longitudinal crack



Pothole

(c)



Faulting



Transverse crack



Polished aggregate

(d)



Rutting



Rutting



Loose aggregate



Figure 114. Representative distresses of each road section: (a) K45, (b) E60 (AC-surfaced pavement section), (c) E60 (PCC-surfaced pavement section), (d) Filbert Avenue, and (e) 295th Street

Figure 115 depicts the cross-sectional structural details of the planned JPCP reconstructions at two locations in Monona County: E60 and 295th Street (Figure 115a) and K45 (Figure 115b).

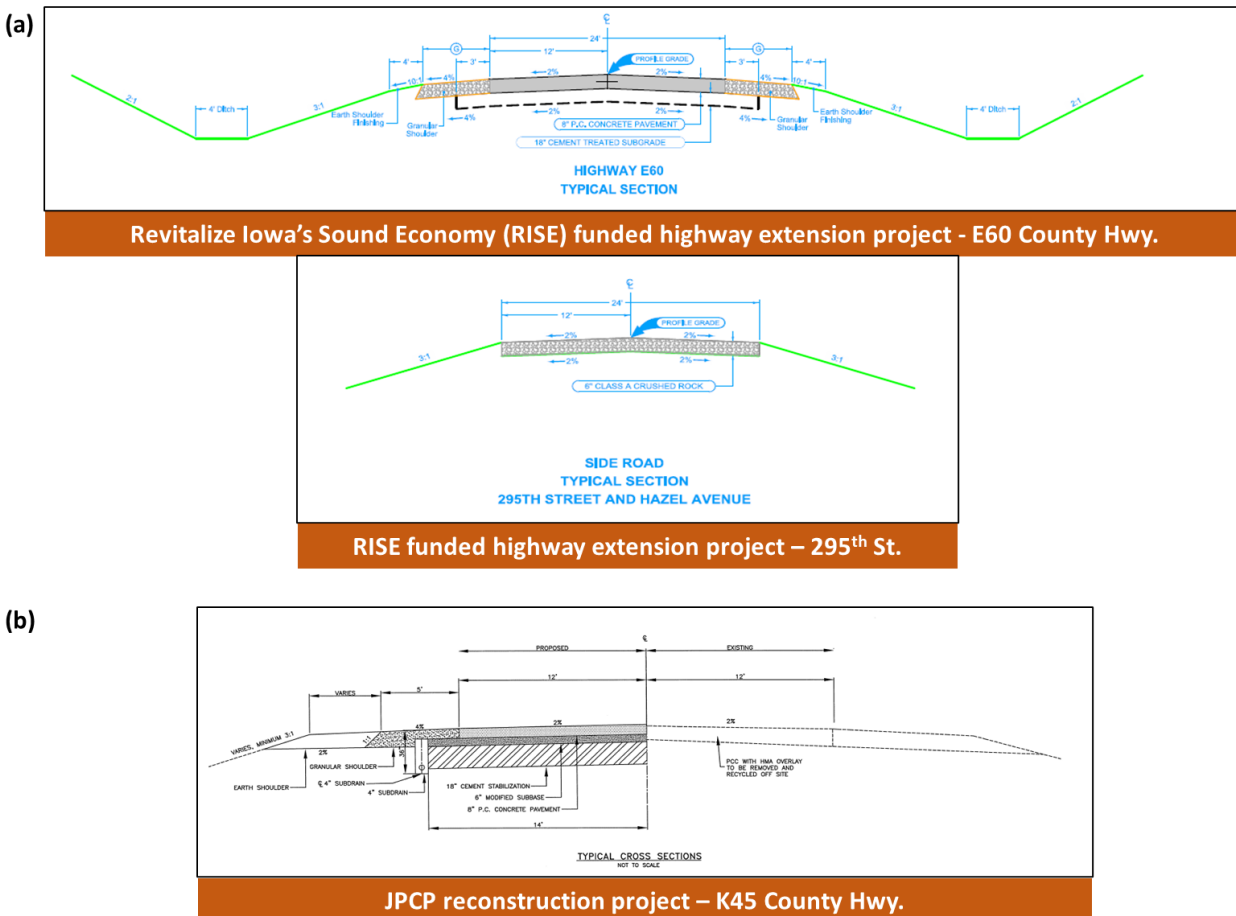


Figure 115. Proposed cross-sectional structural information of reconstruction projects on (a) E60 and 295th Street and (b) K45 scheduled for October 2021 and July 2021, respectively

Forensic Investigation Data from Tama County

The final forensic investigation was conducted in Tama County on a total of five road sections, including one full-depth flexible pavement section (V18) and four granular road sections (190th, 200th, 220th, 240th streets). This investigation took place on July 7, 2022. The primary objectives of this investigation were to assess topographical features, identify distress patterns, evaluate design characteristics, and analyze daily traffic patterns and IRI. Chapter 7 extensively documents the principal findings of the forensic investigation conducted in Tama County, and this appendix section complements the documentation by presenting additional materials such as images and surveys of distress. It is notable that the presence of full-depth flexible pavement sections is uncommon in Iowa, so challenges existed in locating suitable sites for remote sensing system installation. Valuable information provided by the Tama County engineer highlighted the potential existence of such a section, offering an opportunity for the installation of the research team's sensing system, leading to V18 being selected as the designated field instrumentation site for this study.

Overall distress types and features along with corresponding images captured from V18 are depicted in Figure 116. All granular road sections investigated exhibited overall good road conditions, with no significant distresses recorded. For detailed information regarding the severity of these distresses, refer to Chapter 7.

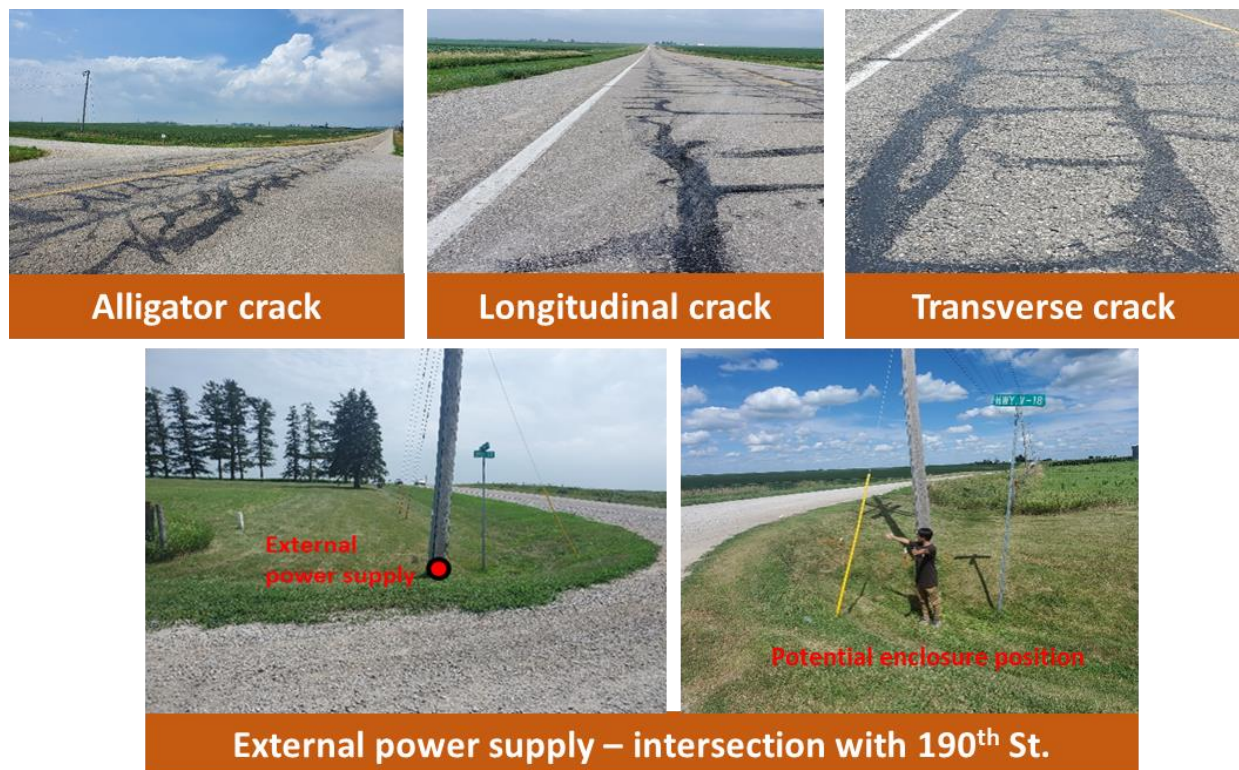


Figure 116. Representative distresses and features of V18

APPENDIX B. INSTALLATION AND UTILIZATION OF P-WIM SYSTEM

Installation Process

This appendix provides detailed information on the components and installation procedures for the P-WIM system. The installation and calibration processes, as well as data collection using the system, primarily adhere to the guidelines outlined in a publication by the Texas A&M Transportation Institute (Prakoso et al. 2022) regarding P-WIM system installation and traffic data analysis.

The main components required for installing the P-WIM system for a single lane include a TRS unit, two piezoelectric sensors, two metal plates, and a piezo channel box, as illustrated in Figure 117. Installation involves placing two metal plates on the surface of the pavement positioned 8 ft apart to span one lane of the roadway, with each piezoelectric sensor affixed to the top of a metal plate. As vehicles pass over the plates, the sensors capture vibration signals that are subsequently transmitted to the TRS unit for recording. The sensors are linked to the TRS unit via the piezo channel box, enabling the TRS to record various parameters such as vehicle class, speed, axle spacing, axle weight, and GVW.

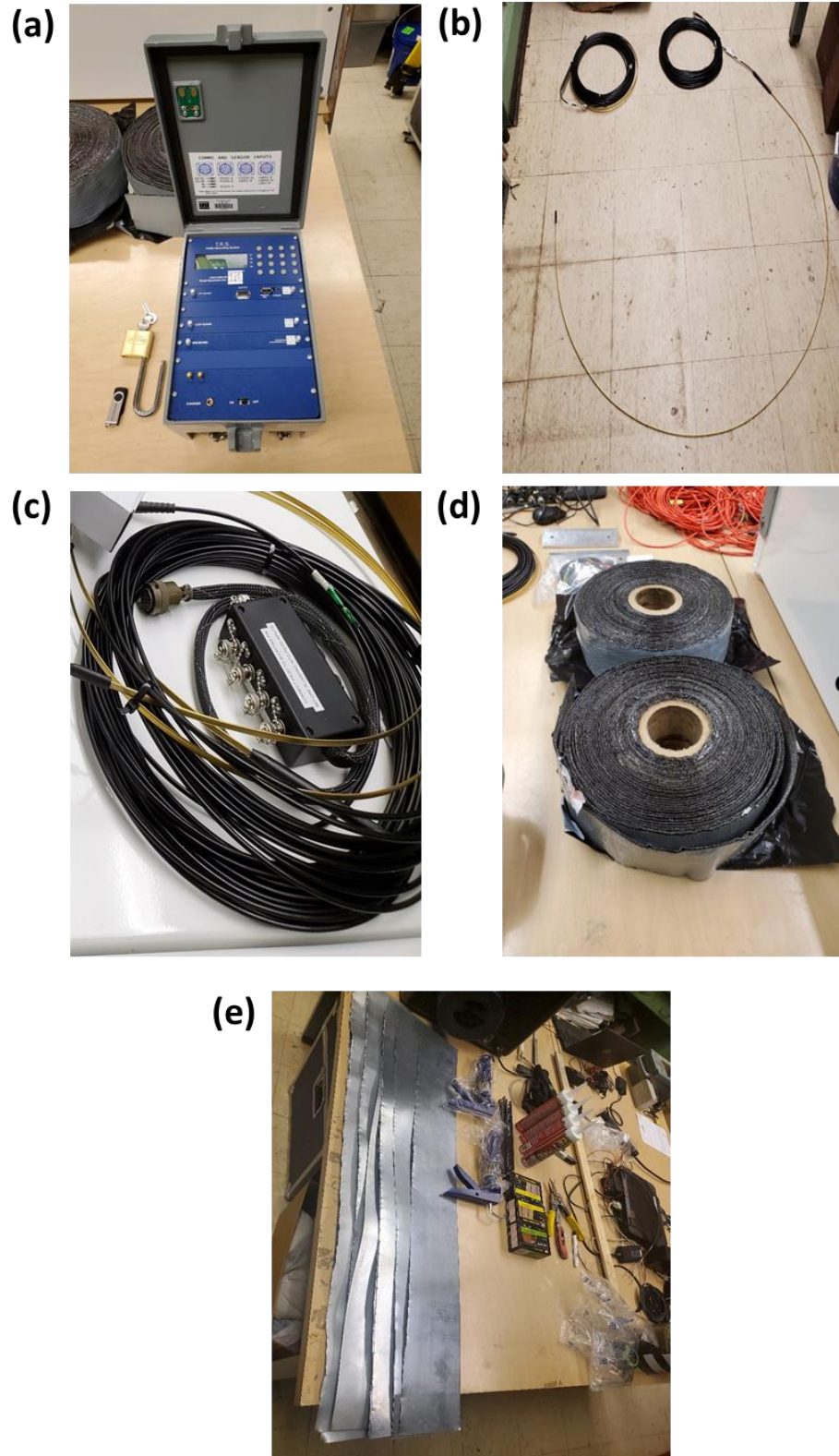


Figure 117. Main components of a P-WIM system: (a) TRS unit, (b) piezoelectric sensors, (c) piezo channel box, (d) mastic tapes, and (e) metal plates

The installation steps are clearly depicted in Figure 118, detailing the following procedures:

- Step 1. Apply silicon adhesive on the sides of the two metal plates in contact with the pavement surface.
- Step 2. Place the two metal plates, spaced 8 ft apart from each other, onto the pavement surface.
- Step 3. Fix the metal plates in place by nailing them to the pavement in addition to the adhesive to ensure proper fixation.
- Step 4. Mount each 8 ft long piezoelectric sensor onto its corresponding 8 ft long metal plate and secure both the sensors and metal plates to the pavement surface using mastic tape.
- Step 5. Install metal ramps as caps to cover the cable connections, the weakest parts when impacted by traffic loadings, by nailing them onto the road shoulder.
- Step 6. Connect sensor cables to the piezo channel box, and subsequently connect the box cable to the TRS unit.



Figure 118. Installation procedures of a P-WIM system

It is important that to ensure safety, appropriate traffic controls should be implemented throughout the entire installation process. The TRS unit can optionally be equipped with a solar panel, enabling continuous operation for several weeks without the need for direct additional charging.

Calibration of Piezoelectric Sensors

Before conducting traffic measurements, calibration of the P-WIM system was essential to ensure the reliability of the collected traffic data. For this purpose, two class 6 trucks, one provided by the Monona County engineer and the other by the Tama County engineer, were utilized to calibrate the P-WIM system, as shown in Figure 119.



Figure 119. Class 6 trucks provided by Monona County engineer (top) and Tama County engineer (bottom)

All trucks were pre-loaded to achieve approximately 16 kips for the steering axle and 34 kips for the tandem axle. The weight of all three axles was accurately measured using static scales located at a quarry before heading to the P-WIM installation section. System calibration involved six operations of the class 6 trucks over a pair of piezoelectric sensors per road section, with the calibration factor adjusted for each run. As indicated in Table 45, the P-WIM systems were satisfactorily calibrated for both K45 and V18, with error percentages between P-WIM measurements and static scale measurements of less than 5%.

Table 45. Calibration of the P-WIM systems installed at K45 and V18

K45 in Monona County				
Trial number	Axle 1 (kips)	Axle 2 (kips)	Axle 3 (kips)	GVW (kips)
1	12.89	14.53	15.18	42.60
2	18.01	19.30	19.83	57.14
3	15.48	17.15	17.71	50.34
4	16.80	17.47	17.91	52.18
5	16.15	17.22	17.41	50.78
6	16.40	17.38	17.50	51.28
Average	15.96	17.18	17.59	50.72
Static-scale measurement	16.27	17.05	17.39	50.71
% error	-1.91%	0.76%	1.15%	0.02%
V18 in Tama County				
Trial number	Axle 1 (kips)	Axle 2 (kips)	Axle 3 (kips)	GVW (kips)
1	17.10	17.52	17.66	52.28
2	16.46	17.24	17.23	50.93
3	16.29	17.08	17.03	50.40
4	16.48	17.24	17.19	50.91
5	16.41	17.11	17.15	50.67
6	16.46	17.18	17.22	50.86
Average	16.53	17.23	17.25	51.01
Static-scale measurement	16.44	17.15	17.21	50.80
% error	0.55%	0.47%	0.23%	0.41%

Traffic Data Collection

Following system calibration, the P-WIM system was operated continuously for several days on K45 and V18 to capture traffic information passing over the piezoelectric sensor installation lane, with particular emphasis on class 9 trucks and superloads. The P-WIM system provides traffic information including vehicle class, speed, number of axles, axle spacing, axle weight, and GVW. Traffic data are stored in the TRS unit as a .000 file, and the raw files can be

downloaded from the TRS in an Excel-compatible (.csv) format using Road Reporter II software. Figure 120 and Figure 121 show examples of the measurement data downloaded from the TRS unit in an Excel format, showcasing traffic data collected from Monona County and Tama County, respectively.

Number	Year	Month	Day	Hour	Minute	Second	Lane	Class	Speed	Num Axles	GVW	Wheelbase	Wt1	SpC1	Wt2	SpC2	Wt3	SpC3	Wt4	SpC4	Wt5	SpC5	Wt6	SpC6	Wt7	SpC7	Wt8	SpC8
1	23	11	9	10	37	7	1	9	57	5	158810	65.4	30480	21.9	29920													
2	23	11	9	10	38	29	1	2	76	2	4170	9.3	2310	9.3	1860													
3	23	11	9	10	39	5	1	10	59	7	222890	65.7	30190	13.3	25580	4.3	33920	4.4	35340	33.3	35080	4.3	35080	6.1	27700			
4	23	11	9	10	39	7	1	2	59	2	4180	9.7	2220	9.7	1990													
5	23	11	9	10	39	39	1	2	56	2	3900	9.9	2220	9.9	1680													
6	23	11	9	10	43	42	1	2	67	2	4890	9.7	2760	9.7	2130													
7	23	11	9	10	44	24	1	2	63	2	7720	9.1	4280	9.1	3460													
8	23	11	9	10	44	49	1	10	63	7	228320	67.5	33740	16.3	27260		6	35080	4.4	35880	31	34280	5	33640	4.8	28420		
9	23	11	9	10	46	3	1	3	64	4	35700	35	6220	14	13140		18.1	7900	2.9	8440								
10	23	11	9	10	46	44	1	3	63	2	8520	12.6	3900	12.6	4620													
11	23	11	9	10	47	47	1	9	63	5	170770	55.3	31170	12.6	35260	4.6	33840	33.8	34540	4.3	35960							
12	23	11	9	10	48	49	1	2	61	2	8520	10.3	4620	10.3	3900													
13	23	11	9	10	54	52	1	2	71	4	10510	25.8	2930	10	4000	12.8	1600	3	1780									
14	23	11	9	10	55	55	1	2	63	2	6580	9.3	3820	9.3	2760													
15	23	11	9	10	56	20	1	2	63	2	7200	9.3	4180	9.3	3020													
16	23	11	9	10	57	45	1	2	64	2	6740	8.4	3720	8.4	3020													
17	23	11	9	10	58	52	1	3	66	2	5240	12.2	3020	12.2	2220													
18	23	11	9	10	59	39	1	3	60	2	10750	12.2	6130	12.2	4620													
19	23	11	9	11	1	18	1	2	58	2	10660	9.4	6220	9.4	4440													
20	23	11	9	11	2	56	1	9	61	5	102200	51.4	32390	12.5	19890	4.3	19440	30.4	17320	4.2	12960							
21	23	11	9	11	6	20	1	2	62	2	5280	8.8	2040	8.8	1240													
22	23	11	9	11	6	50	1	3	68	2	4970	11.9	2930	11.9	2040													
23	23	11	9	11	8	57	1	3	60	2	19720	14.1	10300	14.1	9420													
24	23	11	9	11	14	14	1	2	68	2	9230	10.1	4880	10.1	4350													
25	23	11	9	11	15	7	1	3	70	2	7460	12.4	4260	12.4	3400													
26	23	11	9	11	20	38	1	3	71	2	6570	11.4	3820	11.4	2750													
27	23	11	9	11	22	9	1	3	69	2	10020	13.6	5320	13.6	4700													
28	23	11	9	11	23	38	1	3	60	3	14120	28.2	4180	12.3	4260	15.9	5680											
29	23	11	9	11	24	19	1	2	63	2	7280	9.9	4350	9.9	2930													
30	23	11	9	11	30	35	1	10	42	4	131960	40.3	30900	21.6	35410	4.4	30640	34.3	34990									
31	23	11	9	11	30	35	1	2	42	2	65980	6.3	34720	6.3	31260													
32	23	11	9	11	32	39	1	3	59	2	9590	12.4	5150	12.4	4440													
33	23	11	9	11	33	52	1	6	57	4	117780	36.7	31870	19.1	35700	4.6	33840	13	16250									
34	23	11	9	11	34	4	1	2	62	2	7360	9.6	3900	9.6	3460													
35	23	11	9	11	36	21	1	3	65	2	9520	12.1	4880	12.1	4440													
36	23	11	9	11	39	38	1	3	60	2	6300	11.2	3640	11.2	2660													
37	23	11	9	11	39	46	1	2	48	2	11020	9.5	5600	9.5	5420													
38	23	11	9	11	40	46	1	3	58	2	9320	12.6	4880	12.6	4440													
39	23	11	9	11	40	52	1	2	63	2	8080	9.6	4330	9.6	3550													
40	23	11	9	11	41	2	1	3	56	2	20870	14.1	11990	14.1	8880													
41	23	11	9	11	41	49	1	6	56	4	127170	37.2	34990	19.3	34460	4.8	33480	13.1	24240									
42	23	11	9	11	41	51	1	9	56	5	172270	61.6	33660	18.2	35430	4.4	33120	34.6	34100	4.4	35960							
43	23	11	9	11	47	35	1	2	59	2	8260	9.5	3060	9.5	3200													
44	23	11	9	11	48	51	1	7	45	7	100700	41	5600	19	4150													

<

Figure 120. An example of measurement data collected from Monona County

Number	Year	Month	Day	Hour	Minute	Second	Lane	Class	Speed	Num Axles	GVW	Wheelbase	Wt1	SpC1	Wt2	SpC2	Wt3	SpC3	Wt4	SpC4	Wt5	SpC5	Wt6	SpC6	Wt7	SpC7	Wt8	SpC8
1	23	10	31	10	12	24	1	2	3	2	5650	9	1000	9	4850													
2	23	10	31	10	12	28	1	2	3	2	5600	9	1000	9	4600													
3	23	10	31	10	13	46	1	10	3	5	67200	32.5	2650	4.4	20150	17.9	20200	4.4	12250	5.8	11950							
4	23	10	31	10	19	1	1	2	3	2	6600	9	1050	9	5550													
5	23	10	31	10	19	12	1	2	3	2	1500	9	800	9	700													
6	23	10	31	10	21	4	1	2	3	2	5200	9	850	9	4350													
7	23	10	31	10	21	13	1	2	3	2	6400	9	950	9	5450													
8	23	10	31	10	21	19	1	10	3	4	55050	16.6	2950	4.4	21200	5.6	21200	6.6	9700									
9	23	10	31	10	22	42	1	2	9	2	9400	10.2	1850	10.2	4750													
10	23	10	31	10	23	16	1	2	31	2	3100	10.3	1550	10.3	1550													
11	23	10	31	10	28	57	1	13	3	6	96400	35.6	2900	4.4	21200	4.4	21200	16.4	19300	4.4	19500	6	12300					
12	23	10	31	10	29	14	1	2	3	2	7550	9	1600	9	5950													
13	23	10	31	10	30	16	1	2	33	2	2450	9.4	1400	9.4	1050													
14	23	10	31	10	32	12	1	3	33	2	6350	11.1	2250	11.1	4100													
15	23	10	31	10	32	55	1	2	53	2	5950	10.5	3800	10.5	2150													
16	23	10	31	10	33	4	1	2	63	2	8900	9.9	4750	9.9	4150													
17	23	10	31	10	38	26	1	2	63	2	9700	9	4800	9	4100													
18	23	10	31	10	49	31	1	8	33	4	43300	34.2	8550	12.9	12400	18.3	11450	3	10900									
19	23	10	31	10	49	33	1	2	50	2	2350	9.5	1450	9.5	1100													
20	23	10	31	10	52	28	1	2	59	2	2750	9.5	1550	9.5	1200													
21	23	10	31	10	55		13	1	6	51	3	59000	24.9	16000	20.5	18350	4.4	19050										
22	23	10	31	10	58	10	2	2	50	2	4100	10.8	1000	10.8	2000													
23	23	10	31	10	58	22	1	9	53	5	71400	53.6	16700	16.4	13050	4.2	16850	28.9	12000	4.1	12800							
24	23	10	31	10	58	29	1	2	53	2	10750	9	5450	9	5300													
25	23	10	31	10	59	1	1	2	58	2	9150	9.1	3050	9.1	2100													
26	23	10	31	11	2	13	1	2	47	2	2450	9.4	1400	9.4	1050													
27	23	10	31	11	6	22	1	2	61	2	4050	9.4	2450	9.4	1600													
28	23	10	31	11	9	23	1	2	16	2	4300	9	2350	9	1950													
29	23	10	31	11	9	26	1	2	16	2	4100	9	2150	9	1950													
30	23	10	31	11	14	42	1	2	59	2	6350	9.1	3850	9.1	2500													
31	23	10	31	11	21	55	1	2	52	2	3850	8.6	2250	8.6	1600													
32	23	10	31	11	32	54	1	2	61	2	5850	11.9	3050	11.9	2850													
33	23	10	31	11	39	7	1	2	63	2	2900	9.3	1600	9.3	1300													
34	23	10	31	11	39	59	1	2	55	2	6550	9.1	2800	9.1	3750													
35	23	10	31	11	41	32	1	2	64	3	7900	9.2	4350	9.2	3750													
36	23	10	31	11	42	56	3	4	65	3	10400	54.7	4500	24.7	4500	12.6	2150											
37	23	10	31	11	45	45	1	2	57	2	4700	9.6	2300	9.6	2400													
38	23	10	31	12	3	7	1	3	58	2	9400	12.3	4900	12.3	4500													
39	23	10	31	12	6	24	1	3	66	2	93000	22.8	5000	22.8	19700													
40	23	10	31	12	6	50	1	6	57	3	56900	24.6	18050	20.3	20000	4.3	18850											
41	23	10	31	12	11	5	1	2	66	2	5150	10.4	2750	10.4	2400													
42	23	10	31	12	12	4	1	3	59	2	9850	12.2	5150	12.2	4700													
43	23	10	31	12	13	42	1	5	51	2	23250	14.9	11400	14.9	11850													

Class 10 truck

Class 13 truck

Class 9 truck
(tandem axle weight: 30 kips)

loH
(GVW: 33 kips)

Date and time

Lane

Class, speed, axle #

GVW, axle spacing, axle weights

APPENDIX C. USER GUIDE FOR RISAT

Illustrative Example Using RISAT: Analysis for Dual-Row Modular SHL Traveling on JPCP

This appendix presents a comprehensive analysis example for both JPCP and flexible pavement systems under superload conditions. These examples are intended to offer users practical guidance for conducting pavement analysis using RISAT. Table 46 outlines the input variables and corresponding values applied to RISAT for conducting JPCP analysis when subjected to a single pass of a dual-row modular SHL.

Table 46. Input variables applied to RISAT for analysis of JPCP under dual-row modular SHL

Properties of JPCP system		
Layer	Input variable	Value
PCC layer	Thickness (in.)	8
	Modulus of elasticity (psi)	4,000,000
	CTE (10^{-6} in./in./°F)	4.3
	Temperature gradient (°F/in.)	0
	Transverse joint spacing (ft)	20
	Transverse joint LTE (%)	90
Subgrade	Modulus of elasticity (psi)	13,000
Shoulder	Shoulder type	Full-depth tied PCC shoulder (70% LTE)
Properties of superload: dual-row modular SHL		
Type	Input variable	Value
Dual-row modular SHL	Number of axles	8
	Axle weight (lb)	120,000 per each axle
	Tire pressure (psi)	170 per each tire
	Number of tires per axle	8
	Tire width (in.)	9
	Axle spacing (in.)	59
	Tire spacing (in.)	39
	Outer tire spacing (in.)	213
Additional information required for M-E analysis		
Input variable		Value
Year of road section construction		2020
Year of superload passage		2021
AADTT		1,000
Number of lanes		2
Length of section (mi)		10
Treatment cost (\$)		220,000
Discount rate (%)		5.5

To initiate the RISAT, users are required to double-click on the Microsoft Excel-based file named RISAT.xlsm in order to activate the analysis tool (Figure 122).


Name	Date modified	Type	Size
 RISAT	4/4/2024 4:42 PM	Microsoft Excel M...	16,741 KB

Figure 122. Initiate Microsoft Excel-based file named RISAT.xlsm

When users access RISAT, they will be directed to the navigation panel, where they can choose the predictive model type (Figure 123). Currently, only the AI-based predictive model is available for selection.

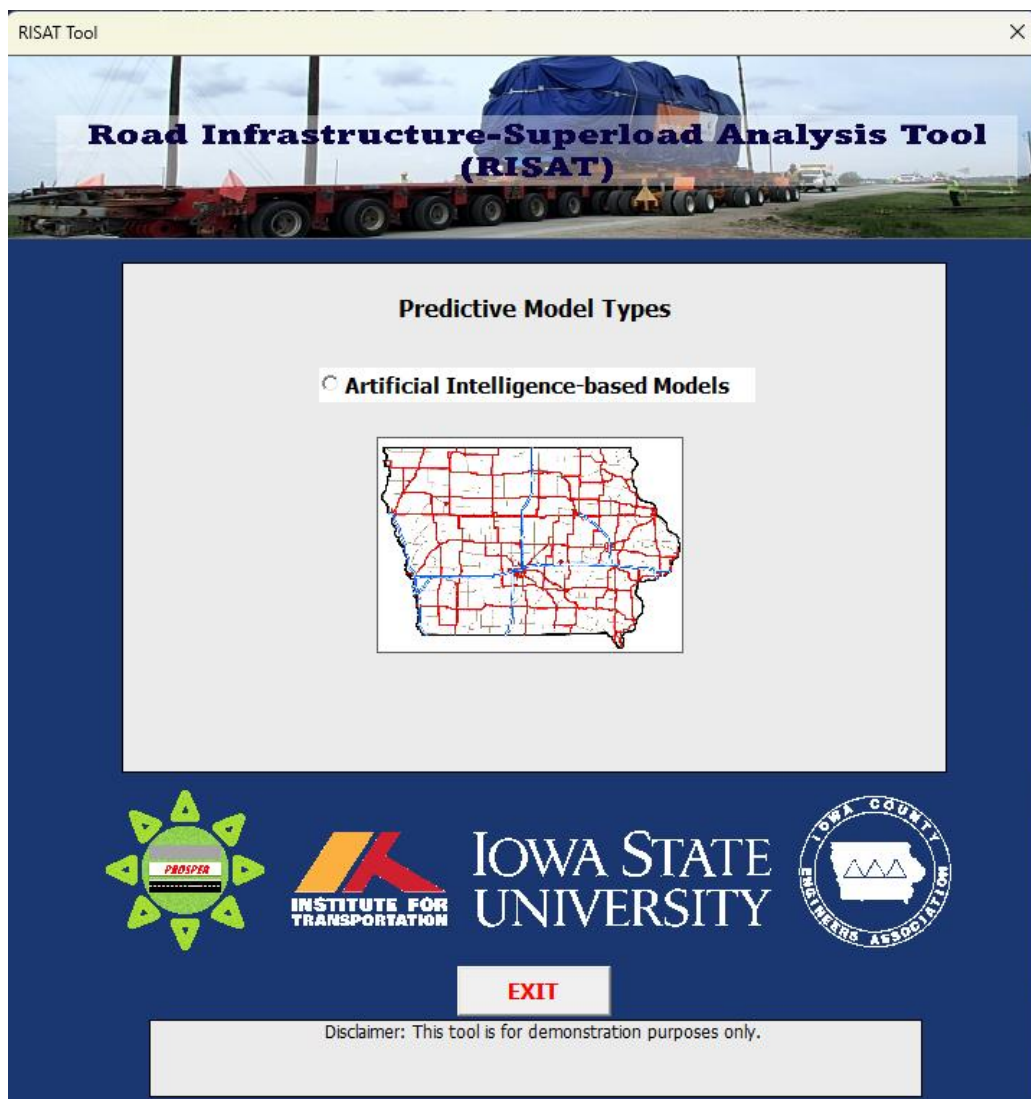


Figure 123. RISAT navigation panel asking users to choose predictive model type

Users will be presented with options to choose the pavement system type for analysis, with available selections of JPCP and flexible pavement (Figure 124).

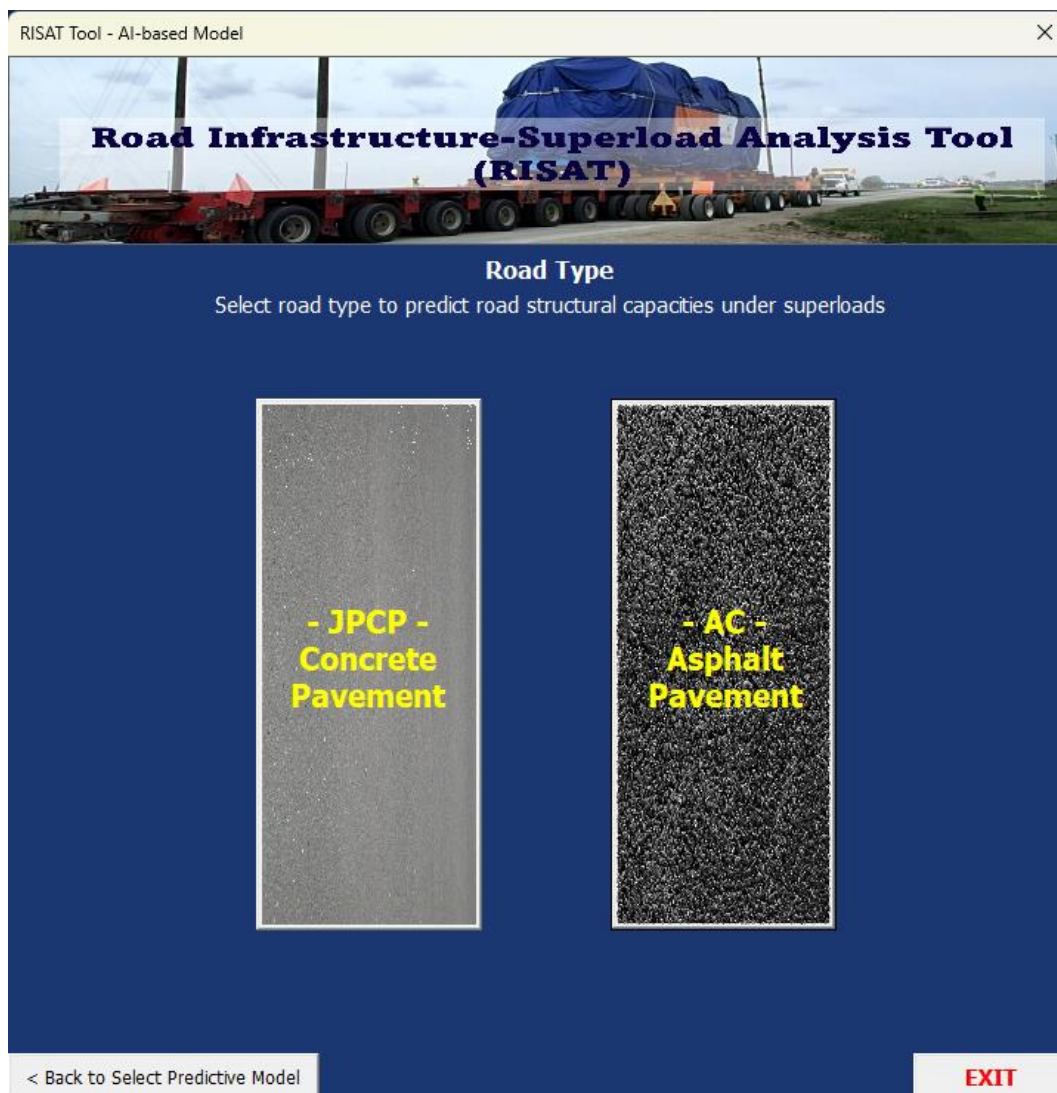


Figure 124. RISAT navigation panel asking users to choose pavement system

Upon selecting the JPCP system, users will encounter options to choose superload type (Figure 125). Users initially select the parent class of superload, among IoH or SHL, from a dropdown list. A secondary dropdown list will then appear, allowing users to specify superload sub-type of the selected superload class.

RISAT Tool - AI-based Model - JPCP

Road Infrastructure-Superload Analysis Tool (RISAT)

Superload Parent Type: Superheavy Load (SHL)

Superload Sub Type: Dual-row modular type

DATA ROAD INFO METADATA

Do you have the following information related to the pavement system?

a. Top PCC layer:

- Thickness,
- Modulus of Elasticity,
- Coefficient of Thermal Expansion,
- Temperature Gradient,
- Transverse Joint Spacing,
- Load Transfer Efficiency

b. Subgrade:

- Modulus of Elasticity,
- Poisson's ratio

c. Shoulder Type


☐ Yes ☐ No

< Back to Select Pavement Type EXIT

Figure 125. RISAT navigation panel asking users to choose superload type

Once users have selected both pavement system and superload type, they will be presented with basic inquiries regarding the availability of property information related to the chosen pavement system and superload (Figure 126). Such properties encompass structural characteristics of the pavement system and loading properties of the superload. Should users possess all the necessary property information, they can indicate their readiness by selecting Yes for both the pavement system and superload questions, but if users lack at least one element of property information for either the pavement system or superload, they can select No. Another question will then be presented, inquiring whether the user is willing to apply the recommended input parameter values provided by RISAT. Users are required to select Yes to this question; otherwise, a warning popup will appear, indicating that users need to properly prepare the property information to proceed with launching the tool.

RISAT Tool - AI-based Model - JPCP



Road Infrastructure-Superload Analysis Tool (RISAT)

Superload Parent Type

Superheavy Load (SHL)

Superload Sub Type

Dual-row modular type

DATA

ROAD INFO

METADATA

Do you have the following information related to the pavement system?

a. Top PCC layer:

- Thickness,
- Modulus of Elasticity,
- Coefficient of Thermal Expansion,
- Temperature Gradient,
- Transverse Joint Spacing,
- Load Transfer Efficiency

b. Subgrade:

- Modulus of Elasticity,
- Poisson's ratio

c. Shoulder Type

☐ Yes ☐ No

< Back to Select Pavement Type

EXIT

RISAT Tool - AI-based Model - JPCP

Road Infrastructure-Superload Analysis Tool (RISAT)

Superload Parent Type

Superheavy Load (SHL)

Superload Sub Type

Dual-row modular type

DATA
ROAD INFO
METADATA

Do you have the following information related to the superload traffic?

a. Loading Configuration

- No. of Axles
- No. of Tires per Axle
- Axle Weight
- Tire Pressure
- Tire Width
- Axle Spacing
- Tire Spacing
- Outer Tire Spacing

b. Traffic Information

- AADTT
- No. of Lanes
- Length of Lane Section
- Treatment Cost
- Discount Rate
- Superload Travel Year during the Service Life

The diagram illustrates the configuration of a Superheavy Load (SHL). It shows a top-down view of the load with various parameters labeled: 'Superheavy Load (SHL)' at the top, 'Outer tire spacing' and 'Tire spacing' at the top, 'Axle weight' and 'Tire pressure' on the left, 'Tire width' and 'Axle spacing' in the middle, and 'No. of tires per axle' at the bottom. A vertical arrow on the right indicates 'Traffic direction'.

☐ Yes
☐ No

< Back

EXIT

Figure 126. RISAT navigation panel asking users to answer basic inquiries regarding the availability of property information related to the chosen pavement system (top) and superload (bottom)

Users are then advised to input basic project details into the navigation panel (Figure 127). Upon completion, users should click on the activated LAUNCH TOOL button to be directed to the designated sub-tool corresponding to the pavement system and superload type previously selected.

RISAT Tool - AI-based Model - JPCP

Road Infrastructure-Superload Analysis Tool (RISAT)

Superload Parent Type: Superheavy Load (SHL)

Superload Sub Type: Dual-row modular type

DATA | ROAD INFO | METADATA

Project Name	Superload Project	<div>LAUNCH TOOL</div> <div>LAUNCH TOOL</div> <div>LAUNCH TOOL</div>
COUNAME	Monona County	
PROJECT_NO	TR-781	
BPRJ	2019	
EPRJ	2024	
CONYR	2020	

Click METADATA for more descriptions.
Click BACK to change input parameters.

< Back

< Back to Select Pavement Type

EXIT

Figure 127. RISAT navigation panel asking users to input basic project information

Upon navigation to the sub-tool, users will notice that the basic project information they inputted in the navigation panel has been transferred to the cells located at the top of the sub-tool interface (Figure 128a). Following this, users must input the properties of the JPCP system into the designated green cells, utilizing US units (Figure 128b). White cells are reserved for automatically converted values derived from the green cell inputs. Users can only type input values into green cells and are not allowed to manually type in any input values in white cells. Users are also prompted to select the shoulder type from four available options: full-depth tied PCC shoulder (70% LTE), full-depth tied PCC shoulder (50% LTE), HMA shoulder, and granular shoulder. It is essential to note that all input variables will be accompanied by an input range and recommended value, and should users input values outside the specified range for any variable, a warning popup will appear (Figure 128c). Once the structural properties of the JPCP system have been entered, a schematic drawing depicting the JPCP structure and illustrating the thickness, transverse joint spacing, and LTE of the PCC layer over the subgrade will be generated (Figure 128d).

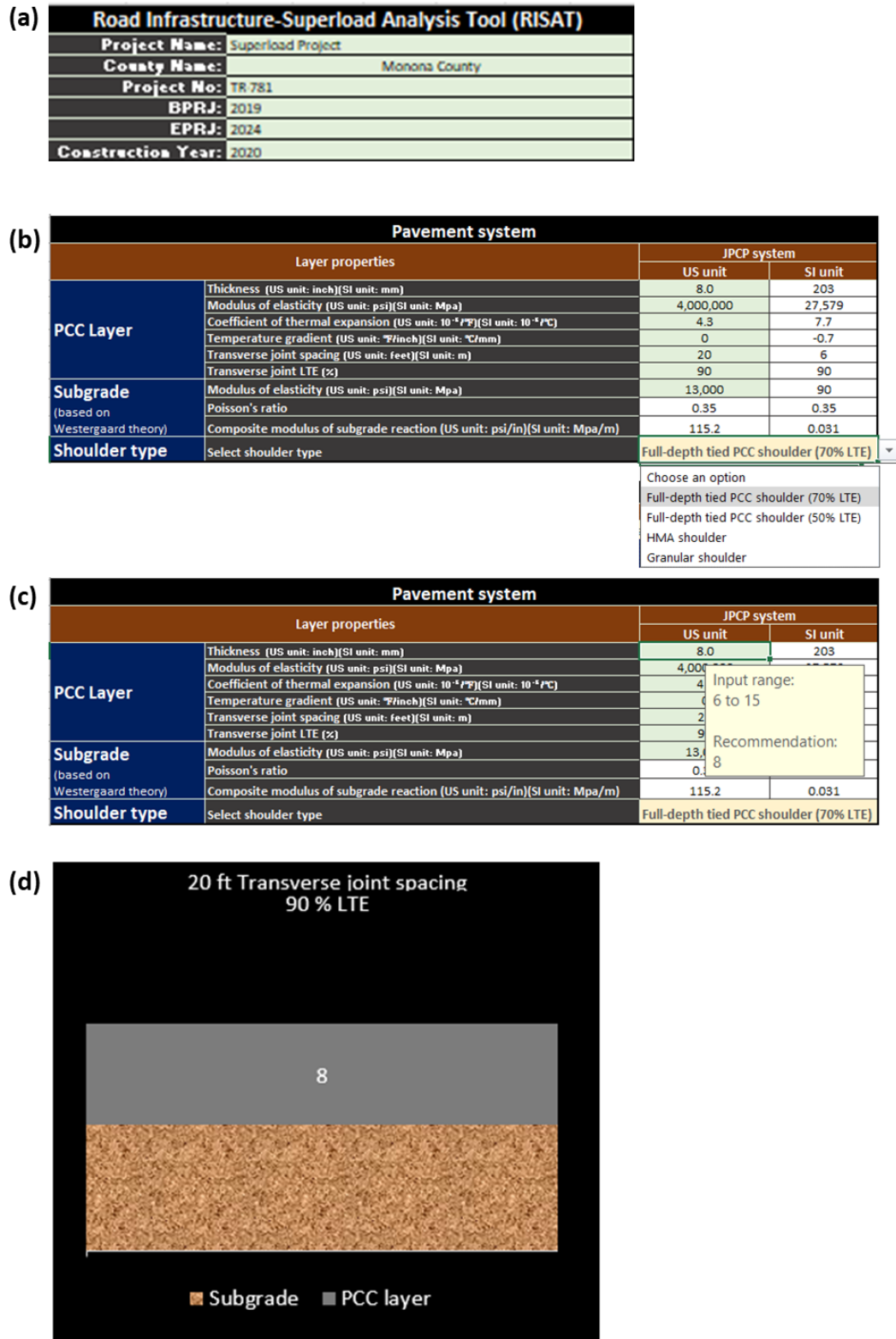


Figure 128. Details of RISAT sub-tool components for JPCP analysis: (a) basic project information, (b) JPCP structural properties, (c) recommended input range and value, and (d) schematic drawing depicting JPCP pavement structure

Users are next required to input loading properties of the dual-row modular SHL into the designated green cells (Figure 129). These properties include number of axles, axle weight, tire pressure, number of tires per axle, tire width, axle spacing, tire spacing, and outer tire spacing. In the axle number cells, users must number axles sequentially from one up to the total number of axles the superload contains, starting from the steering axle to the last axle. Axle weight and tire pressure cells require users to input axle weight and tire pressure for each axle, respectively, from the steering axle to the last axle. The number of tires per axle must be entered for each axle, along with the tire width for tires on each axle. Axle spacing and tire spacing also require user input. Users may input the average tire spacing for each axle if such spacing varies between tires within an axle. The outer tire spacing refers to the total length from the outer edge of the leftmost tire to the outer edge of the rightmost tire within an axle. All property values of input variables are automatically converted from US units to SI units, with both sets of values displayed in the sub-tools for user convenience. If any terminology regarding the loading properties is unclear, users can refer to the schematic drawing illustrating the loading configuration of the superload (Figure 129). This visual aid will provide clarity with respect to the terminology and help users accurately input the required loading properties into the designated cells.

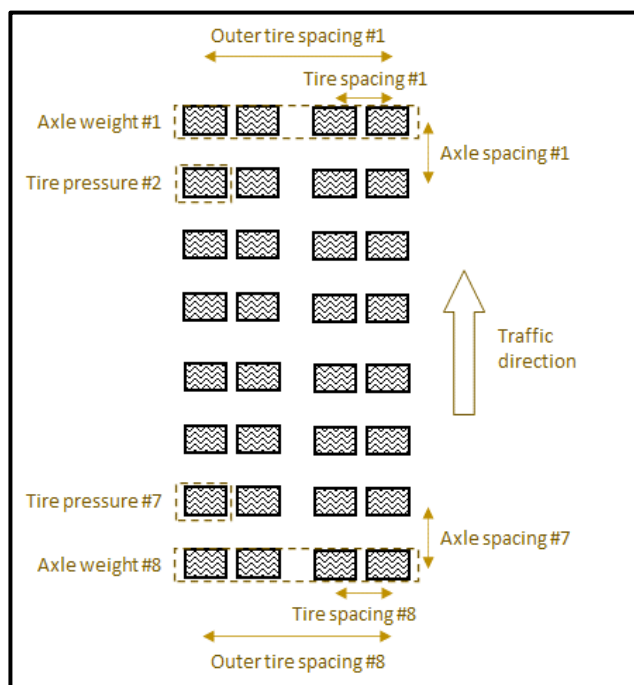
[illegible]

Figure 129. Details of RISAT sub-tool components for JPCP analysis including superload properties (top) and schematic drawing depicting loading configuration of superload (bottom)

Beneath the input cells for superload properties, users will find additional input cells necessary for conducting M-E analysis, in particular for evaluating pavement performance and calculating the RDAC and the reduction in service life (Figure 130). Users are also afforded the option to scale the results of mechanistic-based analysis using in situ data collected from the remote data acquisition system. If users opt for data scaling based on in situ data, the mechanistic-based data will be scaled accordingly. Conversely, selecting no data scaling will result in outputs derived solely from mechanistic-based analysis results.

Additional information for M-E analysis			Data scaling option	
Information for M-E analysis		JPCP system	No data scaling	
Items	Construction year	2020	Choose an option	
	Superload travel year	2021	Data scaling based on in-situ data	
	AADTT	1000	No data scaling	
	Number of lanes	2		
	Length of section (mile)	10		
	Treatment cost (\$)	220000		
	Discount rate (%)	5.5		

Figure 130. Details of RISAT sub-tool components for JPCP analysis, requesting additional information for M-E analysis and providing options for data scaling

Users will consequently obtain outputs such as N_f and damage ratio related to bottom-up and top-down fatigue damages, as well as RDAC and reduction in service life of the JPCP when subjected to a single pass of a dual-row modular SHL (Figure 131).

Estimation of damage ratio			
Fatigue cracking			JPCP system
Calculate bottom-up fatigue damage ratio	N_f	Specified modulus-based	1.03E+04
		Yearly-based	1.11E+04
	Damage ratio	Specified modulus-based	6.07E+06
		Yearly-based	5.31E+09
Calculate top-down fatigue damage ratio	N_f	Specified modulus-based	7.11E+09
		Yearly-based	3.49E+10
	Damage ratio	Specified modulus-based	5.62E+06
		Yearly-based	2.26E+11

Estimation of RDAC and service life reduction			
RDAC and service life reduction			JPCP system
Calculate Road Damage-Associated Cost (RDAC)	RDAC (\$)	Specified modulus-based	147
		Yearly-based	226
	Service life reduction (days)	Specified modulus-based	4
		Yearly-based	4

Figure 131. RISAT outputs related to JPCP under dual-row modular SHL

Users can generate an Excel file that will be located in the same folder where the RISAT is located. This file provides a table summarizing the outputs, and it can be generated by clicking the EXPORT RESULTS button (Figure 132).

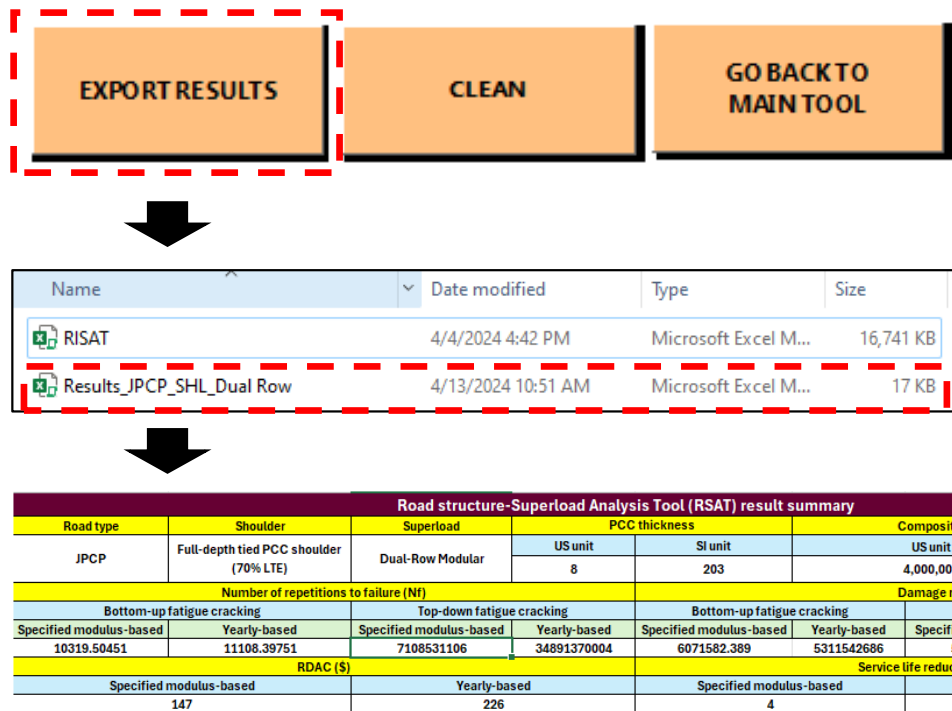


Figure 132. Excel-based output file generation from RISAT regarding JPCP analysis under dual-row modular SHL

Illustrative Example Using RISAT: Analysis for Manure Tanker IoH Traveling on Flexible Pavement

This section offers guidance on analysis steps for flexible pavement under a single pass of a manure tank IoH using RISAT. Table 47 outlines the input variables and corresponding values required for RISAT analysis.

Table 47. Input variables applied to RISAT for analysis of flexible pavement under manure tanker IoH

Properties of flexible pavement system		
Layer	Input variable	Value
AC layer	Thickness (in.)	8
	AC air voids (%)	7
	AC effective binder contents (%)	11
Base layer	Thickness (in.)	8
	Water contents (%)	10
Subbase layer	Thickness (in.)	6
	Water contents (%)	10
Subgrade	Water contents (%)	15.7
All layer	Combination for modulus of elasticity	Fall season-based moduli of elasticity
Properties of superload: manure tanker IoH		
Type	Input variable	Value
Manure tanker IoH	Number of axles	2
	Axle weight (lb)	9,500 per each axle
	Tire pressure (psi)	9 per each tire
	Number of tires per axle	2
	Tire width (in.)	28.3
	Axle spacing (in.)	72
	Tire spacing (in.)	95
	Outer tire spacing (in.)	95
Additional information required for M-E analysis		
Input variable		Value
Year of road section construction		2020
Year of superload passage		2021
AADTT		1,000
Number of lanes		2
Length of section (mi)		10
Treatment cost (\$)		220,000
Discount rate (%)		5.5

The procedure users follow in the navigation panel of RISAT for flexible pavement analysis closely mirrors that used in JPCP analysis, except that users select AC Asphalt Pavement among the two pavement system options and opt for IoH as the superload parent class and select manure tanker as the superload sub-type. For detailed guidance on the navigation panel steps, refer to the previous section of this appendix.

Users are required to input properties of the flexible pavement system into the designated green cells utilizing US units (Figure 133a). White cells are exclusively for automatically converting values derived from the inputs shown in the green cells. Users must select the combination for the modulus of elasticity for all four layers of the flexible pavement system from four available

options: spring, summer, fall, and winter season-based combinations for modulus of elasticity (Figure 133b). It's important to note that all input cells will be guided by an input range and recommended value. If users input values outside the specified range for any variable, a warning popup will appear (Figure 133c). Once the structural properties of the flexible pavement system have been entered, a schematic drawing depicting the flexible pavement structure will be generated (Figure 133d). This schematic will illustrate the thickness of each layer of the flexible pavement structure.

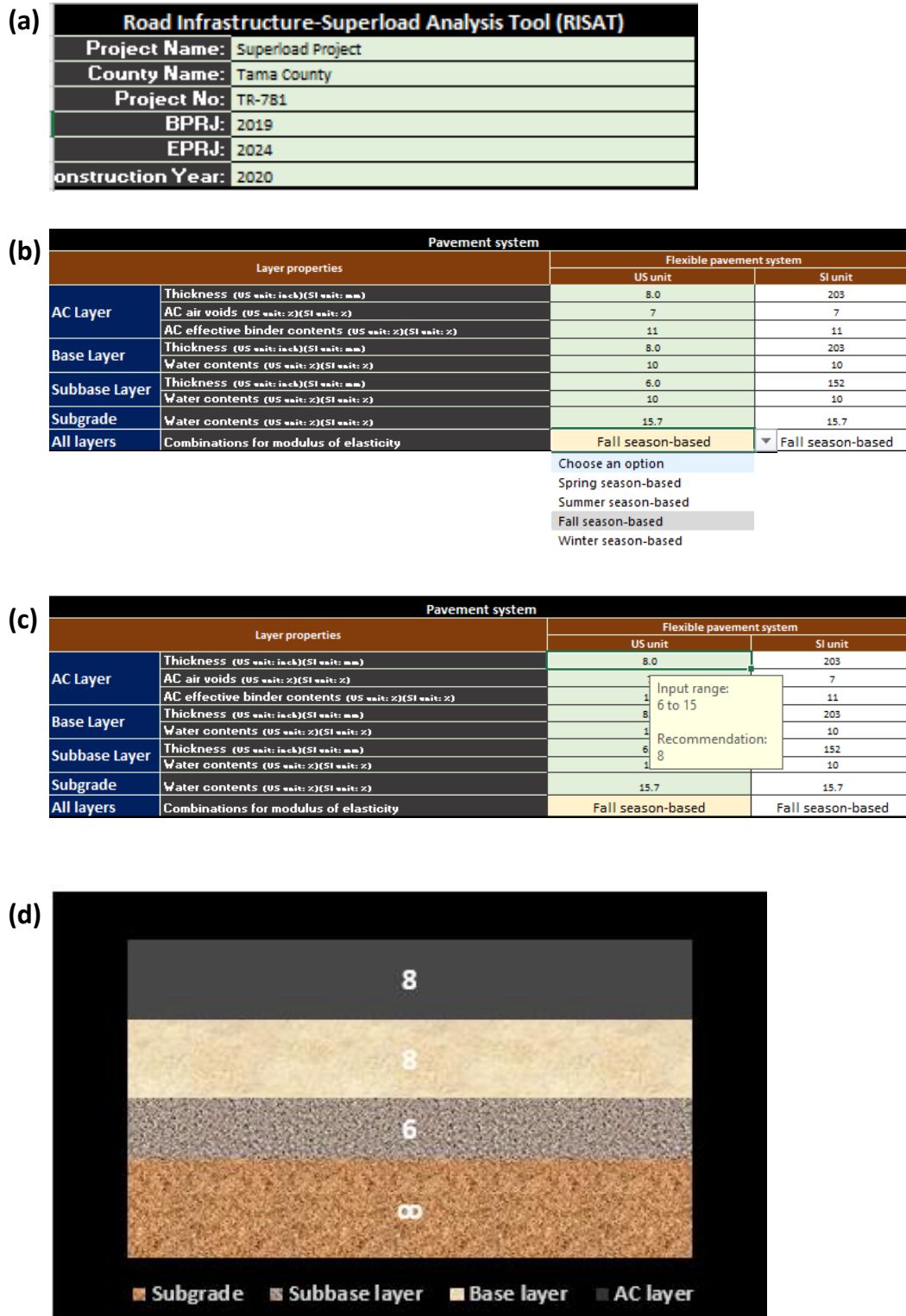


Figure 133. Details of RISAT sub-tool components for flexible pavement analysis: (a) basic project information, (b) flexible pavement structural properties, (c) recommended input range and value, and (d) schematic drawing depicting flexible pavement structure

[illegible]

Beneath the input cells for superload properties, users will find additional input cells necessary for conducting M-E analysis, specifically for evaluating pavement performance and calculating the RDAC and the reduction in service life (Figure 135). Users are also afforded the option to scale the results of mechanistic-based analysis using in situ data collected from the remote data acquisition system. If users opt for data scaling based on in situ data, the mechanistic-based data will be scaled accordingly. Conversely, selecting no data scaling will result in outputs derived solely from mechanistic-based analysis results.

Additional information for M-E analysis			Data scaling option	
Information for M-E analysis		Flexible pavement system		No data scaling
Items	Construction year		2020	Choose an option Data scaling based on in-situ data No data scaling
	Superload travel year		2021	
	AADTT		1000	
	Number of lanes		2	
	Length of section (mile)		10	
	Treatment cost (\$)		220000	
	Discount rate (%)		5.5	

Figure 135. Details of RISAT sub-tool components for flexible pavement analysis, requesting additional information for M-E analysis and providing options for data scaling

Users will consequently obtain outputs such as N_f and damage ratio related to bottom-up fatigue and rutting damages, as well as RDAC and reduction in service life of flexible pavement when subjected to a single pass of a manure tanker IoH (Figure 136).

Estimation of damage ratio			
Fatigue cracking			Flexible pavement system
Calculate bottom-up fatigue damage ratio	N _f	Fall season-based	1132684.299
		Yearly-based	9803391.574
	Damage ratio	Fall season-based	1.212405408
		Yearly-based	1.397261308
Rutting			Flexible pavement system
Calculate rutting damage ratio	N _f	Fall season-based	0.001084727
		Yearly-based	0.000418507
	Damage ratio	Fall season-based	1.005320842
		Yearly-based	0.962597905

Estimation of RDAC and service life reduction			
RDAC and service life reduction			Flexible pavement system
Calculate Road Damage-Associated Cost (RDAC)	RDAC (\$)	Fall season-based	10
		Yearly-based	17
	Service life reduction (days)	Fall season-based	0
		Yearly-based	0

Figure 136. RISAT outputs related to flexible pavement under manure tanker IoH

Users can generate an Excel file that will be located in the same folder where the RISAT is located. This file provides a table summarizing the outputs, and it can be generated by clicking the EXPORT RESULTS button (Figure 137).

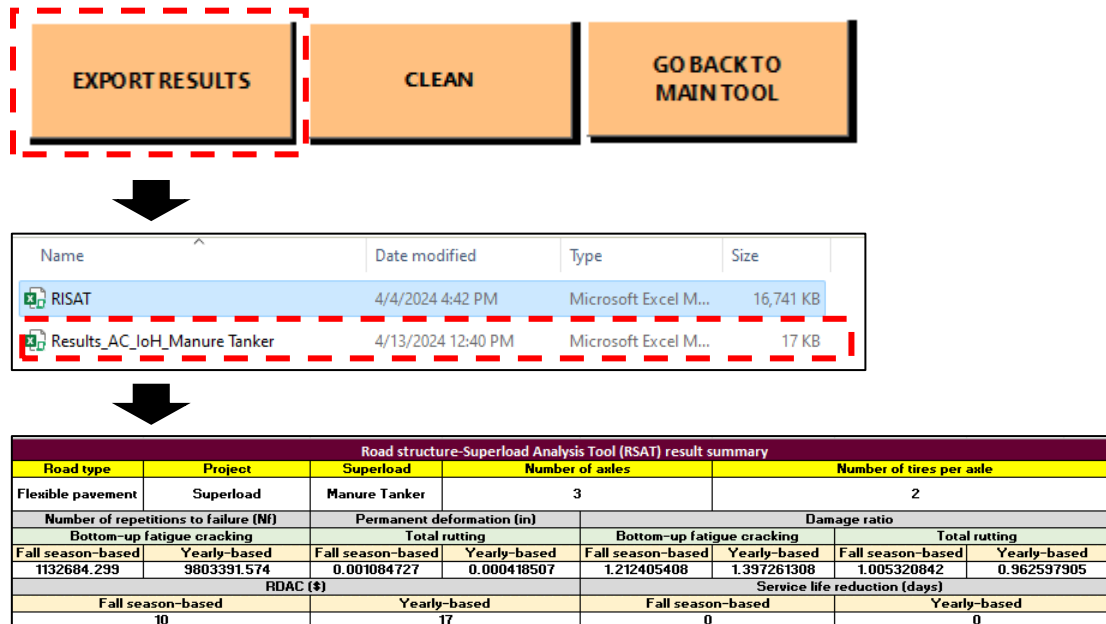


Figure 137. Excel-based output file generation from RISAT regarding the flexible pavement analysis under manure tanker IoH

**THE INSTITUTE FOR TRANSPORTATION IS THE FOCAL POINT FOR TRANSPORTATION
AT IOWA STATE UNIVERSITY.**

InTrans centers and programs perform transportation research and provide technology transfer services for government agencies and private companies;

InTrans contributes to Iowa State University and the College of Engineering's educational programs for transportation students and provides K–12 outreach; and

InTrans conducts local, regional, and national transportation services and continuing education programs.



**IOWA STATE
UNIVERSITY**

Visit InTrans.iastate.edu for color pdfs of this and other research reports.